MALAYSIAN JOURNAL OF SCIENCE
MJS
ISSN 1394-3065

Malaysian Journal of Science

Vol 44 | No 1 | March 2025

MJS in indexed in Scopus, Google Scholar, Chemical Abstracts Service Database, ASEAN Citation Index (ACI), & MyCite.

MALAYSIAN JOURNAL OF SCIENCE
MJS
ISSN 1394-3065

Regular Issue

Malaysian Journal of Science 44 (1): 1-8 (March 2025)
https://mjs.um.edu.my

Lignin and Cellulose Nanofibers from *Bambusa vulgaris* Schrad (Bamboo): An Extraction, Preparation and Characterization Study

Tawakaltu AbdulRasheed-Adeleke[1a], Evans Chidi Egwim[2a], Stephen Shaibu Ochigbo[3b], Adefowope Saheed Alabi[4c], Christopher Chintua Enweremadu[5d] and Joshua Olusegun Okeniyi[6de]*

Abstract: In this paper, lignin and cellulose nanofibers were extracted and prepared from *Bambusa vulgaris* schrad (*B. vulgaris*: bamboo) before being subjected to characterization investigations. These extractions and preparations of the lignin and cellulose nanofibers were carried out chemically using alkali combined with bleaching treatments together with acid hydrolysis and sonication. The cellulose nanofibers were then subjected to morphological and dimensional characterization of the Zetasizer, Scanning Electron Microscopy (SEM) and Transmission Electron Microscopy (TEM) instruments. The functional groups investigation, using Fourier Transform infrared spectroscopy (FTIR), and thermal degradation via the Thermogravimetric analysis (TGA), of the bamboo lignin and of the cellulose nanofibers were also carried out. Results revealed that the percentage yields of the bamboo lignin and bamboo nanofiber were 21.91 wt% and 33.6 wt% respectively. The SEM and TEM investigations indicated the prepared nanofibers were rod-like in morphology, having sizes ranging from 20 to 100 nm. FTIR showed that the lignin extracted from bamboo typified G-S type lignin while the nanofibers are completely devoid of lignin. TGA revealed that the lignin was more thermally stable than the nanofiber under the test conditions. The obtained lignin and cellulose nanofibers showed promise for possible application as reinforcement agents in biodegradable nanocomposite film preparation.

Keywords: *Bamboo, cellulose nanofibers, lignin, materials extraction, materials characterization.*

1. Introduction

Cellulose and lignin are natural organic polymers found mainly in plants. Cellulose is the most widely available biopolymer having straight chain of D-glucose units, which are linked together via the bonds of $\beta(1 \rightarrow 4)$-glycosides (Vazquez et al., 2013). It is a fundamental structural constituent of plants' primary cell wall, and of some species of algae, as well as of the oomycetes. It is also known that some species of bacteria also secrete cellulose for the formation of biofilms (Brethauer et al., 2020; Beloin et al., 2008). In contrast, lignin is a polymeric natural product resulting from trans-coniferyl alcohol, trans-sinapyl alcohol and trans p-coumaryl alcohol polymerization (Harman-Ware et al., 2017). Lignin is a complicated compound that is generally obtained from wood, while it is also a plants' secondary cell walls fundamental component, and that is also present in some algae (Börcsök et al., 2020; Labeeuw et al., 2015; Lebo, et al., 2015; Martone, et al., 2009). Since lignin and hemicellulose are covalently linked, lignin crosslinks diverse polysaccharides of plants, and by this, gives mechanical strength to the plant's cell wall, which extend as structural strength to the whole plant actually (Jawerth et al., 2020; Salmén et al., 2016; Gibson 2012; Chabannes et al., 2001).

Cellulose and lignin have been extracted from many plants using several methods that have been reported by many authors (Dinh Vu et al., 2017; Radotić & Mićić 2016; Yong et al., 2012; Kaushik et al., 2010; Alemdar & Sain, 2008). These extractions, of both cellulose and lignin, have been put into many applications, several of which have also been detailed in the literature (Gopakumar et al., 2018; Atanda, 2015; Zakikhani et al., 2014; Bao et al., 2011). For instance, fibers obtained from these extractions can be in micro or nano form. Currently, the nano form is favored owing to the exceptional effect such as the outstanding mechanical properties that could be obtained from only a little content of the nanofiller. A variety of methods have also been employed for preparing and extracting nanofibers of high purity from cellulosic materials (Shahi et al., 2020; Phanthong et al., 2018; Menon et al., 2017; Xiao et al., 2015; Lu et al., 2013; Saito et al., 2009; Paakko et al., 2007; Elazzouzi-Hafraoui et al., 2008; Alemdar & Sain 2008).

Bambusa vulgaris schrad (*B. vulgaris*: bamboo) is a naturally occurring biomass, which grows plentifully in most of the sub-tropical countries. Also, that *B. vulgaris* contains cellulose fibers imbedded in a lignin matrix makes it to be regarded as a

Authors information:
[a]Department of Biochemistry, Federal University of Technology, Minna, Niger State, NIGERIA. Email: tawarash@yahoo.com[1], c.egwim@futminna.edu.ng[2]
[b]Department of Chemistry, Federal University of Technology, Minna, Niger State, NIGERIA. E-mail: stephenochigbo@futminna.edu.ng[3]
[c]School of Business, Project Management Department, St Lawrence College, Kingston, Ontario, CANADA. E-mail: adefowope.alabi@sl.on.ca[4]
[d]Department of Mechanical, Bioresources and Biomedical Engineering, University of South Africa, Pretoria, SOUTH AFRICA. E-mail: enwercc@unisa.ac.za[5], joshua.okeniyi@covenantuniversity.edu.ng[6]
[e]Department of Mechanical Engineering, Covenant University, Ota, Ogun State, NIGERIA. E-mail: joshua.okeniyi@covenantuniversity.edu.ng[6]
Corresponding Author: joshua.okeniyi@covenantuniversity.edu.ng

Received: January 24, 2023
Accepted: July 5, 2023
Published: March 31, 2025

DOI: https//doi.org/10.22452/mjs.vol44no1.1

composite material. This composite material exhibits many advantages, which among others includes strength, durability, light weight, stiffness, and biodegradability, and by these, *B. vulgaris* has found applications, from time memorial, in many sectors (Rahim et al*.,* 2018; Atanda, 2015; Zakikhani et al*.,* 2014; Atanda, 2015; Bao et al., 2011). Although *B. vulgaris* (bamboo) is readily available in Nigeria, it is highly underutilized (Atanda, 2015), and it has not been extensively studied as a source of nanofibers (Saniwan, et al*.,* 2012; John et al., 2007; Chakraborty et al., 2006). Hence, the focus of this study is on the application of bamboo for preparing and characterizing nanofibers and lignin.

2. Materials and Methods

Materials

Sample materials and chemicals

Collections of the stems of *B. vulgaris* (bamboo) were from the banks of River Gurara at Izom, Niger State, Nigeria. These *B. vulgaris* stems were identified and authenticated at the herbarium of National Institute for Pharmaceutical Research and Development (NIPRD), Idu, Abuja, Nigeria, where a voucher of No NIPRD/H/6793 had been dropped for future reference. Purchased from reputable chemical stores for the study include analytical grades of C_2H_5COH, H_2SO_4 and H_2O_2 (from BDH Chemicals®, England), NaOH (from Kermel®, China), and HCl (from Griffin and George®, England).

Equipment

The equipment employed in this study are: Oven (Gallenkamp® Size 2, 11526E), Autoclave (Patterson Scientific®, Prestige 2100), Digital Weighing Balance (Ohaus Cooperation®, China, Scout Pro SPU601), pH meter (Hanna®, pH 212), Thermogravimetric analyzer (Perkin Elmer® STA 6000), Transmission Electron Microscope (Zeiss Auriga® HRTEM), Scanning Electron Microscope (Zeiss Auriga® HRSEM), Fourier Transform Infrared (Perkin Elmer®, UK, Frontier FT-IR), Ultra Sonicator (Scientz®, China, SB25-12DT), Zetasizer (Malven®, USA, Nano-S series).

B. vulgaris Fiber and Lignin Preparation

The extraction of lignin from *B. vulgaris* followed the method that had been detailed in the research works reported by Yong et al. (2012), Kaushik et al. (2010) and Alemdar & Sain (2008). By these, stalks of *B. vulgaris* were sun-dried before being chopped to smaller pieces. This was followed by grinding the chopped pieces and subsequent screening to a mesh fraction of 40–60 µm. From this ground stalk of *B. vulgaris*, 20 g was soaked in 4% w/w NaOH, for 24 h at room temperature, after which it was filtered and washed with distilled water until the complete elimination of the alkali. Further filtration was carried out for the second time before treatment with 10% w/w NaOH for 4 h in an autoclave maintained at 121 °C. Rewashing of the material with distilled water and subsequent filtration then followed. The filtrate was then acidified with H_2SO_4 to pH = 2 for the precipitation of lignin. The precipitated lignin were then filtered out of the mixture, separated and was then washed severally with water before being dried in an oven set at 40 °C. The supernatant ensuing from the alkali treatment was bleached, at room temperature, in 8 % v/v H_2O_2 for 24 h to obtain *B. vulgaris* fiber, which was washed and filtered over and over again, just like before, for obtaining the fiber material from the plant, for further use.

Preparation of Nanofiber from *B. vulgaris* Fiber

Preparation of nanofiber from *B. vulgaris* fibers was done through acid hydrolysis usage (Saniwan et al., 2012 Kaushik et al., 2010). The *B. vulgaris* fibers were steeped in 10 %w/w HCl with applied ultrasonic agitation, by an ultrasonicator (SB25-12DT, Scientz®, China), for 2 h and at 60 °C. Final washing of the sample material then followed, before the homogenization of the same for 15 min in a Heidolph® DIAX 900 (USA) high shear homogenizer instrument for obtaining *B. vulgaris* nanofibers.

B. vulgaris Nanofiber and *B. vulgaris* Lignin Characterizations

Percentage yield analyses

The determinations of *B. vulgaris* nanofiber and *B. vulgaris* lignin yields were obtained from the dry weight of the sample material that was isolated based on the initial dry weight of grinded *B. vulgaris*.

Nanofiber Particle Size Analyses

Investigation of *B. vulgaris* nanofiber particle sizes in solution employed use of dynamic light scattering (DLS) by the Zetasizer Nano-S series instrument from Malven®, USA, at 173° angle of light scattering, 25°C operating temperature, and 120 sec equilibrating time. For carrying out the particle size analysis, 1 mg of the sample material was dispersed in 10 ml C_2H_5OH before being transferred, using a syringe having 0.22 µm filter coupled to it, into a polystyrene cuvette. This was then placed into in the analysis stage of the Zetasizer equipment for analyzing the *B. vulgaris* nanofiber particle sizes.

Spectra Analyses

Spectra analyses of the *B. vulgaris* nanofiber and *B. vulgaris* lignin were carried out using the Frontier FT-IR, Perkin Elma® (UK) machine, by KBr disc, with spectra range between 4000 and 400 cm^{-1}. This was used for assessing the changes in the chemical structure of the polymer, which could have taken place due to modification.

Thermal Behavior Analyses

The *B. vulgaris* nanofiber and *B. vulgaris* lignin thermal behaviors were studied using the STA 6000 model of Thermogravimetric analyzer (from Perkin Elmer®).

Morphological Analyses

Morphological investigations of the *B. vulgaris* nanofiber were done via use of the HRSEM model of Scanning Electron Microscopy (SEM) instrument (from Zeiss Auriga®) at a voltage of 15 kV. The samples for the SEM analyses were mounted on the stub having two-sided adhesive tape having a thin layer of gold for its coating (Okeniyi et al., 2018; Okeniyi et al., 2017a; Okeniyi et al., 2017b), for the non-conducting *B. vulgaris* nanofibers being investigated. A 350 times the original size were then used as the magnification for taking the images by the SEM equipment, as detailed in Kampeerapappun et al. (2007).

Transmission Electron Microscopy (TEM)

High resolution Transmission electron microscopy (HRTEM) measurements employed the use of the Zeiss Auriga® HRTEM instrument at 100kV. Samples of *B. vulgaris* nanofiber were diluted in distilled water at the ratio of 1 part *B. vulgaris* nanofiber to 20 parts distilled water. Copper grids, at 300-mesh grid sizes, were then dipped in the diluted *B. vulgaris* nanofiber solutions before the grids are dried at ambient temperature. The TEM images of the *B. vulgaris* nanofiber samples were then taken with the microscope. For these, high magnifications at 30,000 and 85,000 times the original sample size were then employed for taking images of the *B. vulgaris* nanofiber samples (Ochigbo et al., 2012; Kampeerapappun et al., 2007).

4. Discussion

Percentage Yields of *B. vulgaris* Nanofiber and Lignin

The images of *B. vulgaris* nanofiber and *B. vulgaris* lignin are presented in Figure 1. The respective percentage yields of these materials are 33.6% and 21.91%, respectively.

Figure 1. Post-processing images of (a) *B. vulgaris* lignin, and (b) *B. vulgaris* nanofiber.

B. vulgaris Nanofiber Size Distribution

The particle size distribution, of the *B. vulgaris* nanofiber sample studied, is presented in Figure 2.

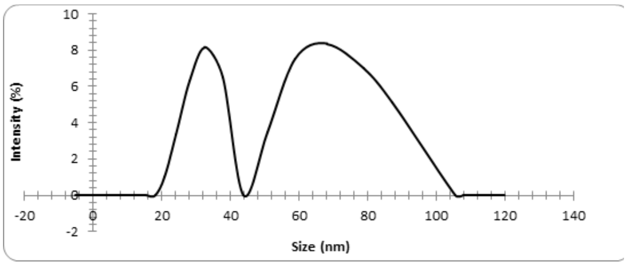

Figure 2. *B. vulgaris* nanofiber particle size distribution.

From Figure 2, the particle size distribution showed that *B. vulgaris* nanofiber had two granulometric distributions with the peak of the first at 30 nm, while the peak of the second is at 70 nm. Also, it could be observed that range of the prepared nanofiber sizes is from 20 nm to 100 nm, which indicates the fibers prepared in the present study are in the nano-sized scale. By this, therefore, the fibers could be suitable for use as fillers in the production of nanocomposite films.

Micrographs of the Prepared *B. vulgaris* Nanofiber

The micrographs, obtained from the SEM and TEM instruments, of the prepared *B. vulgaris* nanofiber, are shown in Figure 3. From Figure 3a, the SEM depicted the prepared *B. vulgaris* nanofibers as rod-like, whereas the micrograph from the TEM instrument, Figure 3b, indicated the prepared nanofibers ranged from 20 nm to 100 nm in size. These results from the TEM equipment confirm the *B. vulgaris* particle size distribution from Figure 2 that had been obtained using another instrument, i.e. the Zetasizer Nano-S series. From Figure 3b, it could also be deduced that the amorphous regions of the nanofiber were transversely cleaved by exposure to hydrochloric acid hydrolysis, thereby reducing the fibers sizes from microns to nanometers (Yong et al., 2012; Azazi-Samir et al., 2005). The result obtained herein exhibited agreement that from Liu et al. (2010), from which the size ranging between 50 nm and 100 nm cellulose nanocrystals were produced from the treatment of strands from bamboo by HNO_3-$KClO_3$ that was followed by acid hydrolysis. In another related study, Krishnan & Ramesh (2013) also reported particle width range from 30 nm to 90 nm for nanofibers obtained from coconut coir fibers, which is just as Zhang et al. (2007) obtained spherically shaped cellulose nanoparticle materials. The difference in shape of the various nanofibers obtained could be ascribed to the type of treatment used. By the morphological results in the present case, the *B. vulgaris* nanofibers, so prepared, are found appropriate as fillers in the productions of starch nanocomposite films.

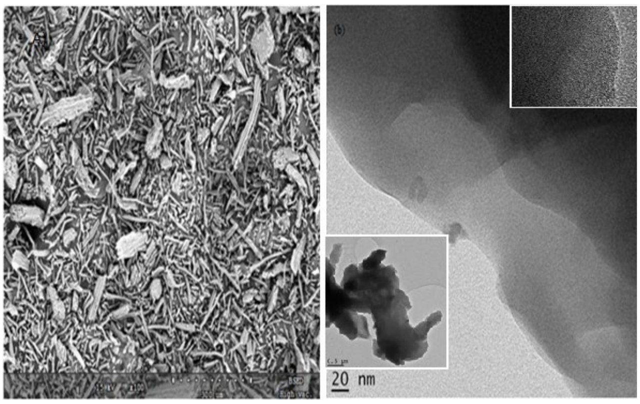

Figure 3. Micrographs of the prepared *B. vulgaris* nanofiber (a) SEM (b) TEM.

FTIR Spectra of *B. vulgaris* Lignin and *B. vulgaris* Nanofiber

The FTIR spectra from the *B. vulgaris* lignin and the *B. vulgaris* nanofiber are presented in Figure 4. The functional groups distribution proposed for assignments at adsorbed frequencies resulting from the FTIR spectra are presented in Table 1 (Okeniyi et al., 2019; Okeniyi & Popoola, 2017; Okeniyi et al., 2017c; Okeniyi et al., 2016; Coates, 2000).

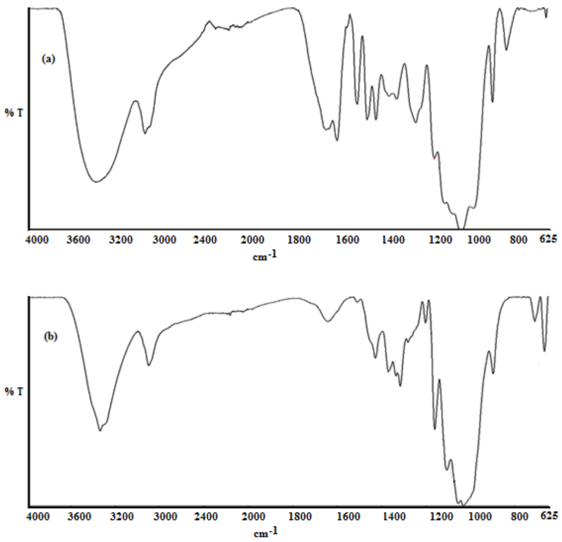

Figure 4. FTIR Spectra of (a) *B. vulgaris* lignin and (b) *B. vulgaris* nanofiber.

Table 1. Assignments of FTIR Spectra Frequencies from *B. vulgaris* lignin and *B. vulgaris* nanofiber.

B. vulgaris **Lignin Frequency (cm^{-1})**	***B. vulgaris*** **Nanofiber Frequency (cm^{-1})**	**Chemical Groups Assignment**
3364	3335	aliphatic and aromatic O–H stretch
2922, 2167	2899	saturated aliphatic C–H stretch
1648	1639	carbonyl stretch (conjugated ketone)
1597, 1506, 1461	-	Aromatic C=C–C rings stretching and bending vibrations
1422	1428	C–H in-plane bend deformation
-	1368	O–H bend induced by groups of phenol
1328	1316	C–O breathing of Syringyl ring
1242	-	C–O breathing of Guaiacyl ring
1159	1160, 1105	C–O stretch vibration of alkyl/cyclic ethers
896, 834	897	C–H ring deformation from di-substituted aryl groups
-	709, 666	O–H out-of-plane bending vibration

From the presented results in Table 1, the following characteristic absorption bands derived from the FTIR spectrum of *B. vulgaris* lignin include the absorption band at 3364 cm^{-1} that is attributed to the stretching vibration of O–H in aliphatic OH and aromatic groups, while the bands in the proximities of 2922 cm^{-1} and of 2167 cm^{-1} respectively corresponds to saturated aliphatic CH_2's asymmetrical and symmetrical stretching bands. The 1648 cm^{-1} absorption band is allocated to the stretching of conjugated carbonyl groups. Absorption bands at 1422 cm^{-1}, 1506 cm^{-1} and 1597 cm^{-1} are attributed to the skeleton vibration of aromatic groups in the *B. vulgaris* lignin. The 1461 cm^{-1} absorption frequency illustrates aromatic ring vibration and C–H deformations, while the adsorption at 1242 cm^{-1} frequency follows from guaiacyl (G) ring breathing with C–O.

In the *B. vulgaris* nanofiber, the 1368 cm^{-1} absorption frequency corresponds to O–H groups of free phenolic compounds. The absorptions at 1316 cm^{-1} from the *B. vulgaris* nanofiber spectra and at 1328 cm^{-1} by the *B. vulgaris* lignin spectra indicate syringyl (S) ring breathing with C-O. The adsorbed frequencies at 896 cm^{-1} and 1159 cm^{-1} are respectively attributed to C–O deformation and ether stretching. Finally, the adsorption at 834 cm^{-1} corresponds to ring vibrations and C–H deformation.

The distributions of functional groups for *B. vulgaris* lignin, in this study, conform to the result reported in literature for Kraft and Klason lignin extracted from pine and wood (Faix, 1991; Zheng-Jun et al., 2012b; Ghatak, 2008; Li, 2011; Ibrahim et al., 2006). In more specific terms, in the system of lignin infrared spectra classified by Faix (1991), the extracted *B. vulgaris* lignin was typically of the G-S type of lignin owing to the consideration that the absorption at 1463 cm^{-1} is of a lower intensity than the band at 1508 cm^{-1}, in that study. Also, the peak of absorption frequency obtained in that study at 1248 cm^{-1} is of a stronger intensity than the peak that was obtained at 1325 cm^{-1}, by Faix (1991).

The spectrum of FTIR obtained from *B. vulgaris* nanofiber compares well with that of *B. vulgaris* lignin, with the contrast that the absorption bands at 1506 cm^{-1} and 1597 cm^{-1}, which correspond to aryl ring of C=C–C stretching from the lignin, are absent. The non-availability of these peaks in *B. vulgaris* nanofiber is attributed to lignin elimination as a result of further acid hydrolysis in *B. vulgaris* nanofiber preparation process. Also, the peak at 1242 cm^{-1} is also absent in the *B. vulgaris* nanofiber, which illustrates the effective elimination of hemicelluloses, lignin and pectin in the process of the *B. vulgaris* nanofiber preparation.

Thermal Behaviors of *B. vulgaris* Lignin and *B. vulgaris* Nanofiber

Presented in Figure 5 are the thermal behaviors of *B. vulgaris* lignin and *B. vulgaris* nanofiber, while the essential parameters of degradation data from the thermal characterizations are plotted in Figure 6.

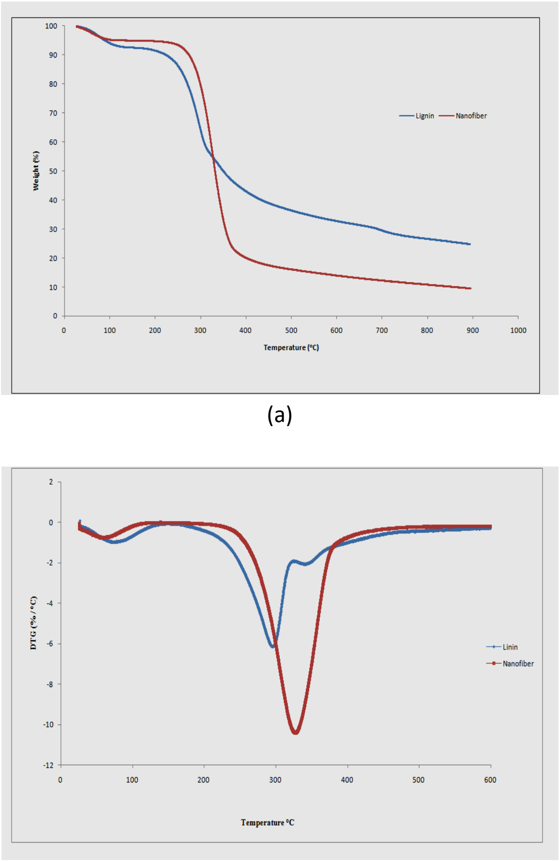

(a)

(b)

Figure 5. TGA thermograms: (a) *B. vulgaris* lignin; (b) *B. vulgaris* nanofiber.

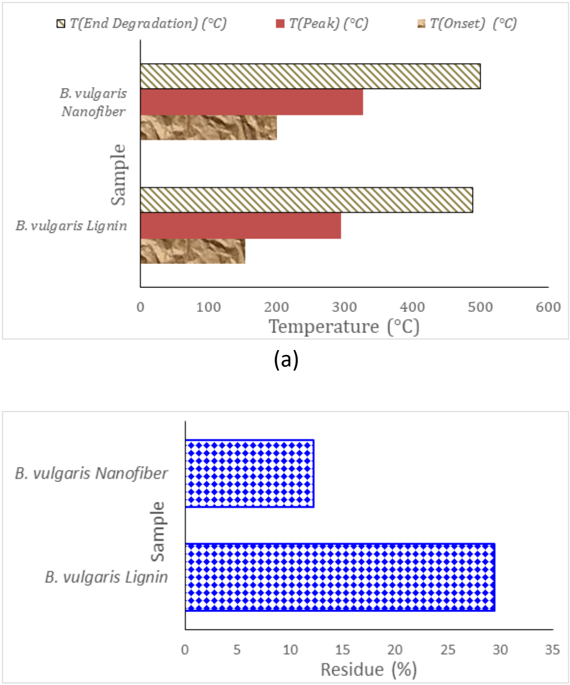

(a)

(b)

Figure 6. Plots of TGA degradation parameters from *B. vulgaris* lignin and *B. vulgaris* nanofiber thermal behavior (a) Temperature data (b) post TGA residue.

From Figure 5, it could be noted that three degradation stages occurred in lignin. The evolution of moisture content of the lignin sample was indicated by the initial weight loss that occurred at the temperature of about 96 °C. The evolution of products that are of low molecular weight such as CO_2, CO and CH_4 occurred at 154 °C and this is termed onset degradation (Visakh et al*.,* 2012a; LeVan, 1989). The peak degradation and end degradation occurred at 295 °C and 488 °C respectively with solid residue of about 29.45%. At temperatures above 500 °C, denoting the third stage, weight loss was no more obvious due to the condensation reactions of aromatic rings that often occur concurrently with decomposition reactions, at this stage, (Zheng-Jun et al*.,* 2012; Visakh et al., 2012a; LeVan, 1989). These observed thermal behaviors by *B. vulgaris* lignin in the present study exhibit similarity with that obtained from reported research works, carried out on other biological materials, by other authors including Shi et al. (2012), Sumin et al. (2012), and Li (2011).

Alternatively, the TGA plotting of the *B. vulgaris* nanofiber sample occurred in two degradation stages, during the pyrolytic degradation process. From this, an onset degradation temperature occurred at around 200 °C, which was higher than the onset degradation temperature of lignin. In the 2nd degradation stage, a sharp decomposition was observed with the peak temperature of decomposition and of end degradation occurring at 328 °C and 500 °C, respectively. Severe weight loss also occurred such that only about 12.2% remained from the initial sample of *B. vulgaris* nanofiber. The lower percentage of residue that was observed in the *B. vulgaris* nanofiber, in comparison to that of the *B. vulgaris* lignin, could be ascribed to the non-availability of mineral substances, generally oxides, in the *B. vulgaris* nanofiber. The thermogravimetric degradation behavior, detailed in the present work from *B. vulgaris* nanofiber, exhibits similarity to results obtained by Visakh et al. (2012b) and LeVan (1989).

Based on the foregoing consideration, it could be inferred that *B. vulgaris* lignin exhibits more thermal stability than the *B. vulgaris* nanofiber, under the condition at which the measurements in the study were carried out. This is in spite of the fact that the degradation occurring from *B. vulgaris* lignin began at lower temperature than the degradation from the *B. vulgaris* nanofiber.

5. Conclusion

Lignin and nanofibers were successfully extracted and prepared from *B. vulgaris* (bamboo). The morphology of the prepared *B. vulgaris* nanofibers were revealed, by SEM and TEM analyses, to be rod-shaped having sizes that range from 20 to 100 nm. FTIR showed that the lignin extracted from *B. vulgaris* is G-S lignin type while the *B. vulgaris* nanofibers are mostly devoid of lignin. TGA showed that the *B. vulgaris* lignin was more thermally stable than that of the *B. vulgaris* nanofiber under the condition that they were measured.

DOI: https://doi.org/10.22452/mjs.vol44no1.1

6. References

Atanda, J. (2015). Environmental impacts of bamboo as a substitute constructional material in Nigeria. *Case Studies in Construction Materials* 3:33–39.

Alemdar, A., Sain, M. (2008). Isolation and characterization of nanofibers from agricultural residues, Wheat straw and soy hulls. *Bioresource Technology,* 99:1664–1671.

Azizi-Samir, M.A.S., Alloin, F., Dufresne, A. (2005). Review of recent research into cellulosic whiskers, their properties and their application in nanocomposite field. *Biomacromolecules*, 6:612–626.

Bao, L., Chen, Y., Zhou, W., Wu, Y., Huang, Y. (2011). Bamboo fibers at poly(ethylene glycol) reinforced poly (butylenes succinate) biocomposites. *Journal of Applied Polymer Science,* 122:2456–2466.

Beloin C., Roux A., Ghigo J.-M. (2008). "*Escherichia coli* Biofilms." In: Romeo, T. (ed.) *Bacterial biofilms. Current Topics in Microbiology and Immunology (Volume 322)*. Springer-Verlag Berlin Heidelberg, 249–289.

Brethauer, S., Shahab, R.L., Studer, M.H. (2020). Impacts of biofilms on the conversion of cellulose. *Applied Microbiology and Biotechnology*, 104:5201–5212.

Börcsök, Z., Pásztory, Z. (2020). The role of lignin in wood working processes using elevated temperatures: an abbreviated literature survey. *European Journal of Wood and Wood Products*, doi:10.1007/s00107-020-01637-3.

Chabannes, M., Ruel, K., Yoshinaga, A., Chabbert, B., Jauneau, A., Joseleau, J.P., Boudet, A.M. (2001). *In situ* analysis of lignins in transgenic tobacco reveals a differential impact of individual transformations on the spatial patterns of lignin deposition at the cellular and subcellular levels. *Plant Journal,* 28(3):271–282

Chakraborty, A., Sain, M., Kortschot, M. (2006). Reinforcing potential of wood pulp-derived microfibers in a PVA matrix. *Holzforschung*, 60:53–8.

Coates, J. (2000). "Interpretation of infrared spectra, a practical approach." In: Meyers, R.A. (Ed.), *Encyclopedia of Analytical Chemistry*, 10815-10837.

Dinh Vu, N., Thi Tran, H., Bui, N.D., Duc Vu, C., Viet Nguyen, H. (2017). Lignin and cellulose extraction from Vietnam's rice straw using ultrasound-assisted alkaline treatment method. *International Journal of Polymer Science*, 2017:1063695.

Elazzouzi-Hafraoui, S., Nishiyama, Y., Putaux, J.L., Heux, L., Dubreuil, F., Rochas, C. (2008). The shape and size distribution of crystalline nanoparticles prepared by acid hydrolysis of native cellulose. *Biomacromolecules*, 9 (1):57–65.

Faix, O. (1991). Classification of lignins from different botanical origins by FT-IR spectroscopy. *Holzforschung,* 45:21–27.

Ghatak, H.R. (2008). Spectroscopic comparison of lignin separated by electrolysis and acid precipitation of wheat straw soda black liquor. *Industrial Crops and Products,* 28(2):206–212.

Gibson, L.J. (2012). The hierarchical structure and mechanics of plant materials. *Journal of the Royal Society Interface*, 9(76):2749–2766.

Gopakumar, D.A., Manna, S., Pasquini, D., Thomas, S. and Grohens, Y. (2018). Nanocellulose: extraction and application as a sustainable material for wastewater purification. In: Hussain, C.M. and Mishra, A.K. (Eds.) *New Polymer Nanocomposites for Environmental Remediation,* Elsevier Inc., 469–486.

Harman-Ware, A.E., Happs, R.M., Davison, B.H. and Davis, M.F. (2017). The effect of coumaryl alcohol incorporation on the structure and composition of lignin dehydrogenation polymers. *Biotechnology for Biofuels*, 10(1):1–11.

Ibrahim, M.N., Mohamad, A.H., Yusop M.R.M. (2006). The effects of lignin purification on the performance of iron complex drilling mud thinner. *Jurnal Teknologi*. 44:83–94.

Jawerth, M.E., Brett, C.J., Terrier, C., Larsson, P.T., Lawoko, M., Roth, S.V., Lundmark, S., Johansson, M. (2020). Mechanical and morphological properties of lignin-based thermosets. *ACS Applied Polymer Materials*, 2(2):668–676.

John, M.J., Anandjiwala, R.D., Pothan, L.A., Thomas, S. (2007). Cellulosic fiber reinforced green composites. *Composite Interface*, 14 (7–9):733–751.

Kampeerapappun, P., Aht-ong, D., Pentrakoon, D. and Srikulkit, K., 2007. Preparation of cassava starch/montmorillonite composite film. *Carbohydrate Polymers*, 67(2):155–163.

Kaushik, A., Singh, M., Verma, G. (2010). Green nanocomposites based on thermoplastic starch and steam exploded cellulose nanofibrils from wheat straw. *Carbohydrate Polymers,* 82:337–345.

Krishnan, V.N., Ramesh, A. (2013). Synthesis and characterization of cellulose nanofibers from coconut coir fibers. *IOSR Journal of Applied Chemistry (IOSR-JAC),* 6(3):18–23.

Labeeuw, L., Martone, P.T., Boucher, Y., Case, R.J. (2015). Ancient origin of the biosynthesis of lignin precursors. *Biology Direct*, 10(1):1–21.

DOI: https://doi.org/10.22452/mjs.vol44no1.1

Lebo, S.E.J., Gargulak, J.D. and McNally, T.J. (2015). Lignin. *Kirk-Othmer Encyclopedia of Chemical Technology*. John Wiley & Sons, Inc. doi:10.1002/0471238961.12090714120914.a01.pub3

LeVan, S.L. (1989). Thermal degradation. In: Scniewind A.P. (Ed.), *Concise Encyclopedia of Wood and Wood-based Materials.* Pergamon Press, New York, 271–273.

Li, J. (2011). Isolation of Lignin from Wood. Saimaa University of Applied Sciences, Imatra Unit of Technology, Degree Programme in Paper Technology. Bachelor's Thesis, 2011.

Liu, D., Zhong, T., Chang, P.R., Li, K., Wu, Q. (2010). Starch composites reinforced by bamboo cellulosic crystals. *Biosource Technology,* 101:2529–2536.

Lu, Y., Sun, Q., She, X., Xia, Y., Liu, Y., Li, J., Yang, D. (2013). Fabrication and characterisation of α-chitin nanofibers and highly transparent chitin films by pulsed ultrasonication Carbohydrate Polymer, 98(2):1497–1504.

Martone, P.T., Estevez, J.M., Lu, F., Ruel, K., Denny, M.W., Somerville, C., Ralph, J. (2009). Discovery of lignin in seaweed reveals convergent evolution of cell-wall architecture. *Current biology, CB* 19(2):169–75.

Menon, M.P., Selvakumar, R., Ramakrishna, S. (2017). Extraction and modification of cellulose nanofibers derived from biomass for environmental application. *RSC Advances*, 7(68):42750–42773.

Ochigbo, S.S., Luyt, A.S., Mofokeng, J.P., Antic, Z., Dramicanin, M.D., Djokovic, V. (2012). Dynamic mechanical and thermal properties of the composites of thermoplastic starch and lanthanum hydroxide nanoparticles. *Journal of Applied Polymer Science,* doi:10.1002/APP.37859.

Okeniyi, J.O., Akinlabi, E.T., Akinlabi, S.A. and Okeniyi, E.T. (2019). Biochemical characterization data from Fourier transform infra-red spectroscopy analyses of *Rhizophora mangle* L. bark-extract. *Chemical Data Collections*, 19:100177.

Okeniyi, J.O., Popoola, A.P.I., Ojewumi, M.E., Okeniyi, E.T. and Ikotun, J.O. (2018). *Tectona grandis* capped silver-nanoparticle material effects on microbial strains inducing microbiologically influenced corrosion. *International Journal of Chemical Engineering*, 2018:7161537.

Okeniyi, J.O., John, G.S., Owoeye, T.F., Okeniyi, E.T., Akinlabu, D.K., Taiwo, O.S., Awotoye, O.A., Ige, O.J., Obafemi, Y.D. (2017a). Effects of *Dialium guineense* based zinc nanoparticle material on the inhibition of microbes inducing microbiologically influenced corrosion. In: Meyers, M.A., Benavides, H.A.C., Brühl, S.P., Colorado, H.A., Dalgaard, E., Elias, C.N., Figueiredo, R.B., Garcia-Rincon, O., Kawasaki, M., Langdon, T.G., Mangalaraja, R.V., Marroquin, M.C.G., da Cunha Rocha, A., Schoenung, J.M., Costa e Silva, A., Wells, M., Yang, W. *Proceedings of the 3rd Pan American Materials Congress*, Springer, Cham, 21–31.

Okeniyi, J.O., Omotosho, O.A., Inyang, M.A., Okeniyi, E.T., Nwaokorie, I.T., Adidi, E.A., Owoeye, T.F., Nwakudu, K.C., Akinlabu, D.K., Gabriel, O.O., Taiwo, O.S. (2017b). Investigating inhibition of microbes inducing microbiologically-influenced-corrosion by *Tectona grandis* based Fe-nanoparticle material. In: *AIP Conference Proceedings*, AIP Publishing LLC, 1814(1):020034.

Okeniyi, J.O. and Popoola, A.P.I. (2017). Understanding eco-friendly anticorrosion prospect on steel-reinforcement in NaCl-immersed concrete from biochemical characterization of *Irvingia gabonensis* leaf. *Contributed Papers from Materials Science and Technology 2017 (MS&T17)*, 1070–1077.

Okeniyi, J.O., Okeniyi, E.T., Ogunlana, O.O., Owoeye, T.F. and Ogunlana, O.E. (2016). Investigating biochemical constituents of *Cymbopogon citratus* leaf: Prospects on total corrosion of concrete steel-reinforcement in acidic-sulphate medium. In: *TMS 2017 146th Annual Meeting & Exhibition Supplemental Proceedings,* Springer, Cham, 341–351.

Paakko, M., Ankerfors, M., Kosonen, H., Nykanen, A., Ahola, S., Osterberg, M., Ruokolainen, J., Laine, J., Larsson, T., Ikkala, O. (2007). Enzymatic hydrolysis combined with mechanical shearing and high-pressure homogenization for nanoscale cellulose fibrils and strong gels. *Biomacromolecules*, 8(6):1934–1941.

Phanthong, P., Reubroycharoen, P., Hao, X., Xu, G., Abudula, A. and Guan, G. (2018). Nanocellulose: Extraction and application. *Carbon Resources Conversion*, 1(1):32–43.

Radotić K., Mićić M. (2016). "Methods for extraction and purification of lignin and cellulose from plant tissues." In: Mićić M. (eds) *Sample Preparation Techniques for Soil, Plant, and Animal Samples*. Springer Protocols Handbooks. Humana Press, New York, NY. doi:10.1007/978-1-4939-3185-9_26

Rahim, W.R.W.A., Idrus, R.M. (2018). Importance and uses of forest product bamboo and rattan: their value to socioeconomics of local communities. *International Journal of Academic Research in Business and Social Sciences*, 8(12):1484–1497.

Saito, T., Hirota, M., Tamura, N., Kimura, S., Fukuzumi, H., Heux, L., Isogai, A. (2009). Individualization of nano-sized cellulose fibrils by direct surface carboxylation using tempo catalyst under neutral conditions. *Biomacromolecules*, 10(7):1992–1996.

Salmén, L., Stevanic, J.S. and Olsson, A.M. (2016). Contribution of lignin to the strength properties in wood fibres studied by dynamic FTIR spectroscopy and dynamic mechanical analysis (DMA). *Holzforschung*, 70(12):1155–1163.

Saniwan, S., Lalita, V. and Chularat, K. (2012). Starch/cellulose biocomposites prepared by high-shear homogenization/compression molding. *Journal of Materials Science and Engineering B,* 2(4):213–222.

Shahi, N., Min, B., Sapkota, B., Rangari, V.K. (2020). Eco-friendly cellulose nanofiber extraction from sugarcane bagasse and film fabrication. *Sustainability*, 12(15):6015.

Shi, Z.J., Xiao, L.P., Xu, F., Sun, R.C. (2012). Physicochemical characterization of lignin fractions sequentially isolated from bamboo (*Dendrocalamus brandisii*) with hot water and alkaline ethanol solution. *Journal of Applied Polymer Science*, 125(4):3290–3301.

Sumin, K., Lingping, X., Lingyan, M., Xueming, Z., Runcang, S. (2012). Isolation and structural characterization of lignin from cotton stalk treated in an ammonia hydrothermal system. *International Journal of Molecular Sciences,* 13:15209–15226.

Vazquez, A., Foresti, M.L., Cerrutti, P., Galvagno, M. (2013). Bacterial cellulose from simple and low cost production media by *Gluconacetobacter xylinus*. *Journal of Polymers and the Environment*, 21(2):545–554.

Visakh, P.M., Sabu, T. Kristiina O., Aji, P.M. (2012a). Crosslinked natural rubber nanocomposites reinforced with cellulose whiskers isolated from bamboo waste: Processing and mechanical/thermal properties. *Composites, Part A,* 43:735–741.

Visakh, P.M., Sabu, T., Kristiina, O., Aji, P.M. (2012b). Effect of cellulose nanofibers isolated from bamboo pulp residue on vulcanized natural rubber. *Bioresources,* 7(2):2156–2168.

Xiao, S., Gao, R., Lu, Y., Li, J., Sun, Q. (2015). Fabrication and characterization of nanofibrillated cellulose and its aerogels from natural pine needles. *Carbohydrate Polymers*, 119:202–209.

Yong, Z., Xiao-Bin, L., Chang, G., Wei-Jun, L., Ju-Ming, Y. (2012). Preparation and characterization of nano crystalline cellulose from bamboo fibers by controlled cellulase hydrolysis. *Journal of Fiber Bioengineering & Informatics*, 5(3):263–271.

Zakikhani, P. Zahari,R. Sultan, M.T.H., Majid, D.L. (2014). Bamboo fibre extraction and its reinforced polymer composite material. *International Journal of Chemical, Nuclear, Metallurgical and Materials Engineering*, 8(4):284–287.

Zhang, J., Elder, T.J., Pu, Y., Ragauskas, A.J., (2007). Facile synthesis of spherical cellulose nanoparticles. *Carbohydrate Polymers*, 69(3):607–611.

DOI: https//doi.org/10.22452/mjs.vol44no1.1

MALAYSIAN JOURNAL OF SCIENCE
MJS
ISSN 1394-3065

Regular Issue

Malaysian Journal of Science 44 (1): 9-15 (March 2025)
https://mjs.um.edu.my

Diversity of Orthoptera at Bukit Ulu Piah, Tambun, Perak, Peninsular Malaysia

Nur Atiqah, S.[1a], Azman, S.[2ab], Izfa Riza, H.[3ab]*, Dzulhelmi, M.N[4c]., Angeline D.D.[5ab] Nur Athirah, A.[6d], Rabiatul Addawiyah, S.[7e] and Wan Nurul 'Ain, W.M.N.[8ab]

Abstract: Orthoptera plays an important role in maintaining the ecosystem and is diversely distributed, with over 29,100 described species worldwide. Bukit Ulu Piah, Tambun, or Perak have ever reported no such description. This study was conducted to identify the diversity of Orthoptera and provide the first Orthoptera species checklist of the area. Net-sweeping sampling was conducted from January to April 2022 (S1, S2, S3, and S4), between 0900 and 1700. The species abundance data were analyzed using PAST software to determine the Shannon diversity index (H'), Margalef index (D_{mg}), and Evenness index (E). A total of 508 specimens from six families—Acrididae, Pyrogomorphidae, Chorotypidae, Tetrigidae, Gryllidae, and Tettigoniidae—were successfully recorded, with Acrididae showing the highest percentage value of 39.5% (15 species). Species composition comprised 38 species in 32 genera within two suborders: Caelifera (21 species) and Ensifera (17 species). *Melanoplus* sp. was the most common and abundant species, with 59 individuals (11.6% of total specimens). Orthoptera diversity in Bukit Ulu Piah, Tambun recorded high diversity (H'= 3.037), high species richness (D_{mg} = 5.939), and uniform species evenness (E = 0.5487). There was no significant difference (F = 0.4316, df=3, $p > 0.05$) in the abundance of Orthoptera across the sampling area, though this study was conducted over a short period. While this checklist provides preliminary information on Orthoptera in this area, a more extensive study should be conducted for a better assessment of its ecological status.

Keywords: *Diversity, Orthoptera, ecosystem, species richness, Bukit Ulu Piah.*

1. Introduction

Orthoptera are insects that have existed since 300 million years ago, during the Carboniferous period (Siedle et al. 2016). To date, it is estimated that over 29,100 species have been identified worldwide, covering all terrestrial ecosystems except the Antarctic continent (Cigliano et al. 2021; Ingrisch & Rentz 2009; Tan & Kamaruddin 2016a). The diversity of Orthoptera is high in tropical areas because it is the most favorable habitat for development and survival compared to other ecosystems (Sperber et al. 2021). As such, more than 2,000 Orthoptera species have been described from tropical Southeast Asia (Tan 2017). Orthoptera is the sixth largest order, consisting of suborder Caelifera (grasshoppers) and Ensiferea (katydids and crickets) (Ingrisch & Rentz 2009). The length of the antennae and the position of the tympanum membrane on the body structure are morphological features that are frequently used in Orthoptera species identification and classification. Caelifera has short antennae (less than 30 segments), and the tympanum membrane (if present) is found in the first abdominal segment, whereas Ensifera has long antennae (more than 100 segments) that resemble hair, and the tympanum membrane (if present) is found in the front tibia (Song 2018).

Orthoptera was first described in Malaysia in 1875 (Stål 1875), and studies in several localities in Peninsular Malaysia have resulted in the discovery of numerous new species such as *Lichnofugia malaya* (Tan & Ingrisch 2014), *Hancockitettix humeratus* (Storozhenko & Pushkar 2017), and *Gryllotalpa permai* (Tan & Kamaruddin 2016b). The more recent records of new species of Orthoptera include *Cycloptiloides bimaculata* (Tan et al. 2021) and *Varitrella (Cantotrella) suikes* sp. nov (Tan et al. 2020) found in Borneo. Generally, the documentation of Orthoptera started long ago, though it remains incomplete. While various studies have been done to record the Orthoptera in Peninsular Malaysia, this has yet to be done in Bukit Ulu Piah, Tambun, Perak.

The presence of Orthoptera is significant to vegetation as it signifies the ecosystem's health. The Orthoptera are important herbivores, becoming a nutritional food source for other predatory animals while also being predators of other smaller

Authors information:
[a]Department of Biological Sciences and Biotechnology, Faculty of Science and Technology, Universiti Kebangsaan Malaysia, 43600 Bangi, Selangor, MALAYSIA. E-mail: atiqahsaupi@gmail.com[1]; as@ukm.edu.my[2]; izfahazmi@ukm.edu.my[3]; angeline_2902@yahoo.com[5]; wannurulainwmn@gmail.com[8]
[b]Centre for Insect Systematics, Faculty of Science and Technology, Universiti Kebangsaan Malaysia, 43600 Bangi, Selangor, MALAYSIA.
[c]Crop Protection & Biosolution Department, FGV R&D Sdn Bhd, Tun Razak Agricultural Research Centre, 27000 Jerantut, Pahang, MALAYSIA. E-mail: dzulhelmi.mn@fgvholdings.com[4]
[d]Institute for Tropical Biology & Conservation, Universiti Malaysia Sabah, Jalan UMS, 88400 Kota Kinabalu, Sabah, MALAYSIA. athirahabdullah@ums.edu.my[6]
[e]Nature and Biodiversity Centre of Excellence (COE), Corporate Sustainability, Petroliam Nasional Berhad (PETRONAS), 50088 Kuala Lumpur, MALAYSIA. E-mail: rabiatul.shamshir@petronas.com[7]
*Corresponding Author: izfahazmi@ukm.edu.my

Received: June 8, 2023
Accepted: June 20, 2024
Published: March 31, 2025

DOI:https//doi.org/10.22452/mjs.vol44no1.2

insects (Tan & Kamaruddin 2016a). Due to their high sensitivity to ecological changes, Orthoptera can potentially serve as a biological indicator in an ecosystem (Fartmann et al. 2012). For example, *Spathosternum prasifernum prasifernum* is one of the Orthopteran species with bioindicator potential for pesticide use (Manna et al. 2020). The absence or extinction of Orthoptera species has been shown to disrupt the stability of the trophic layer structure in an ecosystem (Song 2018; Ngoute et al. 2020). Apart from that, Orthoptera possess economic significance as plant pests that invade from one area to another as a result of high population density (Song 2018). The locusts of the family Acrididae, for instance, were found in high abundance in land cleared for rice, as they feed on the initial growth of grasses. Nevertheless, the locusts are not considered significant rice pests with the appropriate management of the rice field (Le Gall et al. 2019).

Bukit Ulu Piah is a lowland secondary dipterocarp forest hill in the Kinta district, Perak. In early 1917, a tin mine was located on this forested hill (Khoo Salam & Abdur-Razak 2005). As the mining area was closed, most of the areas were converted into smallholder plantations and agricultural areas (Loh 2021). While this hill is nestled against a limestone landscape, most research activities have been focused on the limestone areas. This has led to limited information on the impact of forest clearing for agricultural purposes on the diversity of fauna communities in this area, including the Orthoptera. In order to address the knowledge gaps, this study is conducted with the objectives: 1) to provide a preliminary checklist of Orthoptera species found in Bukit Ulu Piah, and 2) to determine the diversity, richness, and abundance of Orthoptera in the area. This can provide an overview of the ecological status of each Orthopteran species in the area. This preliminary information can be considered the first step toward conserving and preserving the national ecosystem by 2025, fitting with the goals of the Malaysian National Biodiversity Policy.

2. Experimental Methods

Sampling Site

Samples were collected at Bukit Ulu Piah, Tambun, Perak. Bukit Ulu Piah is a lowland, secondary dipterocarp forest in the Kinta district, Perak, situated at 4° 35' 59" N, 101° 09' 59" E. The highest peak of Bukit Ulu Piah stands at an altitude of 175m above sea level. The sampling site comprised vegetated areas, including grasslands, fenced plants, understory vegetation in palm oil tree areas, and slopes covered with shrubs, saplings, tall trees and grass on both sides of the vehicle path to the hill summit.

Sampling Method

Sampling was conducted over four consecutive months: January (S1), February (S2), March (S3), and April (S4) at random times between 0900 and 1700 on each sampling occasion. Each sampling period consisted of two consecutive days during the second week of each month. Active sampling was performed opportunistically by walking along roads and trails of the hill forest (Tan & Kamaruddin 2016b). The sampling involved opportunistic collections through visual observation of plants, fallen trees, leaf litter, and sweeping vegetation using a sweep net measuring 30 cm in length and 25 cm in width.

Laboratory work

All collected specimens were placed in killing bottles containing ethyl acetate vapor to eliminate the insects. The specimens were subsequently preserved and identified before storage in insect boxes. A size-3 insect pin was used to pin Orthoptera specimens through the right side of their pronotum. When pinning grasshopper specimens, the hind wings were stretched to display their distinctive color and wing veining (Triplehorn & Johnson, 2005). Following the pinning procedure, specimens were oven-dried for preservation (Mohamad Salleh 1983). The preserved specimens were then labeled with collection date, location, and collector's name. Specimen identification was conducted primarily by morphospecies using references such as Triplehorn and Johnson (2005), Tan and Kamaruddin (2014, 2016a), Siedle et al. (2016), and Tan (2017). For identification and classification, applications like Picture Insect—Insect ID Pro and websites including Orthoptera Species File Version 19 5.0, Malaysia Biodiversity Information System (MyBIS), and The Biodiversity of Singapore were utilized.

Data Analysis

Species abundance refers to the high number of individuals in a species in comparison to other species. A large number of individuals obtained in the field makes the species dominant. Common species is referred to as the frequency of a species found relative to the number of samplings done at the study location and overall. Therefore, the identified common species have the potential to become abundant, and abundant species are also known as dominant species. One-way ANOVA was conducted to test significant differences in the abundance of Orthoptera in different sampling occasions. Shannon's Diversity Index (H'), Margalef's Index (D_{mg}), and Shannon's Species Evenness Index (E) were used to calculate diversity, species richness, and species evenness, respectively. T-test was conducted as a post-hoc test to determine the significant differences between the diversity value of each sampling occasion. Accumulation curves were generated using the Chao-1 richness estimator (Chao et al. 2020). All statistical analyses were conducted using PAST v4.04 (Hammer & Harper 2001).

3. Results and Discussion

Samplings of Orthoptera were conducted in Bukit Ulu Piah Tambun, Piah, to identify the diversity and abundance of Orthoptera based on samplings in January (S1), February (S2), March (S3), and April (S4). All sampling occasions recorded a total of 508 individuals representing six families and 38 species (Table 1). Out of the 38 species, 21 species are represented by four families (Acrididae, Pyrogomorphidae, Chorotypidae, and Tetrigidae) in suborder Caelifera, while the other 17 species are represented by two families (Gryllidae and Tettigoniidae) in suborder Ensifera. The Acrididae and Tettigoniidae are the most speciose groups, respectively, with *Melanoplus sp.* (Acrididae) identified as the most common and abundant species in Bukit Ulu Piah, with 59 individuals recorded in the four months of sampling.

The overall orthopteran diversity in Bukit Ulu Piah is H'= 3.037, while S2 has the highest diversity (H'= 2.900) of Orthoptera compared to S3 (H'= 2.763), S1 (H'= 2.665), and S4 (H'= 2.608). The difference among groups calculated showed no significant difference (F = 0.4316, df=3, $p > 0.05$). However, the post-hoc t-test on H' value shows a significant difference between S1 and S2 (t= 2.314, df=1, $p < 0.05$) and between S2 and S4 (t= 2.743, df=1, $p < 0.05$). Species richness is highest in S2 (Dmg = 5.538), followed by S3 (Dmg = 4.684), S4 (Dmg = 4.662), and S1 (Dmg = 4.372). The species evenness index (E= 0.5487) almost approaches unity 1.0, indicating nearly uniform species evenness. Chao-1 estimated 23 species for S1, 31 species for S2, and 35 species for S3 and S4. The estimated richness is very close to the observed richness (Table 2).

The accumulation of samples is shown on species-based rarefaction curves over the species richness for the entire sampling of Orthoptera at Bukit Ulu Piah, Tambun, Perak. The graph showed that sampling at these areas has approached but not reached the asymptote (Figure 2). This indicates that four sampling occasions are still insufficient to describe the entire diversity of Orthoptera in Bukit Ulu Piah, Tambun, Perak.

Table 1. Preliminary checklist and abundance of Orthoptera in Bukit Ulu Piah, Tambun, Perak collected from January 2022 (S1) to April 2022 (S4)

Suborder and Family	Species	S1	S2	S3	S4
Suborder Caelifera Acrididae	*Acrida conica* (Fabricius, 1781)	0	2	1	3
	Apalacris varicornis Walker, 1870	0	4	1	1
	Gesonula mundata (Walker, 1870)	0	1	0	0
	Melanoplus sp.	13	13	29	4
	Oxya intricata (Stål, 1861)	2	0	0	0
	Phlaeoba antennata Brunner von Wattenwyl, 1893	9	7	5	18
	Phlaeoba antennata malayensis Bolívar, 1914	0	4	4	0
	Phlaeoba infumata Brunner von Wattenwyl, 1893	11	12	15	18
	Phlaeoba sp.	12	11	14	0
	Pseudoxya diminuta (Walker, 1817)	10	17	18	3
	Pternoscirta caliginosa (Haan, 1842)	2	0	1	0
	Stenocatantops splendens (Thunberg, 1815)	0	0	0	1
	Trilophidia annulata (Thunberg, 1815)	3	4	1	3
	Valanga nigricornis (Burmeister, 1838)	1	2	3	1
	Xenocatantops humilis (Serville, 1838)	0	3	3	0
Pyrogomorphidae	*Atractomorpha* cf. *psittacina* (Haan, 1842)	0	4	6	16
	Tagasta marginella (Thunberg, 1815)	6	16	15	3
Chorotypidae	*Erianthus* sp.	0	0	0	1
Tetrigidae	*Bolivaritettix* sp.	0	1	2	0

DOI:https//doi.org/10.22452/mjs.vol44no1.2

	Coptotettix sp	2	0	1	0
	Macromotettix sp	1	1	0	1
Suborder Ensifera Gryllidae	*Euscyrtus (Osus) concinnus* (Haan, 1844)	0	2	0	2
	Loxoblemmus parabolicus Saussure, 1877	2	1	0	12
	Nisitrus vittatus (Haan, 1844)	1	2	1	1
	Patiscus cf. brevipennis Chopard, 1969	0	0	1	0
	Teleogryllus (Teleogryllus) albipalpus He, 2018	0	1	0	1
	Velarifictorus (Velarifictorus) micado (Saussure, 1877)	0	2	4	1
	Velarifictorus (Velarifictorus) aspersus (Walker, 1869)	1	2	4	0
Tettigoniidae	*Cesasundana lorniensis* Tan, 2014	0	0	3	10
	Conocephalus (Anisoptera) maculatus (Le Guillou, 1841)	9	9	14	5
	Conocephalus (Anisoptera) melaenus (Haan, 1843)	0	0	4	1
	Euconocephalus sp.	0	1	9	4
	Hexacentrus unicolor Serville, 1831	2	1	9	2
	Mecopoda elongata (Linnaeus, 1758)	1	0	0	0
	Phaneroptera brevis Serville, 1838	2	0	0	0
	Phaneroptera falcata (Poda, 1761)	0	5	0	0
	Phaulula macilenta Ichikawa, 2004	1	2	0	0
	Ruspolia lineosa (Walker, 1869)	6	1	0	0
	Sub-Total	97	131	168	112
	TOTAL	508			

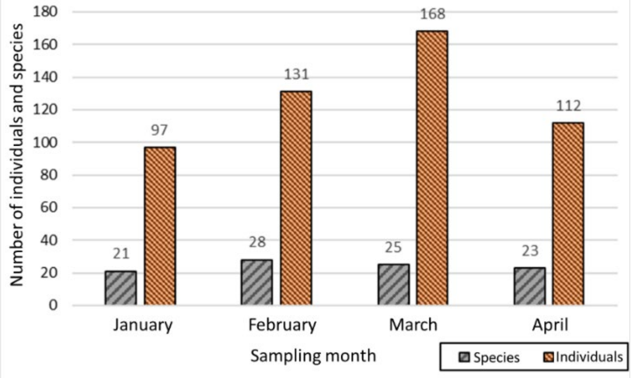

Figure 1. Species composition according to samplings months.

Table 2. Species diversity indices of the orthoptera based on four sampling occasions from January 2022 (S1) to April 2022 (S4)

	S1	S2	S3	S4
Taxa	21	28	25	23
Individuals	97	131	168	112
Margalef, D_{mg}	4.372	5.538	4.684	4.662
Shannon, H'	2.665*	2.900*	2.763	2.608*
Evenness	0.6843	0.6494	0.6340	0.5902
Chao-1	23	31	35	35

***Significant differences shown between S1 and S2, S2 and S4 at P<0.05)**

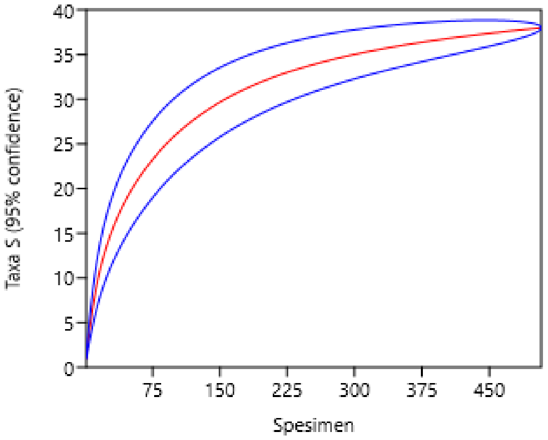

Figure 2. Rarefaction-based accumulation curve indicating the number of species relative to the number of individuals captured throughout the study.

Discussion

Orthoptera is a diverse order with a worldwide distribution. Suborder Caelifera was found in higher abundance than Ensifera, as Caelifera is biologically active during the day, which fits with the sampling period of this study. The active period of grasshoppers starts when the sun rises to enhance their metabolism and boost their foraging and sexual searching activities (Kistner & Belovsky 2017). Therefore, the Caelifera forages for food by locating suitable plant hosts during hot and sunny days. On the other hand, the ensiferans are primarily nocturnal, copulating and foraging during the night (Tan 2019). As the sampling conducted was limited to daytime, a low number of Ensifera were collected in Bukit Ulu Piah, Tambun, and Perak. Future studies should consider collecting the samples both day and night to account for diurnally and nocturnally active species.

Acrididae have been recorded as the most abundant family in Bukit Ulu Piah, dominated by *Melanoplus* sp., a generalist feeder with high habitat adaptability (Schmitz et al. 2015). Other studies have also reported a large species composition of Acrididae, with 8000 identified species belonging to 1500 genera and 25 subfamilies in the world (Shah et al. 2018). The majority of Acrididae are herbivorous and feed on different types of plants depending on hunger levels and dampness of food sources, though most of the grasshoppers have host preferences (Song et al. 2018). Bukit Ulu Piah was also observed to have a diversity of plant species as an ideal food source for the Acrididae, amplifying its abundance and diversity, as also shown in Threllfall et al. (2017).

The Shannon Diversity Index (H’) of Orthoptera in Bukit Ulu Piah is shown to vary between sampling months (S1, S2, S3, and S4). This is due to the fluctuating number of species each month with regard to its growth cycle and breeding phase, which is also influenced by the egg-hatching period of the Orthoptera (Zergoun et al. 2018). The overall diversity index of Orthoptera in Bukit Ulu Piah is H’= 3.037. However, there is no comparable value, as the diversity data of Orthoptera in Malaysia is dispersed through many different sampling methods and measurements. A standardized monitoring practice for Orthoptera will be much needed for a better status analysis of this order in the region.

Nevertheless, a comparison can be made based on the number of families. The number of Orthoptera families sampled in Bukit Ulu Piah, Tambun, was lowest when compared with Bukit Larut, Perak (10 families) (Tan & Kamaruddin 2016a) and Bukit Fraser, Pahang (10 families) (Tan & Kamaruddin 2014). Four families recorded in Bukit Larut and Bukit Fraser were not found in Bukit Ulu Piah. The four absent families in Bukit Ulu Piah are Trigonopterygidae, Gryllacrididae, Gryllotalpidae, and Mogoplistidae. While this study was done in a short period with an accumulation curve that did not reach an asymptote, it is still important to note that the difference in the type of family found might also be caused by geographical variations and the type of habitats. Bukit Larut and Bukit Fraser are highlands with altitudes of more than 1000m above sea level, in comparison with Bukit Ulu Piah, a lowland dipterocarp forest with the highest altitude at only 175m above sea level. Based on this information, it is hypothesized that Trigonopterygidae, Gryllacrididae, Gryllotalpidae, and Mogoplistidae have better adaptations to survive in higher altitudes, though this should be further explored. The absence of the four Orthopteran families may also be caused by the nature of Bukit Ulu Piah as a secondary forest, which has been disturbed by mining activities.

The fluctuating pattern was also shown in the number of Orthoptera individuals, as it peaked in March 2022. The populations are known to be highly influenced by temperature, where they are more active in locomotion for foraging and breeding in higher temperatures. This coincides with March 2022 being the drier season, with lower rain distribution following the final phase of the northeast monsoon. This occurred primarily in the northern region of Peninsular Malaysia, where Bukit Ulu Piah is located. The northern weather station in Chuping recorded a maximum temperature of 34–35 °C in March 2022 (Halid 2022). A study done by Prinster et al. (2020) also recorded an increased number of individuals during the summer or in July, which declined by September, indicating the pivotal role of temperature in determining the distribution of Orthoptera. This suggests that a more thorough study should be conducted to determine any significant correlation between Orthoptera and the abiotic factors of Bukit Ulu Piah.

A species of significant importance, namely *Valanga nigricornis* (n=7), has been recorded in Bukit Ulu Piah. Apart from corn (Prakoso 2017) and sugarcane (Sarjan et al. 2023), this species has been reported to cause severe outbreaks in young oil palm, rubber, and cocoa in the 1980s (Oktafanda 2022). The nymph of V. nigricornis actively feeds in between leaf veins, while the adult feeds on all the leaves. While it has yet to be reported to cause severe infestation in recent years, it is crucial for monitoring to be done continuously in order to assess its status, especially when Bukit Ulu Piah is currently surrounded by multiple agricultural plantations, including rubber, durian, as well as cash crops such as corn.

4. Conclusion

The diversity of Orthoptera at Bukit Ulu Piah, Tambun, Perak, resulted in 38 species dominated by the Suborder Celifera with a high number of Acrididae. The results suggested that a secondary forest such as Bukit Ulu Piah may still hold rich biodiversity despite the disturbance that occured. This study indicates that further intensive sampling needs to be carried out to account for Orthoptera of all ecological strata for a more accurate diversity measurement. In anticipation of growing agricultural areas in Bukit Ulu Piah, a continuous monitoring is also suggested to be done to determine the impact of such activities on the Orthopteran community. It is also important to note that the diversity of Orthoptera in Malaysia remains non-exhaustive, with more new records and species to discover.

5. Acknowledgements

We would like to express our gratitude to the Faculty of Science & Technology, Universiti Kebangsaan Malaysia, for providing financial and facilities support for this study. We highly appreciate and thank the reviewers for their valuable suggestions, which led to substantial improvement of this paper.

6. References

Cigliano, M.M., Braun, H., Eades, D.C. & Otte, D. 2021. *Orthoptera Species File*. Version 5.0/5.0. http://Orthoptera.SpeciesFile.org [access on 15 Oktober 2021].

Chao, A., Kubota, Y., Zelený, D., Chiu, C.H., Li, C.F., Kusumoto, B., Yasuhara, M., Thorn, S., Wei, C.L., Costello, M.J. and Colwell, R.K., 2020. Quantifying sample completeness and comparing diversities among assemblages. *Ecological Research 35*(2): 292-314.

Fartmann, T., Krämer, B., Stelzner, F. & Poniatowski, D. 2012. Orthoptera as ecological indicators for succession in steppe grassland. *Ecological Indicators* 20: 337–344.

Halid, S (2022). Hot weather to stay until May. March 29, 2022 https://www.nst.com.my/news/nation/2022/03/784301/hot-weather-stay-until-may#googlevignette [Accessed 17 February 2024]

Hammer, Ø., & Harper, D. A. 2001. Past: paleontological statistics software package for educaton and data analysis. *Palaeontologia Electronica*, 4(1), 1.

Ingrisch, S. & Rentz, D.C.F. 2009. Orthoptera. in Resh, V.H. & Cardé,R.T. Encyclopedia of Insects. Edition-2. 732-742. USA: Elsevier

Khoo N. & Abdur-Razzaq, L. 2005. Kinta Valley: Pioneering Malaysia’s modern development. Perak: Perak Academy.

Kistner, E.J. and Belovsky, G.E., 2017. Abiotic effects on the clear-winged grasshopper (Orthoptera: Acridae) and its fungal pathogen Entomophaga grylli (Entomophthorales: Entomophthoraceae) in an intermountain bunch-grass prairie. *The Canadian Entomologist*, 149(3): 315-325

Le Gall, M., Overson, R. and Cease, A., 2019. A global review on locusts (Orthoptera: Acrididae) and their interactions with livestock grazing practices. *Frontiers in Ecology and Evolution*, 7: 263

Loh, I. 2021. Fama looking into exporting frozen Tambun pomelo pulp. *The Stars,* 25 Ogos 2021.

Manna, B., Maiti, S. and Das, A., 2020. Bioindicator potential of Spathosternum prasiniferum prasiniferum (Orthoptera; Acridoidea) in pesticide (azadirachtin)-induced radical toxicity in gonadal/nymphal tissues; correlation with eco-sustainability. *Journal of Asia-Pacific Entomology*, 23(2): 350-357.

Mohamad Salleh, M.S. 1983. Pengenalan Serangga. Kota Kinabalu, Malaysia: Japan Overseas Cooperation Volunteers.

Ngoute, C.O., Kekeunou, S., Lecoq, M., Fiemapong, A.R.N., Nyobe, P.C.A.U. & Bilong, C.F.B. 2020. Effect of anthropogenic pressure on grasshopper (Orthoptera: Acridomorpha) species diversity in three forests. *Journal of Orthoptera Research* 29(1):25-34.

Oktafanda, E. 2022. Klasifikasi Citra Kualitas Bibit dalam Meningkatkan Produksi Kelapa Sawit Menggunakan Metode Convolutional Neural Network (CNN). *Jurnal Informatika Ekonomi Bisnis* 4(3): 72-77.

Prakoso, B. 2017. Biodiversitas belalang (Acrididae: ordo Orthoptera) pada agroekosistem (*zea mays l.)* dan ekosistem hutan tanaman di Kebun Raya Baturaden, Banyumas. *Biosfera* 34(2): 80-88.

Prinster, A. J., Resasco, J. & Nufio, C.R. 2020. Weather variation affects the dispersal of grasshopper beyond their elevational ranges*. Ecology and Evolution* 10 (24):14411-14422.

Sarjan, M., Muchlis, M. and Muthahanas, I., 2021. The Diversity of Major Insect Pests at Sugarcane Development Center In Dompu Distrcit, West Nusa Tenggara. *Journal of Science and Science Education*, *2*(1), pp.38-46.

Schmitz, O. J., Buchkowski, R. W., Burghardt, K. T., & Donihue, C. M. 2015. Functional traits and trait-mediated interactions: connecting community-level interactions with ecosystem functioning. In Advances in Ecological Research, pp. 319-343, Cambridge: Academic Press.

DOI:https//doi.org/10.22452/mjs.vol44no1.2

Siedle, K., Tumbrinck, J. & Tzirkalli, E. 2016. Orthoptera. In. Sparrow, D. & John, E. (eds.): An Introduction to the Wildlife of Cyprus. pp. 3-43, Cyprus: Terra Cypria

Song, H., Ricardo, M.P., Woller, D.A. & Cigliano, M.M. 2018. Evolution, Diversifaction, and Biogeography of Grasshoppers (Orthoptera: Acrididae). *Insect Systematics and Diversity* 2(4):1-25.

Sperber, C.F., Zefa, E., de Oliveira, E.C., de Campos, L.D., Bolfarini, M.P., Fianco, M., Lhano, M.G., Vicente, N., Szinwelski, N., de Souza Dias, P.G.B. and Acosta, R.C., 2021. Measuring Orthoptera Diversity. *Measuring arthropod biodiversity: a handbook of sampling methods*, pp.257-287.

Stål, C. 1875. Observations orthopterologiques. 1. Sur une systematisation nouvelle des Phasmides. 2. Sur le systeme des Acdridiides. 3. Diagnoses d' Orthopteres nouveaux. (Orthopterological observations. 1. On a new systematization of Phasmids. 2. On the Acrididae system. 3. Diagnoses of new Orthopthera). *Bihang till Kongliga Svenska Vetenskaps - akademiens Handlingar* 3(14): 1-43.

Storozhenko, S.Y. & Pushkar, T.T. 2017 A New Genus of Pygmy Locusts (Orthoptera: Tetrigidae: Cladonotinae) from the Malay Peninsula. Annales Zoologici 67(1): 47-53

Tan, M.K., Japir, R., Arthur, Y.C. & Rodzay, H.A.W. 2021. New species and taxonomic notes of scaly crickets (Orthoptera: Mogoplistidae: Mogoplistinae) from Borneo. Zootaxa 5048(3): 407-421.

Tan, M.K., Japir, R., Arthur, Y.C. & Rodzay, H.A.W. 2020. New taxa New taxa of crickets (Orthoptera: Grylloidea: Phaloriinae, Phalangopsinae, Itarinae and Podoscirtinae) from Borneo (Brunei Darussalam and Sandakan). hal-02946313Tan, M.K., 2019. Orthoptera species checklist of Bukit Timah Nature Reserve in the Zoological Reference Collection, Singapore. The Garden's Bulletin Singapore, 71(1): 331-338

Tan M.K., Japir, R., Arthur, Y.C. & Robillard, T. 2019. Crickets of the subfamily Eneopterinae (Orthoptera: Grylloidea) from Sandakan, Sabah: one new species and calling songs of a sympatric species. Zootaza 4619(2): 346-363.

Tan, M.K. 2017. Orthoptera in the Bukit Timah and Central Catchment Nature Reserves (Part 2): Suborder Ensifera. Singapore: National University Singapore.

Tan, M. K. & Ingrisch, S. 2014. New taxa and notes of some described species of Agraeciini (Orthoptera: Tettigoniidae: Conocephalinae) from Malay Peninsula. *Zootaxa* 3765(6): 541-556.

Tan, M. K. & Kamaruddin, K.N. 2014. Orthoptera of Fraser's Hill, Peninsular Malaysia. National University Singapore: Lee Kong Chian Natural History Museum.

Tan, M. K. & Kamaruddin, K.N. 2016a. A contribution to the knowledge of orthoptera diversity from Peninsular Malaysia: Bukit Larut, Perak. *Zootaxa* 4111(1): 21-40.

Tan, M. K. & Kamaruddin, K.N. 2016b. A new species of Gryllotalpa mole cricket (Orthoptera: Gryllotalpidae: Gryllotalpinae) from Peninsular Malaysia. *Zootaxa* 4066(5): 552-560.

Triplehorn, C.A. & Johnson, N.F. 2005. Borror and DeLong's Introduction to the Study of Insects. Ed. ke-7. USA: Thomson Brooks/Cole.

Zergoun, Y., Guezoul, O., Sekour, M. & Bouras, N. 2018. Effects of temperatures and rainfall variability on the abundance and idversity of caelifera (Insecta, Orthoptera) in three natural environments in the Mzab Valley, Septentrional Sahara (Algeria). *Tunisian Journal of Plant Protection* 13(2): 217-228.

DOI:https//doi.org/10.22452/mjs.vol44no1.2

MALAYSIAN JOURNAL OF SCIENCE
MJS
ISSN 1394-3065

Regular Issue

Malaysian Journal of Science 44 (1): 16-27 (March 2025)
https://mjs.um.edu.my

A Comparative Study of Various Extraction Techniques for Extracting Antioxidant-Rich Phytoconstituents from *Eryngium foetidum* Leaves Using Spectrophotometric and HPLC Methods

Shanthirasekaram Kokilananthan[1a], Vajira P. Bulugahapitiya[2b]* Harshi Manawadu[3ba] and Chinthaka Sanath Gangabadage[4b]

Abstract: *Eryngium foetidum* L. (Apiaceae) is known to possess numerous healthcare properties and has been utilized in the traditional system of medicine for various health issues. However, scientific data on its phytochemistry and antioxidant properties is limited. Therefore, this study aimed to document the phytochemistry and antioxidant properties of leaves by employing different extraction techniques to obtain plant constituents. Sonication (EN1), Soxhlet (EN2), maceration (EN3), and maceration with heat (EN4) were used as the extraction techniques while water was used as the extracting solvent. HPLC method associated with a PDA detector was developed to compare the phytochemicals profile of *E.foetidium* under different extraction techniques. The antioxidant capacities and the content of saponins (SC), terpenoids (TC), flavonoids (TFC), tannins (TTC), alkaloids (AC), and polyphenolics (TPC) were determined spectrophotometrically. The extraction techniques EN2 and EN4 were identified as yielding the highest overall results and giving a wide range of phytochemicals in the HPLC-PDA method. The quantitative analyses resulted in high SC, TTC, TC, and TPC in the EN4 (185.84±0.54 mg SE/g, 36.99±0.64 mg TAE/g, 0.89±0.01 mM LE/g, and 37.37±0.65 mg GAE/g, respectively) and low in the EN1 extraction techniques. TFC levels in EN2 were high (11.84±0.14 mg QE/g), whereas it was low in EN3. Furthermore, AC was higher in the extraction method EN3 (1.67±0.01 mg AE/g) and lower in the extraction technique EN2. The total antioxidant capacity was higher in the EN4 extract (47.17±0.20 mg Trolox Eq/g) and lower in the EN1 extract. The lowest IC_{50} in the 2,2'-Diphenyl-1-Picrylhydrazyl (DPPH) assay was noted for EN3 extract (12.91±0.02 mg/mL) revealing the highest scavenging activity than the other extracts. Based on HPLC and spectrophotometric applications, maceration with heat (EN4) is recommended for efficiently extracting polyphenols and antioxidants from *E. foetidum* leaves. The application of heat would also improve the extraction efficiency of phytochemicals.

Keywords: *Antioxidants, extraction methods, Eryngium foetidum, HPLC analysis, phytochemicals, spectrophotometric analysis.*

1. Introduction

Eryngium foetidum L. (Apiaceae), long coriander, is a biennial, pungently scented tropical plant that is also known as spiny coriander and Andu in Sinhala (Dalukdeniya & Rathnayaka, 2017; Dawilai, Muangnoi et al., 2013; Garcia et al., 1999; Okon et al., 2013). *E. foetidum* is found in the Kingdom Plantae, Division Tracheophyta, Class Magnoliopsida, Order Apiales, Family Apiaceae, Genus *Eryngium*, and Species *foetidum* (Dalukdeniya & Rathnayaka, 2017). *E. foetidum* is utilized as a healthy food due to its high levels of vitamins, riboflavin, iron, calcium, carotene, and proteins. This plant is utilized in traditional medicine to cure a variety of illnesses, including malaria, hypertension, fevers, vomiting, chills, headaches, asthma, burns, earaches, snake bites, stomachaches, scorpion stings, diarrhea, epilepsy, and arthritis (Dawilai et al., 2013; Eyoum Bille & Nguepi, 2016; Promkum et al., 2012). Because of its strong fragrance, its leaves are utilized as a flavoring in many dishes (Dawilai et al., 2013). *E. foetidum* is also used as a culinary spice and is frequently used in the fragrance and cosmetic industries (Okon et al., 2013). This plant has been shown to have anti-inflammatory, anthelmintic, anticonvulsant, analgesic, anticarcinogenic, anticlastogenic, antibacterial, and antidiabetic action due to the availability of important phytoconstituents, including alkaloids, polyphenolics, flavonoids, saponins, tannins, and terpenoids (Eyoum Bille & Nguepi, 2016; Promkum et al., 2012). Even though *E. foetidum* leaves contain important bioactive molecules, the quality and quantity of phytochemicals extracted depend on the solvents and extraction techniques employed (Anusha et al., 2013; Chandira & Jaykar, 2013; Eyoum Bille & Nguepi, 2016; Lingaraju et al., 2016; Malik et al., 2016; Okon et al., 2013).

The selection of a proper extraction technique is crucial due to the highly complex nature of phytochemical composition and the presence of trace amounts of some phytochemicals. (Cannel, 1998). The extraction methods, namely, maceration, Soxhlet extraction, decoction, percolation, digestion, counter-current extraction, infusion, fermentation, ultrasound-assisted, supercritical fluid, microwave-assisted, distillation methods, etc., are widely used in the extraction of natural products (Abubakar & Haque, 2020; Devgun et al., 2010; Handa et al., 2008; Hanif et al., 2019; Manousi et al., 2019; Mtewa et al., 2018; Pandey & Tripathi, 2014; Stratakos & Koidis, 2016). The extraction method used determines the accuracy and precision of both quantitative and qualitative measurements of plant-based phytoconstituents, as

Authors information:
[a]Department of Chemistry, Facutly of Natural Sciences, The Open University of Sri Lanka, Batticaloa Regional Centre, SRI LANKA. E-mail: skoki@ou.ac.lk[1]
[b]Department of Chemistry, Faculty of Science, University of Ruhuna, Matara 81000, SRI LANKA. E-mail: vajira@chem.ruh.ac.lk[2]; harshicm@chem.ruh.ac.lk[3]; chinthaka@chem.ruh.ac.lk[4]
*Corresponding Author: vajira@chem.ruh.ac.lk

Received: May 3, 2023
Accepted: June 20, 2024
Published: March 31, 2025

DOI: https//doi.org/10.22452/mjs.vol44no1.3

well as the stability of phytochemical components (Azwanida, 2015; Li et al., 2007). Therefore, developing effective and targeted extraction and isolation processes for bioactive natural compounds is required. Chemical profiling using HPLC and phytochemical quantification through spectrophotometric methods must be accurate and efficient methods for comparing different extracts applying varying extraction techniques and selecting the best method to extract antioxidant-rich fractions from *E. foetidum* leaves.

Now, the world's current tendency is to develop healthy, value-added products such as functional foods and nutraceuticals for the prevention of many non-communicable diseases. Therefore, the food industry and natural product researchers would benefit from the outcome of this study. Few research reports are available on the extraction of phytochemicals from *E. foetidum* leaves using water as the extracting solvent (Chandira & Jaykar, 2013; Lingaraju et al., 2016; Malik et al., 2016). Therefore, the objective of the present study was to establish appropriate extraction techniques for extracting highly essential phytoconstituents such as flavonoids, alkaloids, tannins, saponins, terpenoids, polyphenolics, and antioxidant-rich fractions from *E. foetidum* leaves applying HPLC techniques and spectrometric methods and to fill the gap of research literature on *E. foetidum*.

2. Materials and Methodology

Plant Materials and Chemicals

E. foetidum leaves were obtained in Tangalle, Matara, Sri Lanka (longitude 80.7856 ºE and latitude 6.0289 ºN). The specimen was authenticated and deposited (voucher No. AHEAD/DOR 05/C1) in the National Herbarium, Peradeniya, Sri Lanka.

Absolute ethanol (EtOH), acetic anhydride, aluminum chloride anhydrous ($AlCl_3$), ammonium hydroxide (NH_4OH), aromocresol green (BCG), n-butanol, chloroform ($CHCl_3$), copper acetate, copper sulfate ($CuSO_4$), 2,2′-diphenyl-1-picrylhydrazyl (DPPH), dimethyl sulfoxide (DMSO), ferric chloride hexahydrate ($FeCl_3{\cdot}6H_2O$), folin-Ciocalteu reagent (FC reagent), glacial acetic acid (CH_3COOH), gallic acid monohydrate, hydrochloric acid (HCl), lead acetate, linalool, magnesium ribbon (Mg), nitric acid (HNO_3), phosphomolybdic acid, potassium hydroxide (KOH), pyridine, olive oil, sodium chloride (NaCl), sodium carbonate monohydrate ($Na_2CO_3{\cdot}H_2O$), sodium hydroxide (NaOH), sodium nitroprusside, sulfuric acid (H_2SO_4), tannic acid, trolox, and 2,4,6-tripyridyl-s-triazine are classified as AR grade chemicals, benzene, diethyl ether, methanol, and hexane are come under GC grade chemicals and quercetin is comes under HPLC grade. All the chemicals were purchased from Merck and Sigma Aldrich.

Phytochemical Extraction

The collected leaves from *E. foetidum* were dried under shade in a ventilated room for about 24 hours to eliminate moisture from the surface of the washed leaves. A grinder (HL 7756 09) was then used to grind the sample. Four different extraction strategies were employed to select the best method: sonication (EN1, 1 hr, room temperature, 40 kHz), Soxhlet (EN2, 105 ºC, 6 hrs), maceration with agitation (EN3, room temperature, 6 hrs, 1000 rpm), and maceration with agitation upon heating (EN4, 60 ºC, 6 hrs, 1000 rpm) (Kokilananthan, Vajira, Gangabadage, & Harshi, 2022). About 100.00 g of *E. foetidum* leaves and 500.0 mL of distilled water were utilized in all extraction techniques. To ensure the reproducibility of the extraction yields, all four extraction processes were tripled. Cotton plugs and Whatman (No. 1) filter paper was utilized to filter the extracts. At 50 °C, the filtrates were concentrated with a rotary evaporator (Model No: HS-2005S), and the moisture was removed with a freeze dryer (S/No: FD 2020062222, Model: FE-10-MR) (Mtewa et al., 2018). The crude powder obtained was stored at -30 ºC until further application.

Samples Preparation for HPLC Applications

Chemical profiling/ identification with analytical HPLC was used to compare all four aqueous extraction techniques mentioned in this study (Al-Rimawi et al., 2017; Al-Rimawi et al., 2018; Sathyanarayanan et al., 2017). Impurities like nonpolar compounds were removed by, re-extracting the *E. foetidum* leaf aqueous extracts with diethyl ether and dichloromethane (tripled). The water layers of the extracts were concentrated using a rotary vacuum evaporator and then subjected to freeze-drying. For the HPLC applications, 500 ppm solutions of all four of them were prepared.

HPLC-PDA Application for Chemical Profiling of All Four Different Extracts

HPLC analyses were performed with a SHIMADZU LC-20AP liquid chromatograph (Japan) with four solvent delivery system quaternary pumps (FCV-200AL), including a photodiode array detector (SPD-M40). The SHIMADZU LC was comprised of a degasser (DGU-10B), and the analytical line was especially interconnected with an autosampler (SIL-10AP), and column oven (CTO-20AC). All of these modules were linked to the communication bus module (CBM-20A), which was then linked to the computer system, which was running LabSolutions (SHIMADZU) software as a data processor. The compound identification was analyzed by analytical HPLC technique with the analytical column: Shim-pack GIST C18-AQ µm, 4.6 I.D.×150 mm. The analytical method was developed by changing the solvents' polarity and flow rate. Ultra-pure distilled water and methanol were used as the solvents (a solvents system was developed with the help of TLC analysis). After the method was developed with several runs, samples were run with the developed method as follows:

The autosampler injected about 10.0 µL of sample into the column. A gradient solvent system made of ultra-pure water and methanol was used to elute the samples through the column at a flow rate of 1 mL/min. Before injecting into the column, the solvent gradient was set to begin with pure water and end with pure methanol. The samples were monitored by the PDA director with wavelengths ranging from 190 to 800 nm at 35 ºC of column oven temperature.

DOI: https//doi.org/10.22452/mjs.vol44no1.3

Phytochemical Qualitative Analysis

Using established techniques outlined in the literature (Abubakar & Haque, 2020; Gayathri & Kiruba, 2014; Kokilananthan et al., 2022b; Wadood et al., 2013), bioactive substances such as alkaloids, flavonoids, terpenoids, saponins, polyphenolics, tannins, glycosides, coumarin, anthocyanins, phytosterols, quinones, chalcones, and betacyanin were qualitatively tested in all aqueous extracts of *E. foetidum* leaves. Detailed procedures are shown in Table 1.

Table 1: Qualitative tests for phytochemical screening

Phyto- chemicals	Test method	Procedure	Observation for indicating a positive test	Reference
Alkaloids	Mayer's Test	1.0 mL plant extract (1% HCl used for the extraction) + 1.0 mL Mayer's reagent	Creamy white or yellow precipitate	(Banu & Cathrine, 2015)
	Wagner's Test	1.0 mL plant extract (1% HCl used for the extraction) + 1.0 mL Wagner's reagent	A brown or reddish precipitate	
	Dragendroff's Test	1.0 mL plant extract (1% HCl used for the extraction) + 1.0 mL Dragendroff's reagent	Reddish-brown or orange-red precipitate	
Glycosides	Keller-kilani Test	5.0 mL plant extract + 2.0 mL glacial acetic acid + 5% $FeCl_3$ solution (few drops) + 1.0 mL Con. H_2SO_4	A brown ring at the interface or violet ring may emerge under the brown ring, and a greenish ring may grow gradually across the acetic acid layer.	(Biswas, Rogers, McLaughlin, Daniels, & Yadav, 2013; Sawant & Godghate, 2013)
	Modified Borntrager's Test	5.0 mL plant extract+ 5% $FeCl_3$ solution (few drops) → keep mixture in a boiling water bath for 5 min → Extract with benzene → 1% NH_4OH react with benzene layer	Rose-pink color formation	
	Legal's Test	2.0 mL plant extract + 0.5% sodium nitroprusside (1.0 mL) + 2.0 mL pyridine + 2.0 mL NH_4OH (10%)	Pink to blood-red coloration	
Flavonoids	Alkaline reagent Test	5.0 mL plant extract + few drops NaOH (10%) (+ few drops dil. H_2SO_4)	Bright yellow coloration becomes colorless with the addition of acid	(Arya, Thakur, & Kashyap, 2012; Sawant & Godghate, 2013; Shaikh & Patil, 2020; Sheel, Nisha, & Kumar, 2014; Wadood et al., 2013)
	Shinoda Test/ Mg turning Test	2.0 mL plant extract + metal magnesium (0.50 g) + few drops Con. HCl	Pink to red color formation	
	Lead acetate Test	2.0 mL of extract + a few drops of lead acetate (5%)	White or yellow precipitate	
	$AlCl_3$ Test	3.0 mL plant extract + 4.0 mL $AlCl_3$ solution (1%)	Yellow precipitate	
	NH_4OH Test	3.0 mL plant extract + 5.0 mL NH_4OH solution + 1.0 mL Con. H_2SO_4 solution	Yellow color formation	
Saponins	Froth Test	1.0 mL plant extract + 5.0 mL distilled water (Shake well)	The foam formed lasts for 10 minutes	(Biswas et al., 2013; Mohlakoana & Moteetee, 2021)
	Olive Oil Test	10.0 mL plant extract (aqueous) + few drops olive oil → shake well	Creation of an emulsion	

DOI: https//doi.org/10.22452/mjs.vol44no1.3

Tannins	Braymer's Test	2.0 mL plant extract + 2.0 mL $FeCl_3$ (10%)	Appearance of deep greenish-grey or blue-black color	(Savithramma et al., 2011; Venkateswarlu et al., 2014)
	Lead Acetate Test	1.0 mL plant extract + 3 drops lead acetate solution	A creamy gelatinous precipitate	
Terpenoids	Salkowski's Test	1.0 mL plant + 2.0 mL chloroform +2.0 mL Con. H_2SO_4	Golden yellow or reddish-brown in the interphase	(Gayathri & Kiruba, 2014; Sawant & Godghate, 2013)
	Liebermann-Burchardt Test	1.0 mL plant extract + few drops acetic anhydride → boil & cool → Con. H_2SO_4 was added from the wall of the test tube	Brown ring at the interphase of two layers	
	Copper acetate Test	2.0 mL plant extract (aqueous) + a few drops of copper acetate solution (5%)	Development of the emerald-green color	
Poly- phenolics	Ferric Chloride Test	2.0 mL plant extract + few drops alcoholic $FeCl_3$ solution	Development of a bluish-black	(Sawant & Godghate, 2013)
Coumarins	UV light Test	1.0 mL plant extract in test tube → Test tube mouth is covered with NaOH (1N) treated filter paper → heated for a few minutes in a water bath	Yellow fluorescence in the paper under UV light	(Sawant & Godghate, 2013; Rajesh et al., 2014)
	NaOH Test	2.0 mL plant extract + 3.0 mL NaOH (10%)	Formation of yellow color	
Anthocyanins	HCl & NH3 Test	2.0 mL plant extract + 2.0 mL HCl (2 N) + 2.0 mL NH_4OH solution	Development of pink-red to blue-violet coloration	(Sawant & Godghate, 2013)
Chalcones	NaOH Test	2.0 mL plant extract + 2.0 mL NH_4OH solution	Development of the red color	(Sawant & Godghate, 2013)
Phytosterol	Salkowski's Test	2.0 mL plant extract + 2.0 mL chloroform + few drops Con. $H2_sO_4$	Development of golden red	(Sawant & Godghate, 2013)
Betacyanin	NaOH Test	2.0 mL plant extract + 1.0 mL NaOH (2 N) → heated for 5 minutes at 100 ºC	Development of yellow color	(Rajesh et al., 2014)
Quinones	H_2SO_4 Test	2.0 mL plant extract + 1.0 mL Con. $H2_sO_4$	Development of a red color	(Rajesh et al., 2014)

Phytochemical Quantitative Analysis

Each 0.10 g aqueous extract of *E. foetidum* leaves was dissolved in 0.25 mL of DMSO and diluted with 100.0 mL of MeOH to obtain a 1000 ppm concentration solution for phytochemical spectrophotometric analyses. Phytoconstituents such as terpenoids, polyphenolics, alkaloids, flavonoids, tannins, and saponins were determined based on the methods described in the literature (Kokilananthan et al., 2022a; Kokilananthan et al., 2021; Kokilananthan et al., 2020; Kokilananthan et al., 2022b; Shanthirasekaram et al., 2021).

The Folin-Ciocalteu reagent technique was employed to measure the tannin content (TTC) and phenolic content (TPC). In summary, 0.5 mL of the developed sample extract was mixed with 2.5 mL of the FC reagent mixture and permitted to stand for 5 minutes. After that, 2.0 mL of Na_2CO_3 (7.5% w/v) solution was introduced and incubated for 30 minutes. The absorbance was measured at 765 nm. For TTC, tannic acid was utilized as the standard, and the outcomes were measured in mg TAE/g, whereas for TPC, gallic acid was utilized as the standard, and the findings were presented in mg GAE/g.

To evaluate the amount of flavonoids in a sample (TFC), a spectrophotometric approach with a working solution of $AlCl_3$ was employed. In summary, 1.0 mL of sample extract was treated with 0.5 mL of $AlCl_3$ (2%) working solution and 0.5 mL of distilled water and allowed to stand for 10 minutes before detecting absorbance at 425 nm. Quercetin was used as a control, and the findings were reported in mg QE/g.

The terpenoid content (TC) was examined using a spectrophotometric approach with a phosphomolybdic acid working solution. To summarize, 1.0 mL of aqueous phosphomolybdic acid solution (5%) was gradually added to 1.0

mL of sample extract, followed by 1.0 mL of con. H_2SO_4. The mixture was thoroughly mixed and allowed to stand for 30 minutes before being diluted with MeOH to 5.0 mL. At 700 nm, the absorbance was measured. Linalool was used as the standard, and the findings are presented in mM LE/g.

A spectrophotometric method with a vanillin-sulfuric acid working solution was utilized to determine saponin content (SC). Simply put, 8% vanillin (1.0 mL) was mixed with an equal quantity of sample extract before it was placed in an ice bath, followed by 8.0 mL of H_2SO_4 (77%). The test tube was shaken before being placed in a 60 °C oven for 30 minutes. At 540 nm, the absorbance of the solution was measured after it had reached room temperature. The findings were presented in mg SE/g, and saponin was utilized as the standard.

Spectrophotometric analysis was used to determine the alkaloid content (AC) of the samples using a bromocresol green working solution. The plant extract was dissolved in a solution of 2M HCl. 10.0 mL of chloroform was used to rinse 1.0 mL of this supernatant. 0.1M NaOH was used to bring the pH of this produced sample to neutral. This was then combined with freshly prepared BCG solution (5.0 mL) and phosphate buffer solution (pH 4.7, 5.0 mL). The complex mixture was re-extracted with chloroform (1.0, 2.0, 3.0, and 4.0 mL). The extracted complex mixture was adjusted to 10.0 mL using chloroform. At 470 nm, the complex's absorbance was determined. The findings were presented in mg AE/g and measured using atropine as the standard.

Antioxidant Analysis

To test the radical scavenging capability of all aqueous extracts of *E. foetidum* leaves, the DPPH radical scavenging assay, a standardized existing approach published in the literature, was used (Abeysuriya et al., 2021; Blois, 1958; Brand-Williams et al., 1995; Kokilananthan et al., 2021; Kokilananthan et al., 2020). About 100 µL of aqueous extract (in different concentrations) was mixed with the 3.9 µL of 0.06 mM DPPH working solution. The absorbance at 517 nm was measured after 30 minutes in complete darkness. The IC_{50} value for free radical scavenging activity was assessed by a plot of the scavenging effect's percentage versus concentration. , Trolox and ascorbic acid were used as standards. A standard method that has been described in the literature was employed to measure the FRAP value of all obtained extracts from the leaves of *E. foetidum* (Biglari et al., 2008; Firuzi et al., 2005; Gliszczyńska-Świgło, 2006; Kokilananthan et al., 2021; Kokilananthan et al., 2020). The 100 µL test sample was combined with 3.0 mL of freshly prepared FRAP solution. The absorbance at 593 nm was measured after 30 minutes of incubation at 37 °C. The standard Trolox was used for the calibration.

Statistical Analysis

The data was analyzed and compared using Cochran's Q-test (non-parametric statistics) and the T-test (LSD). Statistical analysis were conducted using, R-studio software and SAS OnDemand for Academics: Studio (SAS 9.4). Using means and standard deviations, the data were displayed.

3. Results and Discussion

Extraction of Phytochemical

The yield percentages of all four different aqueous extracts of *E. foetidum* leaves were compared and statistically analyzed; the results are shown in Figures 1 and 2. of the four different extraction techniques (EN1, EN2, EN3, and EN4), the technique EN2 (5.73 ± 0.07%) produced the highest yield, followed by EN4 (5.47 ± 0.06%), EN3 (3.45 ± 0.08%), and EN1 (2.57 ± 0.09%). It is worthy of note that, as shown in Figure 2, statistical analysis data for all four *E. foetidum* leaf extracts revealed that four extraction methods generated different proportions at a 5% significant level. Even though many previous studies have been conducted using different extraction techniques and extracting solvents, most of the reports have not included the yield percentage to compare the results with current findings (Anusha et al., 2013; Eyoum Bille & Nguepi, 2016; Okon et al., 2013).

When comparing the extraction techniques EN3 and EN4, both were carried out under the same circumstances except for temperature; EN3 was carried out at room temperature, while EN4 was carried out at 60 ºC. As a result, there is a significant assertion for extraction yield variations with extraction techniques EN3 and EN4. This implies that the temperature had an impact on the extraction yield, as EN4 had a larger extraction yield than EN3. Although EN1, one of the most sophisticated extraction techniques (Mtewa et al., 2018), was used, its yield percentage was lower than that of the other techniques. This must be due to the extraction period, which is one hour in EN1 at room temperature. As a result, further studies are needed to optimize the extraction parameters, particularly the temperature and time.

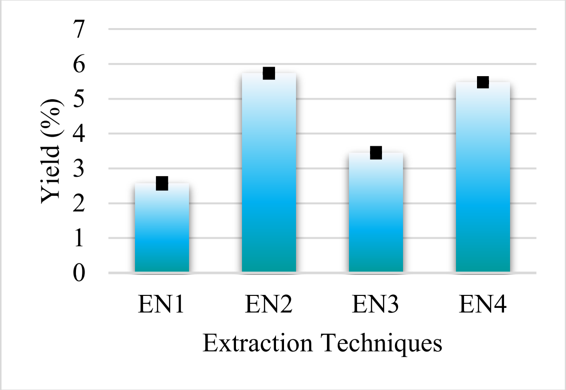

Figure 1: Yield percentage of four different extraction approaches utilized for extracting phytochemicals from *E. foetidum*.

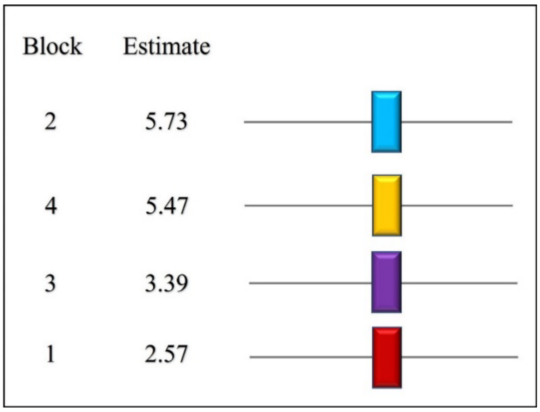

Figure 2: Statistical proof comparing the extraction yields of the four different extraction methods used to extract the phytoconstituents from *E. foetidum* leaves (Block: 1: EN1, 2: EN2, 3: EN3, 4: EN4, Alpha = 0.05, Estimate: the mean values covered by the same bar do not differ significantly.).

HPLC-PDA Chemical Profiling of All Four Different Aqueous Extracts

The HPLC technique was utilized to compare four various aqueous extracts of *E. foetidum* leaves to determine which extraction method would extract most of the phytochemicals from the plant source. As a result, an HPLC method for *E. foetidum* aqueous extracts was established, and the results were compared in various ways. According to the maximum wavelengths of the identified compounds, the extracted substances in all four extracts were first directly examined on HPLC-PDA at different wavelengths, including 254 nm, 204 nm, 654 nm, 734 nm, and 224 nm. The maximum wavelengths of most of the identified substances fall within 654 nm. Figure 3 shows the HPLC-PDA spectra from all four aqueous extracts at 654 nm.

As shown in Table 2, EN2 and EN4 extracts have more peaks or compounds in the HPLC-PDA spectra for all five different wavelengths than the other two extraction techniques. To , only the peaks with areas greater than 5×10^6 counts and heights greater than 4×10^5 counts in the HPLC-PDA spectra at all five different wavelengths were considered. As shown in Table 3, more of the higher-intensity peaks were also found in the extracts obtained by the EN2 and EN4 extraction methods. All the peaks identified in these conditions were studied and tabulated in Table 3 to be more selective.

Table 2: HPLC-PDA spectra peak data with different applications

Methods	**Extraction technique and total no of the peaks**			
	EN1	EN2	EN3	EN4
Wavelength 254 nm, 4nm	152	231	198	215
Wavelength 204 nm, 4nm	168	228	188	233
Wavelength 654 nm, 4nm	154	224	196	212
Wavelength 734 nm, 4nm	154	238	200	212
Wavelength 224 nm, 4nm	155	237	197	215

The summarized data are tabulated in Table 3 based on the peak area and peak height. Table 3 demonstrates that the extraction technique has an impact on the extraction of a single compound. Simply put, all extracts at 254 nm had a single peak at that wavelength, as shown in Table 3, except for EN1, for which there was none. Remarkably, the RT of the observed peaks differs depending on the extraction technique. That indicates that each extraction method is specific to the compounds of interest. Conversely, the same compounds were also found in all four extracts at varying levels of intensity. These findings demonstrate how important the selection extraction technique is in the extraction of desired substances from natural sources.

Table 3: HPLC-PDA spectra peaks data which greater than the area of $5×10^6$ counts and peaks data which is greater than the height of $4×10^5$ counts

Methods	**Functions**	**Total Peaks**	**Peak No**	**Extraction Techniques**							
				EN1		**EN2**		**EN3**		**EN4**	
				RT	**RP**	**RT**	**RP**	**RT**	**RP**	**RT**	**RP**
204 nm, 4nm	Area	4	1	5.32	92.76	4.33	40.94	5.56	30.28	6.19	33.38
			2	77.40	4.06	31.02	12.25	28.11	17.95	42.00	6.93
			3	99.66	3.18	77.61	13.43	77.45	17.30	77.42	17.45
			4	……	……	99.68	33.38	99.66	34.47	99.65	42.25
	Height	5	1	5.32	61.59	4.33	35.56	5.55	39.47	6.18	39.48
			2	31.13	38.41	26.36	16.02	26.30	18.45	31.39	15.7
			3	……	……	31.02	16.51	28.11	42.08	33.69	14.38
			4	……	……	31.15	14.79	……	……	35.00	14.29
			5	……	……	35.92	17.12	……	……	99.65	16.14
224 nm, 4nm	Area	3	1	5.34	100.00	4.34	61.58	5.59	44.41	6.20	38.40
			2	……	……	31.02	38.42	28.11	55.59	42.00	23.96
			3	……	……	……	……	……	……	99.65	37.65
	Height	4	1	31.13	57.23	26.36	25.46	26.30	30.08	6.20	23.88
			2	39.41	42.77	31.02	25.66	28.11	69.92	31.39	27.52
			3	……	……	31.15	22.68	……	……	33.69	23.89
			4	……	……	35.92	26.21	……	……	35.00	24.72
254 nm, 4nm	Area	1	1	……	……	31.02	100.00	28.11	100.00	42.00	100.00
	Height	6	1	31.13	55.39	26.36	18.19	26.30	22.91	27.65	23.49
			2	39.41	44.61	31.02	17.7	28.11	54.19	31.39	27.1
			3	……	……	31.15	15.47	39.45	22.9	32.88	24.27
			4	……	……	35.17	15.53	……	……	35.00	25.14
			5	……	……	35.92	18.09	……	……	……	……
			6	……	……	50.95	15.02	……	……	……	……
654 nm, 4nm	Area	3	1	39.41	100.00	31.01	100.00	28.13	100.00	31.39	34.81
			2	……	……	……	……	……	……	42.00	33.46
			3	……	……	……	……	……	……	68.20	31.73
	Height	6	1	31.13	36.55	26.36	18.72	23.78	14.72	27.65	19.62
			2	39.41	34.97	31.01	17.39	26.30	14.44	31.39	21.71
			3	48.04	28.48	31.15	14.62	28.13	38.82	32.88	20.82
			4	……	……	35.17	16.27	39.45	16.58	35.00	20.69
			5	……	……	35.92	17.69	44.42	15.43	36.61	17.16
			6	……	……	50.95	15.31	……	……	……	……
734 nm, 4nm	Area	3	1	39.41	100.00	31.01	100.00	28.13	100.00	31.39	34.32
			2	……	……	……	……	……	……	42.00	32.52
			3	……	……	……	……	……	……	68.20	33.16
	Height	6	1	25.37	28.28	26.36	18.57	23.78	14.73	27.65	19.58
			2	31.13	37.09	31.01	17.64	26.30	14.79	31.39	21.99
			3	39.41	34.63	31.15	14.63	28.13	38.64	32.88	20.74
			4	……	……	35.17	15.75	39.45	16.42	35.00	20.44
			5	……	……	35.92	17.93	44.42	15.42	36.61	17.26
			6	……	……	50.95	15.49	……	……	……	……

RT: Retention time, RP: Relative percentage

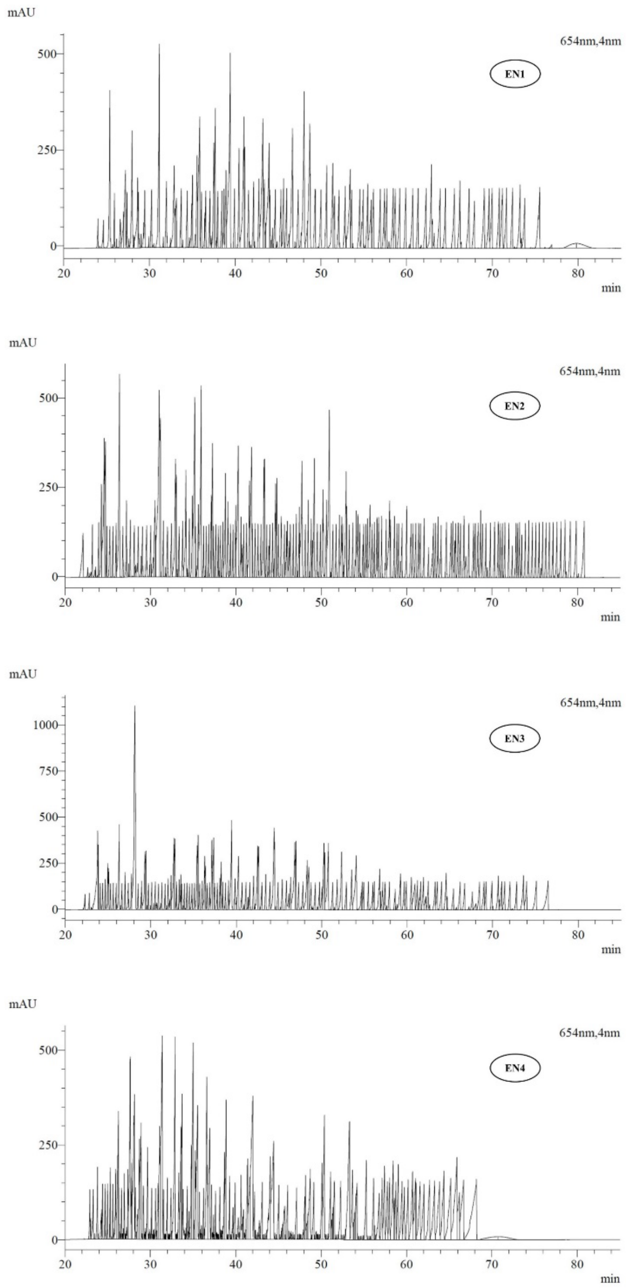

Figure 3: HPLC spectra of all four different aqueous extracts of *E. foetidum* leaves at 654 nm, 4 nm.

Phytochemicals Qualitative Analysis

All four aqueous extracts of *E. foetidum* leaves from four different extraction techniques contained essential phytochemicals such as saponins, terpenoids, alkaloids, polyphenolics, tannins, glycosides, flavonoids, phytosterols, coumarins, quinones, and betacyanins, but not chalcones and anthocyanins. The availability of phytochemicals in all four different aqueous extracts of *E. foetidum* leaves was also supported statistically by statistical analysis using the non-parametric test. Statistical analysis revealed no significant variation in the presence of essential phytoconstituents examined in the four distinct aqueous extracts recovered from *E. foetidum* leaves using four different extraction methods at the 5% significant level. Since no variation in the qualitative analysis of the phytoconstituents was found at the 5% significant level, this study revealed that any of these extraction techniques may be employed to extract phytoconstituents.

Phytochemical Quantitative Analysis

The quantification of AC, TPC, TC, TTC, SC, and TFC in all four distinct aqueous extracts recovered from *E. foetidum* leaves by four different extraction methods exhibited varied quantities, as shown in Table 4. The findings demonstrated the presence of a variety of phytoconstituents in *E. foetidum* leaves, with the SC, TPC, TC, and TTC accounts showing to be greater in the extraction method EN4 (185.84 ± 0.54 mg SE/g, 37.37 ± 0.65 mg GAE/g, 0.89 ± 0.01 mM LE/g, and 36.99 ± 0.64 mg TAE/g, respectively) and smaller in the method EN1. TFC values in extraction technique EN2 were high (11.84 ± 0.14 mg QE/g), but low in extraction technique EN3. In contrast, AC was revealed to be greater in extraction approach EN3 (1.67 ± 0.01 mg AE/g) and lower in extraction approach EN2. As shown in Figure 4, the statistical analysis, the T-test (LSD), strongly disclosed that all of the extraction approaches employed in this research extracted significantly various amounts of saponins, polyphenolics, alkaloids, terpenoids, flavonoids, and tannins at the 5% significant level.

This study demonstrated that when extracting polyphenolics, tannins, saponins, and terpenoids from the leaves of *E. foetidum* using water as a solvent, the EN4 extraction technique is the best method. The EN4 extraction process can extract the majority of significant phytochemicals. The extraction technique EN2 can extract a greater quantity of flavonoids than the other extraction methods utilized in this study. The soxhlet extraction method (EN2) has previously been shown to be a highly effective way to extract flavonoids from medicinal herbs (Kokilananthan et al., 2022a; Kokilananthan et al., 2022b). The current research also found that the extraction technique EN3 is an excellent approach for extracting alkaloids, as previously reported (Kokilananthan et al., 2022a; Kokilananthan et al., 2022b).

Table 4: Phytochemical quantitative analysis data of aqueous extracts from four different extraction approaches utilized for extracting phytochemicals from *E. foetidum*. The values represent the mean and standard deviation of triplicate samples.

Phytochemicals	**Extraction Techniques**			
	EN1	**EN2**	**EN3**	**EN4**
Polyphenolics content (mg GAE/g)	19.73 ± 0.06	30.00 ± 0.40	24.87 ± 0.50	37.37 ± 0.65
Flavonoids content (mg QE/g)	6.33 ± 0.04	11.84 ± 0.14	5.97 ± 0.03	9.22 ± 0.17
Tannins content (mg TAE/g)	19.53 ± 0.05	29.69 ± 0.40	24.61 ± 0.50	36.99 ± 0.64
Terpenoids content (mM LE/g)	0.51 ± 0.00	0.79 ± 0.02	0.67 ± 0.01	0.89 ± 0.01

Saponins content (mg SE/g)	143.22 ± 0.41	171.08 ± 0.90	150.13 ± 0.74	185.84 ± 0.54
Alkaloids content (mg AE/g)	1.61 ± 0.01	0.66 ± 0.01	1.67 ± 0.01	0.70 ± 0.01

Samples were collected at Bukit Ulu Piah, Tambun, Perak. Bukit Ulu Piah is a lowland, secondary dipterocarp forest in the Kinta district, Perak, situated at 4° 35' 59" N, 101° 09' 59" E. The highest peak of Bukit Ulu Piah stands at an altitude of 175m above sea level. The sampling site comprised vegetated areas, including grasslands, fenced plants, understory vegetation in palm oil tree areas, and slopes covered with shrubs, saplings, tall trees and grass on both sides of the vehicle path to the hill summit.

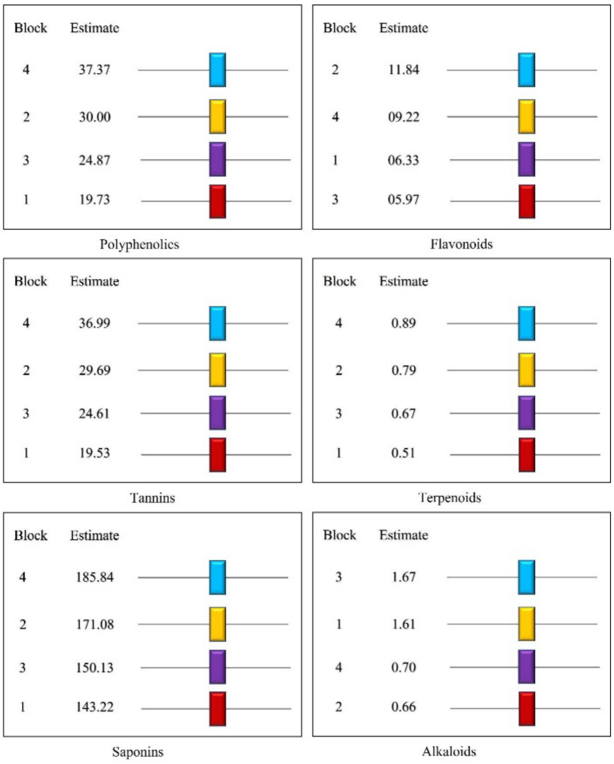

Figure 4: Data from statistical analysis of phytoconstituents quantification of four main extraction methods of *E. foetidum* leaves' aqueous extracts. (Block: 1: EN01, 2: EN02, 3: EN03, 4: EN04, Alpha = 0.05, Estimate: The mean values covered by the same bar do not differ significantly).

Antioxidant Analysis

The antioxidant capacity was seen in all four aqueous extracts of *E. foetidum* leaves prepared using the four different extraction techniques, but it varied greatly between techniques. The total antioxidant power determined by the FRAP assay revealed that the extraction approach EN4 (47.17 ± 0.20 mg Trolox Eq/g) has a greater capacity for antioxidants than all other aqueous extracts of *E. foetidum* leaves. Most notably, all employed extraction approaches have shown significant differences at the 5% significant level, as illustrated in Figures 5 and 6.

Figures 5 and 6 illustrate the results of DPPH radical scavenging effect, which revealed that extraction procedure EN3 (12.91 ±0.02 mg/ml) has relatively higher levels of radical scavenging capacity than the other three methods. However, the radical scavenging capacity of four distinct *E. foetidum* leaf aqueous extracts is substantially lower than that of the standard used, ascorbic acid (139.05 ± 0.05 ppm). Additionally, statistical results revealed that all four aqueous extracts from *E. foetidum* leaves did not have the same scavenging capability at the 5% significant level. The results showed that all four extraction methods utilized in this study resulted in various degrees of antioxidant potential with *E. foetidum* leaves. As a result, the extraction approach EN4 is a well-suited method in all aspects of analysis. According to the current study, extraction methodology EN4 is a well-suited method in every aspect.

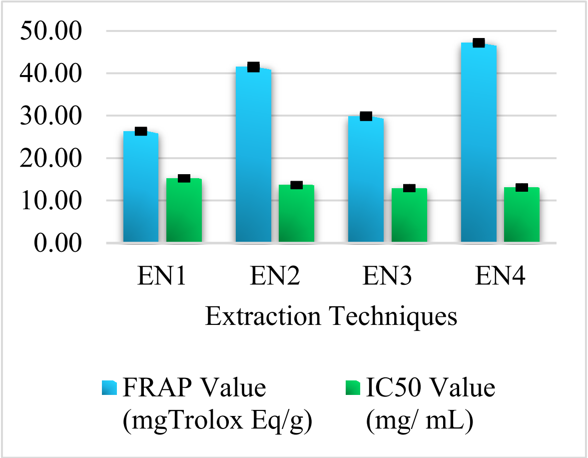

Figure 5: Comparison of antioxidant potential of four different aqueous extracts of *E. foetidum* leaves using FRAP and DPPH assays.

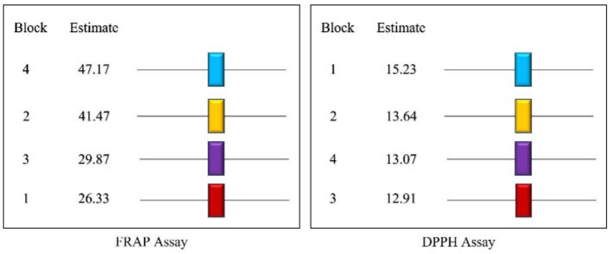

Figure 6: Data from statistical analysis of the antioxidant potential of four distinct extraction methods of *E. foetidum* leaves' aqueous extracts. (Block: 1: EN1, 2: EN2, 3: EN3, 4: EN4, Alpha = 0.05, Estimate: The mean values covered by the same bar do not differ significantly).

As a result, the HPLC application is also detailed, as other phytochemical quantitative and antioxidant analysis results show that EN2 and EN4 are the best extraction methods to extract most of the phytochemicals from the leaves of *E. foetidum*. Notably, while the number of chemical constituents was higher in the extraction technique EN2 than in the extraction technique EN4 based on the HPLC spectra, the antioxidative potential by FRAP assay was higher in the extraction technique EN4. Likely, other quantified phytochemicals, except for flavonoids, were found to be higher in the EN4 extraction technique, whereas the second highest was observed in the EN2 extraction technique, but interestingly, flavonoids were found to be the most abundant in EN2. As a result, this study strongly suggests that the extraction techniques EN2 and EN4 are the best methods for extracting phytochemicals, with EN4 being the most recommended when EN2 and EN4 are compared. Notably, this is the first comprehensive study comparing aqueous extraction techniques with spectrophotometric and HPLC analyses.

4. Conclusion

This study concludes that the EN4 extraction method (maceration with agitation at 60ºC) effectively extracts antioxidants, saponins, polyphenolics, terpenoids, and tannins from *E. foetidum* leaves. The EN2 method (Soxhlet at 105ºC) is optimal for flavonoids, while EN3 (maceration with agitation at room temperature) excels in alkaloid extraction. Although *E. foetidum* leaves have a broad range of bioactive constituents and higher antioxidant properties, the quantity of phytoconstituents and antioxidant potential varies on extraction method. HPLC is the preferred method for analyzing crude phytochemical profile of crude extracts. Thus, choosing the right extraction process is crucial in natural product isolation.

5. Acknowledgement

The authors would like to thank the AHEAD/RA3/RUH/CHE/DOR-No-05 grant for financial support and the Department of Chemistry, University of Ruhuna, Sri Lanka, for supplying the required laboratory facilities.

6. References

Abeysuriya, H. I., Bulugahapitiya, V. P., & Jayatissa, L. P. (2021). Comparative account of vitamin C contents, antioxidant properties, and iron contents of minor fruits in Sri Lanka. *Plant Science Today, 8*(4), 795–803. https://doi.org/10.14719/pst.2021.8.4.1266

Abubakar, A. R., & Haque, M. (2020). Preparation of medicinal plants: basic extraction and fractionation procedures for experimental purposes. *Journal of Pharmacy and Bioallied Sciences, 12*(1), 1-10. https://doi.org/10.4103/jpbs.JPBS_175_19

Al-Rimawi, F., Abu-Lafi, S., Abbadi, J., Alamarneh, A. A., Sawahreh, R. A., & Odeh, I. (2017). Analysis of phenolic and flavonoids of wild *Ephedra alata* plant extracts by LC/PDA and LC/MS and their antioxidant activity. *African Journal of Traditional, Complementary and Alternative Medicines, 14*(2), 130-141. https://doi.org/10.21010/ajtcam.v14i2.14

Al-Rimawi, F., Alakhras, F., Al-Zereini, W. A., Aldal'in, H. K., Abu-Lafi, S., Al-Mazaideh, G. M., & Salman, H. J. A. (2018). HPLC analysis of the chemical composition of selected Jordanian medicinal plants and their bioactive properties. *Original Journal of Chemistry, 34*(5), 2397-2403. http://dx.doi.org/10.13005/ojc/340522

Anusha, S., Madhu, M. L., Seethalakshmy, S., & Nair, S. A. (2013). Antioxidant and antimicrobial activities of methanolic leaf extracts of *Coriandrum sativum* and *Eryngium foetidum* L. *International Journal of Research and Engineering, 2*(8), 28-32.

Arya, V., Thakur, N., & Kashyap, C. (2012). Preliminary phytochemical analysis of the extracts of Psidium leaves. *Journal of Pharmacognosy Phytochemistry, 1*(1), 1-5.

Azwanida, N. (2015). A review on the extraction methods use in medicinal plants, principle, strength and limitation. *Medicinal & Aromatic Plants, 4*(196), 2167-0412. http://dx.doi.org/10.4172/2167-0412.1000196

Banu, K. S., & Cathrine, L. (2015). General techniques involved in phytochemical analysis. *International Journal of Advanced Research in Chemical Science, 2*(4), 25-32.

Biglari, F., AlKarkhi, A. F., & Easa, A. M. (2008). Antioxidant activity and phenolic content of various date palm (*Phoenix dactylifera*) fruits from Iran. *Food Chemistry, 107*(4), 1636-1641. https://doi.org/10.1016/j.foodchem.2007.10.033

Biswas, B., Rogers, K., McLaughlin, F., Daniels, D., & Yadav, A. (2013). Antimicrobial activities of leaf extracts of guava (*Psidium guajava* L.) on two gram-negative and gram-positive bacteria. *International Journal of Microbiology,* 2013. https://doi.org/10.1155/2013/746165

Blois, M. (1958). Antioxidant determinations by the use of a stable free radical. *Nature, 181*(4617), 1199-1200.

Brand-Williams, W., Cuvelier, M.-E., & Berset, C. (1995). Use of a free radical method to evaluate antioxidant activity. *LWT-Food Science and Technology, 28*(1), 25-30. https://doi.org/10.1016/S0023-6438(95)80008-5

Cannel, R. J. (1998). Methods in Biotechnology. Natural Products Isolation. *Humana Press, Totowa, New Jersey, 4*, 1-285.

Chandira, R. M., & Jaykar, B. (2013). Extraction, pharmacological evaluation and formulation of selected medicinal herbs for antidiabetic activity. *International Journal of Pharmacy Teaching & Practices, 4*(1), 458-482.

Dalukdeniya, D., & Rathnayaka, R. (2017). Comparative study on antibacterial and selected antioxidant activities of different *Eryngium Foetidum* extracts. *Journal of Applied Life Sciences International, 12*(4), 1-7. https://doi.org/10.9734/JALSI/2017/34378

Dawilai, S., Muangnoi, C., Praengamthanachoti, P., & Tuntipopipat, S. (2013). Anti-inflammatory activity of bioaccessible fraction from *Eryngium foetidum* leaves. *BioMed Research International, 2013*, 1-8. https://doi.org/10.1155/2013/958567

Devgun, M., Nanda, A., Ansari, S., & Swamy, S. (2010). Recent techniques for extraction of natural products. *Research Journal of Pharmacy Technology, 3*(3), 644-649.

Eyoum Bille, B., & Nguepi, E. (2016). *In vitro* and *in vivo* anti-Helicobacter activities of *Eryngium foetidum* (Apiaceae), *Bidens pilosa* (Asteraceae), and *Galinsoga ciliata* (Asteraceae) against *Helicobacter pylori*. *BioMed Research International, 2016*, 1-7. https://doi.org/10.1155/2016/2171032

Firuzi, O., Lacanna, A., Petrucci, R., Marrosu, G., & Saso, L. (2005). Evaluation of the antioxidant activity of flavonoids by "ferric reducing antioxidant power" assay and cyclic voltammetry. *Biochimica et Biophysica Acta -General Subjects, 1721*(1-3), 174-184. https://doi.org/10.1016/j.bbagen.2004.11.001

Garcia, M., Saenz, M., Gomez, M., & Fernandez, M. (1999). Topical anti-inflammatory activity of phytosterols isolated from *Eryngium foetidum* on chronic and acute inflammation models. *Phytotherapy Research, 13*(1), 78-80. https://doi.org/10.1002/(SICI)1099-1573(199902)13:1<78::AID-PTR384>3.0.CO;2-F

Gayathri, V., & Kiruba, D. (2014). Preliminary phytochemical analysis of leaf powder extracts of *Psidium guajava* L. *International Journal of Pharmacognosy and Phytochemical Research, 6*(2), 332-334.

Gliszczyńska-Świgło, A. (2006). Antioxidant activity of water soluble vitamins in the TEAC (trolox equivalent antioxidant capacity) and the FRAP (ferric reducing antioxidant power) assays. *Food Chemistry, 96*(1), 131-136. https://doi.org/10.1016/j.foodchem.2005.02.018

Handa, S. S., Khanuja, S. P. S., Longo, G., & Rakesh, D. D. (2008). Extraction technologies for medicinal and aromatic plants. *Earth, Environmental and Marine Sciences and Technologies*.

Hanif, M. A., Nisar, S., Khan, G. S., Mushtaq, Z., & Zubair, M. (2019). Essential oils. In: Malik, S. (eds) *Essential Oil Research.* Springer, Cham. https://doi.org/10.1007/978-3-030-16546-8_1

Kokilananthan, S., Bulugahapitiya, V., Manawadu, H., & Gangabadage, C. (2022a). Comparative Evaluation of Different Extraction Techniques on Phytochemicals and Antioxidant Activity of *Psidium Guajava* L. *Tropical Journal of Natural Product Research, 6*(4), 552-557. https://doi.org/10.26538/tjnpr/v6i4.15

Kokilananthan, S., Bulugahapitiya, V. P., Gangabadage, C. S., & Manawadu, H. (2021). Comparative accounts on proximate and phytochemical compositions and antioxidant properties of *Garcinia quaesita* and *Garcinia zeylanica*. *International Journal of Minor Fruits, Medicinal and Aromatic Plants, 7*(2), 59-67. http://doi.org/10.53552/ijmfmap.2021.v07ii02.005

Kokilananthan, S., Vajira, P. B., Gangabadage, C. S., & Harshi, M. (2020). Comparative account on antioxidant properties, proximate and phytochemical compositions of seven guava varieties grown in Sri Lanka. *Journal of Agriculture and Value Addition, 3*(2), 1-16.

Kokilananthan, S., Vajira, P. B., Gangabadage, C. S., & Harshi, M. (2022b). Effect of extraction techniques on phytochemicals and antioxidants activity of *Garcinia quaesita* leaves. *Advances in Technology, 2*(1), 18-30. https://doi.org/10.31357/ait.v2i1.5444

Li, H.-B., Jiang, Y., Wong, C.-C., Cheng, K.-W., & Chen, F. (2007). Evaluation of two methods for the extraction of antioxidants from medicinal plants. *Analytical and Bioanalytical Chemistry, 388*(2), 483-488. https://doi.org/10.1007/s00216-007-1235-x

Lingaraju, D., Sudarshana, M., Mahendra, C., & Rao, K. P. (2016). Phytochemical screening and antimicrobial activity of leaf extracts of *Eryngium foetidum* L.(Apiaceae). *Indo American Journal of Pharmaceutical Research, 6*(2), 4339-4344.

Malik, T., Pandey, D. K., Roy, P., & Okram, A. (2016). Evaluation of phytochemicals, antioxidant, antibacterial and antidiabetic potential of *Alpinia galanga* and *Eryngium foetidum* Plants of Manipur (India). *Pharmacognosy Journal, 8*(5). https://doi.org/10.5530/pj.2016.5.8

Manousi, N., Sarakatsianos, I., & Samanidou, V. (2019). Extraction techniques of phenolic compounds and other bioactive compounds from medicinal and aromatic plants. *Engineering Tools in the Beverage Industry, 3,* 283-314. https://doi.org/10.1016/B978-0-12-815258-4.00010-X

Mohlakoana, M., & Moteetee, A. (2021). Southern african soap plants and screening of selected phytochemicals and quantitative analysis of saponin content. *Resources, 10*(10), 1-18. https://doi.org/10.3390/resources10100096

Mtewa, A. G., Deyno, S., Kasali, F. M., Annu, A., & Sesaazi, D. C. (2018). General extraction, isolation and characterization techniques in drug discovery: A review. *International Journal of Science: Basic and Applied Research, 38*(1), 10-24.

Okon, J., Edet, E., Esenowo, G., & Umoh, N. (2013). Phytochemical screening, analgesic and antiinflammatory properties and Median lethal dose of ethanol leaf extract of wild species of *Eryngium foetidum* L. on Albino rats. *International Journal of Modern Biology and Medicine, 3*(2), 69-77.

Pandey, A., & Tripathi, S. (2014). Concept of standardization, extraction and pre phytochemical screening strategies for herbal drug. *Journal of Pharmacognosy and Phytochemistry, 2*(5), 115-119.

Promkum, C., Butryee, C., Tuntipopipat, S., & Kupradinun, P. (2012). Anticlastogenic effect of *Eryngium foetidum* L. assessed by erythrocyte micronucleus assay. *Asian Pacific Journal of Cancer Prevention, 13*(7), 3343-3347. http://dx.doi.org/10.7314/APJCP.2012.13.7.3343

Rajesh, K. D., Vasantha, S., Rajesh, N., & Panneerselvam, A. (2014). Qualitative and quantitative phytochemical analysis in four pteridophytes. *International Journal of Pharmaceutical Sciences Review and Research, 27*(2), 408-412.

Sathyanarayanan, S., Muniyandi, K., George, E., Sivaraj, D., Sasidharan, S. P., & Thangaraj, P. (2017). Chemical profiling of *Pterolobium hexapetalum* leaves by HPLC analysis and its productive wound healing activities in rats. *Biomedicine and Pharmacotherapy, 95*, 287-297. https://doi.org/10.1016/j.biopha.2017.08.062

Savithramma, N., Rao, M. L., & Suhrulatha, D. (2011). Screening of medicinal plants for secondary metabolites. *Middle-East Journal of Scientific Research, 8*(3), 579-584.

Sawant, R., & Godghate, A. (2013). Qualitative phytochemical screening of rhizomes of *Curcuma longa* Linn. *International Journal of Science, Environment and Technology, 2*(4), 634-641.

Shaikh, J. R., & Patil, M. (2020). Qualitative tests for preliminary phytochemical screening: An overview. *International Journal of Chemical Studies, 8*(2), 603-608. https://doi.org/10.22271/chemi.2020.v8.i2i.8834

Shanthirasekaram, K., Bulugahapitiya, V., Manawadu, H., & Gangabadage, C. (2021). Phytochemicals and antioxidant properties of the leaves of wild guava varieties grown in Sri Lanka. *Journal of Science, 12*(2), 33-46. http://doi.org/10.4038/jsc.v12i2.34

Sheel, R., Nisha, K., & Kumar, J. (2014). Preliminary phytochemical screening of methanolic extract of *Clerodendron infortunatum*. *IOSR Journal of Applied Chemistry, 7*(1), 10-13.

Stratakos, A. C., & Koidis, A. (2016). Methods for extracting essential oils. In: Academic Press. *Essential Oils in Food Preservation, Flavor and Safety*. Elsevier. https://doi.org/10.1016/B978-0-12-416641-7.00004-3

Venkateswarlu, K., Devanna, N., & Prasad, N. (2014). Microscopical and Preliminary Phytochemical Screening of '*Piper betel*'. *PharmaTutor, 2*(4), 112-118.

Wadood, A., Ghufran, M., Jamal, S. B., Naeem, M., Khan, A., & Ghaffar, R. (2013). Phytochemical analysis of medicinal plants occurring in local area of Mardan. *Biochemistry & Analytical Biochemistry, 2*(4), 1-4. http://dx.doi.org/10.4172/2161-1009.1000144

MALAYSIAN JOURNAL OF SCIENCE
MJS
ISSN 1394-3065

Regular Issue

Malaysian Journal of Science 44 (1): 28-33 (March 2025)
https://mjs.um.edu.my

Studies on Essential Oil Extracted from Hippocratae Velutina Leaves in Relation to Chemical Composition, Antioxidant and Antimicrobial Activities

Christiana Ene Ogwuche[1a], Aina Tomilola[2a] and Bawa Hamza[3a]

Abstract: Plants and their constituents have been used as medicines for so many centuries. *Hippocratae velutina* essential oil was analyzed to determine its chemical content, antioxidant activity and antibacterial activity. *H. velutina* was found to contain 0.3% essential oil. By using gas chromatography, one hundred and ninety-five (195) components were discovered to have fourteen major components, with terpenes, making up 75.36% of those components. Beta ocimene has 26.16%; Farnesene, 14.60%; and others (9%), n-alkanes (7.15%), fatty acid-derived substances (6.87%), green leaf volatiles (2.35%), and Shikimate metabolites (9%). With an IC_{50} of 7.14±1.45mg/ml, which is significantly lower than those of the two standards employed, *H. velutina's* aerial parts demonstrated outstanding free radical scavenging activity outcome with DPPH. With MIC values between 0.15 and 0.23 mg/ml for eight out of all ten microorganisms examined, the essential oils of *H. velutina* leaves demonstrated antibacterial activity against selected strains of Gram-negative and Gram-positive bacteria as well as antifungal activities, with a range in the sensitivity of the microorganisms to the oil. According to the findings, the extracted oil from *H. velutina* has bioactive antioxidant phytochemicals capable of inhibiting a wide range of microbial growth. This confirms its use as a folkloric drug against several ailments.

Keywords: *Chemical composition, antimicrobial, antioxidant, H. velutina, essential oil.*

1. Introduction

Essential oils (EOs) are an aromatic blend of active ingredients with a potent aroma that is derived from aromatic plants (Mohamed and Alotaibi, 2023), obtained as a volatile mixture of chemical compounds with a strong aroma. In general, the major compounds found in essential oils determine their bioactivity properties. They have been extensively used for applications such as bactericidal, virucidal, fungicidal, antiparasitic, insecticidal, and medicinal. It is possible to compare the biological activity of the oils to that of pharmacological preparations made synthetically. Therefore, essential oils are hopeful natural extracts that require additional research to determine their potential for use as supplements, preservatives, or antioxidants in the food or pharmaceutical industries (Santana de Oliveira *et al*., 2020). The ability to smell is stimulated by the sense organ and essential oil helps in this regard when inhaled. Phytochemical analysis of these oils revealed the presence of beneficial compounds like terpenes, antioxidants, and esters that help boost the immune system (Elshafie *et al*., 2017). Due to their sweet fragrance, essential oils are used to make fragrances to creams, manufacture perfumes, hand and body washes and lotions. Other uses of essential oils include the treatment of sinus infections, cold sores, sore muscles, wounds, and skin rashes.

H. velutina is from the family of Celastraceae, predominantly in subtropical and tropical Africa and America. There are approximately 1,200 species in the family of Celastraceae, distributed across 100 genera, and they can be found in temperate regions in both hemispheres, with tropical and subtropical regions having the greatest diversity with trees and shrubs predominately, but lianas make up about 30% of species. The Hippocrateoideae and Salacioideae subfamilies (formerly known as the Hippocrateaceae family) are predominately composed of climbers, whereas, the genus Celastrus is the only member of the Celastraceae stricto that is found in the New World. There are just over 100 liana species in 13 genera, mostly found in forest habitats, in the Neotropics, (Biral, 2017).

The plant has long thin leaves which are arranged opposite each other and small flowers. Its leaf seeds act as a medicine for pain relief. The young branches are useful as a binding substance that provides structural stability to the material in use. In Sierra Lone, the leaves are dried and boiled, then, applied to the body to relieve soreness and inflammation. The Igbo of South Nigeria use the plant as a mechanism to keep termites and beetles away from yams, to avoid holes being dug in the yam crop. In Senegal, the plant seeds are used in the management of headaches and fever.

Objective of the Study

The objective of this study is to establish and/or ascertain the medicinal application of extracted essential oil via the examination of the chemical makeup, antioxidant properties, and antibacterial properties of *H. velutina*.

Authors information:
[a]Department of Chemistry, Federal University of Petroleum Resources P.M.B. 1221, Effurun, Delta State, NIGERIA. E-mail: ogwuche.christiana@fupre.edu.ng[1]; clementinatomilola@gmail.com[2]; audu.hamza@fupre.edu.ng[3]
*Corresponding Author: ogwuche.christiana@fupre.edu.ng

Received: June 8, 2023
Accepted: June 20, 2024
Published: March 31, 2025

DOI:https//doi.org/10.22452/mjs.vol44no1.4

Essential oils' chemical content

Depending on the oil, an essential oil might have hundreds to thousands of chemical components. Terpenoids and phenylpropanoid derivatives are the major ingredients in essential oils. Most plants' essential oils are composed primarily of terpenoids. The flavor, smell, and harsh taste of this compound are due to the availability of phenylpropanoid derivatives. From primary metabolites, essential oils from fruits and leaves are said to have biological activities such as antimicrobial and antioxidant activity (Gertrude *et al*., 2022)

2. Experimental Methods

Hippocratea velutina leaves were collected from the botanical garden of the University of Ibadan, Oyo State, Nigeria, and was identified at the Department of Botany, Faculty of Life Sciences, Ahmadu Bello University, Zaria, Nigeria. The plant was verified with the herbarium number ABU030479 by Prof. B.Y. Abubakar. Before extraction, the young leaves were separated from the stalk and cleaned. The leaves of the *H. velutina* were identified using the gas chromatography-mass spectrometry (GC-MS) technique. The hydrodistillation technique was employed in the study to extract essential oil from *H. velutina* leaves. According to the British Pharmacopoeia's guidelines, the oil was extracted using the Hydro distillation process on a Clevenger-type apparatus for 3 hours (Kowalska *et al.,* 1995). Before analysis, the oil production was determined in relation to the matter after the essential oils were collected in n-hexane and kept in the refrigerator at 4°C. The constituents of the essential oils were verified based on their retention variables, which were calculated for a homologous series of n-alkane, and by comparison of fragmentation patterns (NIST data/base/chem station data system) in the mass spectra as reported by (Nicholas *et al.*, 2022).

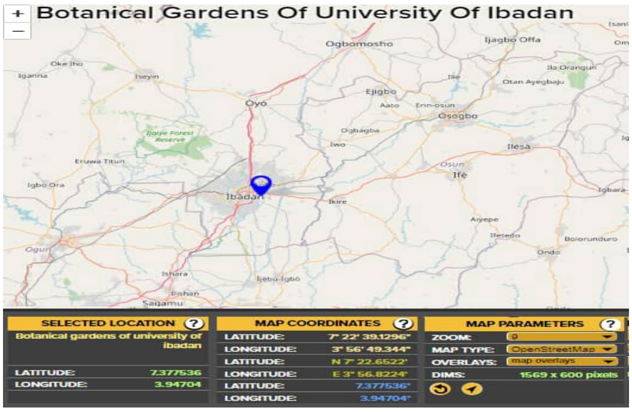

SELECTED LOCATION
Botanical gardens of university of ibadan
LATITUDE: 7.377536
LONGITUDE: 3.94704

MAP COORDINATES
LATITUDE: 7° 22' 39.1296"
LONGITUDE: 3° 56' 49.344"
LATITUDE: N 7° 22.6522'
LONGITUDE: E 3° 56.8224'
LATITUDE: 7.377536°
LONGITUDE: 3.94704°

MAP PARAMETERS
ZOOM: 9
MAP TYPE: OpenStreetMap
OVERLAYS: map overlays
DIMS: 1569 x 600 pixels

Figure1. Map of the botanical Garden, University of Ibadan

Gas Chromatography Mass Spectrometer (GC-MS) Analysis of the Essential Oil

The GC-MS was a split/split-less injector interfaced with mass-selective detector running at 70 eV. It was used in addition to an Agilent 7809A gas for the analysis of the essential oil. The ion source's temperature was set to 200 °C at a scan rate of 1428 amu/sec, with a mass spectral range of m/z 50–700. The GC employed measures 0.25 mm internal diameter, 30 m long, and 0.25 m film thickness (HP-5MS) column. The following temperature settings were set for the oven: an initial temperature of 80 degrees Celsius for 2 minutes, followed by 240 °C for 6 minutes after, increasing by 10 °C/min. A constant flow rate of 1 mL/min of helium was used as the carrier gas. At 1 L, 362 cms^{-1}, and 5.62x10^{4} Pa, respectively, the linear velocity, injection volume, and pressure were changed. The temperature of the oven was fixed at 60 °C which was maintained for 1 minute.

Antioxidant Assay

A modified version of the Bruits method was used to authenticate the ability of the essential oil to possess scavenging activity using diphenylpicryl hydrazine (DPPH). The volatile oil was measured in five different concentrations ranging from 0.015 to 1 mg/mL in test tubes and was vigorously shaken. Incubation was carried out for 30 minutes at room temperature. The absorbance of the treated essential oil samples and blank DPPH solution (control) was thereafter measured at 517nm using a UV/Visible (GS-UZ12) spectrometer. Ascorbic acid and Butylated hydroxyl anisole (BHA) which are established antioxidants served as standards. The analysis was repeatedly done in triplicate and the mean absorbance was calculated. The activities of samples were analyzed using the equation below;

$$\%\text{Inhibition} = \frac{Ab-As}{Ab} \times 100$$

Where the blank's absorbance is Ab, and the sample's absorbance is As.

Antimicrobial Assay

Antimicrobial analysis was determined by the use of the Kirby-Bauer disc diffusion method as reported by Hudzicki (2009) with some adjustments. The microorganisms in use here are as follows; six bacteria which are *Bacillus subtilis, Escherichia coli, Klebsiella pneumonia, Pseudomonas aeruginosa*, *Salmonella typhi,* and *Staphylococcus aureus,* with four fungi*: Aspergillus niger, Candida albicans, Penicillium notatum, and Rhizopus spp*. The microorganisms used were obtained from and identified in the Department of Pharmaceutical Microbiology, University of Ibadan, Oyo State, Nigeria.

Preparation of Sample Solution

In the preparation, 1000 µg/mL of the oil sample was equivalent to 1 mL. Therefore, 500 µg/mL of the essential oil is equivalent to 0.5 mL. More serial dilutions gave different concentrations such as 62.50 µg/ml, 125 µg/ml, and 250 µg/ml, respectively. The test tubes labelled number six (6) and seven (7) were negative control containing (DMSO) while the test tube labelled number eight (8) was the negative control containing n-hexane, positive controls; Gentamycin for bacteria and Tioconazole for fungi, respectively.

Percentage Yield Analysis Result

In this study, the essential oils from *H. velutina* leaves were evaluated for their physical characteristics and percent yield

DOI:https//doi.org/10.22452/mjs.vol44no1.4

(Table 3.1). There is only a 0.3% essential oil output, which is lower than the levels noted by Niko *et al.* (2009) on different plant materials. The method and duration of extraction of essential oils are key factors that greatly influence the quality and quantity of essential oil yields (Samadi, 2022). Interestingly, the chemical makeup of essential oils and percentage yield are usually correlated (Niko *et al.,* 2009).

3. Results and Discussion

Table 1. Appearance and Yield of *H. velutina Essential Oil*

Weight of Sample packed for Extraction (g)	350
Weight of Essential Oil Extracted (g)	0.9
Percentage Yield (%)	0.3
Colour	Colourless
Odour	Herbal light

Gas chromatography Mass Spectrometry Analysis Result

GC-MS was employed in determining the chemical makeup of the essential oils' most potent ingredients of *H. velutina* leaves. A total of one-hundred and ninety-five (195) components were determined from the GC analysis (see Appendix II). From these, fourteen major components amounting to 75.36% contain terpenes (Beta-ocimene, ≥26.16%; Farnesene, ≥14.60%, and others ≥9.24%), *n*-alkanes (≥7.15%), fatty acid-derived compounds (≥6.87%), green leaf volatiles and Shikimate metabolites (≥2.35%) were seen. The structures of these fourteen major components are indicated in Figure 3.1. The Gas Chromatograph for all 195 components present in *H. velutina* leaves essential oil is shown in Appendix I. The presence of different terpenoid compounds has been recorded as the main active components of essential oils, giving such oils high antimicrobial and antioxidant properties.

Table 2. Chemical Composition *H. velutina* Leaves Essential Oil

Compound	Retention Time (minutes)	Percentage Composition (%Area)
Major Components (%Area≥1.00)		
Beta-ocimene	4.6970	26.16
Farnesene	10.800	14.60
Nonacosane	23.229	7.15
n-hexadecanoic acid	15.752	6.87
9,12,15-octadecatrienoic acid, (z,z,z)-	17.373	6.47
Methyl salicylate	6.684	2.35
2-hexadecen-1-ol,3,7,11,15-tetramethyl,acetate, (R-R*,R*-(E))	17.065	2.29
3,7,11-trimethyl-,(s-(z))-1,6,10-dodecatrien-3-ol,	11.424	2.00
(6E,10E,14E,18E)-3-bromo-2,6,10,15,19,23-hexamethyltetracosa-6,10,14,18,22-pentaen-2-ol	22.732	1.43
3-hexen-1-ol,benzoate,(z)-	11.520	1.38
1,8,9-triazabicyclo(4.3.0)nona-6,8-diene	11.585	1.35
2-methyl-5-(1,1,5-trimethyl-5-hexenyl) Furan	10.009	1.14
3,7,11-trimethyl-1,6,10-Dodecatrien-3-ol	16.300	1.11
3,7-dimethyl-(E)-1,3,6-octatriene	4.478	1.06
Minor Components (%Area<1.0)	-	24.64
Total		100.00

Antioxidant assay analysis results

The *H. velutina* leaves essential oil has not been reported of any antioxidant activity. The *H. velutina* leaves scavenging activity of its essential oils using DPPH free radical is shown in Figure 3.2 (a, b, and c) and Tables 3.3 and 3.4 as compared with two known standards (ascorbic acid and butylated hydroxyanisole). The change in absorbance produced by reduced DPPH was used to evaluate the ability of *H. velutina* leaves essential oils to act as free radical scavengers (Table 3.3). Results in Table 3.4 as represented graphically in Figure 3.2 (a, b and c) showed that the scavenging effect of *H. velutina* leaves essential oils is excellent with an IC_{50} of 7.14±1.45 mg/ml which is considerably lower and thus more active than both standards (ascorbic acid: 16.24±1.59 mg/ml; and BHA: 17.60±1.76 mg/ml). A wide variety of foods and medicinal plants contain natural antioxidants. These natural antioxidants, particularly the carotenoids and polyphenols, have a variety of biological effects, including those that are anti-inflammatory, anti-aging, anti-atherosclerosis, and anticancer (Xu *et al.,* 2017). The effect of the combination of the trio compounds tends to be synergetic and thus provides improved results than the isolated compounds. The findings of this antioxidant study support the folkloric usage of the plant as a preventive and curative agent in some diseases. The provided data can enrich a possible comprehensive data of the antioxidant activity of *H. velutina* in the future.

Table 3. Essential Oils' Antioxidant Potential of *H. velutina* Leaves and Standards

Concentration (mg/ml)	Absorbance		
	Essential Oil of	Ascorbic Acid	Butylated Hydroxyanisole (BHA)
1.000	0.01±0.00	0.03±0.01	0.04±0.01
0.500	0.04±0.04	0.04±0.00	0.05±0.01
0.250	0.03±0.00	0.05±0.01	0.06±0.00
0.125	0.1±0.01	0.06±0.01	0.07±0.01

*Values are mean ± standard deviation of triplicate determinations

Table 4. The % Inhibition of the Various Concentrations of *H. velutina* Leaves Essential Oils and Standards

Concentration (mg/ml)	% Inhibition		
	Essential Oil of *H. velutina*	Ascorbic Acid	Butylated Hydroxyanisole (BHA)
1.000	99.37±0.19	97.98±1.06	97.22±1.41
0.500	96.94±1.28	96.97±1.41	96.46±1.40
0.250	97.75±0.87	96.46±1.76	95.45±2.11
0.125	92.17±3.45	95.20±2.11	94.95±2.11
$IC_{50\ (DPPH)}$	7.1412±1.45	16.235±1.59	17.599±1.76

*Values are mean ± standard deviation of triplicate determinations

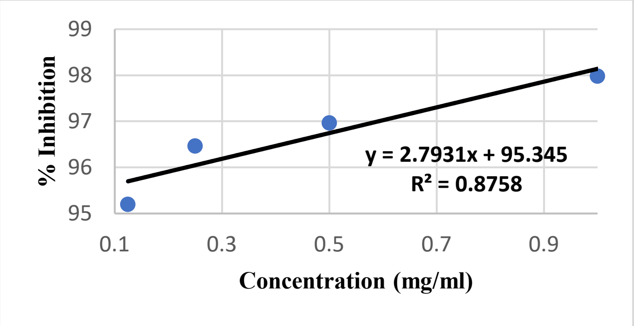

Figure 1. Percentage (%) Inhibition of Ascorbic Acid

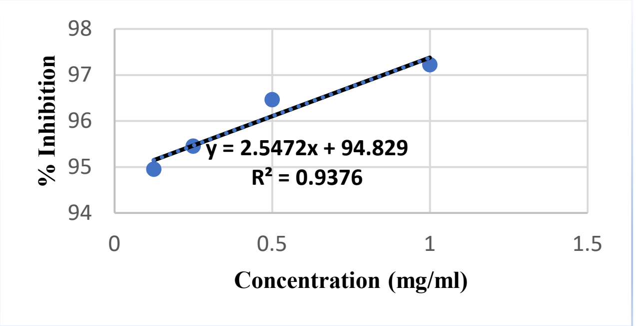

Figure 2. Percentage (%) Inhibition of Butylated Hydroxyanisole (BHA)

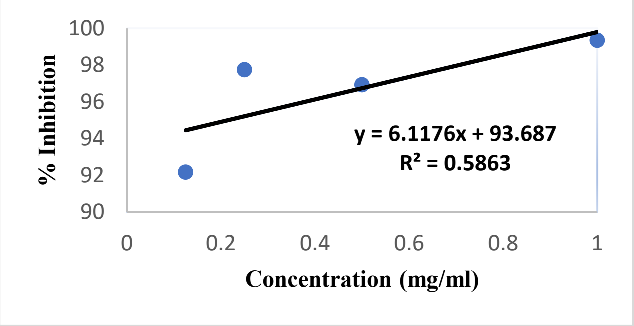

Figure 3. Percentage (%) Inhibition of Essential Oils of *H. velutina*

Antimicrobial Assay Results

Using linear regression graphs based on the measured diameters of the inhibition zones, the minimum inhibitory concentration (MIC) of *H. velutina* leaves essential oil was calculated from the zones of inhibition (Table 3.6). Table 3.5 shows the different isolate concentrations of *H. velutina* leaves essential oils zones of inhibition compared to the control drugs. Three categories of microorganisms were used, with isolates representing each category: gram-negative and gram-positive bacteria, as well as fungi. The results showed that essential oils of *H. velutina* exhibited remarkable antimicrobial properties against some of the tested organisms. Specifically, the oils inhibited the growth of all the gram-positive (*Bacillus subtilis*, *S. aureus*) and gram-negative bacteria (*E. coli*, *K. pneumonia*, *S. typhi,* and *P. aeruginosa*), as well as *C. albican* but were inactive against the other Filamentous fungi (*Penicillumnotatum* and *Rhizopussp*). Observably, the *H. velutina* leaves essential oils exhibited good antimicrobial activities at high concentrations of 100 mg/ml. However, these antimicrobial activities decreased at reduced concentrations as indicated by the varying zones of inhibition (Table 3.5). At a low concentration of 25 mg/ml, the *H. velutina* leaves essential oils could no longer prevent the two fungi species from growing (*Aspergillus niger* and *Candida albicans*) which hitherto inhibited. *H. velutina* leaves essential oils at 12.5 mg/ml concentration could not stop *Bacillus subtilis* and *Salmonella typhi from growing*. *H. velutina* leaves essential oils were not able to prevent the growth of any of the tested microorganisms at 6.25 mg/ml concentration and below. The oil presents the best action as antibacterial, in which *Staphylococcus aureus* was the most susceptible bacteria across all tested concentrations. The *H. velutina* leaves essential oils revealed MIC values for eight out of the ten microorganisms tested, with the MICs ranging from 0.15 and 0.23 mg/ml (Table 3.6). There are no available scholarly reports on the antimicrobial analysis of *H. velutina* leaves, but the anti-bacterial and antifungal properties exhibited by *H. velutina* may be due to some bioactive phytochemicals common to essential oils. Specifically, some terpenes, eugenol, terpineol, carveol, and citronellol have demonstrated quick bactericidal responses against *Salmonella enterica, S. aureus strains*, and *E. coli* respectively (Guimarães *et al*., 2019) with synergetic effects in combination with other phytochemicals (Ayaz *et al*., 2019). Moreover, the activity of aldehydes and their derivatives against pathogenic bacteria for future use in the clinical setting has been reported by (Aljaafari *et al*., 2022). From the antimicrobial results obtained, it could therefore be inferred that the essential oils of *H. velutina* leaves possessed antibacterial activity against Gram-positive/negative bacteria as well as antifungal activities with a varying sensitivity of the microorganisms to the oil. We can therefore suggest that the essential oils of *H. velutina* leave a potentially broad-spectrum antimicrobial agent.

Table 5. *H. velutina* Essential Oil Zones of Inhibition Compared to the Control Drugs

Concentration (mg/ml)	Zone of inhibition* (mm)									
	Pathogenic bacterial species						Pathogenic fungal species			
	SA	EC	BS	PA	KP	ST	CA	AN	PN	RS
100	18.0±0.0	17.0± 0.0	15.0± 0.0	17.0± 0.4	17.0±0.4	15.0± 0.4	13.0± 0.4	13.0± 0.0	--	--
50	16.0± 0.0	15.0± 0.4	13.0± 0.4	15.0± 0.4	15.0±0.4	13.0± 0.4	10.0± 0.0	10.0± 0.0	--	--
25	14.0± 0.0	13.0± 0.4	10.0± 0.0	12.0± 0.0	13.0± 0.4	10.0± 0.0	--	--	--	--
12.5	11.0± 0.5	13.0± 1.4	--	10.0± 0.0	10.0± 0.0	--	--	--	--	--
6.25	--	--	--	--	--	--	--	--	--	--
3.125	--	--	--	--	--	--	--	--	--	--
Negative control**	--	--	--	--	--	--	--	--	--	--
Positive control***	39.0± 0.5	37.0± 0.4	37.0± 0.4	38.0± 0.0	39.0± 0.0	38.0± 0.0	28.0± 0.0	28.0± 0.0	27.0± 0.0	23.0± 1.4

*Values are mean ± standard deviation of triplicate determinations**Negative control: n-Hexane (for Bacteria and fungi); ***Positive Control: Gentamicin (10µg/ml) for bacteria, Tioconazole (30%) for fungi.

AN=*Aspergillus niger*; BS= *Bacillus subtilis*; CA= *Candida albicans;* EC= *Escherichia coli*; KP=*Klebsiella pneumoniae;* PA= *Pseudomonas aeruginosa*; PN=*Penicillum notatum*; RS=*Rhizopus sp;* SA= *Staphylococcus aureus;* ST=*Salmonella typhi;*

Table 6. Antimicrobial Activity of *H. velutina* Leaves Essential Oils Showing MIC.

Microorganisms		Zone of Inhibition* (mm)	MIC** (mg/ml)
Gram Positive			
	Bacillus subtilis	10.0± 0.0	0.18±0.00
	Staphylococcus aureus	11.0± 0.5	0.23±0.01
Gram Negative:			
	Klebsiella pneumoniae	10.0± 0.0	0.22±0.00
	Escherichia coli	13.0± 1.4	0.22±0.02
	Salmonella typhi	10.0± 0.0	0.18±0.00
	Pseudomonas aeruginosa	10.0± 0.0	0.22±0.00
Fungi (Yeast):			
	Candida albicans	10.0± 0.0	0.15±0.00
Filamentous Fungi (mold):	*Aspergillus niger*	10.0± 0.0	0.15±0.00

*Values are of triplicate determinations of standard deviation ± mean

4. Conclusion

Thus, *H. velutina*'s aerial portions were used to extract essential oils, with a 0.3% yield as a result. The existence of major terpenes, fatty acids, and n-alkanes, a crucial element of essential oils, was discovered through chemical elucidation. *H. velutina leaves essential oil* was also subjected to antioxidant as well as antimicrobial analysis. The results indicate that *H. velutina* leaves essential oil have bioactive antioxidants capable of inhibiting a wide range of growth. This confirms the use of the plant as a folkloric drug against several ailments.

5. Acknowledgement

The University of Ibadan provided an encouraging environment for our study endeavour, for which the authors are grateful.

6. References

Aljaafari M., Alkhoori M., Hag-Ali M., Cheng W., Lim S., Loh J., Lai K. (2022). Contribution of Aldehydes and Their Derivatives to Antimicrobial and Immunomodulatory Activities. Molecules. 2;27(11):3589. doi: 10.3390/molecules27113589.

Ayaz M., Ullah F., Sadiq A., Ullah F., Ovais M., Ahmed J., Devkota H. (2019). Synergistic interactions of phytochemicals with antimicrobial agents: Potential strategy to counteract drug resistance. Chem Biol Interact. 1;308:294-303. doi: 10.1016/j.cbi.2019.05.050.

Biral, L. (2017). Celastraceae. In: A.M.R. Anton, F.O. Zuloaga & M.J. Belgrano (eds.). Flora Vascular de la República Argentina, 17: 23-44. Instituto Multidisciplinario de Biología Vegetal, Córdoba (CONICET-UNC).

Elshafie SH., Ippolito C. (2017). "An Overview of the Biological Effects of Some Mediterranean Essential Oils on Human Health", *BioMed Research International*. Pp 1-14. https://doi.org/10.1155/2017/9268468

Gertrude A., Jehoshaphat O, Lawrence S. (2022). Essential Oils from the Fruits and Leaves of Spondias mombin Linn: Chemical composition, Biological Activity and Docking Study. Evidence-Based Complementary and Alternative Medicine, 1 (1)1-14

Guimarães A., Meireles L., Lemos M., Guimarães M., Endringer D., Fronza M., Scherer R. (2019). Antibacterial Activity of Terpenes and Terpenoids Present in Essential Oils.

Molecules. 5;24(13):2471. doi: 10.3390/molecules24132471.

Hudzicki J. (2009). Kirby-Bauer Disk Diffusion Susceptibility Test Protocol. American Society for Microbiology. Pp 1-23

Mohamed, A., Alotaibi, B. (2023). Essential oils of some medicinal plants and their biological activities: a mini review. *J.Umm Al-Qura Univ. Appll. Sci.* **9**, 40–49 https://doi.org/10.1007/s43994-022-00018-1

Nicholas J., Guillermo F. and Methee P. (2022). Fundamental Chemistry of Essential and volatile organic compounds, Methods of Analysis and Authentication. Plants. 11 (6), 789.

Niko R., Polina B. and Radosav P. (2009). Fatty Acid Derived Compounds – The Dominant Volatile Class of the Essential Oil Poor *Sonchus arvensis* subsp.*uliginosus* (Bieb.) Nyman. *Natural Product Communications* 4 (3): 307-456

Samadi M., Zainal Abidin Z., Yoshida H., Yunus R., Awang Biak D. (2020). Towards Higher Oil Yield and Quality of Essential Oil Extracted from *Aquilaria malaccensis* Wood via the Subcritical Technique. Molecules. 26: 25(17):3872. doi: 10.3390/molecules25173872.

Santana de Oliveira, M., Almeida da Costa, W., Gomes Silva, S. (Eds.). (2020). Essential Oils - Bioactive Compounds, New Perspectives and Applications. IntechOpen. doi: 10.5772/intechopen.87266

Xu D., Li Y., Meng X., Zhou T., Zhou Y., Zheng J., Zhang J., Li H. (2017). Natural Antioxidants in Foods and Medicinal Plants: Extraction, Assessment and Resources. Int J Mol Sci. 2017 Jan 5;18(1):96. doi: 10.3390/ijms18010096.

MALAYSIAN JOURNAL OF SCIENCE
MJS
ISSN 1394-3065

Regular Issue

Malaysian Journal of Science 44 (1): 34-41 (March 2025)
https://mjs.um.edu.my

Effect of Natural Deep Eutectic Solvents and Conventional Solvents on Extraction Yield, Antioxidant Activity, and Toxicity of *Peperomia pellucida* (L.) Kunth

Aniza Saini[1a], Mohammad Amil Zulhilmi Benjamin[2b], Nor Azizun Rusdi[3c], Ahmad Hazim Abdul Aziz[4a] and Mohd Azrie Awang[5ad]*

Abstract: *Peperomia pellucida* (L.) Kunth, commonly known as 'Sirih Cina,' is a botanical plant recognised for its traditional application in various therapeutic contexts due to its bioactive compounds. Despite its potential benefits, its properties are sometimes underappreciated. The choice of solvent extraction significantly influences its biological properties. This study investigates the impact of different solvents on the extraction yield, antioxidant activity, and toxicity of *P. pellucida* leaf extracts. The selected solvents include natural deep eutectic solvents (NADES), distilled water, methanol, ethanol, and ethyl acetate. The extraction of *P. pellucida* leaves was conducted using an ultrasonic water bath apparatus. The aluminium chloride colorimetric assay was employed to determine the total flavonoid content (TFC), while the 2,2-diphenyl-1-picrylhydrazyl (DPPH) assay was used to assess antioxidant activity. Moreover, the toxicological assessment of *P. pellucida* leaf extracts was performed using the brine shrimp lethality assay (BSLA) to determine LC_{50} (lethal concentration 50) values. NADES emerged as the most efficient solvent for extraction, yielding the highest extraction yield (17.39 ± 0.03%) and DPPH scavenging activity (83.31 ± 0.03%), while demonstrating non-toxicity in the BSLA (LC_{50} = 1597.62 μg/mL). Although NADES ranked third in terms of TFC, a moderate correlation between TFC and DPPH suggests that factors beyond TFC influence antioxidant activity. Overall, NADES exhibited antioxidant activity and showed non-toxicity towards brine shrimp. Therefore, NADES is a suitable solvent for exploring the medicinal potential of *P. pellucida* leaves as a source for therapeutic applications.

Keywords: *Peperomia pellucida, extraction yield, flavonoids, antioxidant, toxicity.*

1. Introduction

In this era, the extraction of natural compounds from medicinal plants has garnered significant attention due to the abundant presence of bioactive molecules, including phenolic and flavonoid compounds. Extraction solvents are commonly selected based on their polarity. Solvents such as methanol, ethanol, and ethyl acetate, which have high polarity, are often used for extracting polyphenols, while non-polar compounds are better extracted using solvents like hexane (Ng et al., 2020). Achieving effective extraction and purification of antioxidant and phytochemical compounds from plant materials depends on various factors, including duration, temperature, solvent concentration, and polarity. Given the differing polarities of various phytochemicals, no single solvent can effectively extract all compounds. This highlights the importance of carefully selecting suitable solvents to ensure thorough extraction (Nawaz et al., 2020).

Natural deep eutectic solvents (NADES) represent a solvent system comprising natural elements such as organic acids and amines that form a specialised mixture. This innovation is gaining attention as an eco-friendlier substitute for traditional organic solvents in extraction processes. It offers benefits such as being biodegradable, highly soluble, stable, and easy to produce, making it a promising green choice for extracting natural substances (Liu et al., 2018). Despite being less explored for plant extractions, there is increasing evidence supporting NADES as a potential alternative to conventional solvents. For instance, Oomen et al. (2020) found that, despite the high hydrophilicity of NADES, glycosides with greater water affinity were extracted less than their aglycones. This highlights NADES as a potential medium for extracting *Scutellaria baicalensis* compounds with diverse hydrophilic properties. Additionally, NADES proved to be as effective as traditional eco-friendly solvents in extracting polyphenols, offering the added advantage of operating at milder temperatures. This method avoids flammable solvents and utilises sustainable, natural compounds in the extraction of polyphenols from ground coffee (García-Roldán et al., 2023). Their environmentally friendly nature and compatibility with the environment make them a viable green option for natural product extraction (Popovic et al., 2022).

Authors information:
[a]Faculty of Food Science and Nutrition, Universiti Malaysia Sabah, Jalan UMS, 88400 Kota Kinabalu, Sabah, MALAYSIA. E-mail: anizasaini96@gmail.com[1]; hazim.aziz@ums.edu.my[4]
[b]Borneo Research on Algesia, Inflammation and Neurodegeneration (BRAIN) Group, Faculty of Medicine and Health Sciences, Universiti Malaysia Sabah, Jalan UMS, 88400 Kota Kinabalu, Sabah, MALAYSIA. E-mail: mohammad_amil_zulhilmi_dm22@iluv.ums.edu.my[2]
[c]Institute for Tropical Biology and Conservation, Universiti Malaysia Sabah, Jalan UMS, 88400 Kota Kinabalu, Sabah, MALAYSIA. E-mail: azizun@ums.edu.my[3]
[d]Food Security Research Laboratory, Faculty of Food Science and Nutrition, Universiti Malaysia Sabah, Jalan UMS, 88400 Kota Kinabalu, Sabah, MALAYSIA. E-mail: ma.awang@ums.edu.my[5]
*Corresponding Author: ma.awang@ums.edu.my

Received: June 8, 2023
Accepted: June 20, 2024
Published: March 31, 2025

DOI:https//doi.org/10.22452/mjs.vol44no1.5

Peperomia pellucida (L.) Kunth, also referred to as 'Sirih Cina,' is a plant that thrives in moist surroundings. Belonging to the Piperaceae family, it is predominantly distributed across regions such as Central and South America, Africa, Australia, and Southeast Asia (Alves et al., 2019). Its distinct characteristics include heart-shaped leaves, a smooth surface, juicy stems, and shallow roots, contributing to its significance as both a culinary and medicinal asset that benefits human well-being (Alves et al., 2019; Ho et al., 2022). In Southeast Asian countries, *P. pellucida* is frequently employed to manage particular skin issues in Iloilo, Philippines (Tantiado, 2012). Additionally, in Singapore, people use a concoction of the entire plant to alleviate joint discomfort (Siew et al., 2014). Meanwhile, in Malaysia, *P. pellucida* has a longstanding tradition of being used as a plant decoction for managing rheumatism (Ibrahim & Hamzah, 1999). Phytochemical analysis of crude extracts reveals the presence of flavonoids, alkaloids, carbohydrates, carotenoids, depsides, phenols, quinones, sterols, tannins, saponins, azulenes, reducing sugars, and triterpenoids (Alves et al., 2019). Results from a range of in vivo, in vitro, and clinical investigations suggest that extracts of *P. pellucida* exhibit promising pharmacological properties. These extracts have demonstrated potential in various areas, including antioxidant, analgesic, antibacterial, antifungal, anti-inflammatory, antidiabetic, anti-hypercholesterolemia, toxicological, and cytotoxic effects (Alves et al., 2019; Ho et al., 2022). While the extract showed mild toxicity in animal models, it was non-toxic to normal cell lines (HEK-293) compared to HeLa and HepG2 cancer cell lines, as well as to brine shrimps and rodents (Ho et al., 2022).

Despite its potential for various biological activities, the utilisation of *P. pellucida* leaf extract remains limited. Further exploration is necessary to thoroughly examine the choice of suitable solvents for extraction, aiming to uncover environmentally conscious methods and compare them with alternative solvent options. Hence, this study aimed to assess the extraction yield and antioxidant activity of *P. pellucida* leaf extracts using different solvents, including NADES, distilled water, methanol, ethanol, and ethyl acetate. Moreover, the study also sought to evaluate the toxicity levels associated with these extracted compounds.

2. Experimental Methods

Chemicals and Solvents

NADES consisting of choline chloride and lactic acid, along with methanol, ethanol, and ethyl acetate acquired from Merck (Darmstadt, Germany), were employed as solvents for the extraction process. Sigma-Aldrich (Burlington, MA, USA) provided ascorbic acid, aluminium chloride, potassium dichromate, and 2,2-diphenyl-1-picrylhydrazyl (DPPH) reagent.

Plant Materials

P. pellucida leaves were gathered near the Faculty of Food Science and Nutrition, Universiti Malaysia Sabah, Sabah, Malaysia. The fresh samples were washed with tap water to remove surface impurities and subsequently dried using an oven dryer (ED 23, Binder, Neckarsulm, Germany) at 60 °C for 4 h until fully dried (Awang et al., 2021a). Following drying, the samples were finely ground into a consistent powder and stored at 4 °C for future analyses.

NADES Preparation

NADES were prepared using a modified heating and stirring technique based on the method by Rosarina et al. (2022). Choline chloride (a hydrogen bond acceptor, HBA) and lactic acid (a hydrogen bond donor, HBD) were combined in a molar ratio of 1:2. The water content of NADES was adjusted by adding deionised water. These constituents were mixed in a glass beaker at 70 °C under continuous stirring until a clear and homogeneous liquid was obtained. The resulting NADES were then stored at room temperature for subsequent use.

Sample Extraction

This study was conducted using the ultrasonic extraction technique implemented through an ultrasonic water bath. Five types of solvents were utilised: ethanol, methanol, ethyl acetate, distilled water, and NADES. Approximately 5 g of powdered *P. pellucida* leaves were added to 150 mL of an extraction solvent using an ultrasonic water bath (CPX8800H, Branson, Brookfield, CT, USA). The ultrasonic extraction was carried out for 60 min, starting at an initial temperature of 50 °C. The resulting extract supernatant was collected and filtered, while the residue was discarded. The filtered extract underwent further separation under reduced pressure at 45 °C using a rotary evaporator (Laborota 4000, Heidolph, Schwabach, Germany) and was stored in aluminium-wrapped tubes. Subsequently, these tubes were placed in an oven dryer and dried for 24 h at 50 °C to ensure complete solvent evaporation from the samples. The percentage of sample obtained from different solvents was calculated using Eq. (1):

$$\text{Extraction yield (\%)} = \frac{\text{Weight of dried extract (g)}}{\text{Weight of dried sample (g)}} \times 100 \qquad (1)$$

Antioxidant Analysis

Total Flavonoid Content

The total flavonoid content (TFC) of the sample was determined based on the formation of the flavonoid-aluminium complex, as described by Awang et al. (2021b). Approximately 1 mg of the extract was combined with 1 mL of a 2% methanolic-aluminium chloride solution. The complex was allowed to form during a 15-min incubation period and was subsequently measured at a wavelength of 430 nm using a UV-Vis spectrophotometer (Lambda 25, PerkinElmer, Waltham, MA, USA).

DPPH Assay

The DPPH assay was conducted following the protocol outlined by Stephenus et al. (2023), with minor adjustments. Approximately 1 mL of the extract or ascorbic acid (positive control) was combined with 1 mL of methanolic-DPPH solution.

DOI:https//doi.org/10.22452/mjs.vol44no1.5

The mixture was vigorously agitated and subsequently incubated in the absence of light at room temperature for 20 min. The decrease in absorbance was measured at 517 nm against a blank without DPPH using a UV-Vis spectrophotometer. Afterward, the percentage of DPPH radical scavenging activity was determined using Eq. (2):

$$\text{DPPH radical scavenging activity (\%)} = \frac{A_c - A_s}{A_c} \times 100 \qquad (2)$$

where A_c and A_s represent the absorbance values of the control and sample, respectively.

Brine Shrimp Lethality Assay

The brine shrimp lethality assay (BSLA) protocol was adapted from the method outlined by Benjamin et al. (2022), with slight adjustments. Brine shrimp were hatched from brine shrimp eggs in an aerated aquarium filled with seawater over a 48-h period. Once hatched, the nauplii were collected from a well-lit area, ensuring they were free from eggshells, and subsequently used for the assay. One hundred nauplii were meticulously transferred using a micropipette and glass capillary into a petri dish containing 20 mL of seawater.

In each petri dish, 1 mL of the sample was added to 20 mL of the brine shrimp solution and left at room temperature for 24 h in the presence of light. After that, the remaining larvae were enumerated using a magnifying glass. The experiment included a positive control (potassium dichromate) and various concentrations of the extract solution (1000, 500, 300, and 100 µg/mL), with each set containing three tubes. Mortality (%) was calculated using Eq. (3):

$$\text{Mortality (\%)} = \frac{\text{Number of deaths}}{\text{Total number of individuals}} \times 100 \qquad (3)$$

The chronic LC_{50} (lethal concentration 50), representing 50% mortality within 24 h, was used to assess extract toxicity through probit analysis, utilising correlated concentrations and fatality percentages on a probit scale.

Statistical Analysis

The data was gathered in triplicate and provided as the mean ± standard deviation. Statistical analysis was conducted using IBM SPSS Statistics (Version 28). A one-way analysis of variance (ANOVA) was used to assess the data, followed by Tukey's Honestly Significant Difference (HSD) post hoc test to identify significant differences across the samples, with the level of significance set at 95% ($p < 0.05$). For correlation analysis, the Pearson correlation coefficient (r) was used.

3. Results and Discussion

Extraction Yield

An ultrasonic water bath is a device used in extraction processes to enhance the efficiency of extracting compounds from plant materials. It operates by subjecting the mixture of solvent and plant material to high-frequency sound waves, creating microscopic bubbles that implode upon collapsing. This phenomenon, known as cavitation, generates intense local pressure and temperature changes that aid in breaking down the cell walls of the plant and promoting better solvent penetration (Santos & Capelo, 2007; Kallioinen & Mänttäri, 2011). Factors such as frequency, amplitude, solvent choice, temperature, and extraction time influence its effectiveness. The benefits include efficient mass transfer, reduced extraction time, selectivity, and sustainability due to lower energy requirements (Vilkhu et al., 2008; Chemat et al., 2017). Hence, this method optimises extraction yields while maintaining the quality of extracted compounds.

Table 1 presents a comparison of the results obtained from five different solvent types used in *P. pellucida* leaf extracts, showing significant differences. Considering how different solvents interact with plant compounds, NADES stands out due to its strong extraction ability, yielding 17.39 ± 0.04%. This efficacy can be attributed to the unique characteristics of NADES, which allow it to establish robust interactions with the compounds due to its distinct polarity. In contrast, ethyl acetate, characterised by lower polarity, yields the least efficient extraction at 2.87 ± 0.15%, possibly due to its comparatively weaker solvent-target interactions. Distilled water, methanol, and ethanol, which fall within the middle range of polarities, show extraction yields of 8.24 ± 0.05%, 7.46 ± 0.00%, and 6.70 ± 0.02%, respectively, indicating their moderate ability to interact with the compounds of interest.

Table 1. Extraction yield of *P. pellucida* leaf extracts based on different solvents

Solvent Extraction	Extraction Yield (%)
NADES	17.39 ± 0.04^a
Distilled water	8.24 ± 0.05^b
Methanol	7.46 ± 0.00^c
Ethanol	6.70 ± 0.02^d
Ethyl acetate	2.87 ± 0.15^e

The presented data represent means ± standard deviations from triplicates. Distinct letters (within a column) indicate significant differences established through one-way ANOVA and Tukey's HSD test ($p < 0.05$).

The choice of solvent significantly influences the extraction yield. Solvents with different polarities interact differently with the target compounds in plant material (Rezaie et al., 2015). The higher extraction yield obtained with NADES can be attributed to its distinct polarity, which allows it to effectively interact with the compounds and facilitate their release (Hikmawanti et al., 2021). This study also highlighted that diluting NADES with distilled water and increasing the temperature aim to reduce its high viscosity, thereby facilitating the extraction process (Shishov et al., 2020). Furthermore, surface tension and viscosity are crucial factors in ultrasonic extraction. Reduced surface tension and viscosity facilitate the formation of explosive cavities. Liquids with lower viscosity tend to generate stable foam fractions, while those with high viscosity produce larger cavities (Kadoi & Nakae, 2011; Kallioinen & Mänttäri, 2011). Hence, this enhances the diffusion of NADES into plant samples.

On the other hand, solvents with lower polarity, such as ethyl acetate, demonstrated lower extraction yields due to their weaker interactions with the target compounds. This aligns with the findings of Koch et al. (2020), who reported that ethyl acetate has limited efficacy as an extraction solvent in different methods. The lower extraction yield of ethyl acetate, coupled with its lower polarity, could also be influenced by its viscosity. The reduced viscosity of ethyl acetate might hinder its ability to effectively penetrate plant material and establish strong interactions, contributing to the observed lower extraction efficiency (Rezaie et al., 2015). Recent studies highlight that solvent polarity significantly influences the extraction process, affecting the amount and quality of extracted compounds, secondary metabolites, and biological activity (Rafińska et al., 2019). These findings emphasise the importance of selecting the appropriate solvent to achieve better extraction results, particularly in obtaining greater amounts of desired compounds.

Antioxidant Activity

Table 2 presents the outcomes of solvent extraction on *P. pellucida* leaf extracts, including TFC and DPPH scavenging activity. Among the solvents used, ethanol proved to be the most efficient, yielding the highest TFC value of 18.74 ± 0.10 mg RE/g, demonstrating its strong capacity for flavonoid extraction. Furthermore, distilled water yielded a TFC value of 17.89 ± 0.05 mg RE/g, followed by NADES (17.24 ± 0.17 mg RE/g) and methanol (16.43 ± 0.02 mg RE/g). Conversely, ethyl acetate yielded the lowest TFC value at 4.92 ± 0.02 mg RE/g, indicating its relatively limited capacity for flavonoid extraction. These significant variations in TFC values highlight pronounced differences in extraction efficiency among the solvents.

Table 2. Antioxidant activity of *P. pellucida* leaf extracts based on different solvents

Solvent Extraction	TFC (mg RE/g)	DPPH (%)
NADES	17.24 ± 0.17^{c}	83.31 ± 0.03^{b}
Distilled water	17.89 ± 0.05^{b}	70.83 ± 0.44^{d}
Methanol	16.43 ± 0.02^{d}	79.12 ± 0.02^{c}
Ethanol	18.74 ± 0.10^{a}	79.48 ± 0.03^{c}
Ethyl acetate	4.92 ± 0.02^{e}	68.22 ± 0.07^{e}
Ascorbic acid	NA	95.01 ± 0.06^{a}

The presented data represent means ± standard deviations from triplicates. Distinct letters (within a column) indicate significant differences established through one-way ANOVA and Tukey's HSD test ($p < 0.05$).

NA: Not Applicable.

Regarding DPPH scavenging activity (Table 2), the solvents demonstrated the following percentages: NADES exhibited the highest activity at 83.31 ± 0.03%, highlighting its strong antioxidant potential. Meanwhile, ethanol and methanol showed comparable DPPH scavenging activities at 79.48 ± 0.03% and 79.12 ± 0.02%, respectively, indicating their effective free radical neutralisation capabilities. Distilled water recorded a DPPH scavenging activity of 70.83 ± 0.44%, reflecting variations in antioxidant effectiveness. However, ethyl acetate exhibited the lowest DPPH scavenging activity at 68.22 ± 0.07%, suggesting its relatively limited capacity to counteract free radicals.

Polarity is highly sensitive to changes in water content due to hydrogen bonding disruptions, leading to alterations in the polarity index. Therefore, polarity is a crucial aspect of NADES and is closely related to its solubilising ability. The increased antioxidant efficacy of NADES might be attributed to the release of hydrophilic phenolic compounds present in *P. pellucida* leaf extracts (Mohammad Salamatullah et al., 2022). The elevated antioxidant activity in NADES can also be attributed to its unique blend of choline chloride and lactic acid, forming deep eutectic solvents. This combination strengthens hydrogen bond interactions and polarity, facilitating efficient electron donation to counteract DPPH radicals (Doldolova et al., 2021). The notable polarity of NADES further assists in dissolving and extracting hydrophilic antioxidants from the sample, resulting in better scavenging activity when compared to solvents such as ethyl acetate. The distinct composition and polarity of NADES enhance its ability to engage with DPPH radicals, making it a promising solvent choice for antioxidant studies.

Distilled water exhibits slightly lower DPPH activity than NADES due to its lack of solute compounds. In contrast, NADES contains choline chloride and lactic acid, which enhance hydrogen bond interactions and polarity (Ling et al., 2020). These components contribute to electron donation against DPPH radicals, leading to increased antioxidant activity (Jurić et al., 2021). On the other hand, the higher polarity of distilled water and the absence of these solutes hinder its ability to interact with and neutralise DPPH radicals as effectively as NADES. Meanwhile, methanol and ethanol exhibit similar DPPH radical scavenging activities due to their moderate polarity, allowing them to interact moderately with DPPH radicals and demonstrate noticeable scavenging activity (Liu et al., 2018). However, their DPPH activity is weaker compared to NADES, possibly due to differences in specific polarities and interactions with DPPH radicals.

As shown in Table 3, the correlation analysis between TFC and DPPH revealed a moderate positive correlation, with an r value of 0.67. This finding indicates a significant relationship between flavonoids (TFC) and antioxidant activity (DPPH) in *P. pellucida* leaf extracts from different solvents.

Table 3. Correlation analysis between TFC and DPPH of *P. pellucida* leaf extracts.

	DPPH	
	r	***p*-Value**
TFC	0.67*	0.00

* Correlation is significant at the 0.01 level (2-tailed).

The moderate positive correlation indicates that as TFC increases, DPPH scavenging activity tends to increase as well. This aligns with the general understanding that flavonoids are often associated with antioxidant properties, and higher flavonoids may contribute to enhanced free radical scavenging abilities (Aryal et al., 2019). Notably, although NADES ranked third in TFC among the solvents, it exhibited the highest DPPH scavenging activity. While the correlation is moderate, additional factors beyond flavonoids could also influence antioxidant activity, including the presence of other bioactive compounds such as phenolics (Aryal et al., 2019).

Toxicity

As noted by Benjamin et al. (2022), in relation to the BSLA, the toxicity categorisation for plant extracts is as follows: extracts with LC_{50} values exceeding 1000 µg/mL are deemed non-toxic; those ranging from 500 µg/mL to 1000 µg/mL exhibit mild toxicity; and extracts with LC_{50} values below 500 µg/mL are classified as toxic. This assay is commonly used to determine whether an extract ranges from toxic to non-toxic, serving as a preliminary screening for cytotoxicity or safety for consumption (Adelegan et al., 2023; Kharisma et al., 2023). Hence, Table 4 presents the toxicity of *P. pellucida* leaf extracts with various solvents using BSLA. Based on the findings, both NADES and distilled water displayed LC_{50} values > 1000 µg/mL, implying that at concentrations above this threshold, these solvents exerted a non-toxic effect on the test organisms. Conversely, methanol and ethanol had significantly lower LC_{50} values of 403.66 µg/mL and 198.45 µg/mL, respectively, indicating mild toxicity. Ethyl acetate exhibited the lowest LC_{50} at 129.90 µg/mL, indicating toxicity compared to the other solvents. These results highlight the diverse toxic effects of different solvents on the test organisms.

Table 4. BSLA of *P. pellucida* leaf extracts based on different solvents

Solvent Extraction	**Concentration (µg/mL)**	**Mortality (%)**	**LC_{50} (µg/mL)**
NADES	1000	9	1597.62
	500	6	
	300	2	
	100	0	
Distilled water	1000	10	1561.44
	500	5	
	300	3	
	100	0	
Methanol	1000	70	403.66
	500	50	
	300	40	
	100	30	
Ethanol	1000	80	198.45
	500	70	
	300	50	
	100	40	
Ethyl acetate	1000	100	129.90
	500	100	
	300	70	
	100	40	
Potassium dichromate	1000	100	300.66
	500	40	
	300	30	
	100	20	

The high toxicity observed in methanol and ethanol, with LC_{50} values below 500 µg/mL, can be attributed to their properties as common organic solvents. These solvents interact with living systems, resulting in toxicity (Popovici et al., 2021). Similarly, ethyl acetate, which is less polar, exhibited higher toxicity, with an LC_{50} value of 129.90 µg/mL due to its distinct properties and interactions with organisms. Its lower polarity might influence how it interacts with organisms, potentially harming cells and metabolic processes (Al-Saeedi et al., 2017). The increased toxicity of ethyl acetate underscores its unsuitability for applications requiring low toxicity. In contrast, NADES and distilled water exhibited no toxic effects, even at concentrations > 1000 µg/mL, highlighting their potential suitability for various applications without posing substantial harm to organisms. This can be attributed to their unique compositions and low toxicity profiles, making them safe choices for use in environments where minimising harm to living organisms is crucial (Benjamin et al., 2022; Usmani et al., 2023).

The aim of the BSLA was to assess the functional properties of *P. pellucida* leaf extracts. However, a notable gap in global knowledge exists regarding the impact of solvent extracts on the toxicity of these extracts. This study employs the BSLA as a reliable method for the initial assessment of extract toxicity (Ntungwe N et al., 2020). Additionally, the BSLA results for *P. pellucida* leaf extracts are compared using different solvents to explore their

DOI:https//doi.org/10.22452/mjs.vol44no1.5

potential medicinal value for future development as functional food ingredients. The ultimate goal is to formulate products with pharmaceutical and nutraceutical properties. Notably, NADES and distilled water exhibit no harmful effects, even at concentrations > 1000 µg/mL, indicating their potential suitability for various applications without causing significant harm to organisms. Further investigations could explore their in vivo effects using animal models.

4. Conclusion

Overall, NADES stands out as the superior solvent, delivering the highest extraction yield, remarkable antioxidant potential, and non-toxic attributes for *P. pellucida* leaf extracts. NADES emerges as the optimal solvent for *P. pellucida* leaf extraction, yielding both the highest crude extract and moderate TFC. This solvent also exhibits the most potent antioxidant activity, attributed to its ability to control DPPH reactivity kinetics. Notably, NADES demonstrates exceptional non-toxicity, as indicated by an LC_{50} of 1597.62 µg/mL in the BSLA. Therefore, these results highlight the promising role of NADES in advancing therapeutics by harnessing the medicinal value of the plant.

5. Acknowledgement

This study received financial support from Universiti Malaysia Sabah under the Skim Pensyarah Lantikan Baru (SLB2234) scheme.

6. References

Adelegan, A. A., Dokunmu, T. M., & Iweala, E. E. J. (2023). In-vitro antioxidant activity and cytotoxic effect of ethanol leaf extract and fractions of *Olax subscorpioidea* Oliv. (Olacaceae). *Tropical Journal of Natural Product Research*, *7*(8), 3806–3812.

Al-Saeedi, A. H., Al-Ghafri, M. T. H., & Hossain, M. A. (2017). Brine shrimp toxicity of various polarities leaves and fruits crude fractions of *Ziziphus jujuba* native to Oman and their antimicrobial potency. *Sustainable Chemistry and Pharmacy*, *5*, 122–126.

Alves, N. S. F., Setzer, W. N., & da Silva, J. K. R. (2019). The chemistry and biological activities of *Peperomia pellucida* (Piperaceae): A critical review. *Journal of Ethnopharmacology*, *232*, 90–102.

Aryal, S., Baniya, M. K., Danekhu, K., Kunwar, P., Gurung, R., & Koirala, N. (2019). Total phenolic content, flavonoid content and antioxidant potential of wild vegetables from western Nepal. *Plants*, *8*(4), 96.

Awang, M. A., Chua, L. S., Abdullah, L. C., & Pin, K. Y. (2021a). Drying kinetics and optimization of quercetrin extraction from *Melastoma malabathricum* leaves. *Chemical Engineering and Technology*, *44*(7), 1214–1220.

Awang, M. A., Daud, N. N. N. N. M., Ismail, N. I. M., Cheng, P. G., Ismail, M. F., & Ramaiya, S. D. (2021b). Antioxidant and cytotoxicity activity of *Cordyceps militaris* extracts against human colorectal cancer cell line. *Journal of Applied Pharmaceutical Science*, *11*(7), 105–109.

Benjamin, M. A. Z., Ng, S. Y., Saikim, F. H., & Rusdi, N. A. (2022). The effects of drying techniques on phytochemical contents and biological activities on selected bamboo leaves. *Molecules*, *27*(19), 6458.

Chemat, F., Rombaut, N., Sicaire, A.-G., Meullemiestre, A., Fabiano-Tixier, A.-S., & Abert-Vian, M. (2017). Ultrasound assisted extraction of food and natural products. Mechanisms, techniques, combinations, protocols and applications. A review. *Ultrasonics Sonochemistry*, *34*, 540–560.

Doldolova, K., Bener, M., Lalikoğlu, M., Aşçı, Y. S., Arat, R., & Apak, R. (2021). Optimization and modeling of microwave-assisted extraction of curcumin and antioxidant compounds from turmeric by using natural deep eutectic solvents. *Food Chemistry*, *353*, 129337.

García-Roldán, A., Piriou, L., & Jauregi, P. (2023). Natural deep eutectic solvents as a green extraction of polyphenols from spent coffee ground with enhanced bioactivities. *Frontiers in Plant Science*, *13*, 1072592.

Hikmawanti, N. P. E., Ramadon, D., Jantan, I., & Mun'im, A. (2021). Natural deep eutectic solvents (NADES): Phytochemical extraction performance enhancer for pharmaceutical and nutraceutical product development. *Plants*, *10*(10), 2091.

Ho, K. L., Yong, P. H., Wang, C. W., Kuppusamy, U. R., Ngo, C. T., Massawe, F., & Ng, Z. X. (2022). *Peperomia pellucida* (L.) Kunth and eye diseases: A review on phytochemistry, pharmacology and toxicology. *Journal of Integrative Medicine*, *20*(4), 292–304.

Ibrahim, F. H., & Hamzah, N. (1999). The use of medicinal plant species by the Temuan tribe of Ayer Hitam Forest, Selangor, Peninsular Malaysia. *Pertanika Journal of Tropical Agricultural Science*, *22*(2), 85–94.

Jurić, T., Mićić, N., Potkonjak, A., Milanov, D., Dodić, J., Trivunović, Z., & Popović, B. M. (2021). The evaluation of phenolic content, in vitro antioxidant and antibacterial activity of *Mentha piperita* extracts obtained by natural deep eutectic solvents. *Food Chemistry*, *362*, 130226.

Kadoi, K., & Nakae, H. (2011). Relationship between foam stabilization and physical properties of particles on aluminum foam production. *Materials Transactions*, *52*(10), 1912–1919.

DOI:https//doi.org/10.22452/mjs.vol44no1.5

Kallioinen, M., & Mänttäri, M. (2011). Influence of ultrasonic treatment on various membrane materials: A review. *Separation Science and Technology*, *46*(9), 1388–1395.

Kharisma, A. D., Nisa, U. C., & Yasman. (2023). Evaluation of antioxidant activity and toxicity of *Cinnamomum burmannii* B. from different provinces of Indonesia. *Journal of Hunan University Natural Sciences*, *50*(4), 177–188.

Koch, W., Kukuła-Koch, W., Czop, M., Helon, P., & Gumbarewicz, E. (2020). The role of extracting solvents in the recovery of polyphenols from green tea and its antiradical activity supported by principal component analysis. *Molecules*, *25*(9), 2173.

Ling, J. K. U., Chan, Y. S., Nandong, J., Chin, S. F., & Ho, B. K. (2020). Formulation of choline chloride/ascorbic acid natural deep eutectic solvent: Characterization, solubilization capacity and antioxidant property. *LWT*, *133*, 110096.

Liu, Y., Friesen, J. B., McAlpine, J. B., Lankin, D. C., Chen, S.-N., & Pauli, G. F. (2018). Natural deep eutectic solvents: Properties, applications, and perspectives. *Journal of Natural Products*, *81*(3), 679–690.

Mohammad Salamatullah, A., Hayat, K., Mabood Husain, F., Asif Ahmed, M., Arzoo, S., Musaad Althbiti, M., … Bourhia, M. (2022). Effects of different solvents extractions on total polyphenol content, HPLC analysis, antioxidant capacity, and antimicrobial properties of peppers (red, yellow, and green (*Capsicum annum* L.)). *Evidence-Based Complementary and Alternative Medicine*, *2022*, 7372101.

Nawaz, H., Shad, M. A., Rehman, N., Andaleeb, H., & Ullah, N. (2020). Effect of solvent polarity on extraction yield and antioxidant properties of phytochemicals from bean (*Phaseolus vulgaris*) seeds. *Brazilian Journal of Pharmaceutical Sciences*, *56*, e17129.

Ng, Z. X., Samsuri, S. N., & Yong, P. H. (2020). The antioxidant index and chemometric analysis of tannin, flavonoid, and total phenolic extracted from medicinal plant foods with the solvents of different polarities. *Journal of Food Processing and Preservation*, *44*(9), e14680.

Ntungwe N, E., Domínguez-Martín, E. M., Roberto, A., Tavares, J., Isca, V. M. S., Pereira, P., … Rijo, P. (2020). *Artemia* species: An important tool to screen general toxicity samples. *Current Pharmaceutical Design*, *26*(24), 2892–2908.

Oomen, W. W., Begines, P., Mustafa, N. R., Wilson, E. G., Verpoorte, R., & Choi, Y. H. (2020). Natural deep eutectic solvent extraction of flavonoids of *Scutellaria baicalensis* as a replacement for conventional organic solvents. *Molecules*, *25*(3), 617.

Popovic, B. M., Micic, N., Potkonjak, A., Blagojevic, B., Pavlovic, K., Milanov, D., & Juric, T. (2022). Novel extraction of polyphenols from sour cherry pomace using natural deep eutectic solvents – Ultrafast microwave-assisted NADES preparation and extraction. *Food Chemistry*, *366*, 130562.

Popovici, V., Bucur, L., Popescu, A., Schröder, V., Costache, T., Rambu, D., … Badea, V. (2021). Antioxidant and cytotoxic activities of *Usnea barbata* (L.) F.H. Wigg. dry extracts in different solvents. *Plants*, *10*(5), 909.

Rafińska, K., Pomastowski, P., Rudnicka, J., Krakowska, A., Maruśka, A., Narkute, M., & Buszewski, B. (2019). Effect of solvent and extraction technique on composition and biological activity of *Lepidium sativum* extracts. *Food Chemistry*, *289*, 16–25.

Rezaie, M., Farhoosh, R., Iranshahi, M., Sharif, A., & Golmohamadzadeh, S. (2015). Ultrasonic-assisted extraction of antioxidative compounds from Bene (*Pistacia atlantica* subsp. *mutica*) hull using various solvents of different physicochemical properties. *Food Chemistry*, *173*, 577–583.

Rosarina, D., Narawangsa, D. R., Shaffa, N., Chandra, R., Sari, E., & Hermansyah, H. (2022). Optimization of ultrasonic—assisted extraction (UAE) method using natural deep eutectic solvent (NADES) to increase curcuminoid yield from *Curcuma longa* L., *Curcuma xanthorrhiza*, and *Curcuma mangga* Val. *Molecules*, *27*(18), 6080.

Santos, H. M., & Capelo, J. L. (2007). Trends in ultrasonic-based equipment for analytical sample treatment. *Talanta*, *73*(5), 795–802.

Shishov, A., Pochivalov, A., Nugbienyo, L., Andruch, V., & Bulatov, A. (2020). Deep eutectic solvents are not only effective extractants. *Trends in Analytical Chemistry*, *129*, 115956.

Siew, Y.-Y., Zareisedehizadeh, S., Seetoh, W.-G., Neo, S.-Y., Tan, C.-H., & Koh, H.-L. (2014). Ethnobotanical survey of usage of fresh medicinal plants in Singapore. *Journal of Ethnopharmacology*, *155*(3), 1450–1466.

Stephenus, F. N., Benjamin, M. A. Z., Anuar, A., & Awang, M. A. (2023). Effect of temperatures on drying kinetics, extraction yield, phenolics, flavonoids, and antioxidant activity of *Phaleria macrocarpa* (Scheff.) Boerl. (mahkota dewa) fruits. *Foods*, *12*(15), 2859.

Tantiado, R. G. (2012). Survey on ethnopharmacology of medicinal plants in Iloilo, Philippines. *International Journal of Bio-Science and Bio-Technology*, *4*(4), 11–26.

DOI:https//doi.org/10.22452/mjs.vol44no1.5

Usmani, Z., Sharma, M., Tripathi, M., Lukk, T., Karpichev, Y., Gathergood, N., … Gupta, V. K. (2023). Biobased natural deep eutectic system as versatile solvents: Structure, interaction and advanced applications. *Science of The Total Environment*, *881*, 163002.

Vilkhu, K., Mawson, R., Simons, L., & Bates, D. (2008). Applications and opportunities for ultrasound assisted extraction in the food industry — A review. *Innovative Food Science & Emerging Technologies*, *9*(2), 161–169.

MALAYSIAN JOURNAL OF SCIENCE
MJS
ISSN 1394-3065

Regular Issue

Malaysian Journal of Science 44 (1): 42-54 (March 2025)
https://mjs.um.edu.my

Geoelectric Assessment of Regolith Aquifer and Its Vulnerability, in a Typical Basement Complex Terrain, Southwestern Nigeria

Wilfred N. Igboama[1a]*, Morufu T. Aroyehun[2b] and Olaide S. Hammed[3a]

Abstract: Assessment of groundwater potential cum regolith aquifer protective strength was carried out using the electrical resistivity method at Ikole Ekiti, Southwestern Nigeria, to assess its viability and susceptibility. The Vertical Electrical Sounding (VES) technique using the Schlumberger array was adopted. The acquired data was partially curve-matched, forward-modelled, and iterated using WinResist version 1.0 software. Charts, para sections, tables, and maps were generated from the results obtained to aid interpretations. The KH curve type, which indicates good protective capacity, is more predominant in the study area than other curve types. Parasections showed four (4) geoelectric layers, i.e., topsoil, upper saprolite, lower saprolite, and sap rock. A weathered layer is the principal aquifer unit identified in the area; it is appreciably thick, and the basement is fresh. The thickness of regolith ranges from 2 to 56 m, with an appreciable thickness that can sustain moderate groundwater yield in the southern region of Ikole. The layer above the regolith aquifer has an average thickness slightly below 20 m; therefore, areas without lateritic cover will be prone to pollution. The strength of the regolith aquifer was assessed by employing longitudinal conductance (LC) and Geoelectric Layer Susceptibility Index (GLSI) ratings. The inherent weakness of the LC rating (not accounting for the lateritic nature of soil) was complemented by the GLSI rating. The southern region of the study area where groundwater is feasible is evaluated to have moderate protective capacity. Therefore, sources of pollution, such as septic tanks and dump sites, should be located far away from the area.

Keywords: *Aquifer, geoelectric, longitudinal conductance, protective capacity, susceptibility.*

1. Introduction

Geophysical methods and techniques are relevant in groundwater studies, environmental impact assessment (EIA), and engineering site investigation (Ademilua *et al*., 2014). The survey by Olorunfemi and Fasuyi (1993) has shown that geophysical explorations could be successfully applied in developing groundwater feasibility plans at both small and large scales for assessing groundwater flow path. Humans' unavoidable need for water for daily activities has led hydro scientists both in the past and present to design and develop different geophysical methods and techniques used today to explore and exploit groundwater. Examples are gravity, seismic, magnetic, electrical, electromagnetic methods, and most recently, Surface Nuclear Magnetic Resonance (SNMR).

The significance of water to human life and survival on earth cannot be evaluated. Many countries, including Nigeria, suffer from inadequate quantity and quality of fresh surface water, and therefore, the resolve to explore and exploit the abundant groundwater reserves becomes eminent. As groundwater becomes necessary for living activities and human consumption, geophysical methods and techniques are important for exploration, exploitation, and development. Integrating surface and subsurface geophysical measurements can go a long way in helping delineate groundwater occurrence, dynamics, and associated geologic formation.

Numerous researchers, such as Ademilua *et al*., 2014 Akana *et al*., 2016 Alabi *et al*., 2016 and Farid *et al*., 2017, have carried out geophysical projects and research to delineate the properties of subsurface lithological units to examine their hydrogeological significance. Authors such as Srinivasan *et al*., 2013 Akintorinwa and Olowolafe 2013; Kamlesh and Shukla (2014) have specifically conducted studies on groundwater potential and vulnerability using geoelectrical methods. This has proven to be one of the most valuable tools in delineating groundwater (Ndatuwong & Yadav, 2015). Electrical resistivity has been classified as one of the most effective and efficient methods for assessing and exploiting groundwater (Hasan *et al.,* 2018). Agbasi and Edet (2016) have determined the aquifer geometry, depth to the water table, and groundwater quality by analysing the apparent resistivity measured from the electrical survey.

The availability of potable water is a serious problem that is faced not only by rural communities but also by developing regions of the world at large today. The influx of the university community to the study area and the nonfunctional rural water schemes have limited the available water resources. Therefore, there is a need to explore the groundwater potential of the regolith aquifer using geophysical methods, as well as the

Authors information:
[a]Department of Physics, Federal University Oye Ekiti, NIGERIA. E-mail: wilfred.igboama@fuoye.edu.ng[1]; olaide.hammed@fuoye.edu.ng[2]
[b]Department of Geophysics, Federal University Oye Ekiti, NIGERIA E-mail: morufu.aroyehun@fuoye.edu.ng[2]
*Corresponding Author: wilfred.igboama@fuoye.edu.ng

Received: March 16, 2023
Accepted: June 20, 2024
Published: March 31, 2025

DOI:https//doi.org/10.22452/mjs.vol44no1.6

vulnerability of the aquifer since regolith aquifers are vulnerable to pollution. The most common rating for aquifer vulnerability in Southwestern, Nigeria basement complex is the Longitudinal Conductance rating, Adebo *et al.*, (2021); Ayuk, (2019); Eyankware *et al*., 2020; Nwosu and Chinaka (2021), but the existence of resistive lateritic layer (of high protective capacity) which distort the longitudinal conductance ratings (Oni *et al.*, 2017; Ayodele *et al.*, 2022) necessitates the integration of geoelectric layer susceptibility index (GLSI) to compensate for the inherent weakness of longitudinal conductance rating in aquifer vulnerability mapping. The specific objectives of this research are to identify geoelectric layers and their thickness for regolith aquifers across the study area and to assess the vulnerability of the aquifer using LC and GLSI ratings.

2. Location and Accessibility of The Area

The study area, Odo Oro, Ikole, is in southwestern Nigeria (Figure 1). It lies within latitudes 7^0 46′16′′N to 7^{0}48′43′′N and longitudes 5^0 30′ 51′′E to 5^0 32′ 29′′E. It covers 321 km^2 and is approximately 555m above sea level. The area can be accessed through main roads, minor roads, and footpaths.

Relief, Climate and Drainage

The area is located in an undulating terrain within the tropical region of southwestern Nigeria, which has two seasons: wet season (March to October) and dry season(November to February). The average monthly temperature, humidity, and annual rainfall are 28^{0}C, 70%, and 1800mm, respectively, Rahaman (1988). The dendritic study area has a drainage pattern indicating a uniform response of underlying rocks to water absorption.

Geology of the Study Area

Many great scholars have worked on the geology of Nigeria, particularly on Nigeria's basement complex; among such works are the ones of Odeyemi (1977), Grant (1978), and Bayowa *et al*., 2016. Odeyemi (1977) remarked that southwestern Nigeria lies within the basement complex and classified the rock within the region as migmatite-gneiss of Precambrian origin. Grant (1978) opined that the occurrence of geological structures is of tectonic origin. The geological fissures herein deform the caprock and create discontinuities that promote g, groundwater accumulation and storage capacity. The prominent rock types in the study area are migmatite gneiss, granite, and charnokite.

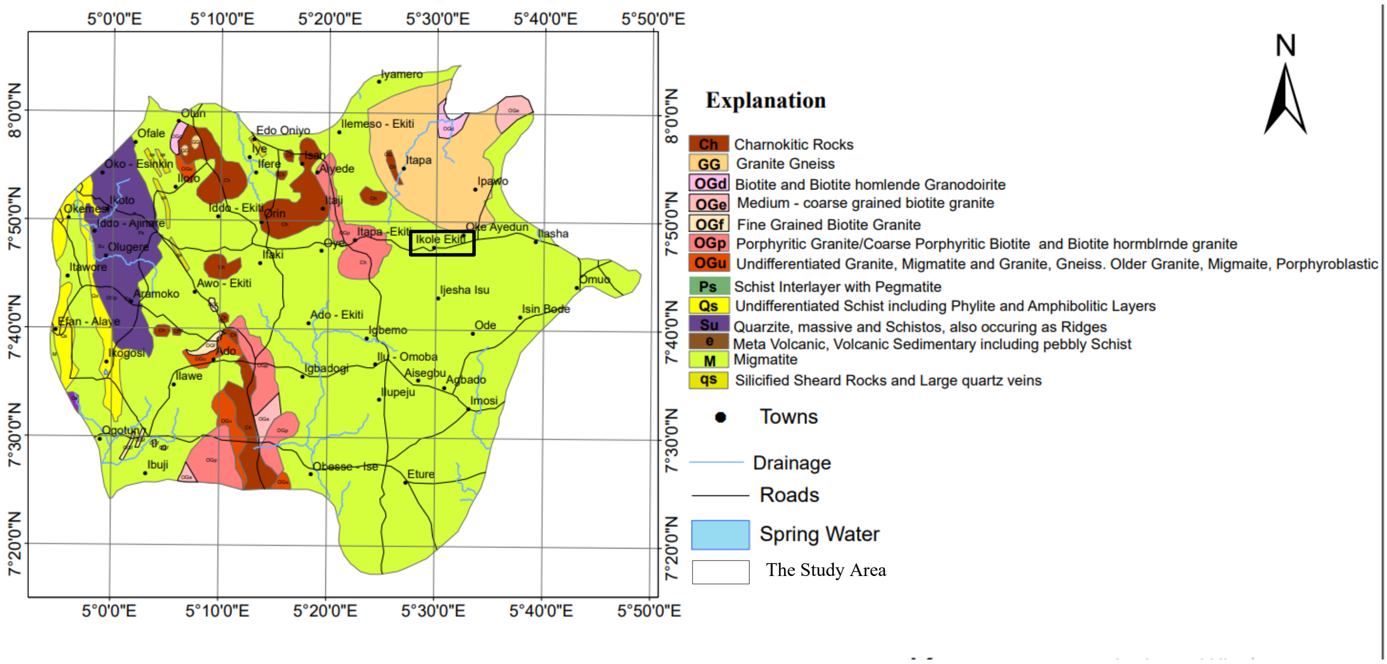

Figure 1. Geological Map of Ekiti highlighting major rock groups

3. Methodology

A Vertical Electrical Sounding (VES) technique using a Schlumberger array was adopted to investigate how resistivity varies with depth at each station point (Figure 2). The Schlumberger array was adopted for this survey because of its effectiveness in subsurface investigation and high penetration depth (Keller and Frishchncht (1996); Abudulawal *et al*., 2015; Anomohanran *et al*., 2017).

Twenty-seven (27) VES stations were equally spread across the area to map the geological sequence (Fig. 3). Half current electrode spacing (AB/2) was used and varied from 1m to 75 m. Vertical Electrical Sounding (VES) data were processed and interpreted quantitatively via partial curve matching techniques. Vander Velpen (2004) involves layer-by-layer fitting of field curves and theoretical curves starting from small electrode spacing. Geoelectric parameters obtained from the partial curve matching were employed as an initial model using WinResist version 1.0

DOI:https//doi.org/10.22452/mjs.vol44no1.6

(Oladapo & Akintorinwa, 2007) for forward modelling. The geoelectric parameters obtained from the iteration were used to draw geoelectric parasections (Figure 3), charts, and maps. Longitudinal Conductance (LC) and Geoelectric Layers Susceptibility Index (GLSI) ratings were calculated to determine the vulnerability of the aquifer as shown in equations (1) and (2), respectively.

$$LC = \frac{h1}{\rho 1} + \frac{h2}{\rho 2} + \frac{h3}{\rho 3} + \cdots + \frac{hn}{\rho n} \ldots\ldots\ldots\ldots\ldots\ldots\ldots\ldots \text{(1),}$$

Abiola et al., (2009)

Where h_i stands for the thickness of layers above the aquifer thickness and ρ_i is the resistivities of layers above the aquifer. LC of 0.7 and above indicates good to excellent protective capacity.

$$GLSI = (((\rho 1r + h1r)/2)) + ((\rho 2r + h2r)/2)) + \cdots + ((\frac{\rho nr + hnr}{2}))/2\,))/N)))\ldots\ldots \text{(2)}$$

Ugwu *et al.*, 2016.

ρ_{1r} stands for resistivity index rating of layer 1,
h_{1r} stands for thickness index rating of layer 1,
ρ_{2r} stands for resistivity index rating of layer 2,
h_{2r} stands for thickness index rating of layer 2,
ρ_{nr} stands for the resistivity index rating of the nth layer
h_{nr} is the thickness index rating of the nth layer,
while N is the numeric value of geoelectric layers upon the aquifer. Index ratings are shown in Table 1 below.

Table 1. Geoelectric Susceptibility Index ratings (Oni *et al.*, 2017).

Lithology	Apparent Resistivity	Vulnerability Index
Laterite	>401	1
Lateritic Sand	151-400	2
Sand	101-150	4
Clayed Sand	51-100	3
Sandy Clay	20-50	2
Clay	< 20	1

Table 2. Geoelectric Susceptibility index of layer thickness (Oni *et al.*, 2017)

Thickness	Index Rating
>20	1
5 – 20	2
2 – 5	3
< 2	4

GSLI between 1.0 to 1.99 means low vulnerability; 2.0 to 2.99 indicates moderate vulnerability; 3.0 to 3.99 indicates high vulnerability, while 4.0 and above is extreme vulnerability Ugwu *et al.*, 2016.

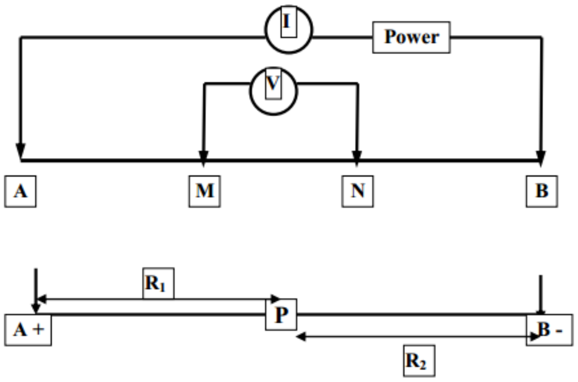

Figure 2. Vertical Electrical Sounding Diagram

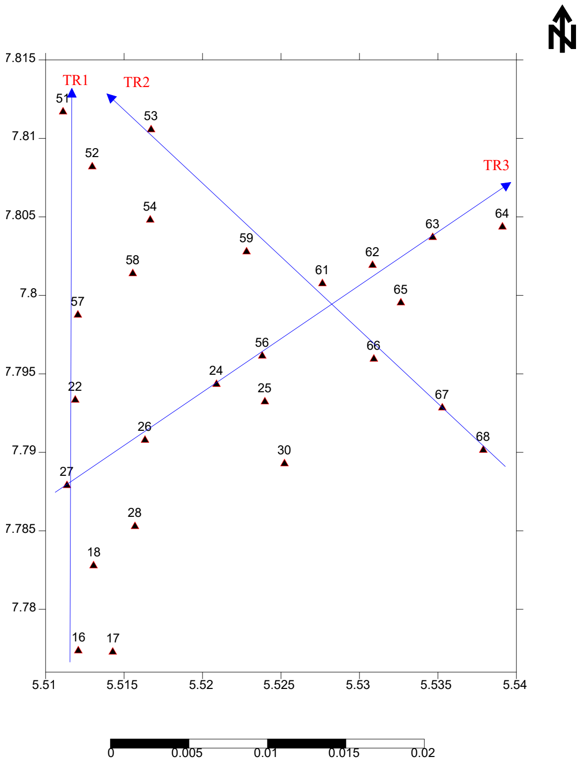

Figure 3. VES Points on the Study Area.

3. Discussion of Results

VES Curve Types

The twenty-seven (27) VES stations occupied generated resistivity sounding curves that varied from 3-layer (H and A) to 4-layers (KH, HA, and AA) as shown in Table 3, and the samples of the curve types are presented in Figures 4-8. Figure 9 shows the frequency of the occurrence of each curve type; the curves were characterised according to their signatures and mirrored the subsurface's layering. The predominant curve type is KH, as highlighted in Figure 6, which depicts a good aquifer protective capacity. KH curve type is one of the signatures of a confined weathered layer/fractured basement aquifer, Olorunfemi and Fasuyi (1993). HA and H curve types could also be suitable regolith aquifers depending on the thickness of each layer. Figure 9 shows the occurrence of each curve type across the study area, while Figure 10 shows how the curve types are distributed relative to the topography of the study area.

Table 3. Geoelectric Characteristics of VES stations

S/N	VES	Longitude	Latitude	Elevation	ρ1	ρ2	ρ3	ρ4	ρ5	h1	h2	h3	h4	Curve Type
1	15	5.509681	7.785528	578	33	199	54	180	-	0.5	4.1	9.8	-	KH
2	16	5.512083	7.777361	579	147	1079	77	936	-	0.7	2.1	15.2	-	KH
3	17	5.514278	7.777278	582	188	1005	335	1756	-	0.4	4.2	37	-	KH
4	18	5.513056	7.782778	585	146	91	218	2736	-	0.7	1.8	14.1	-	KH
5	22	5.511889	7.793333	560	53	45	147	1172	-	0.5	7.3	12.7	-	HA
6	24	5.520889	7.794333	579	190	355	450	6680	-	0.4	3	8.1	-	AA
7	25	5.523972	7.793222	583	107	499	165	546	-	0.7	1.2	8.2	-	KH
8	26	5.516333	7.790778	567	51	41	42	142	-	3.3	5.8	9.7	-	HA
9	27	5.511361	7.787889	575	101	228	31	115	801	1.2	0.4	7.5	5.8	KHA
10	28	5.515694	7.78578	588	169	288	557	-	-	0.9	1.3	-	-	A
11	30	5.525222	7.789278	590	1157	933	541	2902	-	2.7	7.2	45.3	-	QH
12	51	5.511111	7.811694	566	234	232	540	9414	-	1.5	3.2	27.2	-	HA
13	52	5.512974	7.808194	567	208	396	210	290	-	0.8	2.6	12.8	-	KH
14	53	5.516722	7.810556	557	209	765	51	6474	-	0.9	0.7	13	-	KH
15	54	5.516667	7.804806	572	208	114	1470	-	-	1	6.2	-	-	H
16	56	5.523806	7.796139	589	89	177	534	1228	-	1	6	1	-	AA
17	57	5.512056	7.798757	557	86	294	63	547	-	0.8	0.7	8.6	-	KH
18	58	5.515556	7.801389	575	221	2856	135	65	-	0.5	1.5	7.7	-	KQ
19	59	5.522806	7.802778	588	362	748	1383	2886	-	0.5	5	6.3	-	AA
20	61	5.527639	7.80075	586	55	294	86	241	-	0.6	3.3	22	-	KH
21	62	5.530833	7.801917	581	34	143	73	893	-	1	4.7	9.3	-	KH
22	63	5.534667	7.803694	591	218	415	153	2813	-	1.1	3.9	9.2	-	KH
23	64	5.539111	7.804361	591	61	210	311	904	-	0.9	0.3	8.5	-	AA
24	65	5.532639	7.799528	597	173	813	547	6125	-	0.4	2.9	12	-	KH
25	66	5.530917	7.795944	588	127	369	1441	-	-	0.9	6.9	-	-	A
26	67	5.535278	7.792833	586	304	984	377	4345	-	0.6	7	32	-	KH
27	68	5.537889	7.790139	575	312	283	4502	-	-	0.9	3.1	-	-	H

DOI:https//doi.org/10.22452/mjs.vol44no1.6

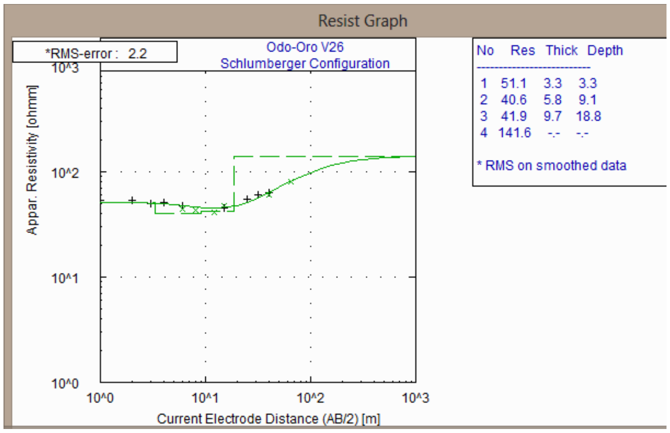

```
*RMS-error :  2.2
Odo-Oro V26
Schlumberger Configuration

No   Res   Thick  Depth
---------------------------
 1   51.1    3.3    3.3
 2   40.6    5.8    9.1
 3   41.9    9.7   18.8
 4  141.6    -.-    -.-

* RMS on smoothed data
```

Figure 4. HA Curve type in the area

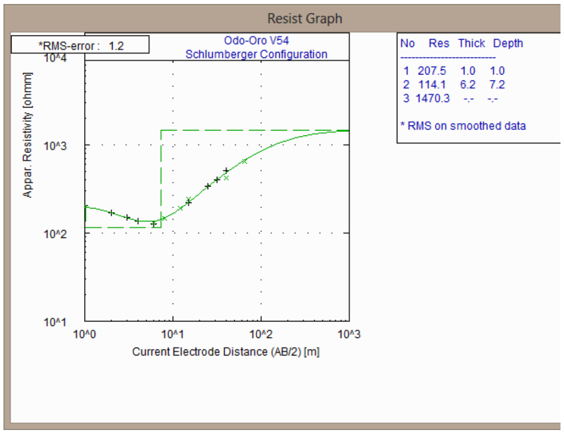

```
*RMS-error :  1.2
Odo-Oro V54
Schlumberger Configuration

No   Res   Thick  Depth
---------------------------
 1   207.5   1.0    1.0
 2   114.1   6.2    7.2
 3  1470.3   -.-    -.-

* RMS on smoothed data
```

Figure 5. H Curve type in the Study Area

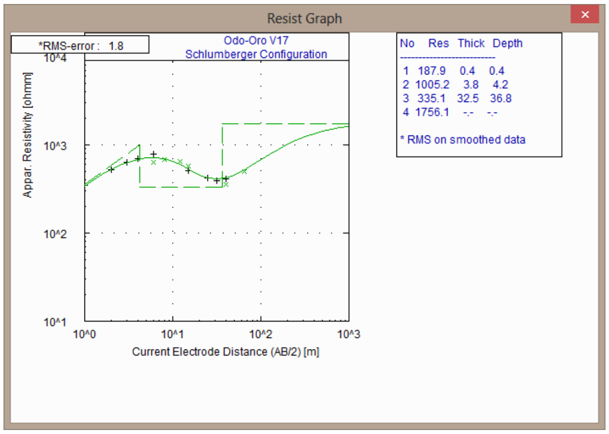

```
*RMS-error :  1.8
Odo-Oro V17
Schlumberger Configuration

No   Res   Thick  Depth
---------------------------
 1   187.9   0.4    0.4
 2  1005.2   3.8    4.2
 3   335.1  32.5   36.8
 4  1756.1   -.-    -.-

* RMS on smoothed data
```

Figure 6. KH Curve type in the area

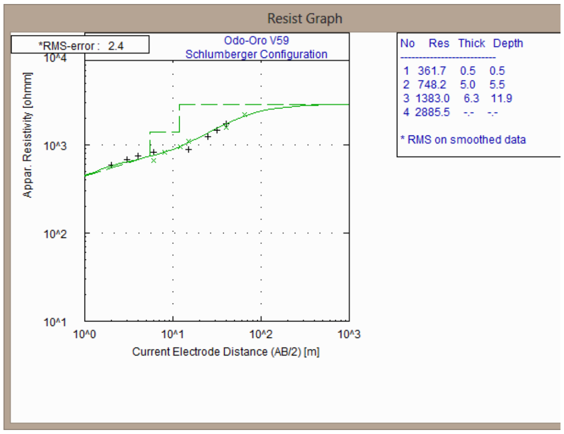

```
*RMS-error :  2.4
Odo-Oro V59
Schlumberger Configuration

No   Res   Thick  Depth
---------------------------
 1   361.7   0.5    0.5
 2   748.2   5.0    5.5
 3  1383.0   6.3   11.9
 4  2885.5   -.-    -.-

* RMS on smoothed data
```

Figure 7. AA Curve type in the Study Area

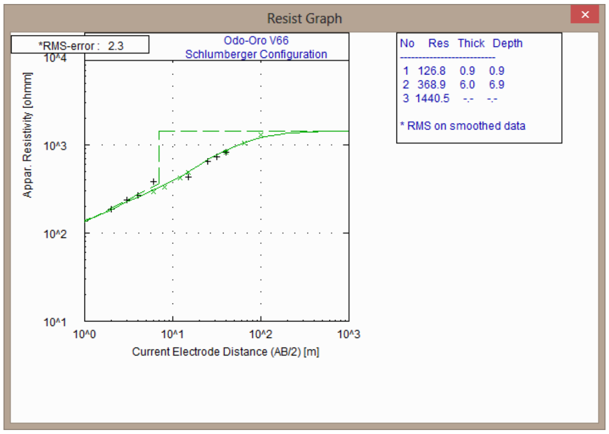

```
*RMS-error :  2.3
Odo-Oro V66
Schlumberger Configuration

No   Res   Thick  Depth
---------------------------
 1   126.8   0.9    0.9
 2   368.9   6.0    6.9
 3  1440.5   -.-    -.-

* RMS on smoothed data
```

Figure 8. A Curve type in the area

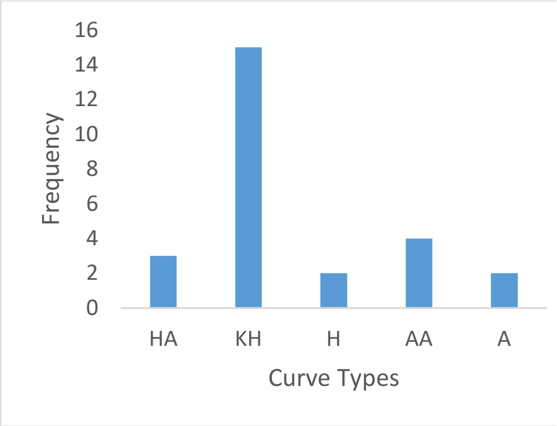

Figure 9. Occurrence of Curve Types in the Area

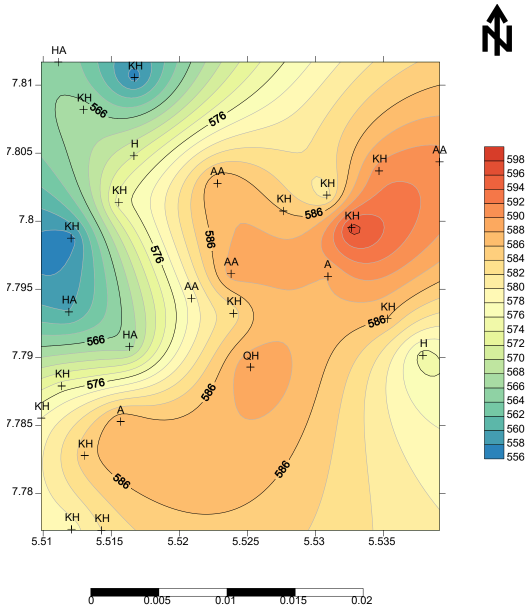

Figure 10. VES Curve (Ohms) Types and their elevation (meter) across the Study Area

Regolith Thickness Map

The regolith thickness, i.e., the depth to the rock head, is a significant factor controlling groundwater accumulation in any basement Complex region. The regolith thickness or overburden in the present study varies from 2 to 56 m across the area, as depicted in Figure 11, which, according to the claims of Oyedele and Olayinka (2012), Ademilua and Eluwole (2013) that the depth of overburden ranges from 1 m to 80 m in southwestern Nigeria. Ademilua and Eluwole (2013) suggested a depth of overburden of 25 m for good groundwater development around the region (of study). Therefore, the southern region of this investigation should be noted for groundwater development, as shown in Figure 11.

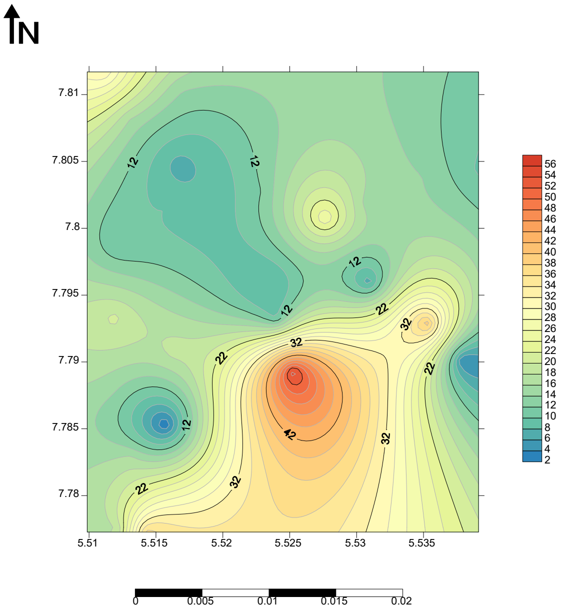

Figure 11. Regolith thickness across the Study Area (meters)

Geoelectric Sections

Three (3) geo-sections were established in the study area. Figures 12, 13, and 14 showed 2-D geoelectric sections along traverses 1, 2, and 3, respectively. TR1 relates VES 16, 27, 22, 57, and 51 (Fig. 11); TR2 relates VES 68, 67, 66, 61, 59, and 53 (Fig. 12); and TR3 relates VES 27, 26, 24, 56, 62 and 63(Fig. 14). The geo-sections showed four layers as topsoil, lateritic layer, weathered layer, and fresh basement. These sections depict thickness and respective resistivity values; the geoelectric sections were characterised as follows.

i. Topsoil - this has resistivity values ranging from 33 - 362 Ω-m. The topsoil has a thickness of 0.4 to 3.3 m.
ii. Upper Saprolite: The upper saprolite is lateritic in nature. Its resistivity value ranged from 199 - 984 Ω-m, having a thickness of 0.7 to 3.1m.
iii. Lower Saprolite: The lower saprolite is weathered and saturated. Its resistivity values vary from 42 - 138 Ω-m with a thickness ranging between 1.5m – 10.0 m.
iv. Saprock: This layer registered resistivity that varied from 142 to 9141 Ω-m.

Layers Thickness above the Aquifer

The thickness of the aquifer layers, among other factors, determines the rate at which the aquifer gets polluted by the surface contaminant. The higher the thickness, the higher the protective capacities, assuming all other conditions are constant. The southwestern region of the area under investigation has the highest thickness, as shown in Figure 15, which is also correlated by layers dominated by KH curves. The thickness of the above aquifer layer and the geological composition of these layers determine the ease with which the aquifer gets polluted. The southwestern region of the study area should be considered for groundwater potential development to avoid pollution.

Longitudinal Conductance (LC)

The longitudinal conductance of the layers above the aquifer was calculated to determine the protective capacity of the aquifers at each VES point. The protective ability of the area is generally poor according to the longitudinal conductance rating. A longitudinal conductance map was generated, as shown in Figure 16, to provide an overview of the aquifer's protective capacity in the entire investigation region. The southwestern part of the area has moderate aquifer protective capacity, which correlates with the area's highest depth of the aquifer layers. The aquifer protective capacity is characterised by the values of the longitudinal conductance unit of rocks' regolith (thickness). In the present study, the longitudinal unit of conductance obtained ranged between 0.02 to 0.44 mhos resulting in the classification of this region as having low to moderate protective capacity as shown in Figure 16 while the region having longitudinal unit of conductance ranged between 0.1 – 0.19 is classified as area of weak protective capacity Rahaman (1988); Odeyemi(1977) and Grant (1978) while 0.7 - 4.9 is classified as good protective capacity, although not obtained in this present study.

Geoelectric Layers Susceptibility Index (GLSI)

In order to examine the inherent weakness in the longitudinal conductance rating of the aquifer protective capacity, GLSI was used as it considers the existence of a lateritic layer in the Nigeria Basement Complex. A GLSI map was generated to give an overall view of the aquifer protection ability in the entire area, as shown in Figure 17. Figure 17 shows that unlike in the southern part, highly vulnerable aquifers in the northern and western areas could be protected by appreciable thickness of lateritic layer (LC does not account for that).

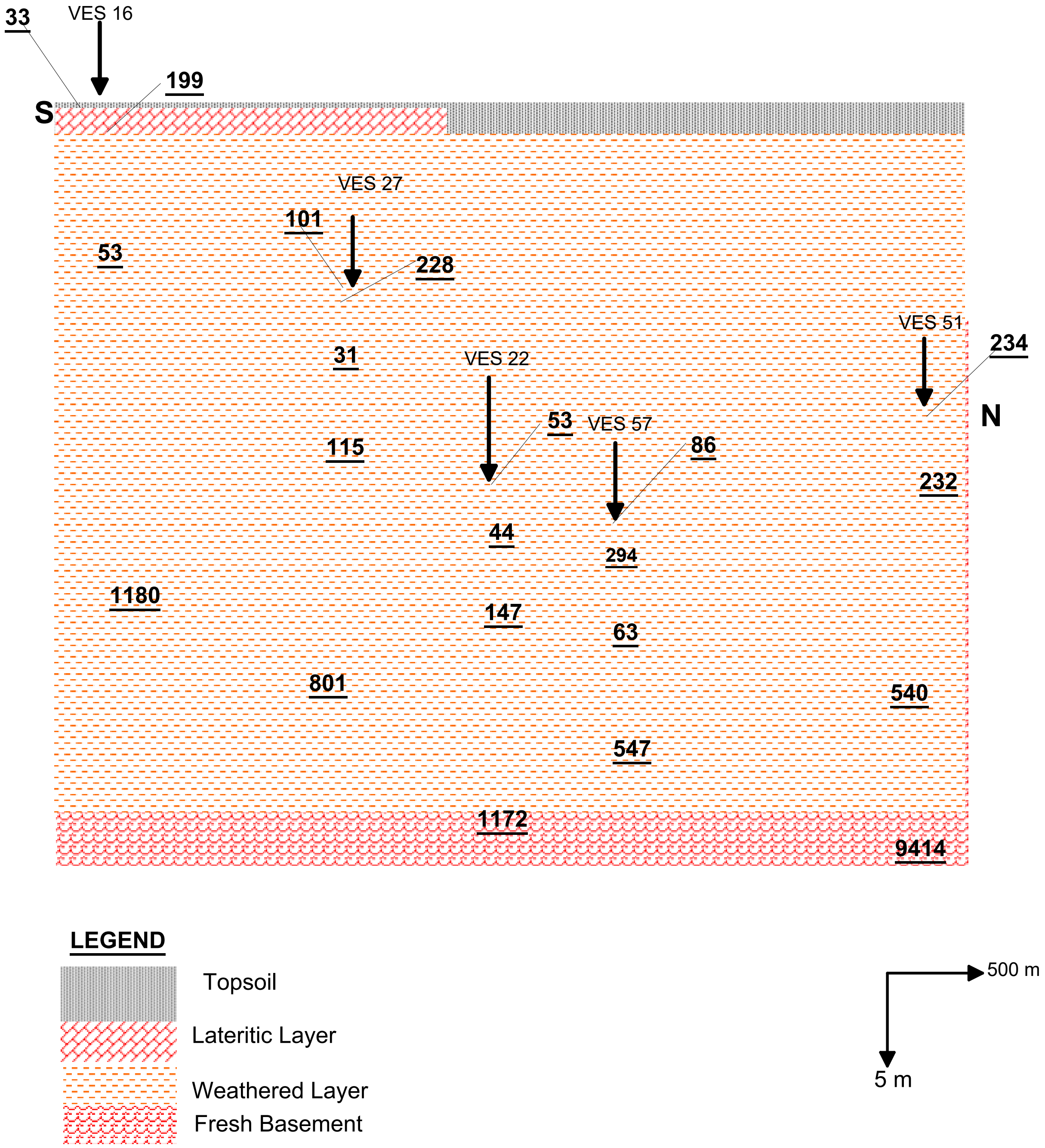

Figure 12. Geo-section of Traverse One (1)

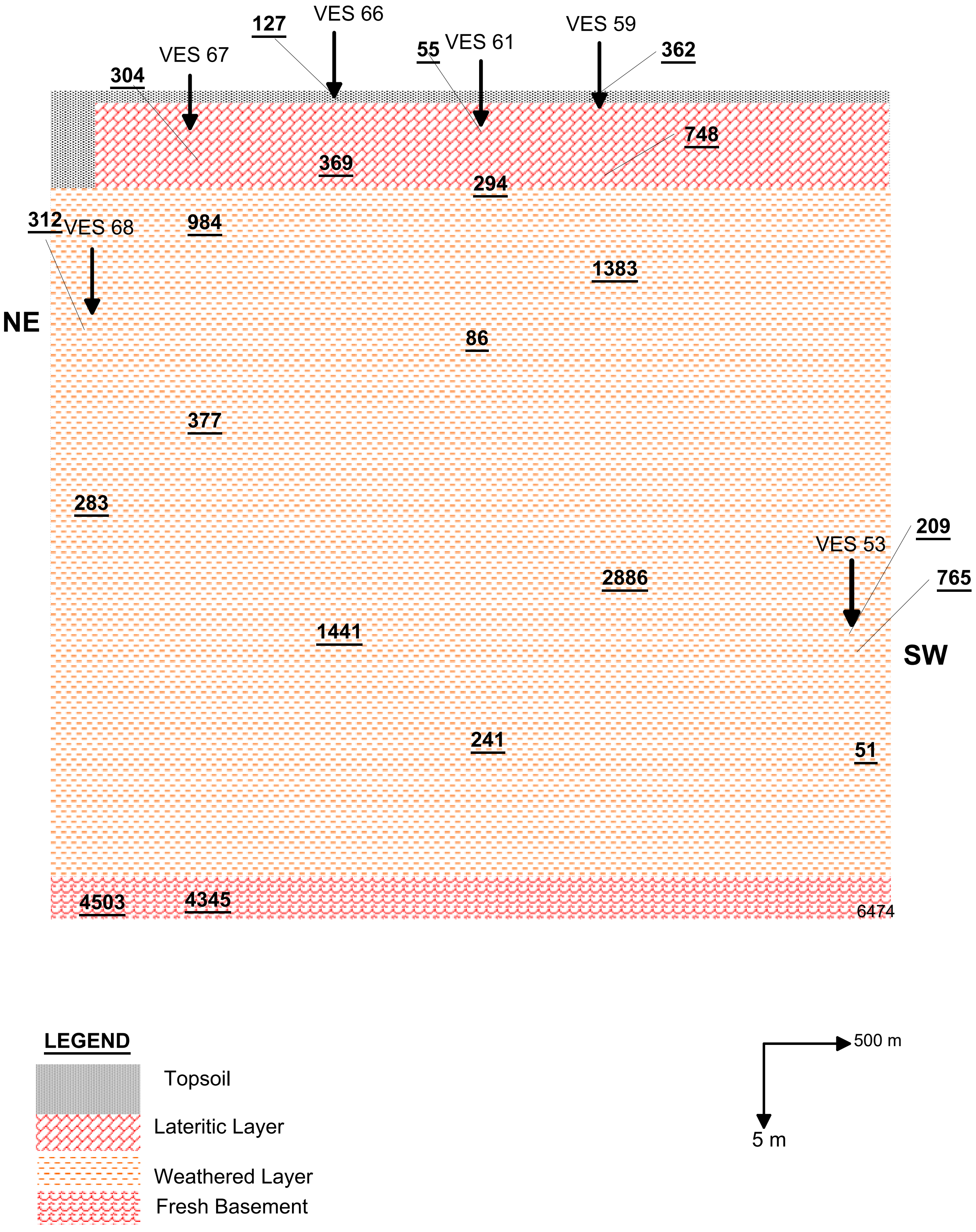

Figure 13. Geo-section of Traverse Two (2)

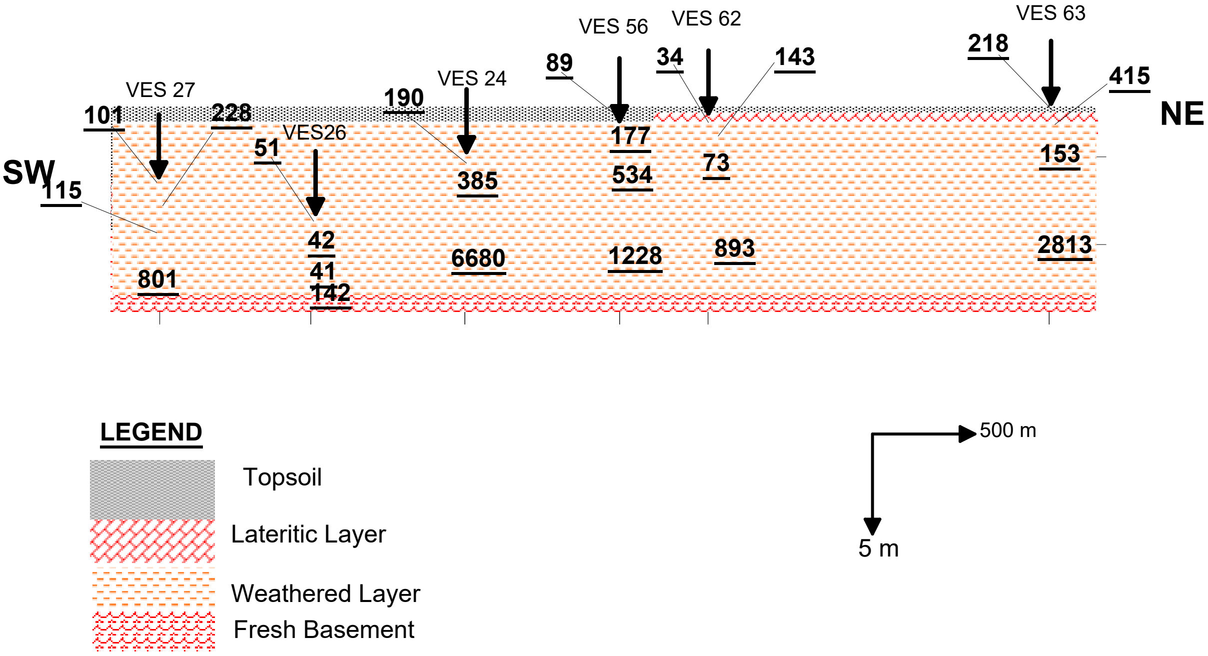

Figure 14. Geo-section along Traverse Three (3)

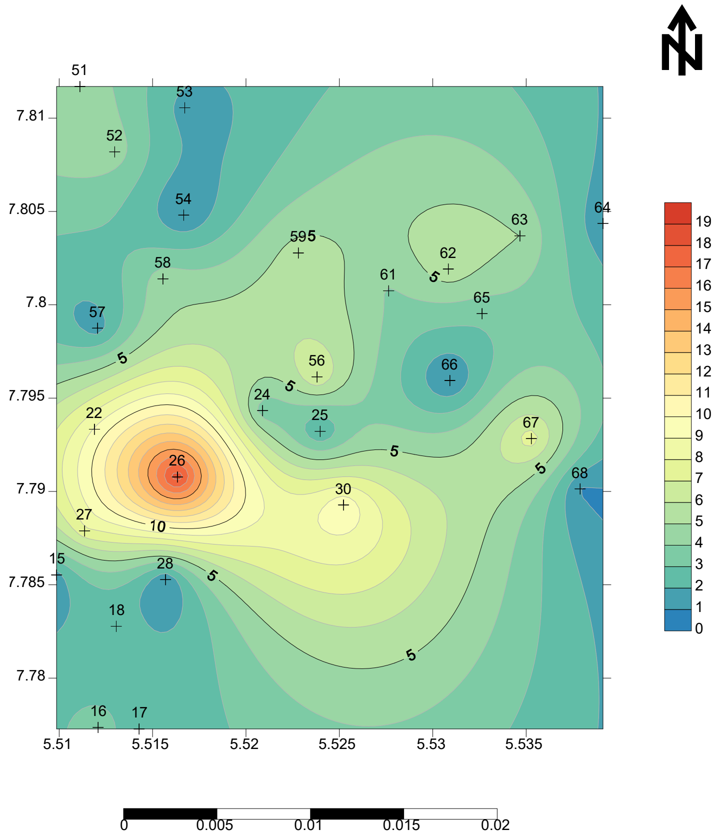

Figure 15. Layer thickness above the aquifer (meters).

DOI:https//doi.org/10.22452/mjs.vol44no1.6

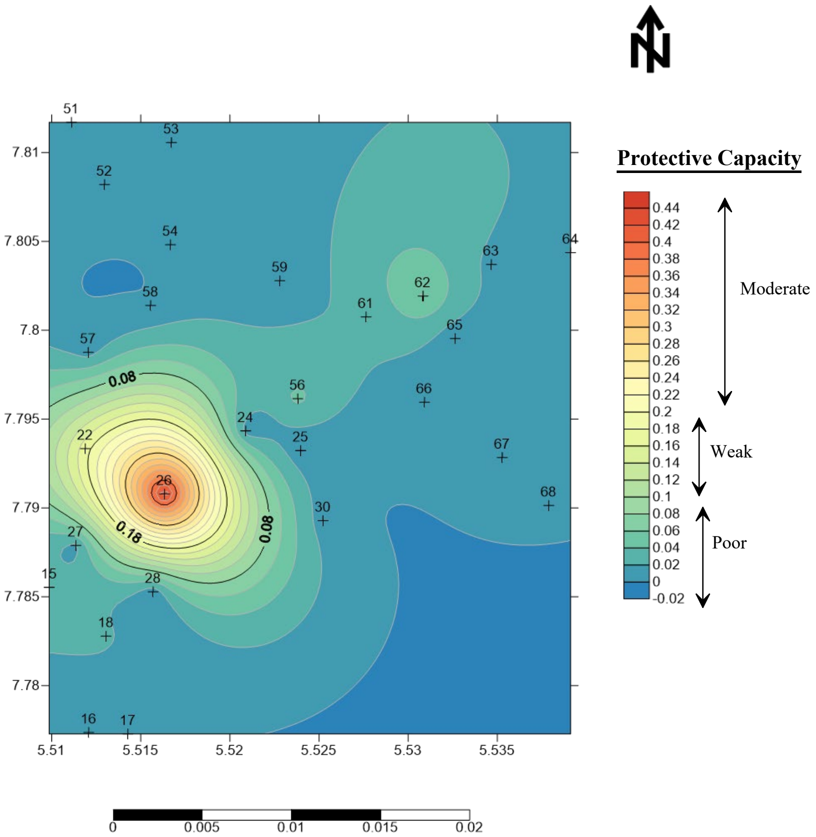

Figure 16. Longitudinal Conductance (Ohms^{-1}), Map of the Study Area.

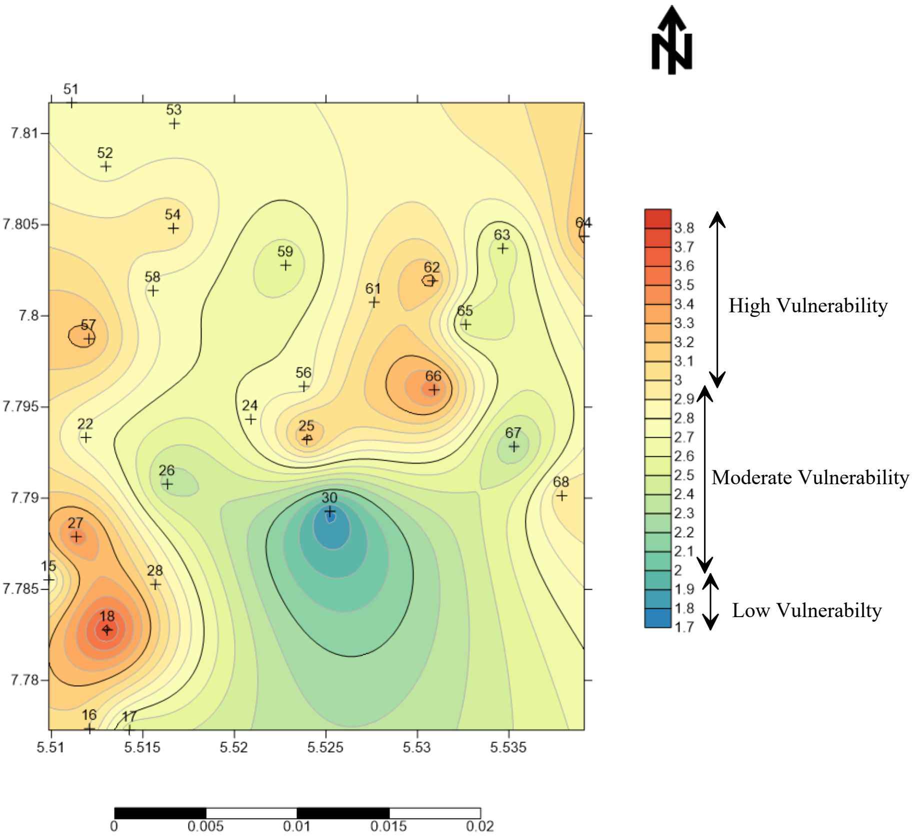

Figure 17. Geoelectric Layers Susceptibility Index (GLSI) Map

DOI:https//doi.org/10.22452/mjs.vol44no1.6

4. Conclusion

Groundwater aquifer potential and protective capacity evaluation at Ikole Ekiti, Southwestern Nigeria, used an electrical resistivity method to determine its viability and susceptibility. The Vertical Electrical Sounding (VES) technique was employed, and the Schlumberger configuration was adopted. The data obtained was partially curve-matched and iterated using WinResist software. The processed results were employed, and charts, geoelectric sections, tables, and maps were generated to aid in interpreting the results.

The thickness of the regolith was appreciable and ranged from 2 to 56 m, which can sustain moderate groundwater yield in the southern region of the area. The weathered layer is the principal aquifer unit in the area, as it is appreciably thick and has a fresh basement. Since the layer thickness above the aquifer is less than 20 m, areas without lateritic cover will be prone to pollution.

The study area's KH curve types are predominant, indicating good protective capacity. The geoelectric sections showed four (4) layers, i.e., topsoil, lateritic, weathered, and fresh basement rock. The lateritic layer has high porosity but very low permeability, making it a good layer to protect the aquifer from surface pollutants. The longitudinal conductance rating and Geoelectric Layer Susceptibility Index (GLSI) rating were employed to assess the aquifer's protective ability. The longitudinal conductance map showed a southwestern area with moderate protective capacity, whereas the GLSI map showed the southern part as a region with moderate to low vulnerability. The inherent weakness of the longitudinal conductance map was complemented by the Geoelectric Layer Susceptibility Index (GLSI) map. Considering the resistivity results alongside the maps obtained using the two models employed, the southern region of the study area is most viable for groundwater exploitation with moderate to low vulnerability. In contrast, groundwater projects in the northern region can only occur after due consideration for contamination mitigations.

5. References

Abiola O., Enikanselu P.A., and Oladapo M.I. (2009). Groundwater Potential and Aquifer Protective Capacity of Overburden Units in Ado-Ekiti, Southwestern Nigeria. International Journal of Physical Sciences, 4, 120-132.

Abudulawal L., Amidu, S. A., Apanpa, K. A., Adeagbo, O. A., and Akinbiyi, O.A. (2015). Geophysical investigation of subsurface water of Erunmu and its environs, southwestern Nigeria, using electrical resistivity method. J. Appl. Sci.15, 741–751. doi: 10.3923/jas.2015.741.751

Adebo Babatunde A, Jemiriwon Emmanuel Tope and Ilugbo Stephen Olubusola, (2021). Assessment of Aquifer Vulnerability Using GIS And Multi-Criteria Analysis Within Lead City University, Southwestern Nigeria, Pakistan Journal of Geology (PJG), volume 5, issue 2, DOI: 10.2478/pjg-2021-0010.

Ademilua O.L., Ojo O.F., Eluwole A.B., Ademilua O.B. (2014). Geophysical survey for groundwater resource appraisal in a basement complex terrain for agricultural purposes; a case study of ABUAD teaching and research farm, Ado Ekiti, Southwest Nigeria.14(5).

Ademilua O.L. and Eluwole, A.B.,(2013). Hydrogeophysical Evaluation of the Groundwater Potential of Afe Babalola University Ado-Ekiti, Southwestern Nigeria. Journal of Emerging Trends in Engineering and Applied Sciences. Vol 4. No. 1, pp. 77-83.

Agbasi, O.E.; Edet, S.E.(2016): Hydro-geoelectric study of aquifer potential in parts of Ikot Abasi local government area, Akwa Ibom state using Electrical Resistivity Soundings. Int. J. Geol. Earth Sci., 2, 1–15. [Google Scholar]

Akana T.S., George G.C., Oki O.A. (2016). Aquifer vulnerability assessment in some towns of Yenagoa, South-South Nigeria. Science and Technology 2016, 6(1): 15-23.

Akintorinwa O.J. and Olowolafe T.S., (2013). Geoelectric evaluation of groundwater prospect within Zion estate, Akure, Southwest, Nigeria. Int. J. Water Resour. Environ. Eng. 5 (1), 12–28.

Alabi O.O., Adeolu O.O. and Akinpelu D.F. (2016). Geophysical investigation for groundwater potential and aquifer protective capacity around Osun State University (UNIOSUN) College of Health Sciences." American Journal of Water Resources 4(6):137-143.

Anomohanran O., Ofomola M. O. and Okocha F. O. (2017). Investigating groundwater in parts of Ndokwa district in Nigeria using geophysical logging and electrical resistivity methods: implications for groundwater exploration. J.Afr. Earth Sci. 129, 108–116. doi: 10.1016/j.jafrearsci.2016.12.008.

Ayodele O. F., Temitope E., Akinfolayan O. (2022). Comparative effect of the lateritic shield in groundwater vulnerability assessment using GLSI and LC models: a case study of Ijero mining site, Ijero-Ekiti; Modeling Earth Systems and Environment, https://doi.org/10.1007/s40808-023-01689-3.

Ayuk M.A. (2019). Groundwater Aquifer Vulnerability Assessment using a Dar-Zarrouk Parameter in a Proposed Aboru Residential Estate, Lagos State, Nigeria; J. Appl. Sci. Environ. Manage. Vol. 23 (12) 2081-2090.

Bayowa O. G., Olorunfemi M.O., Akinluyi F.O., and Ademilua O.L. (2014). Integration of Hydrogeophysicaland Remote Sensing Data in the Assessment of Groundwater Potential of the Basement Complex terrain of Ekiti State, Southwestern Nigeria.IfeJ.Science, 2014,16(3), 353-356.

DOI:https//doi.org/10.22452/mjs.vol44no1.6

Eyankware M.O., Selemo A.O.I., Obasi P.O., Nweke, O.M. (2020). Evaluation Of Groundwater Vulnerability In Fractured Aquifer using Geoelectric Layer Susceptibility Index At Oju, Southern Benue trough Nigeria. Geological Behavior (GBR)63-67.

Farid H.U., Mahmood-Khan Z., Ali A., Mubeen M., Anjum M.N. (2017). Site-specific aquifer characterisation and identification of potential groundwater areas in Pakistan. Pol. J. Environ. Stud. Vol. 26(1):17–27.

Grant N.K. (1978). The structural distinction between a metasedimentary over and an underlying basement in the 600m. y. old pan-African domain of northwestern Nigeria. *West African Bulletin,* pp. 89, 50–58.

Hasan, M.; Shang, Y.; Akhter, G.; Jin, W.(2018): Geophysical assessment of groundwater potential: A case study from Mian Channu Area, Pakistan. Groundwater, 56, 783–796. [Google Scholar] [CrossRef]

Kamlesh P. and Shukla J.P. (2014). Assessment of groundwater vulnerability using GIS-based Drastic technology for the basaltic aquifer of Burhner watershed, Mohgaon block, Mandla (Indian). Curr. Sci. 107 (10).

Keller G. V. and Frishchncht F.C. (1996). Electrical Methods in Geophysical Prospecting. Pergamon Press: New York, NY 1996. p. 96.

Ndatuwong, L.G.; Yadav, G.S.(2015): Application of geo-electrical data to evaluate groundwater potential zone and assessment of overburden protective capacity in part of Sonebhadra district, Uttar Pradesh. Environ. Earth. Sci., 73, 3655–3664. [Google Scholar] [CrossRef]

Nwosu Ikechuchukwu Eugene and Chinaka Joseph Chinedu (2021). Evaluation of Aquifer Potential and Vulnerability of Mbaitoli/Ikeduru Area, Southeastern Nigeria, Using Direct Current Electricity Data; Journal of Research in Environmental and Earth Sciences; Volume 7, Issue 12, pp: 01-11.

Odeyemi I.B. (1977). The basement rocks of Bendel State of Nigeria. Unpublished Ph.D. Thesis University of Ibadan. Nigeria.

Oladapo M.I., & Akintorinwa O.J. (2007). Hydrogeophysical Study of Ogbese, Southwestern, Nigeria. Global Journal of Pure and Applied Sciences, pp. 13, 55–61. http://dx.doi.org/10.4314/gjpas.v13i1.16669.

Olorunfemi M.O. & Fasuyi S.A. (1993). Aquifer types, geoelectric and hydrogeologic characteristics of part of the Central Basement Terrain of Niger State Nigeria. J Afr Earth Sci 16(1):309–317.

Oni T.E., Omosuyi G.O. and Akinlalu A.A. (2017). Groundwater vulnerability assessment using hydrogeologic and geoelectric layer susceptibility indexing at IgbaraOke, Southwestern Nigeria. NRIAG Journal of Astronomy and Geophysics 6 (2017) 452–458.

Oyedele E. A. A and Olayinka A. I. (2012). Statistical evaluation of groundwater potential of Ado-Ekiti, Southwest, Nigeria. Transnational Journal of Science and Technology, 2(6), pp 110–127.

Rahaman M. A. (1988). Recent advances in the study of the basement complex of Nigeria Precambrian geology of Nigeria. *Geological Survey of Nigeria publication*, Kaduna, 11-43.

Srinivasan K., Poongothai S., Chidambaram S. (2013). Identification of groundwater potential zone using GIS and electrical resistivity techniques in and around the Wellington reservoir, Cuddalore district, Tamilnadu, India. Eur. Sci. J. ESJ 9 (17).

Ugwu N.U., Ranganai R.T., Simon R. E. and Ogubazghi G. (2016). Geoelectric Evaluation of Groundwater Potential and Vulnerability of Overburden Aquifers at OniEja Active Open Dumpsite, Osogbo, Southwestern Nigeria. Journal of Water Resource and Protection, 8, 311-329. http://dx.doi.org/10.4236/jwarp.2016.83026.

Vander Velpen, B.P.A. (2004). WinRESIST Version 1.0. Resistivity Sounding Interpretation Software. M.Sc. Research Project, ITC, Delft Netherland.

MALAYSIAN JOURNAL OF SCIENCE
MJS
ISSN 1394-3065

Regular Issue

Malaysian Journal of Science 44 (1): 55-62 (March 2025) https://mjs.um.edu.my

The Resolution and Sensitivity Function of Electrode Arrays in 2D Resistivity Imaging Technique

Ahmed S. Al-Zubedi [1a] and Zaidoon T. Abdulrazzaq [2b]*

Abstract: Two synthetic models are employed to assess the relationship between resolution and sensitivity function of electrode arrays: Dipole-Dipole, Pole-Dipole, Wenner-Schlumberger, and Wenner arrays. Both models were designed with a survey line length of 100 m and minimum electrode spacing of 0.5 m. Each model includes two rectangular structures measuring 3 meters in length and 2 meters in width, positioned at depths from 4.44 meters to 6.44 meters. These structures are separated by 3 meters and 6 meters, respectively. After generating over 20 inverse models, the results indicated that electrode array resolution is not related to the sensitivity function but depends on the separation distance between subsurface structures rather than electrode spacing. Additionally, increased data coverage does not correlate with resolution, as higher measurement density failed to differentiate between separate structures. These factors cannot be considered significant or influential in developing a high-resolution model. Therefore, we recommend combining other geophysical methods with this technique when investigating subsurface structures separated by small distances.

Keywords: *Resolution, sensitivity function, electrode arrays, 2D resistivity imaging technique.*

1. Introduction

One of the greatest near-surface geophysical techniques is the electrical resistivity method, which is commonly applied to investigations in mining, hydrogeology, environmental science, geotechnical engineering, and civil engineering (Storz et al., 2000; Zhou et al., 2004; Al-Zubedi & Thabit, 2016). The best reviews of electrical resistivity tomography (ERT) are provided by Dahlin (2001), Auken et al. (2006), and Loke et al. (2013). This method includes several techniques typically conducted using more than ninety electrode arrays (Szalai & Szarka, 2008). However, the most commonly used electric arrays do not exceed ten arrays. This method encompasses various techniques; 2D and 3D resistivity techniques are valuable tools and provide crucial insights into subsurface imaging. Dipole-dipole, Schlumberger, Wenner, Pole-dipole, Pole-pole, Multiple gradient, and Wenner-Schlumberger arrays are most widely used in these techniques (Al-Zubedi, 2015). Various factors, including target depth, array sensitivity functions, and array resolution, influence the selection of the optimal array for electrical resistivity surveys (Roy & Apparao, 1971; Loke, 2012). Accurately determining the sensitivity function plays a crucial role in obtaining precise measurements of material resistivity, making it essential in 2D and 3D resistivity imaging techniques. The sensitivity function of electrode arrays in 2D and 3D resistivity imaging techniques depends on several factors, including electrode distribution, material type, and imaging technique (3D or 2D) (Neyamadpour, 2010; Aizebeokhai, 2009). Sensitivity is the smallest absolute change that a measurement can detect, making it an absolute quantity. The value indicates how much the resistivity of a subsurface portion will change, affecting the potential that the array measures. The effect of the subsurface zone on the measurement increases with sensitivity function value and depends on electrode placement (Loke, 2012). It reflects the resolution and investigation depth for each array (Chitea & Georgescu, 2009), while array resolution refers to their ability to distinguish and characterize subsurface features with clarity. Resolution varies significantly based on technique type, array used, subsurface material electrical properties, equipment, and data processing methods.The resolution enhancement plays a crucial role in enhancing the quality of resistivity imaging (Loke, et al., 2015). Modern electrode design optimization methods significantly improve the accuracy of 2D resistivity imaging surveys (Al Hagrey, 2012). These optimized arrays enable better differentiation of subsurface structures, such as groundwater flow paths, fractures, and rock layers.

Resolution enhancement works to maximize spatial resolution while minimizing data acquisition time. Thus, optimized datasets can achieve high resolution with fewer data points, particularly in the interwell region of borehole surveys. The sensitivity function indicates how changes in resistivity relate to environmental variables (e.g., soil type, moisture), and by optimizing electrode arrays, we enhance sensitivity to specific subsurface features. Consequently, this leads to more accurate imaging of geological structures and anomalies (Loke et al., 2007; Jiang et al., 2021). Some arrays provide better resolution for vertical changes in

Authors information:
[a]Remote Sensing and Geophysics College, AlKarkh University of Science, Baghdad, IRAQ. Ahmed.Srdah@yahoo.com[1]
[b]Space Research and Technology Center, Scientific Research Commission, Baghdad, 10070, IRAQ. E-mail: zaidoon.taha@live.com[2]

*Corresponding Author: zaidoon.taha@live.com

Received: June 8, 2023
Accepted: June 20, 2024
Published: March 31, 2025

DOI:https//doi.org/10.22452/mjs.vol44no1.7

resistivity, while others provide better resolution for horizontal changes. If we understand the most important influencing factors, we should use the most appropriate array to obtain the best results. This study evaluates variables that directly affect electrode array sensitivity, resolution capability, and the ability to determine subsurface properties to enhance array resolution.

2. Theoretical Background

The application of resistivity imaging techniques has been increasing over the years in areas associated with environmental studies, groundwater prospection, mining, monitoring, and other applications which require better mapping of sites in a fast and efficient way (Giang et al., 2018; Loke et al., 2021; Al-Awsi & Abdulrazzaq, 2022). In particular, dual electrode arrays such as Dipole-Dipole have been most commonly used to perform surveys in 2D and 3D (Prakash et al., 2022). One of the main problems associated with Dipole-Dipole and any type of dual electrode arrays is their relatively low resolution and sensitivity function for certain separation values between electrodes used in data acquisition, resulting in degradation of the final image and considerable error in the estimated image (Abed et al., 2020).

To address the problem of low resolution and sensitivity function in images obtained from dipole-dipole electrode arrays, the research community has been studying and proposing alternatives with two or more steps for image reconstruction. One strategy uses electrodes with guarding configurations, such as pole-pole and pole-dipole in the first step and dipole-dipole in the second step. The cost and additional time required to perform these surveys are the main disadvantages in systems using pole-pole and pole-dipole configurations. Moreover, after implementing these configurations, the dipole-dipole still retains its main limitation. Other models proposed in the literature have resolution requirements compatible with dipole-dipole. However, shortcomings related to decreased accuracy remain present (Gharibi et al., 2005; Kiflu, et al., 2016; Simyrdanis, et al., 2021).

Several papers and studies conducted to determine factors affecting resolutions and array's sensitivity functions of 2D and 3D resistivity techniques in identifying subsurface targets were analyzed and discussed in this paper to identify the most significant factors. The spatial resolutions of these techniques in determining subsurface features were also analyzed and discussed.

Sensitivity Function

The array's sensitivity function is a numerical value that indicates how much a change in a survey area's resistivity affects the potential measured by the array, which means that the sensitivity function depends on the geometric factor of the electrode arrangement. In other words, it is based on the relative positions of the array electrodes. The Fréchet derivative is used to theoretically calculate this value for a homogeneous half-space (McGillivray & Oldenburg, 1990).

Referring to a conventional four-electrode array comprising two current electrodes and two potential electrodes, as shown in Figure (1), the sensitivity function can be computed using the straightforward equation provided by Roy and Apparao (1971):

$$F_{1D}(z) = \frac{2}{\pi} \times \frac{Z}{\sqrt{(a^2+4z^2)}} \quad \dots\dots\dots\dots\dots\dots\dots\dots\dots\dots\dots\dots (1)$$

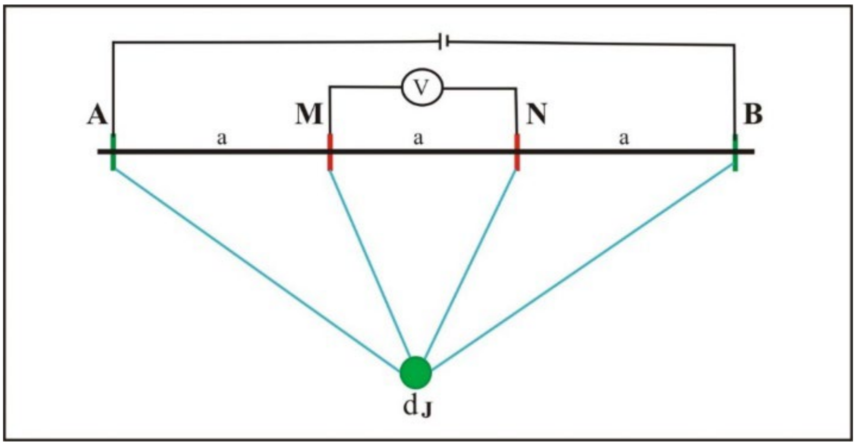

Figure 1. Calculate the sensitivity function for an array of four electrodes (Wiener array) at position ḍ(x,y,z) within a half-space.

In 2D resistivity imaging surveys, the sensitivity function of a homogenous half-space of the different arrays can be calculated by the equation given by Loke and Barker (1995) :

$$F_{2D}(x, z) = \pi\left[\frac{1}{2\alpha^3} - \frac{3a^2}{16\alpha^5}\right], \text{ with } \alpha = 0.25xa^2 + z^2 \quad \dots\dots\dots\dots (2)$$

These equations, which are generally referred to as the depth-investigation characteristic, have been utilized by many researchers to determine the characteristics of diverse arrays in resistivity surveys, both 1D and 2D (Edwards 1977, Barker 1991, Merrick 1997). According to Parker (1991) and Edwards (1977), "median depth of investigation" provides a more reliable approximation. The sensitivity function and depth must be integrated to determine the median depth of investigation. With electrode spacing (a) equal to one meter, the Wenner array's sensitivity function and median depth of investigation equals 0.1730, as shown in Figure (2).

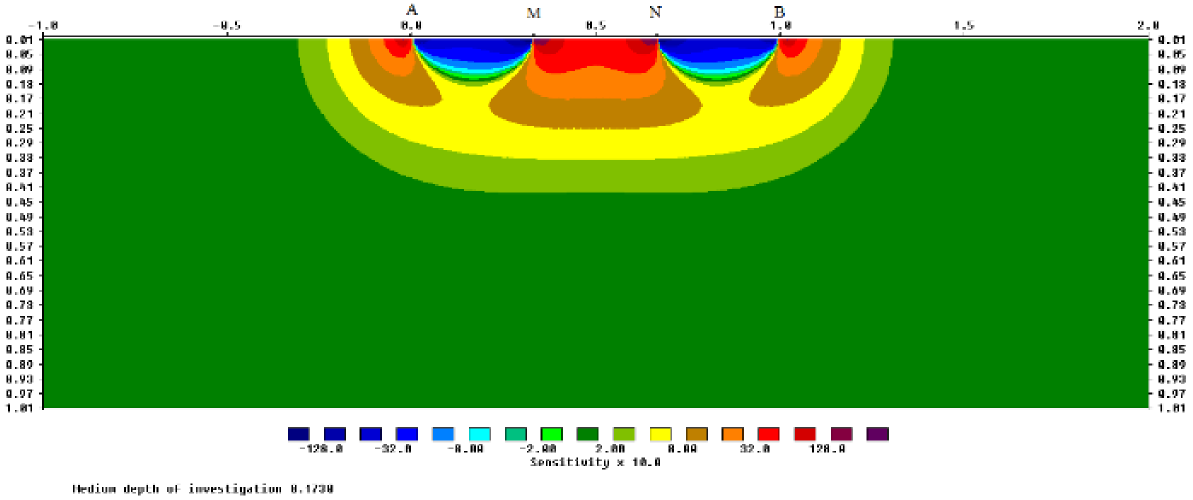

Figure 2. Showed the median depth of investigation and sensitivity function for a Wenner array with a one-meter electrode spacing (a).

The Resolution of Array

The resolution of electrical arrays can be described as the capacity of an array to distinguish two separated targets with a minimum distance between them, such that the two targets can be separately recognized instead of appearing as one target. The resolution can be classified into two types: vertical and horizontal resolution. The array's vertical resolution refers to its capacity to distinguish between two targets located at different depths. Conversely, horizontal resolution describes how two neighboring targets can be positioned horizontally and still be distinguished as two distinct targets rather than one (Kallweit & Wood, 1982).

In mathematics, the Fréchet derivative used in calculating the sensitivity function is defined as the derivative of a function between two Fréchet spaces. It is sometimes known as the strong derivative and can be seen as a generalization of the gradient to arbitrary vector spaces (Long, 2009). Loke (2012) provided an in-depth analysis of the sensitivity patterns of different arrays. According to Okpoli (2013), the sensitivity pattern is the crucial factor in determining the imaging capability of an electrode array. When comparing these arrays' sensitivity levels, the maximum sensitivity values are closest to the electrodes of the various arrays and decrease with depth. In other words, these arrays have lower resolution because the sensitivity function has a graduated value that depends on the distances between the electrodes, particularly the potential electrodes' distance from the nearest current electrode. The value gradually decreases as the distance between the electrodes increases. Since the final results of 2D and 3D resistivity imaging surveys are images or models reflecting the true subsurface resistivity value distribution, which is calculated based on the sensitivity values or Fréchet derivative for a homogeneous half-space (Loke, 2020), the resolution of this image depends significantly on the sensitivity function of the array used and the actual location of the measuring point subsurface.

3. Methodology

Two synthetic models generated more than 20 inverse models for Dipole-Dipole, Wenner-Schlumberger, Pole-Dipole, and Wenner arrays by simulating two 2D numerical models using RES2DMOD software version 2.14.22 (Geotomo software). This approach determined the relationship between resolution and sensitivity function for these arrays and their affecting factors. Both models featured a 100-m-long survey line with 1-m minimum electrode spacing. They contained two rectangular structures, each 3 m long and 2 m wide, located at a depth of 4.44 m and extending to 6.44 m. These structures possessed a resistivity of 30 Ωm within a homogeneous medium of 10 Ωm resistivity. In the first model, the structures were separated by 3 m, while in the second model, they were separated by 6 m, as shown in Figures (3 and 4).

DOI:https//doi.org/10.22452/mjs.vol44no1.7

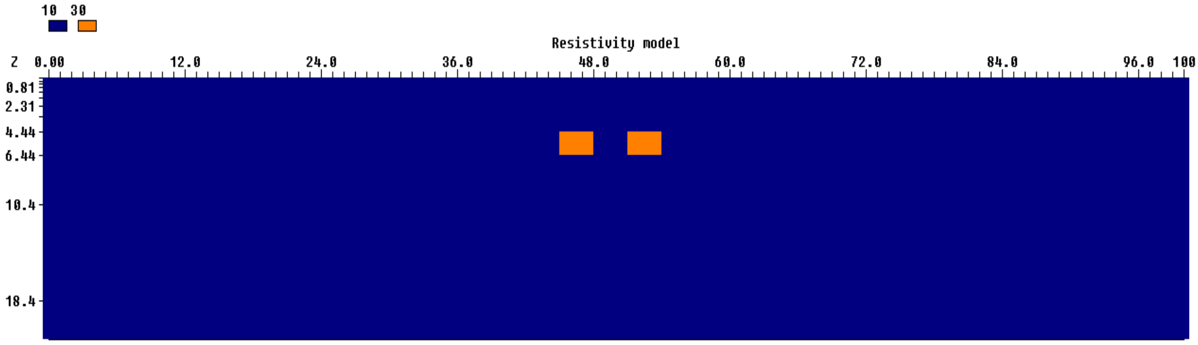

Figure 3. The 2D synthetic model of two structures separated by a distance of 3m.

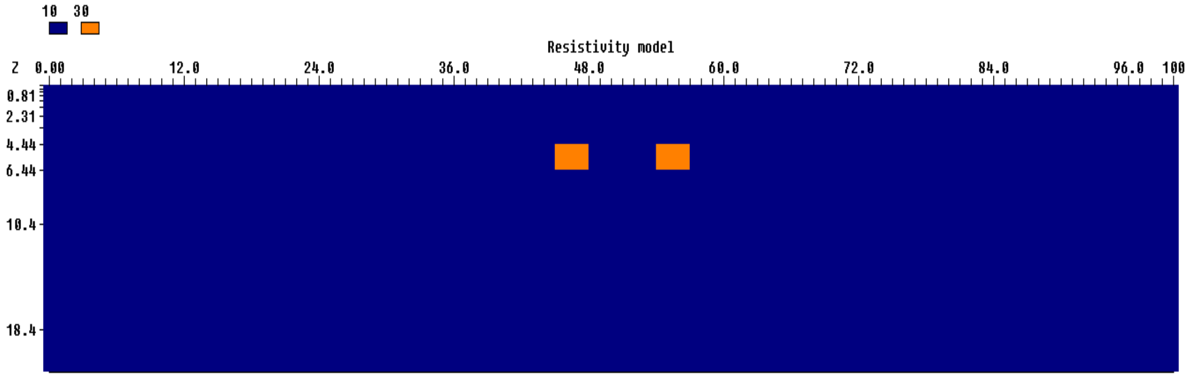

Figure 4. The 2D synthetic model of two structures separated by a distance of 6m.

4. Results and Discussion

After synthetic models are created, apparent resistivity measurements are collected for each model. These measurements are performed with an n-factor of 8a while a-spacing varies from 1a to a maximum of 4a, except for the Wenner array, which uses (33a). This procedure enables higher resolution and maximum investigation depth. The 2D inverse models are created using RES2DINV ver. 3.59 (Geotomo software) with L1 norm (robust) inversion method to obtain optimal boundaries between structures and host materials.

In the first model, where structures are separated by 3m, and after 2 to 5 iterations in generating inverse models for high-resolution imaging, all arrays successfully delineate the depth and extension of these structures. However, the arrays cannot separate them, making them appear as one structure. Therefore, data coverage was increased by raising the factor "n" values to provide overlapping data levels. Nevertheless, the two structures still appeared as a single structure, as shown in Figure (5). Subsequently, the synthetic model was redesigned with an electrode spacing of 0.5m. Yet, all inverse models of the arrays demonstrated difficulty in separating the two structures, as shown in Figure (6) as an example.

DOI:https//doi.org/10.22452/mjs.vol44no1.7

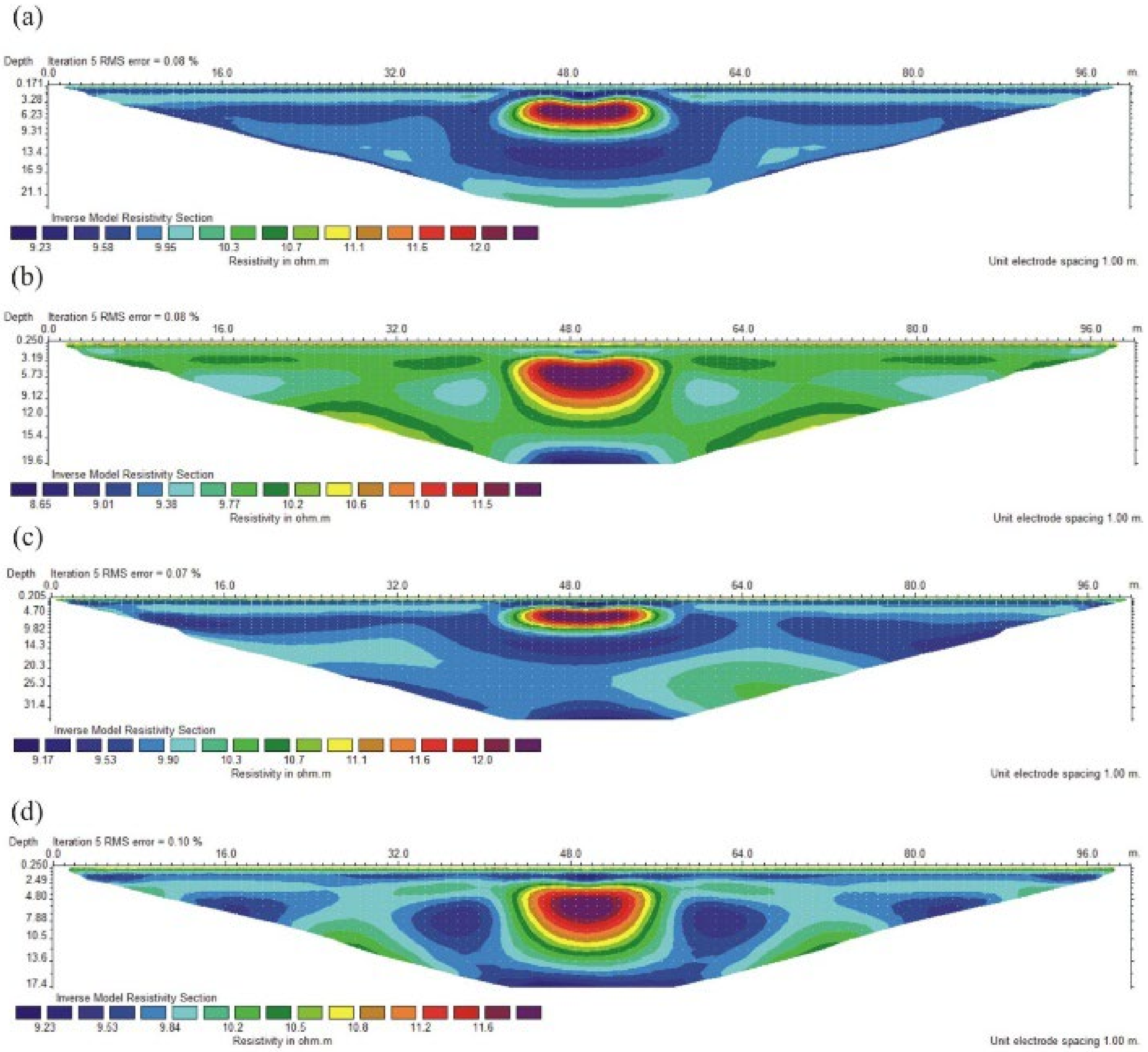

Figure 5. Inverse models of (a) Dipole-Dipole, (b) Wenner-Schlumberger (c) Pole-Dipole and (d) Wenner arrays.

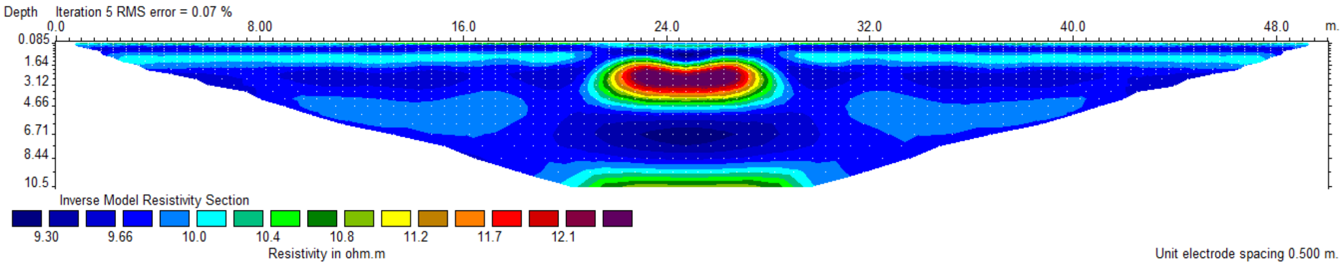

Figure 6. Inverse models of dipole-dipole array with 0.5m electrodes spacing for two structures separated by a distance of 3m.

At a distance of 6 meters between the two structures in the second synthetic model, the inverse models of all arrays successfully identified the structures and displayed them separately, with minor differences in their depth and extent definitions, as illustrated in Figure (7).

DOI:https//doi.org/10.22452/mjs.vol44no1.7

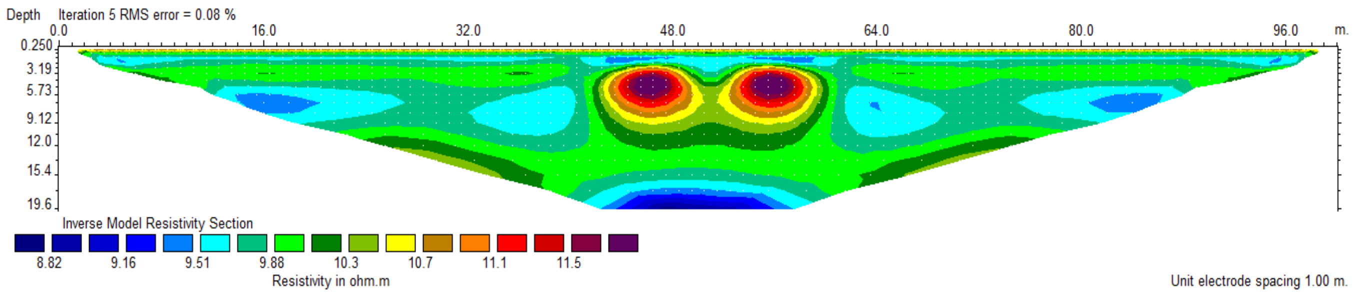

Figure 7. Inverse models of Wenner-Schlumberger array with for two structures separated by a distance of 6m.

In general, these results showed that electrode array resolution is not related to the sensitivity function but depends on the distance between subsurface structures rather than electrode spacing. Furthermore, increased data coverage has no relationship with resolution, as higher measurement density could not distinguish separate structures but showed them as one. Therefore, these factors are not crucial for obtaining a high-resolution model. However, to achieve high resolution, the most important step before electrical resistivity surveys is estimating target depth and geometry to select the optimal array. The distance between targets should be estimated carefully, and other geophysical methods should be integrated when investigating closely spaced subsurface structures.

5. Conclusion

In geophysical methods, including resistivity surveys, measurements are converted into images reflecting subsurface physical property changes. Image resolution depends on measurement accuracy. The sensitivity function and its influencing factors do not significantly affect measurement accuracy or final model resolution. The primary factor affecting electrode array resolution and feature distinction is the distance between targets. This study's key finding include:

- Electrode array resolution relates not to sensitivity function but to the separation distance between subsurface structures rather than electrode spacing.
- Estimating geological conditions before surveying - including subsurface resistivity variations, target depth, geometry, and spacing - helps select arrangements that improve resolution through accurate feature identification.
- Increasing measurement density through overlapping data levels with varied "a" and "n" values cannot provide higher resolution when structures are closely spaced.
- Other geophysical methods should complement electrical resistivity surveys when investigating closely spaced subsurface structures to achieve high-resolution imaging.

6. References

Abed, A. M., Al-Zubedi, A. S., & Abdulrazzaq, Z. T. (2020). Detected of gypsum soil layer by using 2D and 3D electrical resistivity imaging Techniques in university of Anbar. *Iraq, Iraqi Geological Journal*, *53*(2C), 134–144.

Aizebeokhai, A. P., & Olayinka, A. I. (2010). Anomaly effects of arrays for 3d geoelectrical resistivity imaging using orthogonal or parallel 2d profiles. *African Journal of Environmental Science and Technology*, *4*(7), 446-454.

Aizebeokhai, A. P. (2009). *Geoelectrical Resistivity Imaging in Environmental Studies BT - Appropriate Technologies for Environmental Protection in the Developing World: Selected Papers from ERTEP 2007, July 17–19 2007, Ghana, Africa* (E. K. Yanful (ed.); pp. 297–305). Springer Netherlands. https://doi.org/10.1007/978-1-4020-9139-1_28

Al Hagrey, S. A. (2012). 2D optimized electrode arrays for borehole resistivity tomography and CO 2 sequestration modelling. *Pure and Applied Geophysics*, *169*, 1283-1292.

Al-Awsi, M. D., & Abdulrazzaq, Z. T. (2022). Implementing electrical resistivity tomography to delineate soil contamination zone, Southern Baqubah City, Iraq. *Kuwait Journal of Science*, *49*(2).

Al-Hameedawie, M. A. (2013). *Comparison between different electrode arrays in delineating aquifer boundary by using 1D and 2D techniques in north Badra area eastern Iraq*. M. Sc. Thesis, Department of Geology, college of Science, University of Baghdad, Iraq, 142p.

Al-Zeubedi, A. S. (2015). *Principles of electrical resistivity techniques*. LAP LAMBERT Academic Publishing, Germany, p 147.

Al-Zubedi, A. S., & Thabit, J. M. (2016). A comparison between 2D azimuthal and 3D resistivity imaging techniques in determining the subsurface fracture zones within Abu-Jir Fault Zone, Southwest Karbala, Central Iraq. *Near Surface Geophysics*, *14*(5), 413-421.

Al-Zubedi, A. S. (2016). Evaluation of five electrode arrays in imaging subsurface shallow targets; A case study. *Iraqi Bulletin of Geology and Mining*, *16*(2), 39-46.

Auken, E., Pellerin, L., Christensen, N.B., Sørensen, K. (2006). A survey of current trends in near-surface electrical and electromagnetic methods. *Geophysics* 71, G249–G260.

Barker, R. D. (1989). Depth of investigation of collinear symmetrical four-electrode arrays. *Geophysics*, *54*(8), 1031-1037.

Chitea, F., & Georgescu, P. (2009). Sensitivity function for various geoelectric arrays. In *Geophysical Research Abstracts*. University of Bucharest, Faculty of Geology and Geophysics.

Dahlin, T. (2001). The development of DC resistivity imaging techniques. *Comput. Geosci*. 27 (9), 1019–1029.

Dahlin, T., & Zhou, B. (2004). A numerical comparison of 2D resistivity imaging with 10 electrode arrays. *Geophysical prospecting*, *52*(5), 379-398.

Edward, L. S. (1977). A modified pseudosection for resistivity and induced-polarization. *Geophysics*, *42*(5), 1020-1036.

Gharibi, M., & Bentley, L. R. (2005). Resolution of 3-D electrical resistivity images from inversions of 2-D orthogonal lines. *Journal of Environmental and Engineering Geophysics*, *10*(4), 339-349.

Giang, N. V, Kochanek, K., Vu, N. T., & Duan, N. B. (2018). Landfill leachate assessment by hydrological and geophysical data: case study NamSon, Hanoi, Vietnam. Journal of Material Cycles and Waste Management, 20, 1648–1662.

Jiang, L., Tian, G., Wang, B., & Abd El-Raouf, A. (2021). The selection strategy of optimized arrays for 3-D electrical resistivity tomography. In *IOP Conference Series: Earth and Environmental Science* (Vol. 660, No. 1, p. 012002). IOP Publishing.

Kallweit, R. S., & Wood, L. C. (1982). The limits of resolution of zero-phase wavelets. *Geophysics*, *47*(7), 1035-1046.

Kiflu H., S. Kruse , M.H. Loke , P.B.Wilkinson , and D.Harro.(2016). Improving resistivity survey resolution at siteswith limited spatial extent using buried electrode arrays. *Journal of Applied Geophysics* 135 ,338–355.

Loke, M. H. (2012). Tutorial: 2-D and 3D Electrical Imaging Surveys, 165p.

Loke, M. H. (2020). Tutorial: 2-D and 3D Electrical Imaging Surveys, 221p.

Loke, M.H., 2001. Electrical imaging surveys for environmental and engineering studies: a practical guide to 2D and 3D surveys. http://www.geotomosoft.com.

Loke, M. H., Alfouzan, F. A., & Nawawi, M. N. M. (2007). Optimisation of electrode arrays used in 2D resistivity imaging surveys. *ASEG Extended abstracts*, *2007*(1), 1-4.

Loke, M. H., & Barker, R. D. (1995). Least-squares deconvolution of apparent resistivity pseudosections. *Geophysics*, *60*(6), 1682-1690.

Loke, M. H., Chambers, J. E., Rucker, D. F., Kuras, O., & Wilkinson, P. B. (2013). Recent developments in the direct-current geoelectrical imaging method. *Journal of applied geophysics*, *95*, 135-156.

Loke, M.H.; Kiflu, H.; Wilkinson, P.B.; Harro, D.; Kruse, S. (2015). Optimized arrays for 2D resistivity surveys with combined surface and buried arrays. *Near Surface Geophysics*, 13 (2096). 505-517. https://doi.org/10.3997/1873-0604.2015038

Long, K. (2009). Gateaux differentials and Fréchet derivatives. *Course notes, Texas Tech University*. http://www.math.ttu.edu/~klong/5311-spr09/diff.pdf.

Mcgillivray, P. R., & Oldenburg, D. W. (1990). Methods for calculating Frechet derivatives and sensitivities for the non-linear inverse problem: A comparative study. *Geophysical prospecting*, *38*(5), 499-524.

Merrick, N. P. (1997). A new resolution index for resistivity electrode arrays. *Exploration Geophysics*, *28*(2), 106-109.

Neyamadpour, A. (2010). Inversion of 2D and 3D DC resistivity imaging data for high contrast geophysical regions using artificial neural networks. University of Malaya (Malaysia).

Okpoli, C. C. (2013). Sensitivity and resolution capacity of electrode configurations. *International Journal of Geophysics*, *2013*.

Olayinka, A. I., & Yaramanci, U. (2000). Assessment of the reliability of 2D inversion of apparent resistivity data [Link]. *Geophysical Prospecting*, *48*(2), 293-316.

Prakash, A., Abhay Kumar Bharti , Aniket Verma ,and Pradeep Kumar Singh.(2022).Neural network based uncertainty and sensitivity evaluation of electrical resistivity tomography for improved subsurface imaging. *Journal of Asian Earth Sciences*: X8,(http://creativecommons.org/licenses/by-nc-nd/4.0/).

Reiser, F., Dalsegg, E., Dahlin, T., Ganerød, G. V., & Rønning, J. S. (2009). Resistivity modelling of fracture zones and horizontal layers in bedrock.

Roy, A., & Apparao, A. (1971). Depth of investigation in direct current methods. *Geophysics*, *36*(5), 943-959.

Simyrdanis, K., Papadopoulos, N., & Oikonomou, D. (2021). Computation of Optimized Electrode Arrays for 3-D Electrical Resistivity Tomography Surveys. *Applied Sciences*, *11*(14), 6394.

DOI:https//doi.org/10.22452/mjs.vol44no1.7

Storz, H.,W. Storz, and F. Jacobs. 2000. Electrical resistivity tomography to investigate geoelectrical structure of the earth's upper crust. *Geophys. Prospect*. 48:455–471.

Szalai, S., & Szarka, L. (2008). On the classification of surface geoelectric arrays. *Geophysical Prospecting*, *56*(2), 159-175.

Tamssar, A. H. (2013). *An evaluation of the suitability of different electrode arrays for geohydrological studies in karoo rocks using electrical resistivity tomography* (Doctoral dissertation, University of the Free State), South Africa.183p.

Thabit, J. M., & Al-Zubedi, A. S. (2015). Evaluation of three important electrode arrays in defining the vertical and horizontal structures in 2D imaging surveys. *Iraqi Journal of Science*, *56*(2B), 1465-1470.

Zhou, W., Beck, B. F., & Adams, A. L. (2002). Effective electrode array in mapping karst hazards in electrical resistivity tomography. *Environmental geology*, *42*, 922-928.

Zhou, Q. Y., Matsui, H., & Shimada, J. (2004). Characterization of the unsaturated zone around a cavity in fractured rocks using electrical resistivity tomography. *Journal of Hydraulic Research*, *42*(S1), 25-31.

DOI:https//doi.org/10.22452/mjs.vol44no1.7

MALAYSIAN JOURNAL OF SCIENCE
MJS
ISSN 1394-3065

Regular Issue

Malaysian Journal of Science 44 (1): 63-69 (March 2025)
https://mjs.um.edu.my

One Effective Method for Solving Singularly Perturbed Equations

Chori Normuradov[1a], Nasiba Djurayeva[2a*], F. Deraman[3b], M. S. Anuar[4c] and S. M. Asi[5c].

Abstract: Numerical methods are widely used to study the solution of singularly perturbed equations. At the same time, their application to the solution of such equations encounters serious difficulties; they are associated with the presence of a small parameter at the highest derivative and the appearance in the solution area of areas with high frequency-amplitude sawtooth jumps. In this case, the requirements for the efficiency and accuracy of numerical methods increase sharply. Although numerous methods have been developed to date, the question of the effectiveness and accuracy of numerical methods remains open. Until now, different methods with uniform and non-uniform steps have been mainly used to solve singularly perturbed equations. As the value of the small parameter decreases, to increase the accuracy, it is necessary to refine the step of the difference grid. This, in turn, leads to a strong increase in the order of the matrix in the linear algebraic system being solved. Along with difference methods, spectral methods can be used to solve problems. In spectral methods, the solution to the equation is sought in the form of finite series in Chebyshev polynomials. The derivatives present in the equation are determined by differentiating the selected final series. When differentiating series, the order of the approximating polynomials is reduced, and this, in turn, affects the accuracy of the method used. In this paper, it is proposed to use the preliminary integration method to solve singularly perturbed equations. The essence of this method is as follows. The highest derivative and the right-hand side of the differential equation are expanded into finite series in Chebyshev polynomials of the first kind. Unlike spectral methods, in the preliminary integration method the highest derivative is expanded into a finite series. Before solving the problem, the series for the highest derivative is preliminarily integrated until an expression for solving the problem is found in the form of a finite series. When integrating series, unknown integration constants appear; they are determined from additional conditions of the problem. Only after this, the series for solving the derivatives of the right side are put into a singularly perturbed equation and a system of linear algebraic equations is obtained for determining the unknown expansion coefficients. It should be noted that when integrating series, the smoothness of the approximating polynomials improves, and this, in turn, increases the accuracy of the proposed method. At the same time, the order of the matrix of the algebraic system being solved does not increase. This ensures, at the same costs required in the spectral method, that the proposed method can solve a singularly perturbed equation even for small values of the small parameter of the problem. The high accuracy and efficiency of the preliminary integration method are demonstrated when solving a specific inhomogeneous singularly perturbed equation. The results of calculations are presented by comparing the approximate solution with the exact solution of the problem and with approximate solutions obtained by the spectral method.

Keywords: *Inhomogeneous differential equation, boundary value problem, Chebyshev polynomials, preliminary integration, absolute error.*

1. Introduction

The construction of highly accurate and efficient methods for solving inhomogeneous singularly perturbed equations is an urgent problem in applied mathematics.

Let us briefly describe numerical methods aimed at solving singularly perturbed equations.

In [1], a finite-difference method for solving a singularly perturbed equation was proposed. The essence of this method is to replace the derivatives included in the equation with finite differences and solve the resulting system using linear algebra methods. Such a difference scheme requires a fairly fine grid step. When the value of the small parameter is on the order of 10^{-4}, a uniform grid of 100 nodes is used to obtain sufficiently accurate (10^{-3}) results. In [2], in order to reduce the number of grid nodes, it is proposed to use a difference grid with a variable step. However, such a grid depends on several parameters, the choice of which encounters certain difficulties. A technique for constructing a non-uniform mesh for the numerical solution of a singularly perturbed equation was proposed in [3]. In [4], this method was used to solve the eigenvalue problem for an equation with a small parameter at the highest derivative, i.e., for the Orr–Sommerfeld equation. The results of the numerical solution of the Orr-Sommerfeld equation using a non-uniform mesh are

Authors information:
[a]Department of Applied Mathematics and Informatics, Termez State University, Termez city, UZBEKISTAN. E-mail: choribegaliyevich@mail.ru[1]; nasibajt@mail.ru[2]
[b]Institute of Engineering Mathematics, Universiti Malaysia Perlis, 02600 Arau, Perlis, MALAYSIA. E-mail: fatanah@unimap.edu.my[3]
[c]Faculty of Electronic Engineering & Technology, Universiti Malaysia Perlis, 02600 Arau, Perlis, MALAYSIA. E-mail: anuarms@unimap.edu.my[4]; salina@unimap.edu.my[5]
*Corresponding author: nasibajt@mail.ru

Received: June 8, 2023
Accepted: June 20, 2024
Published: March 31, 2025

DOI:https//doi.org/10.22452/mjs.vol44no1.8

presented in [5]. In [6], the results of constructing a non-uniform mesh for solving the Orr-Sommerfeld equation are presented, and the spectrum of eigenvalues for the Poiseuille flow is calculated. The numerical solution of the Orr-Sommerfeld equation using two-dimensional grids is presented in [7]. However, strict conditions are imposed on the parameters of such a grid to correctly describe the hydrodynamic properties of the flow. In [8], an inhomogeneous singularly perturbed second-order equation is solved by the spectral method. Numerical modeling of a fourth-order inhomogeneous singularly perturbed equation using the spectral method is presented in [9]. In the monograph [10], it is proposed to use the spectral grid method for numerical modeling of single-phase and two-phase flows. In this work, the convergence of the method is proved, and estimates of the speed of convergence of the method are obtained. The numerical solution of the Orr-Sommerfeld equation using the spectral-grid method is presented in [11]. The work shows the effectiveness and high accuracy of the proposed method. In [12], a spectral grid method is used to study the hydrodynamic stability of two-phase flows. In the two-phase flow under consideration, the dispersion (carrying) phase is gas, and the dispersed phase is solid particles. Numerical modeling of the Navier-Stokes equations in the system of a vortex and stream function using difference methods with a combination of Chebyshev polynomials of the first kind is presented in [13]. In [14], nonlinear waves with dissipation are numerically simulated by the spectral grid method. In [15], the convergence of the spectral-grid method was proved and estimates of the rate of convergence of the method were obtained for the Burgers equation with initial boundary conditions, where Chebyshev polynomials of the first kind were used. A review of methods for solving the problem of hydrodynamic stability is presented in [16]. In [17], the preliminary integration method was used to numerically simulate the eigenvalue problem of two-phase hydrodynamic flows.

A study of the cited literature and other sources shows that Chebyshev polynomials are widely used to study equations with a small parameter at the highest derivative. From the above review, it is clear that to solve the eigenvalue problem for a single-phase flow (Orr-Sommerfeld equation) and two-phase flow described by the eigenvalue problem for a system of nonlinear ordinary differential equations with a small parameter at the highest derivative, spectral and spectral-grid methods are successfully used.

From the above review, it is clear that works [1-7] are devoted to solving equations with a small parameter with the highest derivative using difference methods on uniform and non-uniform meshes. The following works are devoted to the use of spectral methods for the numerical solution of singularly perturbed equations of the second order [8] and fourth order [9]. In works [10-15], the spectral grid method was used for the numerical modeling of equations with a small parameter at the highest derivative. Numerical modeling of a singularly perturbed equation and a system of such equations using the preliminary integration method is presented in [16-17].

In difference methods, the derivatives included in the equation are replaced by finite differences, and the difference grid is constructed using a special transformation.

In spectral and spectral-grid methods, the solution to the equation is expanded into a finite series in Chebyshev polynomials. The derivatives present in a singularly perturbed equation are found by differentiating the selected finite series. It should be noted that when differentiating a series, the order of the approximating polynomials decreases (for example, with double differentiation, a polynomial of the fourth degree becomes a polynomial of the second degree), and this, in turn, affects the accuracy of the calculations. In the preliminary integration method, in contrast to spectral methods, not the solution of the equation, but the highest derivative is expanded into a finite series in Chebyshev polynomials. The lower derivatives and the solution to the singularly perturbed equation are found by preliminary integration of the series for the highest derivative. It should be noted that when integrating a finite series, the order of the approximating polynomials increases (for example, when integrating twice, a polynomial of the second degree becomes a polynomial of the fourth degree), the polynomials become smoother. We emphasize that both during differentiation and integration of a finite series, the order of the algebraic system being solved does not increase.

2. Problem Statement

In this work, to solve the problem posed in [4], the method of preliminary integration with polynomials is used. In the pre-integration method, singularity zones are not identified and do not depend on their location. The highest derivative of the differential equation and the right-hand side are expanded into a series of polynomials. By first integrating the series for the highest derivative, expressions for all lower derivatives and the desired solution are found in the form of series in polynomials. The integration constants that appear in this case are found from the conditions for satisfying the corresponding boundary conditions. Only after this the necessary series are put into the differential equation and a system of equations is obtained regarding the coefficients of the expansion of the series for the highest derivative. By solving the resulting system, the expansion coefficients are determined and placing them in the required series, it is possible to determine the values of the solution and its derivatives of any order, up to the highest derivative.

Let it be necessary to solve the following inhomogeneous singularly perturbed equation:

$$\varepsilon\frac{d^2u}{dy^2}+\frac{1}{2}\frac{du}{dy}=\frac{1}{8}\left(y+1\right),\quad y\in(-1,1), \tag{1}$$

with boundary conditions

$$u\left(-1\right)=u\left(+1\right)=0, \tag{2}$$

where is ε is a small parameter.

The trial function of the problem (1) and (2) has the form [4]:

DOI:https//doi.org/10.22452/mjs.vol44no1.8

$$u(y)=\frac{\varepsilon-0,5}{1-e^{-1/\varepsilon}}\left(1-\varepsilon^{-(y+1)/2\varepsilon}\right)-\varepsilon\frac{y+1}{2}+\frac{(y+1)^2}{8}.$$

3. Solution Method

The highest derivative of the differential equation (1) and the right part of *f(y)* are searched for in the form of series:

$$\frac{d^2u}{dy^2}=\sum_{j=0}^{N}a_jT_j(y), \qquad f(y)=\sum_{i=0}^{N}b_iT_i(y), \tag{3}$$

where $T_j(y)$ are Chebyshev polynomials of the first kind.

After a two-time preliminary integration of the series (3), we have:

$$\frac{du}{dy}=\sum_{j=0}^{N+1}\sum_{i=0}^{N}f_{ji}^{(1)}a_iT_j(y)+C_1T_0(y), \tag{4}$$

$$u(y)=\sum_{j=0}^{N+2}\sum_{i=0}^{N}f_{ji}^{(0)}a_iT_j(y)+C_1T_1(y)+C_2T_0(y), \tag{5}$$

where C_1, C_2 are unknown integration constants. To determine them, we use the boundary conditions (2) and use the following properties of polynomials: $T_n(\pm1)=(\pm1)^n$.

Then, we have:

$$u(+1)=\sum_{j=0}^{N+2}\sum_{i=0}^{N}f_{ji}^{(0)}a_i+C_1+C_2=0, \tag{6}$$

$$u(-1)=\sum_{j=0}^{N+2}\sum_{i=0}^{N}(-1)^j f_{ji}^{(0)}a_i-C_1+C_2=0. \tag{7}$$

Adding equation (6) and (7), we get

$$u(+1)+u(-1)=\sum_{j=0}^{N+2}\sum_{i=0}^{N}f_{ji}^{(0)}a_i+\sum_{j=0}^{N+2}\sum_{i=0}^{N}(-1)^j f_{ji}^{(0)}a_i+2C_2=0.$$

From here, we define the constant C_2 as follows:

$$C_2=-\frac{1}{2}\sum_{i=0}^{N}\left[\sum_{j=0}^{N+2}f_{ji}^{(0)}+(-1)^j f_{ji}^{(0)}\right]a_i.$$

Similarly, subtracting equation (7) from equation (6), we determine the constant C_1 :

$$C_1=\frac{1}{2}\sum_{i=0}^{N}\left[\sum_{j=0}^{N+2}\left((-1)^j f_{ji}^{(0)}-\sum_{j=0}^{N+2}f_{ji}^{(0)}\right)\right]a_i,$$

We now introduce the following notation:

$$\delta_i^{(0)}=\sum_{j=0}^{N+2}f_{ji}^{(0)}, \qquad \bar{\delta}_i^{(0)}=\sum_{j=0}^{N+2}(-1)^j f_{ji}^{(0)}.$$

Then, the expressions for constants C_1 and C_2 have the following form:

$$C_1=\frac{1}{2}\sum_{i=0}^{N}\left[\bar{\delta}_i^{(0)}+\delta_i^{(0)}\right]a_i, \tag{8}$$

$$C_2=-\frac{1}{2}\sum_{i=0}^{N}\left[\delta_i^{(0)}+\bar{\delta}_i^{(0)}\right]a_i. \tag{9}$$

Formulas (4) and (5), considering constants (7) and (9), are written in the following general form:

$$u^{(\beta)}(y)=\sum_{j=0}^{N+2-\beta}\sum_{i=0}^{N}g_{ji}^{(\beta)}a_iT_j(y), \qquad \beta=0,1, \tag{10}$$

where

$$g_{ji}^{(1)}=f_{ji}^{(1)}+\delta_{j,0}\frac{1}{2}\left(\bar{\delta}_i^{(0)}-\delta_i^{(0)}\right), \tag{11}$$

$$g_{ji}^{(0)}=f_{ji}^{(0)}+\delta_{j,1}\frac{1}{2}\left(\bar{\delta}_i^{(0)}-\delta_i^{(0)}\right)-\delta_{j,0}\frac{1}{2}\left(\delta_i^{(0)}-\bar{\delta}_i^{(0)}\right). \tag{12}$$

Here,

$\delta_{ij}=\begin{cases}1, if\ i=j,\\ 0, if\ i\neq j,\end{cases}$ denotes the Kronecker symbol.

Finally, substituting series (3) and (10) into (1) and equating the coefficients for the same degrees of polynomials, we obtain the following linear algebraic system for determining the expansion coefficients $a_{0,}a_1a_2...,a_n$:

$$\sum_{k=0}^{n}\left[\varepsilon\delta_{ik}+\frac{1}{2}g_{ik}^{(1)}\right]a_k=b_i, \qquad i=0,1,2,...,n. \tag{13}$$

The right part of the system (13) is defined as follows:
It is known that

$$f(y)=\frac{1}{8}(y+1)=\sum_{i=0}^{N}b_iT_i(y). \tag{14}$$

DOI:https//doi.org/10.22452/mjs.vol44no1.8

Hence, the coefficients in formula (14) are determined by the following inverse transformation [9-12]:

$$b_i = \frac{2}{Nc_i}\sum_{l=0}^{N}\frac{1}{c_l} f\left(y_l\right) T_i\left(y_l\right), \qquad i = 0,1,\dots,N,$$

or

$$b_i = \frac{2}{8Nc_i}\sum_{l=0}^{N}\frac{1}{c_l}\left(y_l+1\right) T_i\left(y_l\right), \qquad i = 0,1,\dots,N,$$

where $c_0 = c_N = 2,\ c_1 = 1,\ \ if\ \ l \neq 0; N,\ y_l = \cos\frac{\pi l}{N}$ is the collocation nodes for Chebyshev polynomials of the first kind.

Here is an algorithm for calculating constants [16-17]:

$$\delta_i^{(\beta)} = \sum_{j=0}^{N+2-\beta} f_{ji}^{(\beta)}, \qquad \bar{\delta}_i^{(\beta)} = \sum_{j=0}^{N+2-\beta}\left(-1\right)^j f_{ji}^{(\beta)},\ \ \beta = 0,1,$$

where

$$f_{ji}^{(1)} = \delta_{j,i+1}\beta_i^{(1)} + \delta_{j,i-1}\zeta_i^{(1)},$$

$$f_{ji}^{(0)} = \delta_{j,i+2}\beta_i^{(0)} + \delta_{j,i}\zeta_i^{(0)} + \delta_{j,i-2}\mu_i^{(0)}.$$

Here, constants β, ζ, μ are calculated as follows:

$$\beta_i^{(1)} = \frac{c_i}{2\left(i+1\right)},\ i \geq 0, \quad \beta_i^{(0)} = \frac{\beta_i^{(1)}}{2\left(i+2\right)},\ \ i \geq 0,$$

$$\zeta_i^{(1)} = \frac{-1}{2\left(i-1\right)},\ i \geq 2, \quad \zeta_i^{(0)} = \frac{\zeta_i^{(1)} - \beta_i^{(1)}}{2i},\ \ \ i \geq 1,$$

$$\mu_i^0 = \frac{-\zeta_i^{(1)}}{2\left(i-2\right)},\ \ i \geq 3.$$

4. Discussion of The Results

Let us present the results of numerical calculations obtained by the preliminary integration method for solving the boundary value problem (1)-(3) when the value of a small parameter is for different numbers of polynomials. N=10, 20, 30,40 and 50.

Table 1 shows the results of the polynomials $y_l = \cos\frac{\pi l}{N}$ calculated in the nodes $l = 0,1,2,\dots,N$, when $N = 10.$ For small numbers of polynomials, the influence of a small parameter on the dynamics of the numerical solution is observed. In this case, high-frequency-amplitude sawtooth jumps appear in the numerical solution. At the same time, it should be noted that the smaller the value of a small parameter ε, the more sawtooth jumps appear.

Table 1. Comparison of the trial function and numerical solution ($N = 10$)

Nodes Y$_l$ on l	u_e - trial function	u_a - numerical solution	$\Delta = \left\|u_e - u_a\right\|$ error
3	-0,4708209	0,47920272	0,9500237
5	-0,37	0,5750956	0,9450956
7	-0,1828062	0,7588535	0,9416597
9	-0,0239276	0,8996691	0,9235967

From the results in Table 1, with a small number of polynomials, the trial function and numerical solutions are very different. These results are clearly presented in Figure 1.

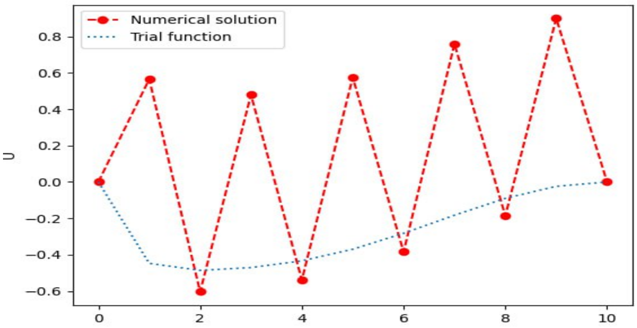

Figure 1. Dynamics of changes in the trial function and numerical solution ($N = 10$).

From Figure 1, it can be seen that when approximating a solution with a small number of Chebyshev polynomials, sawtooth jumps of high amplitude appear.

Now, we gradually increase the number of approximating polynomials. In Table 2, the results obtained by the method of preliminary integration when $N = 20$ with a same value of parameter, $\varepsilon = 10^{-2}$ are presented.

Table 2. Comparison of trial function and numerical solutions

Nodes Y$_l$ on l	u_e - trial function	u_a - numerical solution	$\Delta = \left\|u_e - u_a\right\|$ error
4	-0,486361	-0,488502	0,002141
8	-0,433773	-0,435351	0,001579
12	-0,282354	-0,283755	0,001401
16	-0,089977	-0,091128	0,001151

In Table 2, the numerical solution of the (1)-(3) is found with absolute accuracy $\Delta = 10^{-1}$. For clarity, the results of Table 2 are presented graphically in Figure 2.

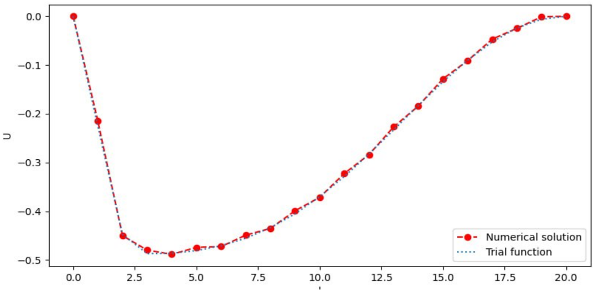

Figure 2. Dynamics of changes in the trial function and numerical solution ($N = 20$).

In Table 2 and Figure 2, the pre-integration method provides very fast convergence of the numerical solution since the absolute error of the solution decreases sharply.

The resulting Table 3 shows the relationship between the maximum error and approximating polynomials at a value of a small parameter, $\varepsilon = 10^{-2}$.

Table 3. The relationship between the absolute error and polynomials.

Number of polynomials, N	15	20	25	30	35	40	45	50
Absolute error, Δ	10^{-2}	10^{-3}	10^{-4}	10^{-5}	10^{-7}	10^{-9}	10^{-11}	10^{-13}

According to Table 3, with increasing polynomials, the absolute error decreases as a geometric progression. Now, we present the results of the calculation when the value of the small parameter is $\varepsilon = 10^{-2}$, i.e. 10 times less than the case discussed above. It should be noted that almost all of the above methods become unsuitable for studying the dynamics of changes in the solution of the problem (1)-(2) with this small parameter value of $\varepsilon = 10^{-3}$. In this case, as noted above, high-frequency-amplitude sawtooth jumps are clearly manifested in the solution area. In Table 4, the results are given when the number of polynomials is equal to $N = 40$, $\varepsilon = 10^{-3}$.

Table 4. Comparison of the trial function and numerical solution ($N = 40$).

Nodes Yl on l	u_e - trial function	u_a-numerical solution	$\Delta = \left\|u_e - u_a\right.$ - error
15	-0,451674	0,702899	1,154572
25	-0,260715	0,893573	1,154287
35	-0,037298	1,115398	1,152696

It can be seen that with the value of the small parameter of $\varepsilon = 10^{-3}$, the numerical solution is very different from the trial function. This is explained by the fact that the number of approximating polynomials is not enough to display the dynamics of changes in the solution of the problem.

The results given in Table 4 will be represented graphically in Figure 3.

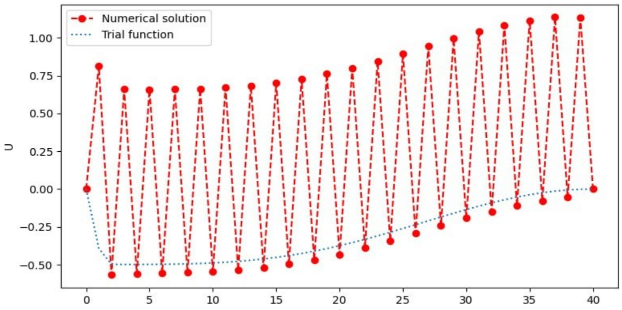

Figure 3. Dynamics of changes in the trial function and numerical solution ($N = 40$).

It can be seen that the frequency and amplitude of the sawtooth are too high.

In Table 5, the results of the polynomials are $N = 60$, $\varepsilon = 10^{-3}$.

Table 5. Comparison of the trial function and numerical solution ($N = 60$).

Nodes Yl on l	u_e - trial function	u_a - numerical solution	$\Delta = \left\|u_e - u_a\right\|$ error
10	-0,4968	-0,5010	0,0042
20	-0,4680	-0,4720	0,0040
30	-0,3745	-0,3785	0,0039
40	-0,2225	-0,2225	0,0040
50	-0,0647	-0,0685	0,0038

The results in Table 5 are clearly illustrated in Figure 4.

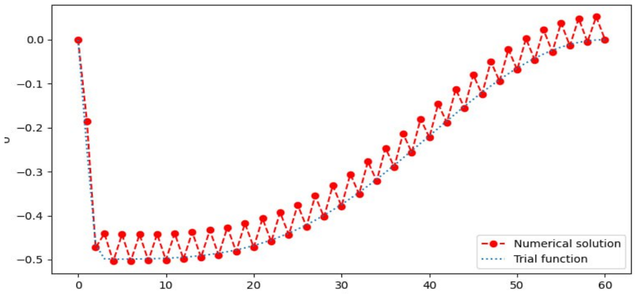

Figure 4. Dynamics of changes in the trial function and numerical solution ($N = 60$).

In Figure 4, the amplitude of the sawtooth jumps is significantly small, and the maximum error is of the order of $\Delta = 10^{-1}$.

The results of comparing the trial function and numerical solution when $N = 100$ and $\varepsilon = 10^{-3}$ are shown in Table 6.

DOI:https//doi.org/10.22452/mjs.vol44no1.8

Table 6. Comparison of trial function and numerical solutions ($N=100$)

Nodes Y_l at l	u_e -trial function	u_a-numerical solution	$\Delta=\|u_e-u_a$ Error
10	0,498725	-0,498729	4,14*10^{-6}
20	0,494536	-0,494539	3,30*10^{-6}
30	0,477966	-0,477969	3,09*10^{-6}
40	0,439663	-0,439667	3,00*10^{-6}
50	0,374500	-0,374503	2,96*10^{-6}
60	0,285464	-0,285467	2,92*10^{-6}
70	0,184661	-0,184664	2,86*10^{-6}
80	0,090837	-0,090839	2,72*10^{-6}
90	0,024148	-0,024150	2,18*10^{-6}

Graphical representations of the results of calculations given in Table 6 are shown in Figure 5.

According to Figure 5, the numerical solution practically coincides with the trial function of problem (1)-(2) and with the small parameter $\varepsilon=10^{-3}$. The maximum error will be of the order of $\Delta=10^{-5}$.

Here, Table 7 shows th establishing relationship between the error and approximating Chebyshev polynomials at a small parameter value of $\varepsilon=10^{-3}$.

Table 7. The relationship between the error and polynomials ($\varepsilon=10^{-3}$)

Number of polynomials, N	60	70	80	90	100
Error, Δ	10^{-1}	10^{-2}	10^{-3}	10^{-4}	10^{-5}

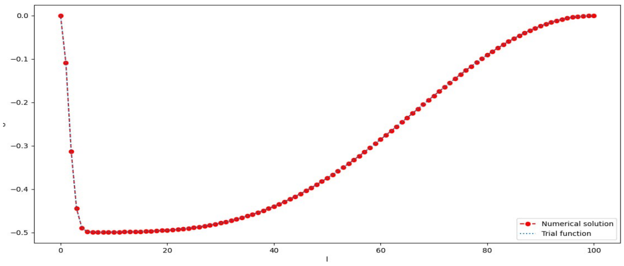

Figure 5. Dynamics of changes in the trial function and numerical solution ($N=100$).

From Table 7, with an increase in the number of approximating Chebyshev polynomials, the maximum absolute error decreases with the rate of geometric progression and, at the same time, the value of a small parameter. All numerical results were obtained using a Python program.

The main criterion for assessing the effectiveness of an arbitrary numerical method is the number of arithmetic operations. When approximating a singularly perturbed equation by difference and spectral or by the preliminary integration method, a system of linear algebraic equations is obtained. The order of the matrix in a linear algebraic system depends on the number of difference grid nodes (N) or the number of polynomials used in finite Chebyshev series in the spectral method or the preliminary integration method (N). Let us assume that the resulting algebraic system is solved by the Gaussian method. It is known that the formula calculates the number of arithmetic operations in the Gauss method

$$Q=\frac{2}{3}N^3.$$

Let us compare the effectiveness of the methods used to solve a singularly perturbed equation in terms of the number of arithmetic operations and accuracy.

We present the results in Table 8.

Table 8. Comparison of methods in terms of efficiency and accuracy at $\varepsilon=10^{-2}$.

Method	Number N	Number of arithmetic operations Q	Maximum absolute error Δ
Finite-difference [3]	20	5333	0.1195
	50	83333	0.0521
Spectral [8]	10	666	0.97
	20	5333	0.0027
	50	83333	10^{-10}
Pre-integration method	10	666	0.95
	20	5333	0.0021
	50	83333	10^{-13}

From the results given in Table 8 it is clear that the preliminary integration method has high accuracy and efficiency. Thus, the pre-integration method is a universal and reliable mathematical tool for solving a singularly perturbed equation.

5. Conclusion

i. For the numerical solution of an inhomogeneous singularly perturbed equation, a new high-precision and efficient method is proposed - the method of preliminary integration.

ii. The inhomogeneous singularly perturbed equation is solved by the proposed method for various values of the small parameter of the problem.

iii. Comparison of the obtained results with the exact solution of the problem and the approximate solution obtained by the spectral method shows the high accuracy and efficiency of the preliminary integration method.

iv. Tabular and graphical results illustrating the accuracy and efficiency of the method are presented.

DOI:https//doi.org/10.22452/mjs.vol44no1.8

6. References

Abutaliev F. B., Normurodov Ch. B Mathematical modeling of the problem of hydrodynamic stability, Tashkent:Fan va texnologiya:2011:188

Bakhvalov K.S (1969) Towards optimization of methods for solving boundary value problems in the presence of a boundary layer, 4(9): 841-859.

Krylov A.A., Malykhina I.D (1968) Solving the eigenvalue problem for the Orr-Sommerfeld equation using the difference method. Comput. methods and programming. 11:44-54.

Liseikin V. D., Yanenko N. N (1981) On a uniformly convergent algorithm for the numerical solution of a second-order ordinary differential equation with a small parameter at the highest derivative, Numerical methods in continuum mechanics,12:45–56.

Loer St (1969) Examination of the stability of disturbed boundary- layer flow by a numerical method, Phys. fluids. 12(12):139-143

Normurodov Ch. B (2005) On one effective method for solving the Orr-Sommerfeld equation, Mathematical Modeling-Moscow, 9(17):35-42.

Normurodov Ch. B (2007) Mathematical modeling of hydrodynamic problems for two-phase plane-parallel flows, Mathematical Modeling-Moscow, 6(19): 53-60.

Normurodov Ch. B., Abdurakhimov B. F., Djurayeva N. T., Viswanathan K. K., Saravanan D (2023) Application of the Preliminary Integration Method for Numerical Simulation of Two-Phase Hydrodynamic Flows, European Chemical Bulletin, 12: 959-968. ISSN 2063-5346. Open Access E-journal.

Normurodov Ch. B., Djurayeva N. T (2022) Review of methods for solving the problem of hydrodynamic stability. Problems of Computational and Applied mathematics, 1(38):83-90

Normurodov Ch. B., Kholiyarov Ch. E., Gulomkodirov K. A., Djurayeva N. T (2022) Numerical simulation of the inverse problem for the vortex-current equation. AIP Conf. Proc., 2637:040018. http://dx.doi.org/10.1063/5.0118605.

Normurodov Ch. B., Tilovov M.A., Tursunova B.A., Djurayeva N.T (2023) Numerical modeling of inhomogeneous singularly perturbed fourth-order boundary value problems using the spectral method. Problems of Computational and Applied mathematics, 5(52): 83-90

Normurodov Ch. B., Toyirov A. X., Yuldashev Sh. M (2022) Numerical modeling of a wave in a nonlinear medium with dissipation. AIP Conf. Proc., 2637:040005, http://dx.doi.org/10.1063/5.0118459.

Normurodov Ch.B., Toyirov A. Kh., Ziyakulova Sh.A., Viswanathan K.K (2024) Convergence of Spectral- Grid Method for Burgers Equation with Initial- Boundary Conditions. Mathematics and Statistics, 12(2):115-125. DOI: 10.13189/ms.2024.120201.

Normurodov Ch. B., Tursunova B. A (2023) Numerical modeling of the boundary value problem of an ordinary differential equation with a small parameter at the highest derivative by Chebyshev polynomials of the second kind, Results in Applied Mathematics, 19:1-5.

Thomas H.H (1953) The stability of plane Poiseuille flow, Phys.rev, 4(91):780-783.

Zharilkasinov A., Liseykin V.D., Skobelev B.Yu., Yanenko N.N (1983) Application of a non-uniform grid for the Orr-Sommerfeld numerical solution, Numerical methods of continuum mechanics. 5(14): 45-54.

Zharilkasinov A., Skobelev B.Yu., Yanenko N.N (1984) Effective non-uniform mesh for the Orr-Sommerfeld equation and Poiseuille flow spectrum. (Preprint/RAN.Sib.department. Institute of Theor. And Applied Mechanics), 21: 35.

MALAYSIAN JOURNAL OF SCIENCE
MJS
ISSN 1394-3065

Regular Issue

Malaysian Journal of Science 44 (1): 70-86 (March 2025)
https://mjs.um.edu.my

On the Kronecker Structure of linearization of Cubic Two-Parameter Eigenvalue Problems

Niranjan Bora[1a]* and Bharati Borgohain[2b]

Abstract: Linearization is a conventional approach to studying matrix polynomials of the form $P(\lambda):=\sum_{j=1}^{k}\lambda^j A_j$, where $A_j\in\mathbb{C}^{n\times n}$. It converts the matrix polynomial $P(\lambda)$ into a matrix pencil of the form $L(\lambda):=A+\lambda B$ of high dimension, where A and B are matrices over $\mathbb{C}$, and λ is the spectral parameter. In this paper, we consider Cubic two-parameter eigenvalue problems $(\mathbb{CTEP})$ and study their three different linearization processes. Using linearization techniques, a $\mathbb{CTEP}$ is first converted into a linear two-parameter eigenvalue problem $(\mathbb{L2EP})$ with coefficient matrices of different sizes. The main advantage of these linearizations lies in the fact that, after transforming them into suitable linearized forms, existing numerical techniques for linear multiparameter eigenvalue problems $(\mathbb{LMEP})$ can be applied to solve the $\mathbb{CTEP}$ without solving the original problem. While solving $\mathbb{CTEP}$ by formulating suitable linearizations, several transformations are generally used. This study reports on these transformations, which have not been studied completely due to the complexity of their Kronecker structures. The ranks of the associated Delta matrices are also calculated in a detailed manner to bring out the benefits of using the Tracy-Singh product over others.

Keywords: *Cubic two-parameter eigenvalue problem, Linear two-parameter eigenvalue problem, linearization, matrix polynomial, Tracy-Singh product.*

1. Introduction

One-parameter matrix polynomials arise in many physical applications and have received significant attention from researchers (Dmytryshyn et al., 2020; Fabbender & Saltenberger, 2018; Gohberg et al., 2009). However, the literature on two-parameter matrix polynomials remains limited (Hochstenbach et al., 2015; Jarlebring et al., 2009). The standard form of a two-parameter matrix polynomial of degree k is given by

$$\mathbb{P}(\lambda,\mu):=\sum_{i=0}^{k}\sum_{j=0}^{k-i}\lambda^i\mu^jP_{ij}=\sum_{j=0}^{k}\mathbb{E}_j(\lambda,\mu), \qquad (1)$$

where $P_{ij}\in\mathbb{C}^{n\times n}$, $\lambda,\mu\in\mathbb{C}$ are spectral parameters and $\mathbb{E}_j(\lambda,\mu)$ is a homogeneous matrix polynomial of degree j such that,

$$\mathbb{E}_j(\lambda,\mu):=\sum_{l=0}^{j}\lambda^{j-l}\mu^lP_{jl} \qquad (2)$$

The standard form of the Polynomial two-parameter eigenvalue problem $(\mathbb{PTEP})$, which is the generalization of the Polynomial eigenvalue problem $(\mathbb{PEP})$, comprises two bivariate matrix polynomials of the form

$$\begin{aligned}\mathbb{P}_1(\lambda,\mu)x_1&:=\sum_{i=0}^{k}\sum_{j=0}^{k-i}\lambda^i\mu^jA_{ij}x_1=0,\\ \mathbb{P}_2(\lambda,\mu)x_2&:=\sum_{i=0}^{k}\sum_{j=0}^{k-i}\lambda^i\mu^jB_{ij}x_2=0,\end{aligned} \qquad (3)$$

where $A_{ij}\in\mathbb{C}^{n_1\times n_1}$; $B_{ij}\in\mathbb{C}^{n_2\times n_2}$ and $x_i\in\mathbb{C}^{n_i}$, $i:=1,2$ are non zero vectors. The problem is to find the scalars $\lambda,\mu\in\mathbb{C}$ and the corresponding non zero vectors $x_i\in\mathbb{C}^{n_i}$, $i:=1:2$ such that $\mathbb{P}_j(\lambda,\mu)x_j:=0$. The pair $(\lambda,\mu)\in\mathbb{C}^2$ is called the eigenvalue and the corresponding tensor product $x:=x_1\otimes x_2$ is called the right eigenvectors. Similarly, a tensor product $v_1\otimes v_2$ is called a left eigenvector of the $\mathbb{PTEP}$ if $v_i\neq 0$; $i:=1:2$, satisfies $v_i^*\mathbb{P}_i(\lambda,\mu)=0$. For $k=2$, the Equation defined in (3) is reduced to a Quadratic two-parameter eigenvalue problem $(\mathbb{QTEP})$, and for $k=3$, it is reduced to a $\mathbb{CTEP}$.

Authors information:
[a]Department of Mathematics, Dibrugarh University Institute of Engineering and Technology,
Assam-786004, INDIA. niranjanbora11@gmail.com[1]
[b]Department of Mathematics, Dibrugarh University, Assam-786004, INDIA. E-mail: bharatiborgohain3@gmail.com[2]

*Corresponding Author: niranjanbora11@gmail.com

$\mathbb{PTEP}$ topic emerges in the analysis of critical delay differential equations (Jarlebring & Hochstenbach, (2009); Meerbergen et al., (2013)). For instance, the neutral commensurate differential equations (Hochstenbach et al., (2005)) with multiple delays (m>1) (Hochstenbach et al., (2015)). Two methodological approaches exist to address this phenomenon. The first approach enables parametrization of surfaces or curves corresponding to the critical delay using m-1 independent variables. The second approach posits that the delays are commensurate, functioning as integer multiples of a specific delay value τ≥0. The delay

Received: August 18, 2023
Accepted: January 14, 2024
Published: March 31, 2025

DOI:https//doi.org/10.22452/mjs.vol44no1.9

differential equation featuring commensurate delays, wherein delays operate as integer multiples of a delay value τ, is

$$N_0\dot{x}(t) = \sum_{k=0}^{m} M_k\, x(t-\tau k), \tag{4}$$

where $M_k, N_0 \in \mathbb{C}^{n\times n}$. The associated eigenvalue problem is,

$$\left(\sum_{k=0}^{m} e^{k\tau\lambda}\, M_k - \lambda N_0\right) x = 0. \tag{5}$$

In stability analysis, the purely imaginary eigenvalues are preferred. For this reason, consider $\lambda = i\omega$ and $\mu = e^{i\tau\omega}$. Their conjugates are $\bar{\lambda} = -\lambda$ and $\bar{\mu} = \mu^{-1}$. Taking complex conjugates of the Equation (5) and rearranging terms we obtain,

$$\begin{aligned} -\bar{M}_m x &= \lambda\mu^m \bar{N}_0 x + \sum_{k=1}^{m} \mu^k\, \bar{M}_{m-k} x, \\ M_0 y &= \lambda N_0 y - \sum_{k=1}^{m} \mu^k\, \bar{M}_k y. \end{aligned} \tag{6}$$

Equation (6) motivates the study of the eigenvalue problem in the following form

$$\begin{aligned} M_1 x &= \lambda \sum_{k=0}^{m} \mu^k\, N_{1,k} x + \sum_{k=1}^{m} \mu^k\, C_{1,k} x, \\ M_2 y &= \lambda \sum_{k=0}^{m} \mu^k\, N_{2,k} y + \sum_{k=1}^{m} \mu^k\, C_{2,k} y, \end{aligned} \tag{7}$$

which is the general form of $\mathbb{PTEP}$. $\mathbb{PTEP}$ also arises in the study of bivariate polynomials (Plestenjak, 2017; Plestenjak & Hochstenbach, 2016), and the references therein.

There are two types of numerical approaches for solving $\mathbb{PTEP}$: those that deal directly with the problem and those that compute eigenvalues of linearized forms. The usual method to solve the $\mathbb{PTEP}$ defined in (3) is by linearizing it into an $\mathbb{L2EP}$ of larger dimension. The linearized version of problem (3) is singular and can be solved by adopting the method proposed in (Dooren, 1997; Muhič & Plestenjak, 2009; Košir & Plestenjak, 2022). Moreover, the Jacobi-Davidson method developed in Hochstenbach et al. (2015) can be applied directly to $\mathbb{PTEP}$ instead of the linearized problem. Linearization is a classical approach to investigating the $\mathbb{PEP}$. Details on linearization of one-parameter matrix polynomials are found in the works of Mackey et al. (2006), Bueno et al. (2018), Das and Alam (2019), Das (2020), Higham et al. (2006), and Lancaster (2008), and the references therein. Literature on linearizations for quadratic matrix polynomials is found in Kressner and Glibić (2023) and Lancaster and Zaballa (2021). The linearization process influences the sensitivity of eigenvalues. Therefore, it is important to identify potential linearizations and study their constructions. The linearized form of two-parameter polynomials has a somewhat complicated structure compared to the one-parameter case. Literature on linearization of $\mathbb{QTEP}$ is found in the works of Tisseur and Meerbergen (2001), Muhič and Plestenjak (2010), and Hochstenbach et al. (2012), and numerical methods are found in Plestenjak (2016) and Dong (2022). In this paper, we provide a general framework for the canonical structure of the linearized form of $\mathbb{CTEP}$, which can be considered a continuing thread to study the general $\mathbb{PTEP}$ of degree k.

This paper is organized as follows: Section 2 contains basic preliminaries. Section 3 contains the problem formulation and its basic theory. Section 4 contains a unified framework on different linearization techniques of $\mathbb{CTEP}$. In Section 5, the ranks of delta matrices involved in $\mathbb{CTEP}$ are derived. A numerical example is presented in Section 6 to compare the linearization classes, and finally, in Section 7, a conclusion is drawn on the whole work.

2. Preliminaries

The following basic definitions and results are applied throughout the paper: $A \in \mathbb{C}^{n_1\times n_2}$ is the matrix of size $n_1 \times n_2$ over $\mathbb{C}$. A^{-1}, A^T and A^* represents the inverse, transpose and conjugate transpose of the matrix A, respectively. The Euclidean norm of the matrix A is denoted by $\|A\|$ and the standard Kronecker product is denoted by $\otimes$.

Definition 1. (Henderson et al., (1983)) *The Kronecker Product* $(\otimes)$ *for two matrices A and B is defined as* $A \otimes B = \{a_{ij}B\}$, *where* a_{ij} *are the elements in* i^{th} *row and* j^{th} *column of the matrix A.*

Definition 2. (Tracy & Singh, (1972)) *Tracy–Singh product of partitioned matrices: Let an* $m \times n$ *matrix A be partitioned into the* $m_i \times n_j$ *blocks* A_{ij} *and a* $p \times q$ *matrix B into the* $p_k \times q_l$ *blocks* B_{kl} *such that* $m = \sum_{i=1}^{r} m_i$, $n = \sum_{j=1}^{s} n_j$, $p = \sum_{k=1}^{t} p_k$, $q = \sum_{l=1}^{u} q_l$. *The Tracy–Singh product* $A \odot B$ *is a* $mp \times nq$ *matrix, defined as* $A \odot B = \left(A_{ij} \odot B\right)_{ij} = \left(\left(A_{ij} \otimes B_{kl}\right)_{kl}\right)_{ij}$, *where the (ij)*th *block of the product is the* $m_i p \times n_j q$ *matrix* $A_{ij} \odot B$, *of which the (kl)th subblock equals the* $m_i p_k \times n_j q_l$ *matrix* $A_{ij} \otimes B_{kl}$.

For example, if we take $A = \begin{pmatrix} A_{11} & A_{12} \\ A_{21} & A_{22} \end{pmatrix}$ *and* $B = \begin{pmatrix} B_{11} & B_{12} \\ B_{21} & B_{22} \end{pmatrix}$; *then the Tracy-Singh product is defined as,*

$$A \odot B = \begin{pmatrix} A_{11} \odot B & A_{12} \odot B \\ A_{21} \odot B & A_{22} \odot B \end{pmatrix} = \begin{pmatrix} A_{11} \otimes B_{11} & A_{11} \otimes B_{12} & A_{12} \otimes B_{11} & A_{12} \otimes B_{12} \\ A_{11} \otimes B_{21} & A_{11} \otimes B_{22} & A_{12} \otimes B_{21} & A_{12} \otimes B_{22} \\ A_{21} \otimes B_{11} & A_{21} \otimes B_{12} & A_{22} \otimes B_{11} & A_{22} \otimes B_{12} \\ A_{21} \otimes B_{21} & A_{21} \otimes B_{22} & A_{22} \otimes B_{21} & A_{22} \otimes B_{22} \end{pmatrix}$$

DOI:https//doi.org/10.22452/mjs.vol44no1.9

We will denote the Tracy-Singh Product by a map TSP.

Definition 3. (Muhič & Plestenjak, (2010))) *Tracy-Singh reordering of two block matrices* A *and* B *is given by a map* TSR*, such that* $TSR(A \otimes B) = A \odot B$*, i.e., we reorder the columns and rows of the Kronecker product* $A \otimes B$*, to obtain the Tracy-Singh product.*

Theorem 1. (Tracy & Jinadasa, (1989)) *When* A *and* B *can be partitioned into equal-sized blocks, then Tracy-Singh product* $A \odot B$ *and the Kronecker product* $A \otimes B$ *are permutation equivalent.*

Definition 4. (Hochstenbach, (2003)) *The generalized eigenvalue problem (*$\mathbb{GEP}$*) is to find the pair* (λ, x) *that satisfies the matrix equation of the form* $Ax = \lambda Bx$*, where* A *and* B *are any matrices over* $\mathbb{C}$*,* x *is a non-zero vector, and* λ *is the spectral parameter.*

Definition 5. (Atkinson, (1972)) $\mathbb{LMEP}$ *is to find the scalars* $\lambda_i \in \mathbb{C}$ *and the corresponding non-zero vectors* $x_i \in \mathbb{C}^{m_i}$ *such that,*

$$\mathbb{W}(X, \Omega) = \begin{cases} \mathbb{W}_1(\lambda)x_1 \\ \dots \\ \mathbb{W}_n(\lambda)x_n \\ \frac{1}{2}(x_1^* x_1 - 1) \\ \dots \\ \frac{1}{2}(x_n^* x_n - 1) \end{cases} = 0, \tag{8}$$

where $\mathbb{W}_i(\lambda) := -A_{i0} + \sum_{j=1}^{n} \lambda_j A_{ij}$*;* $A_{ij} \in \mathbb{C}^{m_i \times m_i}$*;* $i := 1{:}n$*;* $j := 0{:}n$*.* $\mathbb{L2EP}$ *being the special case of* $\mathbb{LMEP}$ when $\mathrm{n} = 2$.

Definition 6. (Hochstenbach et al., (2012)) *Let* $\mathbb{Q}(\lambda, \mu) := \sum_{i=0}^{k} \sum_{j=0}^{k-i} \lambda^i \mu^j P_{ij}$ *be any* $n \times n$ *matrix polynomial. Then, an* $ln \times ln$ *linear matrix polynomial* $\mathbb{L}(\lambda, \mu) = L_0 + \lambda L_1 + \mu L_2$ *is a linearization of* $\mathbb{Q}(\lambda, \mu)$ *if there exist polynomials* $\mathcal{M}(\lambda, \mu)$ *and* $\mathcal{N}(\lambda, \mu)$*, whose determinant is a non-zero constant independent of* λ *and* μ*, such that* $\begin{bmatrix} \mathbb{Q}(\lambda, \mu) & 0 \\ 0 & I_{(l-1)n} \end{bmatrix} = \mathcal{M}(\lambda, \mu)\mathbb{L}(\lambda, \mu)\mathcal{N}(\lambda, \mu)$.

3. General Theory of $\mathbb{CTEP}$

The standard form of $\mathbb{CTEP}$, which is being the special case $\mathbb{PTEP}$ when $k = 3$, is given by

$$\begin{aligned} \mathbb{P}_1(\lambda, \mu)x_1 = 0, \\ \mathbb{P}_2(\lambda, \mu)x_2 = 0, \end{aligned} \tag{9}$$

where
$\mathbb{P}_1(\lambda, \mu) = \lambda^3 A_{30} + \lambda^2 \mu A_{21} + \lambda \mu^2 A_{12} + \mu^3 A_{03} + \lambda^2 A_{20} + \lambda \mu A_{11} + \mu^2 A_{02} + \lambda A_{10} + \mu A_{01} + A_{00}$;

$\mathbb{P}_2(\lambda, \mu) = \lambda^3 B_{30} + \lambda^2 \mu B_{21} + \lambda \mu^2 B_{12} + \mu^3 B_{03} + \lambda^2 B_{20} + \lambda \mu B_{11} + \mu^2 B_{02} + \lambda B_{10} + \mu B_{01} + B_{00}$; and A_{ij}, B_{ij} are $n \times n$ matrices over $\mathbb{C}$; $i := 1{:}2$, $j := 0{:}9$ such that at least one of the matrices $A_{30}, A_{03}, B_{30}, B_{03}, A_{21}, A_{12}, B_{21}, B_{12}$ is nonzero.

The $\mathbb{CTEP}$ appears in prior work (Muhič & Plestenjak, 2010) (Example 20), where the problem is linearized into a $\mathbb{L2EP}$. However, the authors did not provide proof of the Kronecker structure involved in theory, similar to the quadratic case, due to the complexity arising in the respective Kronecker canonical structure. For a given $\mathbb{CTEP}$ defined in (9), we investigate the $\mathbb{L2EP}$,

$$\begin{aligned} \mathbb{L}^{(1)}(\lambda, \mu)w_1 = \left(\mathbb{L}_0^{(1)} + \lambda \mathbb{L}_1^{(1)} + \mu \mathbb{L}_2^{(1)}\right) w_1 = 0 \\ \mathbb{L}^{(2)}(\lambda, \mu)w_2 = \left(\mathbb{L}_0^{(2)} + \lambda \mathbb{L}_1^{(2)} + \mu \mathbb{L}_2^{(2)}\right) w_2 = 0 \end{aligned} \tag{10}$$

where $w_i \in \mathbb{C}^{6n}\ 0$; $\mathbb{L}_j^{(i)} \in \mathbb{C}^{6n \times 6n}, i := 1{:}2, j = 0{:}2$, such that (10) agrees with the eigenvalues of (9). Converting the problem into a system of joint $\mathbb{GEP}$ in the tensor product space is considered the de facto method, known as the Delta method (Atkinson, 1972) for spectral analysis of the problem. The equivalence between the problem $\mathbb{L2EP}$ and the corresponding joint $\mathbb{GEP}$ can be established by transforming the problem into a commuting pair of specific operator matrices with the following operator determinants,

$$\Delta_0 := \mathbb{L}_1^{(1)} \otimes \mathbb{L}_2^{(2)} - \mathbb{L}_2^{(1)} \otimes \mathbb{L}_1^{(2)}$$

$$\Delta_1 := \mathbb{L}_2^{(1)} \otimes \mathbb{L}_0^{(2)} - \mathbb{L}_0^{(1)} \otimes \mathbb{L}_2^{(2)}; \Delta_2 := \mathbb{L}_0^{(1)} \otimes \mathbb{L}_1^{(2)} - \mathbb{L}_1^{(1)} \otimes \mathbb{L}_0^{(2)} \tag{11}$$

Then each Δ_i, $i := 1{:}2$ is $N \times N$ matrices, where $N := 36n^2$. The system (10) is referred to as singular or nonsingular, according to the operator matrix Δ_0 specified in Equation (11). The proof for the singularity of Δ_0 has been discussed in Section 5, along with the other two operator matrices Δ_1 and Δ_2 using Tracy-Singh product. For spectral analysis, the linear $\mathbb{PTEP}$ is generally considered as nonsingular and a commuting tuple of the form $\Gamma := (\Gamma_1, \Gamma_2)$ is used, where $\Gamma_i := \Delta_0^{-1}\Delta_i$; $i := 1,2$ and is equivalent to a system of joint $\mathbb{GEP}$ of the form given by,

$$\Delta_j u = \lambda_j \Delta_0 u; \quad j := 1,2; \qquad (12)$$

where $u = w_1 \otimes w_2 \in \mathbb{C}^N$ is a decomposable tensor. System (10) is called linearization of $\mathbb{CTEP}$ defined in (9).

Theorem 2. (Atkinson, (1972); Muhič & Plestenjak, (2010)) *For given values α_0, α_1 and α_2, the homogeneous problem,*

$$\left(\eta_0 \mathbb{L}_0^{(1)} + \eta_1 \mathbb{L}_1^{(1)} + \eta_2 \mathbb{L}_2^{(1)}\right) w_1 = 0$$
$$\left(\eta_0 \mathbb{L}_0^{(2)} + \eta_1 \mathbb{L}_1^{(2)} + \eta_2 \mathbb{L}_2^{(2)}\right) w_2 = 0 \qquad (13)$$

satisfies the following equivalent conditions

1. *The matrix $\Delta = \sum_{i=0}^{2} \alpha_i \Delta_i$ is singular.*

2. *There exists an eigenvalue (η_0, η_1, η_2) of the system (12) such that $\sum_{i=0}^{2} \eta_i \alpha_i = 0$*

The same result for nonsingularity has been stated in the following way also.

Theorem 3. (Atkinson, (1972); Muhič & Plestenjak, (2010)) *The homogeneous* $\mathbb{LMEP}$

$$\textstyle\sum_{j=0}^{k} \eta_j A_{ij} x_i = 0 \qquad \textit{(14)}$$

where $A_{ij} \in \mathbb{C}^{n_i \times n_i}$, for $i = 1, \dots, k$ and $j = 0, \dots, k$ is said to be nonsingular if there exists a nonsingular linear combination of the operator determinants Δ_i's, i.e., $\Delta = \sum_{i=0}^{k} \alpha_i \Delta_i$. This is equivalent to the condition that, if $\eta = (\eta_0, \eta_1, \dots, \eta_k)$ is an eigenvalue of (14), then $\sum_{i=0}^{k} \alpha_i \eta_i \neq 0$.

Theorem 4. (Cox et al., (2005)) *(Bezout's theorem) Two projective curves of orders n and m with no common component has precisely nm points of intersection counting multiplicities.*

4. Linearization of $\mathbb{CTEP}$

In this section, we present three different types of linearization techniques of $\mathbb{CTEP}$. Two of them are the general linearization, resulting in a singular $\mathbb{L2EP}$, with coefficient matrices of size $6n \times 6n$ and $9n \times 9n$, respectively. The singularity conditions for the associated $\mathbb{GEP}$ is shown with the help of Tracy-Singh reordering in Δ_i's. The third type of linearization is done by replacing nonlinear terms with new variables, which formulates a nonsingular linear nine-parameter eigenvalue problem ($\mathbb{L9EP}$) so that more efficient methods for solving nonsingular problems can be applied in this case.

Standard Linearization

For a given $\mathbb{CTEP}$, and by following definition 5, we can linearize the $\mathbb{CTEP}$ into a $\mathbb{L2EP}$ (Muhič & Plestenjak, 2010) of the form,

$$\left(\begin{bmatrix} A_{00} & A_{10} & A_{01} & A_{20} & A_{11} & A_{02} \\ 0 & -I & 0 & 0 & 0 & 0 \\ 0 & 0 & -I & 0 & 0 & 0 \\ 0 & 0 & 0 & -I & 0 & 0 \\ 0 & 0 & 0 & 0 & -I & 0 \\ 0 & 0 & 0 & 0 & 0 & -I \end{bmatrix} + \lambda \begin{bmatrix} 0 & 0 & 0 & A_{30} & A_{21} & A_{12} \\ I & 0 & 0 & 0 & 0 & 0 \\ 0 & 0 & 0 & 0 & 0 & 0 \\ 0 & I & 0 & 0 & 0 & 0 \\ 0 & 0 & I & 0 & 0 & 0 \\ 0 & 0 & 0 & 0 & 0 & 0 \end{bmatrix} + \mu \begin{bmatrix} 0 & 0 & 0 & 0 & 0 & A_{03} \\ 0 & 0 & 0 & 0 & 0 & 0 \\ I & 0 & 0 & 0 & 0 & 0 \\ 0 & 0 & 0 & 0 & 0 & 0 \\ 0 & 0 & 0 & 0 & 0 & 0 \\ 0 & 0 & I & 0 & 0 & 0 \end{bmatrix}\right) \begin{bmatrix} x_1 \\ \lambda x_1 \\ \mu x_1 \\ \lambda^2 x_1 \\ \lambda\mu x_1 \\ \mu^2 x_1 \end{bmatrix} = 0,$$

$$\left(\begin{bmatrix} B_{00} & B_{10} & B_{01} & B_{20} & B_{11} & B_{02} \\ 0 & -I & 0 & 0 & 0 & 0 \\ 0 & 0 & -I & 0 & 0 & 0 \\ 0 & 0 & 0 & -I & 0 & 0 \\ 0 & 0 & 0 & 0 & -I & 0 \\ 0 & 0 & 0 & 0 & 0 & -I \end{bmatrix} + \lambda \begin{bmatrix} 0 & 0 & 0 & B_{30} & B_{21} & B_{12} \\ I & 0 & 0 & 0 & 0 & 0 \\ 0 & 0 & 0 & 0 & 0 & 0 \\ 0 & I & 0 & 0 & 0 & 0 \\ 0 & 0 & I & 0 & 0 & 0 \\ 0 & 0 & 0 & 0 & 0 & 0 \end{bmatrix} + \mu \begin{bmatrix} 0 & 0 & 0 & 0 & 0 & B_{03} \\ 0 & 0 & 0 & 0 & 0 & 0 \\ I & 0 & 0 & 0 & 0 & 0 \\ 0 & 0 & 0 & 0 & 0 & 0 \\ 0 & 0 & 0 & 0 & 0 & 0 \\ 0 & 0 & I & 0 & 0 & 0 \end{bmatrix}\right) \begin{bmatrix} x_2 \\ \lambda x_2 \\ \mu x_2 \\ \lambda^2 x_2 \\ \lambda\mu x_2 \\ \mu^2 x_2 \end{bmatrix} = 0. \qquad (15)$$

Comparing Equation (15) with that of the Equation (10), we have,

$$\mathbb{L}_0^{(1)} = \begin{bmatrix} A_{00} & A_{10} & A_{01} & A_{20} & A_{11} & A_{02} \\ 0 & -I & 0 & 0 & 0 & 0 \\ 0 & 0 & -I & 0 & 0 & 0 \\ 0 & 0 & 0 & -I & 0 & 0 \\ 0 & 0 & 0 & 0 & -I & 0 \\ 0 & 0 & 0 & 0 & 0 & -I \end{bmatrix}, \quad \mathbb{L}_1^{(1)} = \begin{bmatrix} 0 & 0 & 0 & A_{30} & A_{21} & A_{12} \\ I & 0 & 0 & 0 & 0 & 0 \\ 0 & 0 & 0 & 0 & 0 & 0 \\ 0 & I & 0 & 0 & 0 & 0 \\ 0 & 0 & I & 0 & 0 & 0 \\ 0 & 0 & 0 & 0 & 0 & 0 \end{bmatrix},$$

$$\mathbb{L}_2^{(1)} = \begin{bmatrix} 0 & 0 & 0 & 0 & 0 & A_{03} \\ 0 & 0 & 0 & 0 & 0 & 0 \\ I & 0 & 0 & 0 & 0 & 0 \\ 0 & 0 & 0 & 0 & 0 & 0 \\ 0 & 0 & 0 & 0 & 0 & 0 \\ 0 & 0 & I & 0 & 0 & 0 \end{bmatrix}, \mathbb{L}_0^{(2)} = \begin{bmatrix} B_{00} & B_{10} & B_{01} & B_{20} & B_{11} & B_{02} \\ 0 & -I & 0 & 0 & 0 & 0 \\ 0 & 0 & -I & 0 & 0 & 0 \\ 0 & 0 & 0 & -I & 0 & 0 \\ 0 & 0 & 0 & 0 & -I & 0 \\ 0 & 0 & 0 & 0 & 0 & -I \end{bmatrix},$$

$$\mathbb{L}_1^{(2)} = \begin{bmatrix} 0 & 0 & 0 & B_{30} & B_{21} & B_{12} \\ I & 0 & 0 & 0 & 0 & 0 \\ 0 & 0 & 0 & 0 & 0 & 0 \\ 0 & I & 0 & 0 & 0 & 0 \\ 0 & 0 & I & 0 & 0 & 0 \\ 0 & 0 & 0 & 0 & 0 & 0 \end{bmatrix}, \mathbb{L}_2^{(2)} = \begin{bmatrix} 0 & 0 & 0 & 0 & 0 & B_{03} \\ 0 & 0 & 0 & 0 & 0 & 0 \\ I & 0 & 0 & 0 & 0 & 0 \\ 0 & 0 & 0 & 0 & 0 & 0 \\ 0 & 0 & 0 & 0 & 0 & 0 \\ 0 & 0 & I & 0 & 0 & 0 \end{bmatrix}.$$

For the first Equation in (15), consider,

$$\Lambda = \begin{bmatrix} 1 \\ \lambda \\ \mu \\ \lambda^2 \\ \lambda\mu \\ \mu^2 \end{bmatrix}, \text{ and } w_1 = \Lambda \otimes x_1 = \begin{bmatrix} x_1 \\ \lambda x_1 \\ \mu x_1 \\ \lambda^2 x_1 \\ \lambda\mu x_1 \\ \mu^2 x_1 \end{bmatrix}.$$

Thus, x_1 is an eigenvector corresponding to the eigenvalue (λ, μ) of $\mathbb{P}_1(\lambda, \mu)$ from Equation (9) if and only if $w_1 = \Lambda \otimes x_1$ is an eigenvector corresponding to the eigenvalue (λ, μ) of $\mathbb{L}^{(1)}(\lambda, \mu)$ from Equation (10). Now, using the definition 6, we demonstrate that $\mathbb{L}^{(1)}(\lambda, \mu)$ is a linearization of $\mathbb{P}_1(\lambda, \mu)$. For that define

$$\mathcal{N}(\lambda, \mu) = \begin{bmatrix} I_n & 0 & 0 & 0 & 0 & 0 \\ \lambda I_n & 0 & 0 & 0 & 0 & I_n \\ \mu I_n & 0 & 0 & 0 & I_n & 0 \\ \lambda^2 I_n & 0 & 0 & I_n & 0 & 0 \\ \lambda\mu I_n & 0 & I_n & 0 & 0 & 0 \\ \mu^2 I_n & I_n & 0 & 0 & 0 & 0 \end{bmatrix},$$

$$\mathcal{M}(\lambda, \mu) = \begin{bmatrix} I_n & \mathrm{S}_1(\lambda, \mu) & \mathrm{S}_2(\lambda, \mu) & \mathrm{A}_{20} + \lambda \mathrm{A}_{30} & \mathrm{A}_{11} + \lambda \mathrm{A}_{21} & \mathrm{A}_{02} + \lambda \mathrm{A}_{12} + \mu \mathrm{A}_{03} \\ 0 & 0 & \mu I_n & 0 & 0 & -I_n \\ 0 & 0 & \lambda \mathrm{I_n} & 0 & -I_n & 0 \\ 0 & \lambda I_n & 0 & -I_n & 0 & 0 \\ 0 & 0 & -I_n & 0 & 0 & 0 \\ 0 & -I_n & 0 & 0 & 0 & 0 \end{bmatrix},$$

where $S_1(\lambda, \mu) = A_{10} + \lambda A_{20} + \lambda^2 A_{30}$ and $S_2(\lambda, \mu) = A_{01} + \lambda A_{11} + \lambda^2 A_{21} + \mu A_{02} + \lambda\mu A_{12} + \mu^2 A_{03}$. Then we can check that,

$$\mathcal{M}(\lambda, \mu)\mathbb{L}^{(1)}(\lambda, \mu)\mathcal{N}(\lambda, \mu) = \begin{pmatrix} \mathbb{P}_1(\lambda, \mu) & 0 \\ 0 & I_{5n} \end{pmatrix}.$$

Thus, we have det $\mathbb{P}_1(\lambda, \mu) = \alpha$ det $\mathbb{L}^{(1)}(\lambda, \mu)$, for some $\alpha \neq 0$. This indicates that $\mathbb{L}^{(1)}(\lambda, \mu)$ is a llinearization of $\mathbb{P}_1(\lambda, \mu)$ and it preserves the eigenvalues of $\mathbb{P}_1(\lambda, \mu)$. Similarly, we can also check for the second Equation of (15).

Khazanov Linearization

This approach was presented by Khazanov (2007). In this approach, we first write $\mathbb{P}_1(\lambda, \mu)$ as a polynomial in λ.

$$(\lambda^3 A_{30} + \lambda^2(\mu A_{21} + A_{20}) + \lambda(\mu^2 A_{12} + \mu A_{11} + A_{10}) + (\mu^3 A_{03} + \mu^2 A_{02} + \mu A_{01} + A_{00})x_1 = 0. \qquad (16)$$

Now, by using the first companion form, Equation (16) can be linearized as,

$$\left(\lambda \begin{bmatrix} 0 & 0 & A_{30} \\ 0 & I & 0 \\ I & 0 & 0 \end{bmatrix} + \begin{bmatrix} \mu^3 A_{03} + \mu^2 A_{02} + \mu A_{01} + A_{00} & \mu^2 A_{12} + \mu A_{11} + A_{10} & \mu A_{21} + A_{20} \\ 0 & 0 & -I \\ 0 & -I & 0 \end{bmatrix}\right) \begin{bmatrix} x_1 \\ \lambda x_1 \\ \lambda^2 x_1 \end{bmatrix} = 0. \qquad (17)$$

Now, by considering the polynomial in μ, we obtain

$$\left(\mu^3 \begin{bmatrix} A_{03} & 0 & 0 \\ 0 & 0 & 0 \\ 0 & 0 & 0 \end{bmatrix} + \mu^2 \begin{bmatrix} A_{02} & A_{12} & 0 \\ 0 & 0 & 0 \\ 0 & 0 & 0 \end{bmatrix} + \mu \begin{bmatrix} A_{01} & A_{11} & A_{21} \\ 0 & 0 & 0 \\ 0 & 0 & 0 \end{bmatrix} + \begin{bmatrix} A_{00} & A_{10} & \lambda A_{30} + A_{20} \\ 0 & \lambda I & -I \\ \lambda I & -I & 0 \end{bmatrix}\right) \begin{bmatrix} x_1 \\ \lambda x_1 \\ \lambda^2 x_1 \end{bmatrix} = 0. \qquad (18)$$

By using the first companion form for linearization, we have

$$\left(\mu\begin{bmatrix} 0 & 0 & \begin{bmatrix} A_{03} & 0 & 0 \\ 0 & 0 & 0 \\ 0 & 0 & 0 \end{bmatrix} \\ 0 & I_{3n} & 0 \\ I_{3n} & 0 & 0 \end{bmatrix} + \begin{bmatrix} \begin{bmatrix} A_{00} & A_{10} & \lambda A_{30}+A_{20} \\ 0 & \lambda I & -I \\ \lambda I & -I & 0 \end{bmatrix} & \begin{bmatrix} A_{01} & A_{11} & A_{21} \\ 0 & 0 & 0 \\ 0 & 0 & 0 \end{bmatrix} & \begin{bmatrix} A_{02} & A_{12} & 0 \\ 0 & 0 & 0 \\ 0 & 0 & 0 \end{bmatrix} \\ 0 & 0 & -I_{3n} \\ 0 & -I_{3n} & 0 \end{bmatrix}\right)\begin{bmatrix} x_1 \\ \lambda x_1 \\ \lambda^2 x_1 \\ \mu x_1 \\ \lambda\mu x_1 \\ \lambda^2\mu x_1 \\ \mu^2 x_1 \\ \lambda\mu^2 x_1 \\ \lambda^2\mu^2 x_1 \end{bmatrix} = 0, \qquad (19)$$

which can also be rewritten as

$$\left(\mu\begin{bmatrix} 0 & 0 & 0 & 0 & 0 & 0 & A_{03} & 0 & 0 \\ 0 & 0 & 0 & 0 & 0 & 0 & 0 & 0 & 0 \\ 0 & 0 & 0 & 0 & 0 & 0 & 0 & 0 & 0 \\ 0 & 0 & 0 & I_n & 0 & 0 & 0 & 0 & 0 \\ 0 & 0 & 0 & 0 & I_n & 0 & 0 & 0 & 0 \\ 0 & 0 & 0 & 0 & 0 & I_n & 0 & 0 & 0 \\ I_n & 0 & 0 & 0 & 0 & 0 & 0 & 0 & 0 \\ 0 & I_n & 0 & 0 & 0 & 0 & 0 & 0 & 0 \\ 0 & 0 & I_n & 0 & 0 & 0 & 0 & 0 & 0 \end{bmatrix} + \begin{bmatrix} A_{00} & A_{10} & \lambda A_{30}+A_{20} & A_{01} & A_{11} & A_{21} & A_{02} & A_{12} & 0 \\ 0 & \lambda I_n & -I_n & 0 & 0 & 0 & 0 & 0 & 0 \\ \lambda I_n & -I_n & 0 & 0 & 0 & 0 & 0 & 0 & 0 \\ 0 & 0 & 0 & 0 & 0 & 0 & -I_n & 0 & 0 \\ 0 & 0 & 0 & 0 & 0 & 0 & 0 & -I_n & 0 \\ 0 & 0 & 0 & 0 & 0 & 0 & 0 & 0 & -I_n \\ 0 & 0 & 0 & -I_n & 0 & 0 & 0 & 0 & 0 \\ 0 & 0 & 0 & 0 & -I_n & 0 & 0 & 0 & 0 \\ 0 & 0 & 0 & 0 & 0 & -I_n & 0 & 0 & 0 \end{bmatrix}\right)\begin{bmatrix} x_1 \\ \lambda x_1 \\ \lambda^2 x_1 \\ \mu x_1 \\ \lambda\mu x_1 \\ \lambda^2\mu x_1 \\ \mu^2 x_1 \\ \lambda\mu^2 x_1 \\ \lambda^2\mu^2 x_1 \end{bmatrix} = 0. \quad (20)$$

This is equivalent to

$$\lambda\begin{bmatrix} 0 & 0 & A_{30} & 0 & 0 & 0 & 0 & 0 & 0 \\ 0 & I_n & 0 & 0 & 0 & 0 & 0 & 0 & 0 \\ I_n & 0 & 0 & 0 & 0 & 0 & 0 & 0 & 0 \\ 0 & 0 & 0 & 0 & 0 & 0 & 0 & 0 & 0 \\ 0 & 0 & 0 & 0 & 0 & 0 & 0 & 0 & 0 \\ 0 & 0 & 0 & 0 & 0 & 0 & 0 & 0 & 0 \\ 0 & 0 & 0 & 0 & 0 & 0 & 0 & 0 & 0 \\ 0 & 0 & 0 & 0 & 0 & 0 & 0 & 0 & 0 \\ 0 & 0 & 0 & 0 & 0 & 0 & 0 & 0 & 0 \end{bmatrix} + \mu\begin{bmatrix} 0 & 0 & 0 & 0 & 0 & 0 & A_{03} & 0 & 0 \\ 0 & 0 & 0 & 0 & 0 & 0 & 0 & 0 & 0 \\ 0 & 0 & 0 & 0 & 0 & 0 & 0 & 0 & 0 \\ 0 & 0 & 0 & I_n & 0 & 0 & 0 & 0 & 0 \\ 0 & 0 & 0 & 0 & I_n & 0 & 0 & 0 & 0 \\ 0 & 0 & 0 & 0 & 0 & I_n & 0 & 0 & 0 \\ I_n & 0 & 0 & 0 & 0 & 0 & 0 & 0 & 0 \\ 0 & I_n & 0 & 0 & 0 & 0 & 0 & 0 & 0 \\ 0 & 0 & I_n & 0 & 0 & 0 & 0 & 0 & 0 \end{bmatrix}$$

$$+\begin{bmatrix} A_{00} & A_{10} & A_{20} & A_{01} & A_{11} & A_{21} & A_{02} & A_{12} & 0 \\ 0 & 0 & -I_n & 0 & 0 & 0 & 0 & 0 & 0 \\ 0 & -I_n & 0 & 0 & 0 & 0 & 0 & 0 & 0 \\ 0 & 0 & 0 & 0 & 0 & 0 & -I_n & 0 & 0 \\ 0 & 0 & 0 & 0 & 0 & 0 & 0 & -I_n & 0 \\ 0 & 0 & 0 & 0 & 0 & 0 & 0 & 0 & -I_n \\ 0 & 0 & 0 & -I_n & 0 & 0 & 0 & 0 & 0 \\ 0 & 0 & 0 & 0 & -I_n & 0 & 0 & 0 & 0 \\ 0 & 0 & 0 & 0 & 0 & -I_n & 0 & 0 & 0 \end{bmatrix}\begin{bmatrix} x_1 \\ \lambda x_1 \\ \lambda^2 x_1 \\ \mu x_1 \\ \lambda\mu x_1 \\ \lambda^2\mu x_1 \\ \mu^2 x_1 \\ \lambda\mu^2 x_1 \\ \lambda^2\mu^2 x_1 \end{bmatrix} = 0. \qquad (21)$$

This linearization is called Khazanov Linearization. Proceeding similarly for $\mathbb{P}_2(\lambda,\mu)$, the respective linearization can be obtained. In the place of the first companion form of linearizations in Equations (17) and (19), if we use different forms of linearizations, we obtain further linearizations with $9n \times 9n$ matrices. The size of the matrices in the Khazanov linearization in Equation (21) is $9n \times 9n$, which is larger than that of the Standard linearization ($6n \times 6n$). Thus, the Khazanov linearization is numerically less efficient than that of the Standard linearization. Moreover, one can further deduce the standard linearization from the Khazanov linearization of (21).

Linearization Like Method

Consider the $\mathbb{CTEP}$ defined in (9), we introduce the new variables $\alpha = \lambda^3$, $\beta = \lambda^2\mu$, $\gamma = \lambda\mu^2$, $\delta = \mu^3$, $\eta = \lambda^2$, $\nu = \lambda\mu$ and $\sigma = \mu^2$. The $\mathbb{CTEP}$ can be rewritten as a linear $\mathbb{L}9\mathbb{EP}$ as follows:

$$\begin{aligned}
(\alpha A_{30} + \beta A_{21} + \gamma A_{12} + \delta A_{03} + \eta A_{20} + \nu A_{11} + \sigma A_{02} + \lambda A_{10} + \mu A_{01} + A_{00})x_1 &= 0,\\
(\alpha B_{30} + \beta B_{21} + \gamma B_{12} + \delta B_{03} + \eta B_{20} + \nu B_{11} + \sigma B_{02} + \lambda B_{10} + \mu B_{01} + B_{00})x_2 &= 0,\\
\left(\begin{bmatrix}0&0&0\\0&1&0\\0&0&0\end{bmatrix} + \lambda\begin{bmatrix}0&0&-1\\-1&0&0\\0&0&0\end{bmatrix} + \alpha\begin{bmatrix}1&0&0\\0&0&0\\0&0&0\end{bmatrix}\right)\begin{bmatrix}1\\\lambda\\\lambda^2\end{bmatrix} &= 0,\\
\left(\begin{bmatrix}0&0&0\\0&1&0\\0&0&0\end{bmatrix} + \lambda\begin{bmatrix}0&0&0\\-1&0&0\\0&0&0\end{bmatrix} + \mu\begin{bmatrix}0&0&-1\\0&0&0\\0&0&0\end{bmatrix} + \beta\begin{bmatrix}1&0&0\\0&0&0\\0&0&0\end{bmatrix}\right)\begin{bmatrix}1\\\lambda\\\lambda^2\end{bmatrix} &= 0,\\
\left(\begin{bmatrix}0&0&0\\0&1&0\\0&0&0\end{bmatrix} + \lambda\begin{bmatrix}0&0&-1\\0&0&0\\0&0&0\end{bmatrix} + \mu\begin{bmatrix}0&0&0\\-1&0&0\\0&0&0\end{bmatrix} + \beta\begin{bmatrix}1&0&0\\0&0&0\\0&0&0\end{bmatrix}\right)\begin{bmatrix}1\\\mu\\\mu^2\end{bmatrix} &= 0,\\
\left(\begin{bmatrix}0&0&0\\0&1&0\\0&0&0\end{bmatrix} + \mu\begin{bmatrix}0&0&-1\\-1&0&0\\0&0&0\end{bmatrix} + \delta\begin{bmatrix}1&0&0\\0&0&0\\0&0&0\end{bmatrix}\right)\begin{bmatrix}1\\\mu\\\mu^2\end{bmatrix} &= 0,\\
\left(\begin{bmatrix}0&0&0\\0&1&0\\0&0&0\end{bmatrix} + \lambda\begin{bmatrix}0&-1&0\\-1&0&0\\0&0&0\end{bmatrix} + \eta\begin{bmatrix}1&0&0\\0&0&0\\0&0&0\end{bmatrix}\right)\begin{bmatrix}1\\\lambda\\\lambda^2\end{bmatrix} &= 0,\\
\left(\begin{bmatrix}0&0&0\\0&1&0\\0&0&0\end{bmatrix} + \lambda\begin{bmatrix}0&0&0\\-1&0&0\\0&0&0\end{bmatrix} + \mu\begin{bmatrix}0&-1&0\\0&0&0\\0&0&0\end{bmatrix} + \nu\begin{bmatrix}1&0&0\\0&0&0\\0&0&0\end{bmatrix}\right)\begin{bmatrix}1\\\lambda\\\lambda^2\end{bmatrix} &= 0,\\
\left(\begin{bmatrix}0&0&0\\0&1&0\\0&0&0\end{bmatrix} + \mu\begin{bmatrix}0&-1&0\\-1&0&0\\0&0&0\end{bmatrix} + \sigma\begin{bmatrix}1&0&0\\0&0&0\\0&0&0\end{bmatrix}\right)\begin{bmatrix}1\\\mu\\\mu^2\end{bmatrix} &= 0. \quad (22)
\end{aligned}$$

It can be seen that if $\big((\lambda,\mu),\ x_1 \otimes x_2\big)$ is an eigenpair of the $\mathbb{CTEP}$ defined in (9), then

$$\left((\lambda,\mu,\lambda^2,\lambda\mu,\mu^2,\lambda^3,\lambda^2\mu,\lambda\mu^2,\mu^3), x_1 \otimes x_2 \otimes \begin{bmatrix}1\\\lambda\\\lambda^2\end{bmatrix} \otimes \begin{bmatrix}1\\\lambda\\\lambda^2\end{bmatrix} \otimes \begin{bmatrix}1\\\mu\\\mu^2\end{bmatrix} \otimes \begin{bmatrix}1\\\mu\\\mu^2\end{bmatrix} \otimes \begin{bmatrix}1\\\lambda\\\lambda^2\end{bmatrix} \otimes \begin{bmatrix}1\\\lambda\\\lambda^2\end{bmatrix} \otimes \begin{bmatrix}1\\\mu\\\mu^2\end{bmatrix}\right)$$

is an eigenpair of (22). For $\mathbb{L}9\mathbb{EP}$, the associated system of $\mathbb{GEP}$ becomes $\Delta_j u = \lambda_j \Delta_0 u;\ \ j := 1, \ldots, 9$ (Atkinson, 1972). Khazanov linearization and the Standard linearization produce a singular $\mathbb{L}2\mathbb{EP}$. On the other hand, the linearization method produces a nonsingular $\mathbb{L}9\mathbb{EP}$, which can be shown by the following lemma.

Lemma 8. The homogeneous version of the nine-parameter problem defined in (22) is nonsingular.

Proof. We consider,

$$\lambda = \frac{\tilde{\lambda}}{\tilde{\kappa}}, \mu = \frac{\tilde{\mu}}{\tilde{\kappa}}, \gamma = \frac{\tilde{\gamma}}{\tilde{\kappa}}, \delta = \frac{\tilde{\delta}}{\tilde{\kappa}}, \eta = \frac{\tilde{\eta}}{\tilde{\kappa}}, \nu = \frac{\tilde{\nu}}{\tilde{\kappa}}, \sigma = \frac{\tilde{\sigma}}{\tilde{\kappa}}$$

Multiplying each Equation of (22) by $\tilde{\kappa}$, the homogeneous version of the problem is obtained as,

$$\begin{aligned}
\det\big(\tilde{\alpha}A_{30} + \tilde{\beta}A_{21} + \tilde{\gamma}A_{12} + \tilde{\delta}A_{03} + \tilde{\eta}A_{20} + \tilde{\nu}A_{11} + \tilde{\sigma}A_{02} + \tilde{\lambda}A_{10} + \tilde{\mu}A_{01} + \tilde{\kappa}A_{00}\big) &= 0,\\
\det\big(\tilde{\alpha}B_{30} + \tilde{\beta}B_{21} + \tilde{\gamma}B_{12} + \tilde{\delta}B_{03} + \tilde{\eta}B_{20} + \tilde{\nu}B_{11} + \tilde{\sigma}B_{02} + \tilde{\lambda}B_{10} + \tilde{\mu}B_{01} + \tilde{\kappa}B_{00}\big) &= 0,\\
\tilde{\alpha}\tilde{\kappa} - \widetilde{\lambda^3} &= 0,\\
\tilde{\beta}\tilde{\kappa} - \widetilde{\lambda^2}\tilde{\mu} &= 0,\\
\tilde{\gamma}\tilde{\kappa} - \tilde{\lambda}\widetilde{\mu^2} &= 0,\\
\tilde{\delta}\tilde{\kappa} - \widetilde{\mu^3} &= 0,\\
\tilde{\eta}\tilde{\kappa} - \widetilde{\lambda^2} &= 0,\\
\tilde{\nu}\tilde{\kappa} - \tilde{\lambda}\tilde{\mu} &= 0,\\
\tilde{\sigma}\tilde{\kappa} - \widetilde{\mu^2} &= 0. \qquad (23)
\end{aligned}$$

Now consider $(\tilde{\kappa}, \tilde{\lambda}, \tilde{\mu}, \tilde{\alpha}, \tilde{\beta}, \tilde{\gamma}, \tilde{\delta}, \tilde{\eta}, \tilde{\nu}, \tilde{\sigma})$ to be an eigenvalue of (23) such that $\tilde{\alpha} = 0$. Then, the equations defined in (23) transform into

$$\begin{aligned}
\det\big(\tilde{\beta} A_{21} + \tilde{\gamma} A_{12} + \tilde{\delta} A_{03} + \tilde{\eta} A_{20} + \tilde{\nu} A_{11} + \tilde{\sigma} A_{02} + \tilde{\lambda} A_{10} + \tilde{\mu} A_{01} + \tilde{\kappa} A_{00}\big) &= 0, \\
\det\big(\tilde{\beta} B_{21} + \tilde{\gamma} B_{12} + \tilde{\delta} B_{03} + \tilde{\eta} B_{20} + \tilde{\nu} B_{11} + \tilde{\sigma} B_{02} + \tilde{\lambda} B_{10} + \tilde{\mu} B_{01} + \tilde{\kappa} B_{00}\big) &= 0, \\
-\widetilde{\lambda^3} &= 0, \\
\tilde{\beta}\tilde{\kappa} - \widetilde{\lambda^2}\tilde{\mu} &= 0, \\
\tilde{\gamma}\tilde{\kappa} - \tilde{\lambda}\widetilde{\mu^2} &= 0, \\
\tilde{\delta}\tilde{\kappa} - \widetilde{\mu^3} &= 0, \\
\tilde{\eta}\tilde{\kappa} - \widetilde{\lambda^2} &= 0, \\
\tilde{\nu}\tilde{\kappa} - \tilde{\lambda}\tilde{\mu} &= 0, \\
\tilde{\sigma}\tilde{\kappa} - \widetilde{\mu^2} &= 0.
\end{aligned} \tag{24}$$

From the third Equation, we have $\tilde{\lambda} = 0$. After substituting its value in the subsequent equations of (24) we obtain

$$\tilde{\beta}\tilde{\kappa} = 0,\ \tilde{\gamma}\tilde{\kappa} = 0,\ \tilde{\delta}\tilde{\kappa} = \mu^3,\ \tilde{\eta}\tilde{\kappa} = 0,\ \tilde{\nu}\tilde{\kappa} = 0,\ \tilde{\sigma}\tilde{\kappa} = \mu^2.$$

For all of these conditions, two cases may arise.

3. If $\tilde{\kappa} = 0$, then the sixth and the last Equation in (24) give $\mu = 0$. Thus, the remaining equations become,

$$\begin{aligned}
\det\big(\tilde{\beta} A_{21} + \tilde{\gamma} A_{12} + \tilde{\delta} A_{03} + \tilde{\eta} A_{20} + \tilde{\nu} A_{11} + \tilde{\sigma} A_{02}\big) &= 0, \\
\det\big(\tilde{\beta} B_{21} + \tilde{\gamma} B_{12} + \tilde{\delta} B_{03} + \tilde{\eta} B_{20} + \tilde{\nu} B_{11} + \tilde{\sigma} B_{02}\big) &= 0,
\end{aligned}$$

   which has no solution in the general case.

4. If $\tilde{\kappa} \neq 0$, then for each of the above conditions, we obtain

$$\tilde{\beta} = 0,\ \tilde{\gamma} = 0,\ \tilde{\delta} = \frac{\widetilde{\mu^3}}{\tilde{\kappa}},\ \tilde{\eta} = 0,\ \tilde{\nu} = 0,\ \tilde{\sigma} = \frac{\widetilde{\mu^2}}{\tilde{\kappa}}.$$

   Considering the value of δ, we obtain the above system (24) as follows,

$$\begin{aligned}
\det\Big(\frac{\widetilde{\mu^3}}{\tilde{\kappa}} A_{03} + \frac{\widetilde{\mu^2}}{\tilde{\kappa}} A_{02} + \frac{\tilde{\mu}}{\tilde{\kappa}} A_{01} + A_{00}\Big) &= 0 \\
\det\Big(\frac{\widetilde{\mu^3}}{\tilde{\kappa}} B_{03} + \frac{\widetilde{\mu^2}}{\tilde{\kappa}} B_{02} + \frac{\tilde{\mu}}{\tilde{\kappa}} B_{01} + B_{00}\Big) &= 0
\end{aligned}$$

This has no solutions in general. Thus, the problem defined in Equation (22) does not have an eigenvalue with $\alpha = 0$. It follows Theorem 3, where the operator matrix Δ_3 is nonsingular. Similarly, the operator matrices Δ_i for $i = 4, \ldots, 9$ are nonsingular. ☐

5. Ranks of Delta Matrices

In Muhič & Plestenjak (2010), the Kronecker structures for the Delta matrices of the $\mathbb{QTEP}$ have been discussed extensively to prove the similarity between the eigenvalues of the linearized form and the original nonlinear form. Due to the complex Kronecker structures for the standard linearization (15) of $\mathbb{CTEP}$ defined in (9), they did not attempt to prove their ranks and related theory. The ranks of the Delta matrices will help us discover interesting structures and prove the singularity of the $\mathbb{L}2\mathbb{EP}$ defined in (15). These results can be viewed as a continuing series of proofs demonstrating that, in accordance with Theorem 17 in Muhič & Plestenjak (2010), the eigenvalues of (15) and (9) are identical.

Determining the rank of Delta matrices is crucial to understanding the nature and number of eigenvalues. Through rank determination, we show that all linear combinations of the corresponding operator determinants are singular. When determining the ranks of the Delta matrices, it is more straightforward to work with the Tracy-Singh product rather than the Kronecker product, as demonstrated by Definitions 2, 3, and 4.

Finding the rank of Δ_0

Consider the operator determinant $\varDelta_0$ defined in (11). The structures of sub-matrices of $\varDelta_0$ become

$$\mathbb{L}_0^{(1)}=\begin{bmatrix} A_{00} & A_{10} & A_{01} & A_{20} & A_{11} & A_{02}\\ 0 & -I & 0 & 0 & 0 & 0\\ 0 & 0 & -I & 0 & 0 & 0\\ 0 & 0 & 0 & -I & 0 & 0\\ 0 & 0 & 0 & 0 & -I & 0\\ 0 & 0 & 0 & 0 & 0 & -I \end{bmatrix},\quad \mathbb{L}_1^{(1)}=\begin{bmatrix} 0 & 0 & 0 & A_{30} & A_{21} & A_{12}\\ I & 0 & 0 & 0 & 0 & 0\\ 0 & 0 & 0 & 0 & 0 & 0\\ 0 & I & 0 & 0 & 0 & 0\\ 0 & 0 & I & 0 & 0 & 0\\ 0 & 0 & 0 & 0 & 0 & 0 \end{bmatrix},$$

$$\mathbb{L}_2^{(1)}=\begin{bmatrix} 0 & 0 & 0 & 0 & 0 & A_{03}\\ 0 & 0 & 0 & 0 & 0 & 0\\ I & 0 & 0 & 0 & 0 & 0\\ 0 & 0 & 0 & 0 & 0 & 0\\ 0 & 0 & 0 & 0 & 0 & 0\\ 0 & 0 & I & 0 & 0 & 0 \end{bmatrix},\mathbb{L}_0^{(2)}=\begin{bmatrix} B_{00} & B_{10} & B_{01} & B_{20} & B_{11} & B_{02}\\ 0 & -I & 0 & 0 & 0 & 0\\ 0 & 0 & -I & 0 & 0 & 0\\ 0 & 0 & 0 & -I & 0 & 0\\ 0 & 0 & 0 & 0 & -I & 0\\ 0 & 0 & 0 & 0 & 0 & -I \end{bmatrix},$$

$$\mathbb{L}_1^{(2)}=\begin{bmatrix} 0 & 0 & 0 & B_{30} & B_{21} & B_{12}\\ I & 0 & 0 & 0 & 0 & 0\\ 0 & 0 & 0 & 0 & 0 & 0\\ 0 & I & 0 & 0 & 0 & 0\\ 0 & 0 & I & 0 & 0 & 0\\ 0 & 0 & 0 & 0 & 0 & 0 \end{bmatrix},\mathbb{L}_2^{(2)}=\begin{bmatrix} 0 & 0 & 0 & 0 & 0 & B_{03}\\ 0 & 0 & 0 & 0 & 0 & 0\\ I & 0 & 0 & 0 & 0 & 0\\ 0 & 0 & 0 & 0 & 0 & 0\\ 0 & 0 & 0 & 0 & 0 & 0\\ 0 & 0 & I & 0 & 0 & 0 \end{bmatrix}.$$

If we apply the Tracy-Singh reordering to $\varDelta_0$, we obtain

$$TSR(\varDelta_0)=\begin{bmatrix} 0 & S\\ T & 0 \end{bmatrix},$$

where $S\in\mathbb{C}^{6n^2\times 18n^2}$ and $T\in\mathbb{C}^{30n^2\times 18n^2}$. The block structure representation of S is found to be of the form $S=[A\quad B\quad C]$; where

$$A=\begin{bmatrix} 0 & 0 & 0 & 0 & 0 & A_{30}\otimes B_{03}\\ 0 & 0 & 0 & 0 & 0 & 0\\ A_{30}\otimes I & 0 & 0 & 0 & 0 & 0\\ 0 & 0 & 0 & 0 & 0 & 0\\ 0 & 0 & 0 & 0 & 0 & 0\\ 0 & 0 & A_{30}\otimes I & 0 & 0 & 0 \end{bmatrix},$$

$$B=\begin{bmatrix} 0 & 0 & 0 & 0 & 0 & A_{21}\otimes B_{03}\\ 0 & 0 & 0 & 0 & 0 & 0\\ A_{21}\otimes I & 0 & 0 & 0 & 0 & 0\\ 0 & 0 & 0 & 0 & 0 & 0\\ 0 & 0 & 0 & 0 & 0 & 0\\ 0 & 0 & A_{21}\otimes I & 0 & 0 & 0 \end{bmatrix},$$

$$C=\begin{bmatrix} 0 & 0 & 0 & -A_{03}\otimes B_{30} & -A_{03}\otimes B_{21} & A_{12}\otimes B_{03}-A_{03}\otimes B_{12}\\ -A_{03}\otimes I & 0 & 0 & 0 & 0 & 0\\ A_{12}\otimes I & 0 & 0 & 0 & 0 & 0\\ 0 & -A_{03}\otimes I & 0 & 0 & 0 & 0\\ 0 & 0 & -A_{03}\otimes I & 0 & 0 & 0\\ 0 & 0 & A_{12}\otimes I & 0 & 0 & 0 \end{bmatrix}$$

Similarly, the block representation of T can be determined as

$$T=\begin{bmatrix} D & 0 & 0\\ E & 0 & 0\\ 0 & F & 0\\ 0 & 0 & G\\ 0 & 0 & H \end{bmatrix},$$

where $D=\begin{bmatrix} 0 & 0 & 0 & 0 & 0 & I\otimes B_{03}\\ 0 & 0 & 0 & 0 & 0 & 0\\ I\otimes I & 0 & 0 & 0 & 0 & 0\\ 0 & 0 & 0 & 0 & 0 & 0\\ 0 & 0 & 0 & 0 & 0 & 0\\ 0 & 0 & I\otimes I & 0 & 0 & 0 \end{bmatrix},$

$$E=\begin{bmatrix}0&0&0&-I\otimes B_{30}&-I\otimes B_{21}&-I\otimes B_{12}\\-I\otimes I&0&0&0&0&0\\0&0&0&0&0&0\\0&-I\otimes I&0&0&0&0\\0&0&-I\otimes I&0&0&0\\0&0&0&0&0&0\end{bmatrix},$$

$$F=\begin{bmatrix}0&0&0&0&0&I\otimes B_{03}\\0&0&0&0&0&0\\I\otimes I&0&0&0&0&0\\0&0&0&0&0&0\\0&0&0&0&0&0\\0&0&I\otimes I&0&0&0\end{bmatrix},$$

$$G=\begin{bmatrix}0&0&0&0&0&I\otimes B_{03}\\0&0&0&0&0&0\\I\otimes I&0&0&0&0&0\\0&0&0&0&0&0\\0&0&0&0&0&0\\0&0&I\otimes I&0&0&0\end{bmatrix},$$

$$H=\begin{bmatrix}0&0&0&-I\otimes B_{30}&-I\otimes B_{21}&-I\otimes B_{12}\\-I\otimes I&0&0&0&0&0\\0&0&0&0&0&0\\0&-I\otimes I&0&0&0&0\\0&0&-I\otimes I&0&0&0\\0&0&0&0&0&0\end{bmatrix}.$$

Considering the matrices $A_{03}, A_{30}, A_{12}, A_{21}, B_{30}$ and B_{03}as nonsingular, we conclude that the rank of S is $6n^2$ and the rank of T is$14n^2$. Thus, the rank of Δ_0 can be found as $20n^2 < 36n^2$.

Since Δ_0 is singular, the associated $\mathbb{L}2\mathbb{EP}$ defined in (15) is also singular. Using a similar technique, the singularity of Khazanov linearization can be proven as well.

Finding the rank of Δ_1

Consider a related problem

$$\mathbb{P}_1'(\lambda,\mu)=A_{00}+\mu A_{01}+\mu^2A_{02}+\mu^3A_{03},$$

$$\mathbb{P}_2'(\lambda,\mu)=\mathbb{P}_2(\lambda,\mu)=\lambda^3B_{30}+\lambda^2\mu B_{21}+\lambda\mu^2B_{12}+\mu^3B_{03}+\lambda^2B_{20}+\lambda\mu B_{11}+\mu^2B_{02}+\lambda B_{10}+\mu B_{01}+B_{00}\quad(25)$$

By linearizing $\mathbb{P}_1'(\lambda,\mu)$, we get

$$L_1'(\lambda,\mu)=\begin{bmatrix}A_{00}&A_{01}&A_{02}\\0&0&-I\\0&-I&0\end{bmatrix}+\mu\begin{bmatrix}0&0&A_{03}\\0&I&0\\I&0&0\end{bmatrix}.$$

$\mathbb{P}_2'(\lambda,\mu)$ is linearized as in $\mathbb{P}_2(\lambda,\mu)$.

$$L_2'(\lambda,\mu)=\begin{bmatrix}B_{00}&B_{10}&B_{01}&B_{20}&B_{11}&B_{02}\\0&-I&0&0&0&0\\0&0&-I&0&0&0\\0&0&0&-I&0&0\\0&0&0&0&-I&0\\0&0&0&0&0&-I\end{bmatrix}+\lambda\begin{bmatrix}0&0&0&B_{30}&B_{21}&B_{12}\\I&0&0&0&0&0\\0&0&0&0&0&0\\0&I&0&0&0&0\\0&0&I&0&0&0\\0&0&0&0&0&0\end{bmatrix}+\mu\begin{bmatrix}0&0&0&0&0&B_{03}\\0&0&0&0&0&0\\I&0&0&0&0&0\\0&0&0&0&0&0\\0&0&0&0&0&0\\0&0&I&0&0&0\end{bmatrix}$$

Now, these two linearizations can be rewritten in the form of (10), where the coefficient matrices are

$$\mathbb{L}_0^{(1)}=\begin{bmatrix}A_{00}&A_{01}&A_{02}\\0&0&-I\\0&-I&0\end{bmatrix},\quad\mathbb{L}_1^{(1)}=0,\quad\mathbb{L}_2^{(1)}=\begin{bmatrix}0&0&A_{03}\\0&I&0\\I&0&0\end{bmatrix}$$

and

$$\mathbb{L}_0^{(2)}=\begin{bmatrix}B_{00}&B_{10}&B_{01}&B_{20}&B_{11}&B_{02}\\0&-I&0&0&0&0\\0&0&-I&0&0&0\\0&0&0&-I&0&0\\0&0&0&0&-I&0\\0&0&0&0&0&-I\end{bmatrix},\quad\mathbb{L}_1^{(2)}=\begin{bmatrix}0&0&0&B_{30}&B_{21}&B_{12}\\I&0&0&0&0&0\\0&0&0&0&0&0\\0&I&0&0&0&0\\0&0&I&0&0&0\\0&0&0&0&0&0\end{bmatrix}$$

$$\mathbb{L}_2^{(2)} = \begin{bmatrix} 0 & 0 & 0 & 0 & 0 & B_{03} \\ 0 & 0 & 0 & 0 & 0 & 0 \\ I & 0 & 0 & 0 & 0 & 0 \\ 0 & 0 & 0 & 0 & 0 & 0 \\ 0 & 0 & 0 & 0 & 0 & 0 \\ 0 & 0 & I & 0 & 0 & 0 \end{bmatrix}.$$

Then,

$$\Delta_1' = \mathbb{L}_2^{(1)} \otimes \mathbb{L}_0^{(2)} - \mathbb{L}_0^{(1)} \otimes \mathbb{L}_2^{(2)}.$$

This shows that Δ_1' is non-singular.

Let Δ_1' be singular. By Theorem 6, the system (10) has an eigenvalue $(\eta_0, 0, \eta_2)$ such that $(\eta_0, \eta_2) \neq (0,0)$. As in the general case, $\mathbb{L}_2^{(2)}$ is nonsingular, so $\eta_0 \neq 0$, which indicates that the original problem has an eigenvalue of the form $(0, \mu)$. Therefore, Δ_1' has to be nonsingular.

By the Tracy-Singh product of Δ_1, we have

$$TSP(\Delta_1) = \begin{bmatrix} S_{11} & S_{12} & S_{13} & S_{14} & S_{15} & S_{16} \\ 0 & S_{22} & 0 & 0 & 0 & 0 \\ S_{31} & 0 & S_{33} & 0 & 0 & 0 \\ 0 & 0 & 0 & S_{44} & 0 & 0 \\ 0 & 0 & 0 & 0 & S_{55} & 0 \\ 0 & 0 & S_{63} & 0 & 0 & S_{66} \end{bmatrix};$$

where

$$S_{11} = \begin{bmatrix} 0 & 0 & 0 & 0 & 0 & -A_{00} \otimes B_{03} \\ 0 & 0 & 0 & 0 & 0 & 0 \\ -A_{00} \otimes I & 0 & 0 & 0 & 0 & 0 \\ 0 & 0 & 0 & 0 & 0 & 0 \\ 0 & 0 & 0 & 0 & 0 & 0 \\ 0 & 0 & -A_{00} \otimes I & 0 & 0 & 0 \end{bmatrix},$$

$$S_{12} = \begin{bmatrix} 0 & 0 & 0 & 0 & 0 & -A_{10} \otimes B_{03} \\ 0 & 0 & 0 & 0 & 0 & 0 \\ -A_{10} \otimes I & 0 & 0 & 0 & 0 & 0 \\ 0 & 0 & 0 & 0 & 0 & 0 \\ 0 & 0 & 0 & 0 & 0 & 0 \\ 0 & 0 & -A_{10} \otimes I & 0 & 0 & 0 \end{bmatrix},$$

$$S_{13} = \begin{bmatrix} 0 & 0 & 0 & 0 & 0 & -A_{01} \otimes B_{03} \\ 0 & 0 & 0 & 0 & 0 & 0 \\ -A_{01} \otimes I & 0 & 0 & 0 & 0 & 0 \\ 0 & 0 & 0 & 0 & 0 & 0 \\ 0 & 0 & 0 & 0 & 0 & 0 \\ 0 & 0 & -A_{01} \otimes I & 0 & 0 & 0 \end{bmatrix},$$

$$S_{14} = \begin{bmatrix} 0 & 0 & 0 & 0 & 0 & -A_{20} \otimes B_{03} \\ 0 & 0 & 0 & 0 & 0 & 0 \\ -A_{20} \otimes I & 0 & 0 & 0 & 0 & 0 \\ 0 & 0 & 0 & 0 & 0 & 0 \\ 0 & 0 & 0 & 0 & 0 & 0 \\ 0 & 0 & -A_{20} \otimes I & 0 & 0 & 0 \end{bmatrix},$$

$$S_{15} = \begin{bmatrix} 0 & 0 & 0 & 0 & 0 & -A_{11} \otimes B_{03} \\ 0 & 0 & 0 & 0 & 0 & 0 \\ -A_{11} \otimes I & 0 & 0 & 0 & 0 & 0 \\ 0 & 0 & 0 & 0 & 0 & 0 \\ 0 & 0 & 0 & 0 & 0 & 0 \\ 0 & 0 & -A_{11} \otimes I & 0 & 0 & 0 \end{bmatrix},$$

$$S_{16}=\begin{bmatrix} A_{03}\otimes B_{00} & A_{03}\otimes B_{10} & A_{03}\otimes B_{01} & A_{03}\otimes B_{20} & A_{03}\otimes B_{11} & A_{03}\otimes B_{02}-A_{02}\otimes B_{03}\\ 0 & -A_{03}\otimes I & 0 & 0 & 0 & 0\\ -A_{02}\otimes I & 0 & -A_{03}\otimes I & 0 & 0 & 0\\ 0 & 0 & 0 & -A_{03}\otimes I & 0 & 0\\ 0 & 0 & 0 & 0 & -A_{03}\otimes I & 0\\ 0 & 0 & -A_{02}\otimes I & 0 & 0 & -A_{03}\otimes I \end{bmatrix},$$

$$S_{31}=S_{63}=\begin{bmatrix} I\otimes B_{00} & I\otimes B_{10} & I\otimes B_{01} & I\otimes B_{20} & I\otimes B_{11} & I\otimes B_{02}\\ 0 & -I\otimes I & 0 & 0 & 0 & 0\\ 0 & 0 & -I\otimes I & 0 & 0 & 0\\ 0 & 0 & 0 & -I\otimes I & 0 & 0\\ 0 & 0 & 0 & 0 & -I\otimes I & 0\\ 0 & 0 & 0 & 0 & 0 & -I\otimes I \end{bmatrix},$$

$$S_{22}=S_{33}=S_{44}=S_{55}=S_{66}=\begin{bmatrix} 0 & 0 & 0 & 0 & 0 & I\otimes B_{03}\\ 0 & 0 & 0 & 0 & 0 & 0\\ I\otimes I & 0 & 0 & 0 & 0 & 0\\ 0 & 0 & 0 & 0 & 0 & 0\\ 0 & 0 & 0 & 0 & 0 & 0\\ 0 & 0 & I\otimes I & 0 & 0 & 0 \end{bmatrix}.$$

Now, by the Tracy-Singh reordering of Δ_1', we obtain

$$TSR(\Delta_1')=\begin{pmatrix} S_{11} & S_{13} & S_{16}\\ S_{31} & S_{33} & S_{36}\\ S_{61} & S_{63} & S_{66} \end{pmatrix}.$$

If we perform Tracy-Singh reordering in Δ_1, then we have

$$TSR(\Delta_1)=\begin{bmatrix} S_{11} & S_{13} & S_{16} & S_{14} & S_{15} & S_{12}\\ S_{31} & S_{33} & 0 & 0 & 0 & 0\\ 0 & S_{63} & S_{66} & 0 & 0 & 0\\ 0 & 0 & 0 & S_{44} & 0 & 0\\ 0 & 0 & 0 & 0 & S_{55} & 0\\ 0 & 0 & 0 & 0 & 0 & S_{22} \end{bmatrix}.$$

Since $TSR(\Delta_1')$ is nonsingular, the remaining diagonal block entries S_{22}, S_{44}, and $S_{55}$of $TSR(\Delta_1)$ yield a maximal rank $9n^2$, assuming B_{03} is nonsingular. Thus, this shows that the matrix Δ_1 is of rank $27n^2$.

Finding the rank of Δ_2

Consider a related problem, where

$\mathbb{P}_1'(\lambda,\mu)=A_{00}+\lambda A_{10}+\lambda^2A_{20}+\lambda^3A_{30}$,

$\mathbb{P}_2'(\lambda,\mu)=\mathbb{P}_1(\lambda,\mu)=\lambda^3B_{30}+\lambda^2\mu B_{21}+\lambda\mu^2B_{12}+\mu^3B_{03}+\lambda^2B_{20}+\lambda\mu B_{11}+\mu^2B_{02}+\lambda B_{10}+\mu B_{01}+B_{00}$ (26)

By linearizing $\mathbb{P}_1'(\lambda,\mu)$, we obtain

$$L_1'(\lambda,\mu)=\begin{bmatrix} A_{00} & A_{10} & A_{20}\\ 0 & 0 & -I\\ 0 & -I & 0 \end{bmatrix}+\lambda\begin{bmatrix} 0 & 0 & A_{30}\\ 0 & I & 0\\ I & 0 & 0 \end{bmatrix}.$$

$\mathbb{P}_2'(\lambda,\mu)$ is linearized as in $\mathbb{P}_2(\lambda,\mu)$.

$$L_2'(\lambda,\mu)=\begin{bmatrix} B_{00} & B_{10} & B_{01} & B_{20} & B_{11} & B_{02}\\ 0 & -I & 0 & 0 & 0 & 0\\ 0 & 0 & -I & 0 & 0 & 0\\ 0 & 0 & 0 & -I & 0 & 0\\ 0 & 0 & 0 & 0 & -I & 0\\ 0 & 0 & 0 & 0 & 0 & -I \end{bmatrix}+\lambda\begin{bmatrix} 0 & 0 & 0 & B_{30} & B_{21} & B_{12}\\ I & 0 & 0 & 0 & 0 & 0\\ 0 & 0 & 0 & 0 & 0 & 0\\ 0 & I & 0 & 0 & 0 & 0\\ 0 & 0 & I & 0 & 0 & 0\\ 0 & 0 & 0 & 0 & 0 & 0 \end{bmatrix}+\mu\begin{bmatrix} 0 & 0 & 0 & 0 & 0 & B_{03}\\ 0 & 0 & 0 & 0 & 0 & 0\\ I & 0 & 0 & 0 & 0 & 0\\ 0 & 0 & 0 & 0 & 0 & 0\\ 0 & 0 & 0 & 0 & 0 & 0\\ 0 & 0 & I & 0 & 0 & 0 \end{bmatrix}.$$

Now, these two linearizations can be rewritten in the form of (10), where the coefficient matrices become

$$\mathbb{L}_0^{(1)}=\begin{bmatrix} A_{00} & A_{10} & A_{20}\\ 0 & 0 & -I\\ 0 & -I & 0 \end{bmatrix},\quad \mathbb{L}_1^{(1)}=\begin{bmatrix} 0 & 0 & A_{30}\\ 0 & I & 0\\ I & 0 & 0 \end{bmatrix},\quad \mathbb{L}_2^{(1)}=0,$$

and

$$\mathbb{L}_0^{(2)} = \begin{bmatrix} B_{00} & B_{10} & B_{01} & B_{20} & B_{11} & B_{02} \\ 0 & -I & 0 & 0 & 0 & 0 \\ 0 & 0 & -I & 0 & 0 & 0 \\ 0 & 0 & 0 & -I & 0 & 0 \\ 0 & 0 & 0 & 0 & -I & 0 \\ 0 & 0 & 0 & 0 & 0 & -I \end{bmatrix}, \quad \mathbb{L}_1^{(2)} = \begin{bmatrix} 0 & 0 & 0 & B_{30} & B_{21} & B_{12} \\ I & 0 & 0 & 0 & 0 & 0 \\ 0 & 0 & 0 & 0 & 0 & 0 \\ 0 & I & 0 & 0 & 0 & 0 \\ 0 & 0 & I & 0 & 0 & 0 \\ 0 & 0 & 0 & 0 & 0 & 0 \end{bmatrix}$$

$$\mathbb{L}_2^{(2)} = \begin{bmatrix} 0 & 0 & 0 & 0 & 0 & B_{03} \\ 0 & 0 & 0 & 0 & 0 & 0 \\ I & 0 & 0 & 0 & 0 & 0 \\ 0 & 0 & 0 & 0 & 0 & 0 \\ 0 & 0 & 0 & 0 & 0 & 0 \\ 0 & 0 & I & 0 & 0 & 0 \end{bmatrix}.$$

Then,

$$\Delta_2' = \mathbb{L}_0^{(1)} \otimes \mathbb{L}_1^{(2)} - \mathbb{L}_1^{(1)} \otimes \mathbb{L}_0^{(2)}.$$

We claim that Δ_2' of the related problem is nonsingular.

Let us consider Δ_2' to be singular. By Theorem 6, the related system (10) has an eigenvalue $(\eta_0, \eta_1, 0)$ such that $(\eta_0, \eta_1) \neq (0,0)$. As in the general case, the matrix $\mathbb{L}_1^{(2)}$ is nonsingular, so $\eta_0 \neq 0$, which indicates that the original problem has an eigenvalue of the form $(\lambda, 0)$. So Δ_2' must be nonsingular.
By the Tracy-Singh product of Δ_2, we have,

$$TSP(\Delta_2) = \begin{bmatrix} S_{11} & S_{12} & S_{13} & S_{14} & S_{15} & S_{16} \\ S_{21} & S_{22} & 0 & 0 & 0 & 0 \\ 0 & 0 & S_{33} & 0 & 0 & 0 \\ 0 & S_{42} & 0 & S_{44} & 0 & 0 \\ 0 & 0 & S_{53} & 0 & S_{55} & 0 \\ 0 & 0 & 0 & 0 & 0 & S_{66} \end{bmatrix},$$

where

$$S_{11} = \begin{bmatrix} 0 & 0 & 0 & A_{00} \otimes B_{30} & A_{00} \otimes B_{21} & A_{00} \otimes B_{12} \\ A_{00} \otimes I & 0 & 0 & 0 & 0 & 0 \\ 0 & 0 & 0 & 0 & 0 & 0 \\ 0 & A_{00} \otimes I & 0 & 0 & 0 & 0 \\ 0 & 0 & A_{00} \otimes I & 0 & 0 & 0 \\ 0 & 0 & 0 & 0 & 0 & 0 \end{bmatrix},$$

$$S_{12} = \begin{bmatrix} 0 & 0 & 0 & A_{10} \otimes B_{30} & A_{10} \otimes B_{21} & A_{10} \otimes B_{12} \\ A_{10} \otimes I & 0 & 0 & 0 & 0 & 0 \\ 0 & 0 & 0 & 0 & 0 & 0 \\ 0 & A_{10} \otimes I & 0 & 0 & 0 & 0 \\ 0 & 0 & A_{10} \otimes I & 0 & 0 & 0 \\ 0 & 0 & 0 & 0 & 0 & 0 \end{bmatrix},$$

$$S_{13} = \begin{bmatrix} 0 & 0 & 0 & A_{01} \otimes B_{30} & A_{01} \otimes B_{21} & A_{01} \otimes B_{12} \\ A_{01} \otimes I & 0 & 0 & 0 & 0 & 0 \\ 0 & 0 & 0 & 0 & 0 & 0 \\ 0 & A_{01} \otimes I & 0 & 0 & 0 & 0 \\ 0 & 0 & A_{01} \otimes I & 0 & 0 & 0 \\ 0 & 0 & 0 & 0 & 0 & 0 \end{bmatrix},$$

$$S_{14} = \begin{bmatrix} -A_{30} \otimes B_{00} & -A_{30} \otimes B_{10} & -A_{30} \otimes B_{01} & A_{20} \otimes B_{30} - A_{30} \otimes B_{20} & A_{20} \otimes B_{21} - A_{30} \otimes B_{11} & A_{20} \otimes B_{12} - A_{30} \otimes B_{02} \\ A_{20} \otimes I & A_{30} \otimes I & 0 & 0 & 0 & 0 \\ 0 & 0 & A_{30} \otimes I & 0 & 0 & 0 \\ 0 & A_{20} \otimes I & 0 & A_{30} \otimes I & 0 & 0 \\ 0 & 0 & A_{20} \otimes I & 0 & A_{30} \otimes I & 0 \\ 0 & 0 & 0 & 0 & 0 & A_{30} \otimes I \end{bmatrix},$$

$$S_{15} = \begin{bmatrix} -A_{21} \otimes B_{00} & -A_{21} \otimes B_{10} & -A_{21} \otimes B_{01} & A_{11} \otimes B_{21} - A_{30} \otimes B_{20} & A_{11} \otimes B_{21} - A_{21} \otimes B_{11} & A_{11} \otimes B_{12} - A_{21} \otimes B_{02} \\ A_{11} \otimes I & A_{21} \otimes I & 0 & 0 & 0 & 0 \\ 0 & 0 & A_{21} \otimes I & 0 & 0 & 0 \\ 0 & A_{11} \otimes I & 0 & A_{21} \otimes I & 0 & 0 \\ 0 & 0 & A_{11} \otimes I & 0 & A_{21} \otimes I & 0 \\ 0 & 0 & 0 & 0 & 0 & A_{21} \otimes I \end{bmatrix},$$

$$S_{16} = \begin{bmatrix} -A_{12}\otimes B_{00} & -A_{12}\otimes B_{10} & -A_{12}\otimes B_{01} & A_{02}\otimes B_{21} - A_{30}\otimes B_{20} & A_{02}\otimes B_{21} - A_{12}\otimes B_{11} & A_{02}\otimes B_{12} - A_{12}\otimes B_{02} \\ A_{02}\otimes I & A_{12}\otimes I & 0 & 0 & 0 & 0 \\ 0 & 0 & A_{12}\otimes I & 0 & 0 & 0 \\ 0 & A_{02}\otimes I & 0 & A_{12}\otimes I & 0 & 0 \\ 0 & 0 & A_{02}\otimes I & 0 & A_{12}\otimes I & 0 \\ 0 & 0 & 0 & 0 & 0 & A_{12}\otimes I \end{bmatrix},$$

$$S_{21} = \begin{bmatrix} -I\otimes B_{00} & -I\otimes B_{10} & -I\otimes B_{01} & -I\otimes B_{20} & -I\otimes B_{11} & -I\otimes B_{02} \\ 0 & I\otimes I & 0 & 0 & 0 & 0 \\ 0 & 0 & I\otimes I & 0 & 0 & 0 \\ 0 & 0 & 0 & I\otimes I & 0 & 0 \\ 0 & 0 & 0 & 0 & I\otimes I & 0 \\ 0 & 0 & 0 & 0 & 0 & I\otimes I \end{bmatrix},$$

$$S_{22} = S_{33} = S_{44} = S_{55} = S_{66} = \begin{bmatrix} 0 & 0 & 0 & -I\otimes B_{30} & -I\otimes B_{21} & -I\otimes B_{12} \\ -I\otimes I & 0 & 0 & 0 & 0 & 0 \\ 0 & 0 & 0 & 0 & 0 & 0 \\ 0 & -I\otimes I & 0 & 0 & 0 & 0 \\ 0 & 0 & -I\otimes I & 0 & 0 & 0 \\ 0 & 0 & 0 & 0 & 0 & 0 \end{bmatrix},$$

$$S_{42} = \begin{bmatrix} -I\otimes B_{00} & -I\otimes B_{10} & -I\otimes B_{01} & -I\otimes B_{20} & -I\otimes B_{11} & -I\otimes B_{02} \\ 0 & I\otimes I & 0 & 0 & 0 & 0 \\ 0 & 0 & I\otimes I & 0 & 0 & 0 \\ 0 & 0 & 0 & I\otimes I & 0 & 0 \\ 0 & 0 & 0 & 0 & I\otimes I & 0 \\ 0 & 0 & 0 & 0 & 0 & I\otimes I \end{bmatrix},$$

$$S_{53} = \begin{bmatrix} -I\otimes B_{00} & -I\otimes B_{10} & -I\otimes B_{01} & -I\otimes B_{20} & -I\otimes B_{11} & -I\otimes B_{02} \\ 0 & I\otimes I & 0 & 0 & 0 & 0 \\ 0 & 0 & I\otimes I & 0 & 0 & 0 \\ 0 & 0 & 0 & I\otimes I & 0 & 0 \\ 0 & 0 & 0 & 0 & I\otimes I & 0 \\ 0 & 0 & 0 & 0 & 0 & I\otimes I \end{bmatrix}.$$

By using the Tracy-Singh reordering of Δ_2', we have

$$\mathrm{TSR}(\Delta_2') = \begin{pmatrix} \mathrm{S}_{11} & \mathrm{S}_{12} & \mathrm{S}_{14} \\ \mathrm{S}_{21} & \mathrm{S}_{22} & \mathrm{S}_{24} \\ \mathrm{S}_{41} & \mathrm{S}_{42} & \mathrm{S}_{44} \end{pmatrix}.$$

Again, with the Tracy-Singh reordering of Δ_2, we obtain

$$TSR(\Delta_2) = \begin{bmatrix} S_{11} & S_{12} & S_{14} & S_{13} & S_{15} & S_{16} \\ S_{12} & S_{22} & 0 & 0 & 0 & 0 \\ 0 & S_{42} & S_{44} & 0 & 0 & 0 \\ 0 & 0 & 0 & S_{33} & 0 & 0 \\ 0 & 0 & 0 & 0 & S_{55} & 0 \\ 0 & 0 & 0 & S_{53} & 0 & S_{66} \end{bmatrix}.$$

Since $TSR(\Delta_2')$ is nonsingular, the remaining block entries S_{33}, S_{53}, S_{55} and S_{66} of $TSR(\Delta_2)$ give us a maximal rank of $12n^2$, assuming B_{ij} are nonsingular. Thus, this shows that the matrix Δ_2 is of rank $30n^2 < 36n^2$.

In the next section, we consider a randomly generated $\mathbb{CTEP}$, where the coefficients matrices are taken as real diagonal matrices. Then, we compare the eigenvalues obtained through the standard linearization and the Khazanov linearization processes. The results obtained in the case of the standard linearization via MatParEig Package (Muhič & Plestenjak, 2010) are considered the correct ones. On this basis, the approximation for the eigenvalues are found via an algorithm designed in MATLAB.

The linearization-like method reduced $\mathbb{CTEP}$ into a nine-parameter linear problem, the $\mathbb{L}9\mathbb{EP}$. It requires more computational time to find the numerical solution due to an increase in the number of linear equations. Moreover, the dimensions of the corresponding Δ_i matrices induced via Kronecker product also increase, making them sparse and computationally inefficient. Therefore, the linearization-like method is slower than the other two methods. The analytical comparison of the linearization-like method with the other two methods is omitted here due to the time complexity issues in calculating the corresponding Kronecker structure.

DOI:https//doi.org/10.22452/mjs.vol44no1.9

6. Numerical Example

Consider a $\mathbb{CTEP}$,

$$\mathbb{P}_1(\lambda,\mu)x_1 = (\lambda^3A_{30} + \lambda^2\mu A_{21} + \lambda\mu^2A_{12} + \mu^3A_{03} + \lambda^2A_{20} + \lambda\mu A_{11} + \mu^2A_{02} + \lambda A_{10} + \mu A_{01} + A_{00})x_1 = 0;$$

$$\mathbb{P}_2(\lambda,\mu)x_2 = (\lambda^3B_{30} + \lambda^2\mu B_{21} + \lambda\mu^2B_{12} + \mu^3B_{03} + \lambda^2B_{20} + \lambda\mu B_{11} + \mu^2B_{02} + \lambda B_{10} + \mu B_{01} + B_{00})x_2 = 0;$$

with randomly generated diagonal matrices, A_{ij} and B_{ij} of order 2 × 2.

$$A_{00} = \begin{bmatrix} 0.8147 & 0 \\ 0 & 0.9134 \end{bmatrix}, A_{10} = \begin{bmatrix} 0.6324 & 0 \\ 0 & 0.5469 \end{bmatrix}, A_{01} = \begin{bmatrix} 0.9575 & 0 \\ 0 & 0.9706 \end{bmatrix},$$

$$A_{20} = \begin{bmatrix} 0.9572 & 0 \\ 0 & 0.1419 \end{bmatrix}, A_{11} = \begin{bmatrix} 0.4218 & 0 \\ 0 & 0.9595 \end{bmatrix}, A_{02} = \begin{bmatrix} 0.6557 & 0 \\ 0 & 0.9340 \end{bmatrix},$$

$$A_{30} = \begin{bmatrix} 0.6787 & 0 \\ 0 & 0.3922 \end{bmatrix}, A_{21} = \begin{bmatrix} 0.6555 & 0 \\ 0 & 0.0318 \end{bmatrix}, A_{12} = \begin{bmatrix} 0.2769 & 0 \\ 0 & 0.8235 \end{bmatrix},$$

$$A_{03} = \begin{bmatrix} 0.6948 & 0 \\ 9 & 0.0344 \end{bmatrix},$$

$$B_{00} = \begin{bmatrix} 0.1869 & 0 \\ 0 & 0.6463 \end{bmatrix}, B_{10} = \begin{bmatrix} 0.7094 & 0 \\ 0 & 0.6797 \end{bmatrix}, B_{01} = \begin{bmatrix} 0.6551 & 0 \\ 0 & 0.4984 \end{bmatrix},$$

$$B_{20} = \begin{bmatrix} 0.9597 & 0 \\ 0 & 0.2238 \end{bmatrix}, B_{11} = \begin{bmatrix} 0.7513 & 0 \\ 0 & 0.6991 \end{bmatrix}, B_{02} = \begin{bmatrix} 0.8909 & 0 \\ 0 & 0.1386 \end{bmatrix},$$

$$B_{30} = \begin{bmatrix} 0.1493 & 0 \\ 0 & 0.2543 \end{bmatrix}, B_{21} = \begin{bmatrix} 0.8143 & 0 \\ 0 & 0.3500 \end{bmatrix}, B_{12} = \begin{bmatrix} 0.1966 & 0 \\ 0 & 0.4377 \end{bmatrix},$$

$$B_{03} = \begin{bmatrix} 0.3517 & 0 \\ 0 & 0.5497 \end{bmatrix}.$$

To compare the numerical results obtained from Standard linearization and Khanzadeh linearization, we used the MultiParEig toolbox developed by Plestenjak (2023) on a Windows 11 operating system with an AMD Ryzen 5 5500U 2.10 GHz processor. The results are shown below.

Table 1

Standard Linearization		Khazanov Linearization	
λ	μ	λ	μ
1.0092+0.0000i	-1.4499+0.0000i	1.0092 + 0.0000i	-1.4499+0.0000i
-0.3421+0.0000i	-0.7805+0.0000i	-0.3421 +0.0000i	-0.7805+0.0000i
-0.3432±0.8405i	-0.9510±0.0087i	-0.3432±0.8405i	-0.9510±0.0087i
-1.3114±0.2309i	-0.9173±1.4685i	-1.3114±0.2309i	-0.9173±1.4685i
-1.0672±0.1223i	-0.3852±0.9591i	-1.0672±0.1223i	-0.3852±0.9591i
-0.7862+0.0000i	-0.5743 +0.0000i	-0.7862 +0.0000i	-0.5743+0.0000i
0.3349±0.0446i	-0.5398±0.8207i	0.3349±0.0446i	-0.5398±0.8207i
-1.0856+0.0000i	0.7836 + 0.0000i	-1.0854+0.0000i	0.7776 + 0.0000i
-1.5614±0.2974i	-0.0133±1.7493i	-1.5614±0.2974i	-0.0133±1.7493i
-1.0610±0.0111i	-0.0168±0.5738i	-1.0602±0.0109i	-0.0098±0.5834

DOI:https//doi.org/10.22452/mjs.vol44no1.9

0.3768±0.6614i	0.3238±1.0721i	0.3768±0.6614i	0.3238±1.0721i
-0.1068±1.2095i	-0.0491±0.5295i	-0.4227±3.7101i	1.8669±0.5291i
-1.0224±0.5267i	-0.6265±0.5461i	0.2789±1.4519i	-1.1613±0.1619i
-1.0978+0.0000i	-0.7238 +0.0000i	-1.0978+0.0000i	-0.7238+0.0000i
1.1408 + 0.0000i	-90.1367+0.0000i	0.3469 + 0.0000i	-1.0288+0.0000i
-0.3051±0.7180i	0.1179±0.8142i	-0.4267±0.6475i	0.1663±0.9384i
-7.9598±6.4034i	-4.9047±5.8520i	0.6625±0.4573i	0.3300±1.3700i
0.8733±0.0768i	0.0933±1.6336i	0.5203±0.7182i	-1.0214±0.4763i
0.3425±1.2010i	-0.7668±0.1594i	0.2367±1.0175i	-0.7182±0.4862i
-0.0348±0.3753i	-0.8454±0.1057i	-1.0498±0.4383i	-0.4927±0.4840i
0.2789±1.4519i	-1.1613±0.1619i	-0.4080±1.4486i	0.2030±0.6769i

By Bézout's theorem, a $\mathbb{CTEP}$ has $9n^2$ eigenvalues; therefore, the problem considered above has $9n^2 = 9.2^2 = 36$ eigenvalues. Both methods calculate all the eigenvalues of the problem. The Standard linearization provides the exact eigenvalues. Through comparisons of the eigenvalues obtained by Khazanov linearization, we find that most eigenvalues, except for a few, match those obtained from the Standard linearization. In the MATLAB environment, the execution time for the Standard Linearization process is 1.267792 seconds, while Khazanov Linearization takes 0.431789 seconds. The Khazanov linearization is faster due to the small size of the coefficient matrix and the absence of antidiagonal elements. For small-ordered matrices, Khazanov linearization may be preferable to Standard Linearization. However, Standard linearization consistently yields better results when dealing with higher-order matrices.

7. Conclusion

We described the Kronecker canonical structures of $\mathbb{CTEP}$ obtained through different linearization processes, including standard linearization, Khazanov linearization, and transformation to $\mathbb{L9EP}$. These approaches can be used to find numerical solutions of $\mathbb{CTEP}$ by applying existing numerical methods to solve $\mathbb{LMEP}$s. We compared the first two singular linearizations through a numerical example. The calculation via $\mathbb{L9EP}$ is omitted here due to its higher computational time requirements. The Kronecker structures of Δ_i matrices for i:=0:2 have not been extensively studied because of their complex structures in $\mathbb{CTEP}$. These structures and their ranks can assist in developing proofs for the number of manifolds via algebraic geometry in various methods (Dong, (2022)). All results are novel and serve as a foundation for further study of the Delta matrices of $\mathbb{PTEP}$ of degree k.

Acknowledgment: The authors express their deep gratitude for the comments and valuable suggestions provided by the two anonymous reviewers, which considerably improved the paper. The authors also thank Dibrugarh University for providing all necessary facilities during their research work.

Funding: There are no funding sources.

Conflict of interest: All authors declare that there is no conflict of interest.

8. References

Atkinson F V. (1972). Multiparameter eigenvalue problems, *Academic Press, New York.*

Bueno M I., Dopico F M., Furtado S., Medina L. (2018). A block-symmetric linearization of odd degree matrix polynomials with optimal eigenvalue condition number and backward error, *Calcolo*, 55: 32.

Cox D., Little J., O'shea D. (2005). Using Algebraic Geometry, *Springer Verlag, New York*.

Das R K., Alam R. (2019). Automatic recovery of eigenvectors and minimal bases of matrix polynomials from generalized Fiedler pencils with repetition, *Linear Algebra Appl.* 569, 78-112.

Das B. (2020). Linearizations and distance problems associated with matrix polynomials, Ph.D. thesis, IIT Guwahati, India.

Dmytryshyn A., Johansson S., Kagström B., Dooren P V. (2020). Geometry of Matrix Polynomial Spaces, *Foundations Comput. Math.* 20, 423-450.

Dong B. (2022). The Homotopy Method for the Complete Solution of Quadratic Two-parameter Eigenvalue Problems, *J. Scientific Comput*. 90:18.

Dooren P V. (1997). The computation of Kronecker's canonical form of a singular pencil, *Linear Algebra Appl.* 27, 103-141.

Fabbender H., Saltenberger P. (2018). Block Kronecker ansatz spaces for matrix polynomials, *Linear Algebra Appl.* 542, 118-148.

Gohberg I., Lancaster P., Rodman L. (2009). Matrix Polynomials, *Society for Industrial and Applied Mathematics*, *Philadelphia.*

Henderson H V., Pukelsheim F., Searle S R. (1983). On the history of the kronecker product, *Linear Multilinear Algebra 14*, 113-120.

Higham N J., Mackey D. S., Tisseur F. O. (2006). The Conditioning of Linearizations of Matrix Polynomials*, SIAM J. Matrix Anal. Appl*. 28(4), 1005-1028.

Hochstenbach M E. (2003). Subspace methods for eigenvalue problems, Ph.D thesis, Department of Mathematics and Computer Science, TU Eindhoven.

Hochstenbach M E., Muhič A., Plestenjak B. (2012). On linearizations of the quadratic two-parameter eigenvalue problems, *Linear Algebra Appl.* 436(8), 2725-2743.

Hochstenbach M E., Košir T., Plestenjak B. (2005). A Jacobi-Davidson type method for the nonsingular two-parameter eigenvalue problem, *SIAM J. Matrix Anal. Appl.* 26, 477-497.

Hochstenbach M E., Muhič A., Plestenjak B. (2015). Jacobi–Davidson methods for polynomial two-parameter eigenvalue problems*, J. Comput. Applied Math*. 288, 251-263.

Jarlebring E., Hochstenbach M E. (2009). Polynomial two-parameter eigenvalue problems and matrix pencil methods for stability of delay-differential equations, *Linear Algebra Appl*. 431, 369–380.

Khazanov V B. (2007). To solving spectral problems for multiparameter polynomial matrices, *J. Math. Sci.* 141, 1690-1700.

Košir T., Plestenjak B. (2022). On the singular two-parameter eigenvalue problem II*. *Linear Algebra Appl.* 649, 433-451.

Kressner D., Glibić I Š. (2023). Singular quadratic eigenvalue problems: Linearization and weak condition numbers*, BIT Numer. Math*., Article no. 18.

Lancaster P. (2008). Linearization of regular matrix polynomials, *Elect. J. Linear Algebra*. 17, 21-27.

Lancaster P., Zaballa I. (2021). Spectral theory for self-adjoint quadratic eigenvalue problems - a review, *Elect. J. Linear Algebra*. 37, 211-246.

Mackey D S., Mackey N., Mehl C., Mehrmann V. (2006). Vector Spaces of Linearizations for Matrix Polynomials, *SIAM J. Matrix Anal. Appl.* 28(4), 971-1004.

Meerbergen K., Schröder C., Voss H. (2013). A Jacobi-Davidson method for two-real-parameter nonlinear eigenvalue problems arising from delay-differential equations, *Numer. Linear Algebra Appl.* 20(5), 852–868.

Muhič A., Plestenjak B. (2009). On the singular two-parameter eigenvalue problem, *Elect. J. Linear Algebra* 18, 420-437.

Muhič A., Plestenjak B. (2010). On quadratic two-parameter eigenvalue problem and its linearization, *Linear Algebra Appl*. 432, 2529-2542.

Plestenjak B. (2023). MultiParEig, https://www.mathworks.com/matlabcentral/fileexchange/47844-multipareig, MATLAB Central File Exchange, Retrieved December 3, 2023.

Plestenjak B. (2016). Numerical methods for nonlinear two-parameter eigenvalue problems, *BIT Numer. Math*. 56, 241–262.

Plestenjak B. (2017). Minimal determinantal representations of bivariate polynomials, *Linear Algebra Appl.* 532, 550–569.

Plestenjak B., Hochstenbach M E. (2016). Roots of bivariate polynomial systems via determinantal representations, *SIAM J. Scientific Comput*. 38, A765–A788.

Tisseur F., Meerbergen K. (2001). The Quadratic Eigenvalue Problem, *SIAM Rev.* 43(2), 235-286.

Tracy D S., Singh R P. (1972). A new matrix product and its applications in matrix differentiation. Statistica Neerlandica. 26 (4): 143–157.

Tracy D S., Jinadasa K G. (1989). Partitioned Kronecker products of matrices and applications, Canad. J. Statist. 17, 107-120.

DOI:https//doi.org/10.22452/mjs.vol44no1.9

MALAYSIAN JOURNAL OF SCIENCE
MJS
ISSN 1394-3065

Regular Issue

Malaysian Journal of Science 44 (1): 87-92 (March 2025) https://mjs.um.edu.my

Enhancing the Spectroscopic Properties of Rhodamine B Via the Nano-Concentration Effect

Hanan Auda Naif[1a]*, Ruba Al-Obaidi[2a] and Oday M. Abdulmunem[3a]

Abstract: Developing nano-liquid materials with ultra-low concentrations leads to new or improved methods, as well as resolving issues in previous studies. Nano-liquid materials require special treatment because they are very sensitive materials. Many techniques have been developed, including the optical cavity technique, which depends on increasing the path length of the light beam between two dielectric mirrors to obtain more accurate and sensitive measurements. This method also provides beneficial information about the chemical composition. In this study, broadband cavity-enhanced absorption spectroscopy was used at a range of visible wavelengths to obtain spectra of rhodamine B ($C_{28}H_{31}ClN_2O_3$) at room temperature. The liquid phase of rhodamine B was chosen because it is the most complicated and volatile phase. The spectral analyses showed the fine structure of the aqueous solution of rhodamine B and the different molecular dynamics. The processes of the electron dynamics inside the molecules also changed at the ultra-low sample concentrations achieved working at the nanomolar scale. Combining experimental and data analysis via simulation programs has many benefits, such as reducing the time needed to study the materials, as it presents a typical design with fewer issues. In addition, costly, scarce, or difficult-to-store materials should be studied at low concentrations, and these combined studies can yield results without using these materials. The novelty of our research is the successful study of low concentrations of liquid samples. The high quality of the data, demonstrated by the goodness-of-fit parameters, allows for further analyses. Spectral analysis of nano-concentrations of rhodamine B shows new multiphoton absorption processes that drive the shifts in peak intensity. The solvent interaction effects caused changes in the binding energy states of the molecular structure of the sample. Here, we present a new spectral analysis of rhodamine B in aqueous solution using the broadband cavity-enhanced absorption spectroscopy (BBCEAS) technique.

Keywords: *Broadband cavity, nano-concentrations, Rhodamine B, enhanced absorption spectra, simulation program*

1. Introduction

Earlier investigations have focused on studying molecular structures with optical cavity techniques, such as cavity ring-down spectroscopy (CRDS), cavity-enhanced absorption spectroscopy (CEAS), and broadband cavity-enhanced absorption (BBCEAS), which is the main improvement obtained using a broadband light source. Engeln et al. (1998) have investigated using a narrow band light source with a high-finesse optical cavity to obtain high-resolution optical absorption spectra through the accidental synchronisation of the laser frequency with the cavity frequency, which led to extracting the absorption and polarisation rotation. This study presented the spectra of oxygen, ammonia, and water in a cell and the spectra of molecular oxygen and ammonia in a slit-jet expansion (Engeln et al., 1998). In 2003, Fiedler and co-workers demonstrated a new highly sensitive technique depending on incoherent broad-band cavity-enhanced absorption spectroscopy (IBBCEAS). They have used this technique to measure the weak transitions in molecular oxygen, which were found between 15865 and 1593 cm^{-1}, as well as the absorption spectrum of gaseous azulene in the region 628–670 nm, where several vibronic transitions appeared (Fiedler et al., 2003). Another BBCEAS study has been reported by Qu et al. in 2013. Using a Griess assay, they used this technique to measure Rh6G dye at 527 nm and determine the nitrite concentration. A low-cost webcam was used as a detector, reducing the cost of this technique (Qu et al., 2013). In general, a BBCEAS system consists of a broadband light source, an optical cavity formed by two high-quality dielectric mirrors, and a multiplex detector, such as a CCD spectrometer, to monitor the absorption spectra depending on the variation in the wavelength (Engeln et al., 1998; Islam et al., 2007, Naif et al, 2024).

BBCEAS has been used to make many advances, especially in the study of the liquid phase, the most complex and changeable liquid molecular phase. One such study was performed by Fiedler et al. in 2005 to determine the weak transitions in the liquid phase (Franck–Condon inhibited absorption of the fifth C-H stretching overtone in liquid benzene) using a modified double-beam UV-visible spectrometer. This study is the first to use BBCEAS in the liquid phase (Fiedler et al., 2005). In 2007 and 2009, Islam et al. and Seatohul et al. used BBCEAS with an LED light source in the liquid phase with 2-mm and 20-cm wide cells, respectively. These

Authors information:
[a]Mustansiriyah University, College of Science, Physics Department, Baghdad, IRAQ. E-mail: h.naif@uomustansiriyah.edu.iq[1]; ruba@uomustansiriyah.edu.iq[2]; munem@uomustansiriyah.edu.iq[3]
*Corresponding Author: h.naif@uomustansiriyah.edu.iq

Received: May 31, 2023
Accepted: November 22, 2023
Published: March 31, 2025

DOI:https//doi.org/10.22452/mjs.vol44no1.10

studies produced the most sensitive liquid phase absorption measurements (Islam et al., 2007; Seatohul et al., 2009). Moreover, in the work of Bajuszova et al. (2017), the higher sensitivity of BBCEAS was combined with liquid phase stopped-flow kinetics to measure fast reactions by slowing down the reaction rate using a lower concentration of reagents (Bajuszova et al., 2017). Naif et al. (2021) have reported the spectral behaviour of very low concentrations of coumarin dye and showed applications of these measurements in photonics (Naif et al., 2021).

In previous studies, the spectral properties of rhodamine B have been studied on sliver surfaces by Rai et al. (Rai et al., 1988), and the molecular structure of these dyes has been studied using the near-infrared fluorescence technique (Grzybowski et al., 2018; Lian et al., 2019; Wu et al., 2018; Xia et al., 2019). The influence of solvents on the absorption and fluorescence spectra of rhodamine B at different concentrations at room temperature has been studied by Ali et al. in 2012 (Ali et al.,2012). The current study studied the molecular structure and the fast and ultrafast molecular dynamics of rhodamine B ($C_{28}H_{31}ClN_2O_3$) using the BBCEAS technique.

2. Materials and Methods

Sample Preparation

To determine the molecular dynamics and structure of rhodamine B, nine concentrations from 4.70 to 47.01 nM were prepared from 0.0225 g of rhodamine B (Sigma Aldrich). First, the rhodamine B was dissolved in 100 mL of deionised water to obtain a stock solution of 4.7mM. Then, the samples were prepared by taking 0.001, 0.002, 0.003, 0.004, 0.005, 0.006, 0.007, 0.008, 0.009, and 0.01 mL from the stock solution and then dissolving each in a 100-mL volumetric flask with deionised water.

Apparatus

This study used the BBCEAS technique to study the molecular structure and dynamics. A BBCEAS system includes three parts: 3 W white LED (Lumileds-SR-12, USA), which is used as a light source with an output power equal to ~5mW; the optical cavity, which contains two dielectric high reflectivity mirrors (R ≥ 0.99) (Layertec, Germany); and an Andor spectrometer (Andor Shamrock 163 Czerny-Turner spectrograph, UK), which was connected to the optical cavity using a 2m fibre optic cable (Ocean optics, USA). A quartz cuvette (Hellma, UK) of 1 cm thickness and 4 cm length was used to hold the sample.

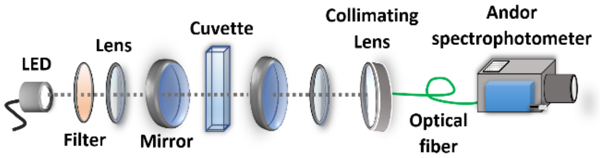

Figure 1. A schematic diagram of BBCEAS setup.

Molecular structure

Rhodamine B was chosen for study due to its important uses in medicine and other fields. Rhodamine B belongs to a group of dye molecules with a large molecular weight of approximately 479.02 g/mol. The molecular system contains a conjugated double-bond structure (see Figure 2). The chemical formula of the molecule is $C_{28}H_{31}ClN_2O_3$.

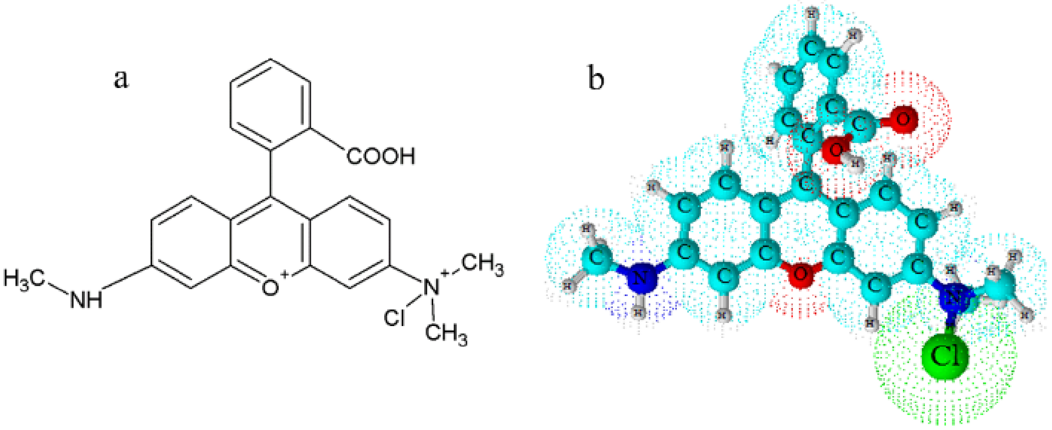

Figure 2: (a) Rhodamine B molecule and (b) a 3-D plot of $C_{28}H_{31}ClN_2O_3$ molecular structure.

Absorption and Transmission Spectra Detection

For the absorption assay, the spectra of rhodamine B in aqueous solution were measured using a broadband light source technique, BBCEAS. Different sample concentrations were prepared to study the effects of ultra-low concentrations (nanomolar scale). The absorption spectra were collected at excitation wavelengths between 500 and 600 nm. The absorption peak at 556 nm dominates the spectra due to the high absorption intensity of the incident photons. The liquid phase analyses of the representative transmission spectra were measured under the same conditions as the absorption spectra. The experimental settings were kept the same to maintain the same environment for measurement, and the LED source was installed between 500 and 600 nm.

3. Results and Discussion

The measured absorption spectra of rhodamine B are shown in Figure 3. To improve the detection statistics, representative absorption spectra were measured every 2 minutes as the accumulation signal and for 60 minutes for all recorded spectra.

The detected peak amplitude decreased at low and ultra-low sample concentrations due to the small number of molecules per unit volume, which changes at different sample concentrations. Figure 3 shows the collective absorption spectra of rhodamine B aqueous solution measured at 4.70 to 47.01 nM.

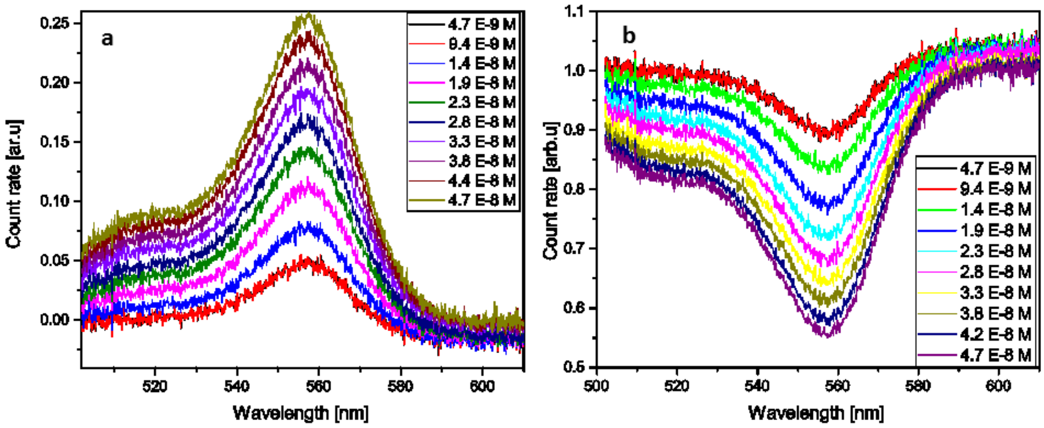

Figure 3. (a) Absorption and (b) transmission spectra of an aqueous solution of rhodamine B at different concentration ranges. The concentration (4.7 E-9M) disappeared behind the concentration (9.4E-9M) because their values were close together

For high sample concentrations, the intensity of the absorbed photons at the approximate peak position of 565.590 nm is high but reduced for lower sample concentrations. High sample concentrations resulted in a high molecular density per unit volume of solution, which changed the absorption cross-section and increased the number of absorbed incident photons. Consequently, the number of excited electrons per incident photon increased, changing the molecular dynamics. At low concentrations, the spectra show reduced intension of the absorption peaks observed in rhodamine B. The decrease occurs between 535 and 588 nm (Figure 3).

For a more detailed analysis, the data were fitted to the asymmetric double sigmoidal (ADS) function, where y_o is the offset, A is the peak amplitude (normalized), W_1 is the full width at half maximum, and W_2 and W_3 are the width and variance of the low- and high-energy side, respectively (see equation below):

$$y = y_o + A\frac{1}{1+e^{-\frac{(x-x_c)+W_1/2}{W_2}}}\left(1-\frac{1}{1+e^{-\frac{(x-x_c)+W_1/2}{W_3}}}\right)$$

The effect of the concentration of rhodamine B on the position of the central peak is shown in Figure 4(a). Increasing sample concentration shifted the peak centre to higher wavelengths, indicating changes to the structure of rhodamine B. The liquid phase of rhodamine B in high concentrations shows different molecular dynamics properties. At high concentrations of rhodamine B, the molecules absorbed photons of long wavelengths (low-energy photons), and the central peaks shifted to 565.590 nm at a concentration of 4.715E−8 M. This phenomenon is driven by molecular processes, such as the multiphoton absorption process (Chen et al., 2006). The high number of molecules per unit volume raised the rate of the absorption photons, which is reflected in Figure 4(b) as a sharp rise in the peak amplitude due to increasing sample concentration. In Figure 4(c), the stability of the FWHM (width W_1) of the peaks obtained from the ADS function agrees with the sample concentrations. The FWHM of the peaks changed slightly with increased sample concentration.

The large error bars of some points in the figure are due to the fitting process; low-concentration spectra did not match the experimental data exactly. In Figures 4(d) and (e), the variance of the photon absorption rate increased with the rate of the signal of the high and low sides of the peaks. These conflict actions of the rhodamine B molecules appear at lower wavelengths, from approximately 500 to 540 nm, where the high side of the peak tail rises, and at the low sides of the peak tails between 560 and 600 nm. Moreover, the behaviour of the low and high sides of the peak tails (widths W_3 and W_2) relate to different absorption processes of the rhodamine B molecules, where the orientation of the molecules plays a significant role in changing the binding energy of the molecules (Millan et al., 2016). On the low side of the peak tails, the molecules absorb photon energy between 2 and 2.2 eV), and on the high side, the molecules absorb photons of 2.3 to 2.5 eV.

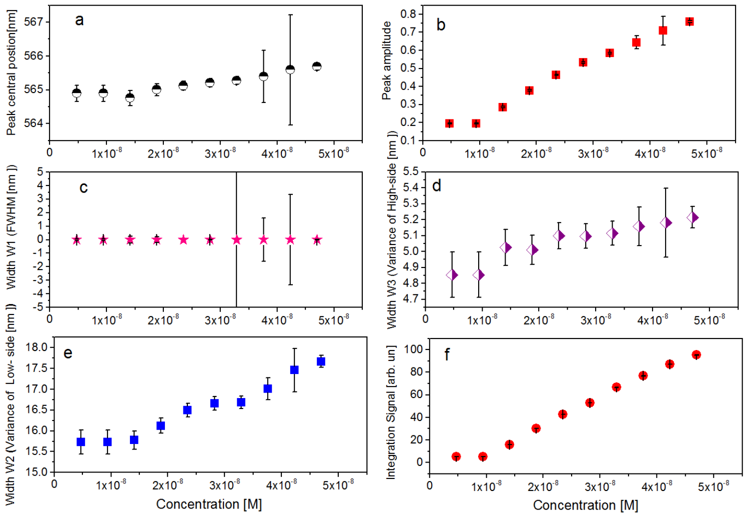

Figure 4. Absorption spectra of aqueous solutions of rhodamine B ($C_{28}H_{31}ClN_2O_3$) at different concentrations.

The peaks in Figures 4 (a) and (b) show the effect of the rhodamine B concentration on the peak centre and peak amplitude, respectively. Figures 4 (c) and (d) show the full width at half maximum of the peaks (FWHM) with the variance on the low side of the peak tails (W_3) and the high side of the peak tails (W_2), with the integration absorption signal indicated in Figures 4 (e) and (f).

The changing absorption processes are also related to the water molecules, which change the solvation binding energy (Jensen, 2015). The analyses from the ADS fits have small error bars, as shown in Figure 4. The unique structure of the molecules results in the spatial properties of the sample. The integration signal of the detected photons was calculated for every spectrum measured in the sample and channel F from Figure 4. The increase in the integrated signal with increasing sample concentration is due to the high absorption rate of the high-concentration molecules.

The spectra in Figure 5(a) indicate the different behaviours of the molecules and the shifts in the centres of the peaks with increasing sample concentrations. Figure 5(b) shows the reduction of the peak amplitude of the transmission spectra due to the increased sample concentrations due to the increased number of transmitted photons at a specific wavelength. In Figure 5(c), the FWHM (W_1) were quasi-stable with high sample concentrations, as also seen in the absorption spectra analysis. From these analyses, different absorption processes happened within the inner molecular orbitals.

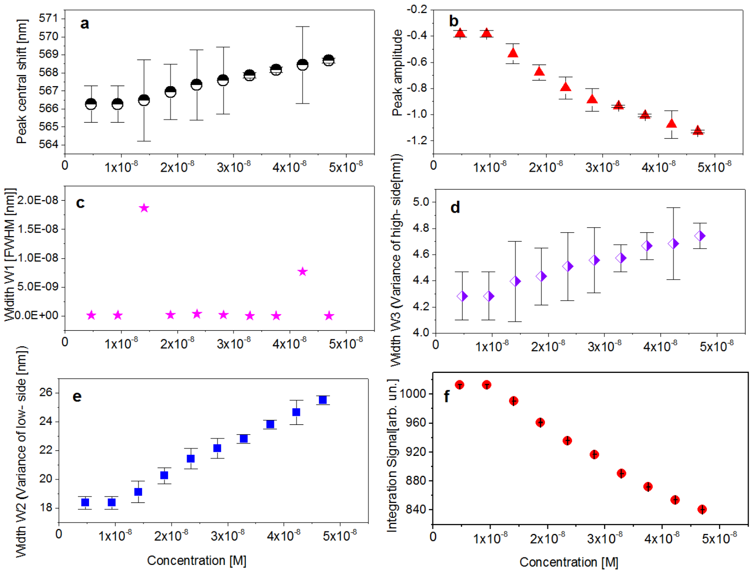

Figure 5. Transmission spectra of aqueous solutions of rhodamine B at different concentrations.

In Figure 5(a), peaks are fitted to the ADS function. The analyses show the effect of the concentration of the liquid phase of rhodamine B on the position of the peak centres. The peak amplitude is shown with the FWHM in Figures 5(b) and (c). The variance of the low side of the peak tails (W_3) and the variance of the high side of the peak tails (W_2) are illustrated in Figures 5(d) and (e), with the integration absorption signal given in Figure 5(f). In Figures 5 (d) and (e), the low and high sides of the peak tails

(W_2 and W_3) of the obtained spectra were fitted to the ADS function. These analyses showed that the high and low sides of the tails of the peaks increased with higher sample concentrations. The high and low sides of the peak tails indicate a change in the structural dynamics of the molecules. This effect was also achieved when peaks were detected by absorption and when the integration transmitted signal was reduced by increasing the sample concentration (Figure 5(f)).

4. Conclusion

The cavity-enhanced absorption spectroscopy technique has been demonstrated using an LED-based light source. Furthermore, the effect of ultra-low sample concentrations was studied. The experimental setup was developed to achieve optimum overlap with the reflectivity of the cavity mirrors for the largest differential absorption cross-section of a target molecule. High-quality broadband BBCEAS spectra were obtained under conditions with a substantial mismatch in the peak wavelength of the LED output (500–600 nm). Quantitative absorption and transmission spectra measurements were collected at ultra-low sample concentrations. The spectra were fitted to the ADS function, and analysis indicated a change in the molecular structure and the dynamics when the sample concentrations reached ultra-low nanomolar scale concentrations. This shifted in the central peak position and changed the peak amplitude, FWHM, and integration signal of both absorption and transition spectra. These indicators can be explained by changes in the absorption and transition processes of the rhodamine B molecule due to slight changes in the binding energy of the energetic states of the molecules. The vibrational and rotation energies of molecules also change due to the solvent effect, leading to changes in the electronic transitions. As a result, the molecular dynamics rotations, vibrations, and transitions of rhodamine B also change slightly due to molecule–molecule interactions from changes to the molecular distance between the sample and the solution in high and low concentrations. This was observed from the change in the spectra fit to the ADS function for every sample concentration.

5. Acknowledgements

The authors acknowledge the Physics Department, College of Science, Mustansiriyah University. Baghdad, Iraq.

6. Declaration of Interest Statement

We, the co-authors in the tagged research "Enhance the Optical Properties of Rhodamine B via Nano concentrations Effect", acknowledge and recognize that there is no intersection of interests between researchers participating in the research or the institution to which we belong.

7. References

Ali RA, Abdul-Munem OM, Abd AN. 2012. Study the spectroscopic characteristics of Rhodamine B Dye in Ethanol and Methanol mixture and Calculation the Quantum Efficiency. Baghdad Science Journal 9

Bajuszova Z, Naif H, Ali Z, McGinnis J, Islam M. Cavity enhanced liquid-phase stopped-flow kinetics. Analyst. 2018; 143(2): 493-502.

Chen S, Liu B-F, Fu L, Xiong T, Liu T, et al. 2006. Continuous wave-based multiphoton excitation fluorescence for capillary electrophoresis. Journal of Chromatography A 1109:160-6

Engeln R, Berden G, Peeters R, Meijer G. 1998. Cavity enhanced absorption and cavity enhanced magnetic rotation spectroscopy. Review of scientific instruments 69:3763-9

Fiedler SE, Hese A, Ruth AA. 2003. Incoherent broad-band cavity-enhanced absorption spectroscopy. Chemical physics letters 371:284-94

Grzybowski M, Taki M, Senda K, Sato Y, Ariyoshi T, et al. 2018. A Highly Photostable Near-Infrared Labeling Agent Based on a Phospha-rhodamine for Long-Term and Deep Imaging. Angewandte Chemie International Edition 57:10137-41

Islam M, Seetohul LN, Ali Z. 2007. Liquid-phase broadband cavity-enhanced absorption spectroscopy measurements in a 2 mm cuvette. Applied spectroscopy 61:649-58

Jensen JH. 2015. Predicting accurate absolute binding energies in aqueous solution: thermodynamic considerations for electronic structure methods. Physical Chemistry Chemical Physics 17:12441-51

Lian X, Wei M-Y, Ma Q. 2019. Nanomedicines for near-infrared fluorescent lifetime-based bioimaging. Frontiers in Bioengineering and Biotechnology 7:386

Millan S, Satish L, Kesh S, Chaudhary YS, Sahoo H. 2016. Interaction of lysozyme with rhodamine B: a combined analysis of spectroscopic & molecular docking. Journal of Photochemistry and Photobiology B: Biology 162:248-57

Naif HA, Abbas AM, Al-Kadhemy MFH (2024) Investigate spectroscopic experimental and theoretical model for hemoglobin nanoscale solution. Baghdad Sci J 21(2):0465–0465. https://doi.org/10.21123/bsj.2023.7775

Naif HA, Saeed AA, Al-Kadhemy MFH. Spectral Behaviour of the low concentrations of Coumarin 334 with Broadband Cavity Enhanced Absorption Spectroscopy. Baghdad Sci J. 2022; 19(2): 0438.

Qu Z, Engstrom J, Wong D, Islam M, Kaminski CF. 2013. High sensitivity liquid phase measurements using broadband cavity enhanced absorption spectroscopy (BBCEAS) featuring a low cost webcam based prism spectrometer. Analyst 138:6372-9

Rai V. 1988. Optical properties of Rhodamine B and Rhodamine 6G on silver surfaces. Pramana 31:313-22

Fiedler SE, Hese A, and Ruth A A.2005. Incoherent brand-band cavity- enhanced absorption spectroscopy of liquids. Rev. Sci. Instrum. 76, 023107.

Seetohul LN, Ali Z, Islam M. 2009. Liquid-phase broadband cavity enhanced absorption spectroscopy (BBCEAS) studies in a 20 cm cell. Analyst 134:1887-9

Wu Z, Yuan X, Zeng G, Jiang L, Zhong H, et al. 2018. Highly efficient photocatalytic activity and mechanism of Yb3+/Tm3+ codoped In2S3 from ultraviolet to near infrared light towards chromium (VI) reduction and rhodamine B oxydative degradation. Applied Catalysis B: Environmental 225:8-21

Xia S, Fang M, Wang J, Bi J, Mazi W, et al. 2019. Near-infrared fluorescent probes with BODIPY donors and rhodamine and merocyanine acceptors for ratiometric determination of lysosomal pH variance. Sensors and Actuators B: Chemical 294:1-13

DOI:https//doi.org/10.22452/mjs.vol44no1.10

MALAYSIAN JOURNAL OF SCIENCE
MJS
ISSN 1394-3065

Regular Issue

Malaysian Journal of Science 44 (1): 93-100 (March 2025)
https://mjs.um.edu.my

Role of Mango in the Production of Wine: A Review

Mohd Kamran[1a]*, Kokab Askari[2b], Bhavya Trivedi[3c], Rupak Nagraik[4d] Mohammad Faisal[5e], Aditi Nayek[6a], Gorantla Leeladhar[7a], Aryan Singh[8a], Shivam[9a], Thrunshi Hiloto[10a] and Rohit Joshi[11a]

Abstract: Mango is considered to be one of the most cultivated tropical fruits around the world. India is one of the largest producers of mango, accounting for an estimated 45% of the total world mango fruit production. India exported 27,872 metric tons of mango, worth 327.45 crores in 2020-21. Mango is a perishable fruit with a very short shelf life, which leads to wastage. To minimize or utilize the wastage, alternative mango-based products are being produced. Mango wine is one of the alternatives for surplus mango production. It is cost-effective and helps minimize post-harvest losses. The Philippines is the largest manufacturer of mango-based alcoholic beverages, such as mango wine and rum. Locally, mango wine is a popular home-based alcoholic beverage in the Philippines. India and Kenya are also experiencing significant growth in fruit wine production. The available literature on the production and characterization of mango wine briefly describes the fermentation and characterization procedures followed. The physiochemical properties and volatile composition of mango wine, including ethanol, esters, total soluble solids, and sensory analysis, are also highlighted in the review. The study provides evidence that the antioxidants and immunoboosters can reduce the risk of chronic infections.

Keywords: *Mango wine, fermentation, fruit wine, physiochemical analysis, mango pulp*

1. Introduction

In tropical and subtropical regions, the mango (*Mangifera indica L.*) is a beloved fruit. Its exceptional aroma, enticing fragrance, exquisite taste, and high nutritional value have distinguished it as one of the finest fruits. One of the most important and commonly cultivated fruits in the tropics is the mango (*Mangifera indica*), a member of the cashew family (*Anacardiaceae*). There exist several varieties of mango trees, which are believed to originate from southern Asia, particularly Myanmar and the Indian state of Assam. Mangoes are rich in Vitamins A, C, and D. India holds the position of the leading mango producer globally, contributing nearly 50% of the total production. Other significant mango-producing countries include China, Thailand, Mexico, Pakistan, the Philippines, Indonesia, Brazil, Nigeria, and Egypt. India alone accounts for 12 million tons, representing approximately 52% of the global output of 23 million tons. Global mango production, averaging 22 million metric tons per year, has been increasing. Asia dominates 75% of the production, followed by South and North America, which have around 10% each. Uttar Pradesh (23.86%), Andhra Pradesh (22.14%), Karnataka (11.71%), Bihar (8.79%), Gujarat (6.00%), and Tamil Nadu (5.09%) are the leading mango-producing states in India. India exports mangoes to over 40 countries, with the UAE (61.79%), Bangladesh (11.41%), the United Kingdom (8.92%), Saudi Arabia (3.79%), Kuwait (2.32%), and Bahrain (2.19%) being the top importers of Indian mangoes (National Horticulture Board).

In tropical and subtropical regions, the mango (*Mangifera indica L.*) is a beloved fruit. Its exceptional aroma, enticing fragrance, exquisite taste, and high nutritional value have distinguished it as one of the finest fruits. One of the most important and commonly cultivated fruits in the tropics is the mango (*Mangifera indica*), a member of the cashew family (*Anacardiaceae*). There exist several varieties of mango trees, which are believed to originate from southern Asia, particularly Myanmar and the Indian state of Assam. Mangoes are rich in Vitamins A, C, and D. India holds the position of the leading mango producer globally, contributing nearly 50% of the total production. Other significant mango-producing countries include China, Thailand, Mexico, Pakistan, the Philippines, Indonesia, Brazil, Nigeria, and Egypt. India alone accounts for 12 million tons, representing approximately 52% of the global output of 23 million tons. Global mango production, averaging 22 million metric tons per year, has been increasing. Asia dominates 75% of the production, followed by South and North America, which have around 10% each. Uttar Pradesh

Authors information:
[a]School of Applied and Life Sciences, Uttaranchal University, Dehradun, 248007, INDIA. E-mail: leeladhar.gorantla392@gmail.com[1]; nayekmegha01@gmail.com[6]; leeladhar.gorantla392@gmail.com[7]; aryansingh24083@gmail.com[8]; marathashivam730@gmail.com[9]; hilotothrunshi@gmail.com[10]; rohitjoshi0021@gmail.com[11]
[b]Maharishi Markandeshwar deemed to be university, Ambala, INDIA. E-mail: dr.kokabaskari@mmumullana.org[2]
[c]School of Agriculture Maya Devi University, Selaqui, Dehradun, INDIA. E-mail: drbhavyatrivedi@maya.edu.in[3]
[d]Department of Biotechnology, Graphic Era (Deemed to be University), Dehradun, Uttarakhand, 248002, INDIA. E-mail: rupak.nagraik@gmail.com[4]
[e]School of Agriculture, Forestry & Fisheries, Jigyasa University, Dehradun 248197, Uttarakhand, INDIA. E-mail: faisal_fri@yahoo.com[5]
*Corresponding Author: leeladhar.gorantla392@gmail.com

Received: January 3, 2023
Accepted: December 19, 2023
Published: March 31, 2025

DOI:https//doi.org/10.22452/mjs.vol44no1.11

(23.86%), Andhra Pradesh (22.14%), Karnataka (11.71%), Bihar (8.79%), Gujarat (6.00%), and Tamil Nadu (5.09%) are the leading mango-producing states in India. India exports mangoes to over 40 countries, with the UAE (61.79%), Bangladesh (11.41%), the United Kingdom (8.92%), Saudi Arabia (3.79%), Kuwait (2.32%), and Bahrain (2.19%) being the top importers of Indian mangoes (National Horticulture Board).

Alphonso: The Portuguese commander Afonso de Albuquerque inspired the name of the Alphonso mango, sometimes referred to as the King of Mangoes. Due to its unparalleled flavor and texture, Alphonso is the most sought-after mango cultivar globally. Grown in the Konkan region of Maharashtra, Alphonso is credited with establishing the mango as India's national fruit. The Konkan region's Alphonso mango has been granted the Geographical Indication designation.

Langra: Varanasi is a renowned destination for mango enthusiasts in India, known for its Langra variety of mangoes. The tale of a farmer who nurtured this particular type of mango is well-known among locals. The Banarasi Langra mango, available between June and July, is famous for its flavor and lemon-yellow skin. Dasheri, Himsagar, Kishan Bhog, and Chausa are other varieties of mangoes cultivated in India. (Detailed project report mango ready to serve manufacturing unit – IIFPT, Tanjavur)

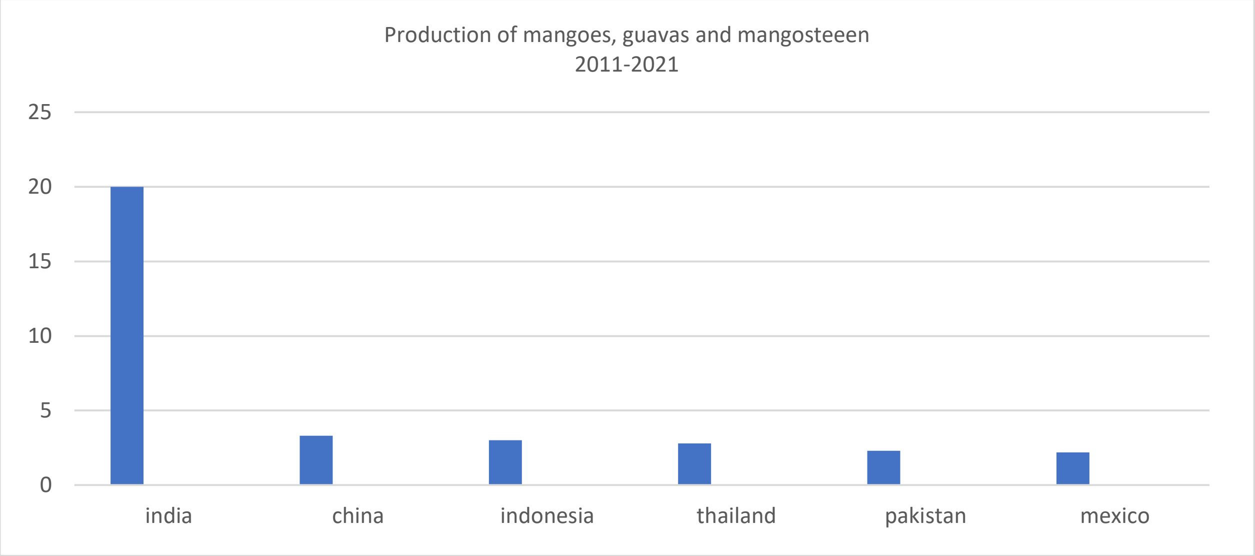

Figure 1. Graphical representation of production of mangoes, guavas and mangosteens in 2001-2021. (Source: Food and agriculture organization report 2021)

2. Reason for Mango Wine Production

Despite grapes being the primary raw material used to make wine, there is a growing interest in finding other fruits, such as apricot, apple, and palm sap, that are ideal for making wine. Local fruits that are inexpensive and easily accessible are utilized as an alternative to grapes in nations where they are not widely available. In developing nations like India, there is a 20–30% loss in fruit production due to post-harvest issues, improper use, along with processing technology. Converting garbage into value-added goods like wine is a clever solution to this issue. The production of mango wine is in high demand worldwide for several reasons, some of which are listed below. Mangoes are abundantly available throughout the season due to advanced technologies in the agriculture sector. This leads to an increase in fruit waste production. Fruit waste accumulates due to deteriorated, unsightly fruit skin colors, and improper storage temperatures. One of the most cost-effective ways to reduce fruit waste, in this case, is the production of wine from mango fruit. Figure 2 illustrates the increased revenue brought in by using mangoes in wine production, generating around 5,500 USD for 1 tonne of mangoes. This clearly demonstrates that producing wine is an efficient way to utilize surplus mango fruit.

DOI:https//doi.org/10.22452/mjs.vol44no1.11

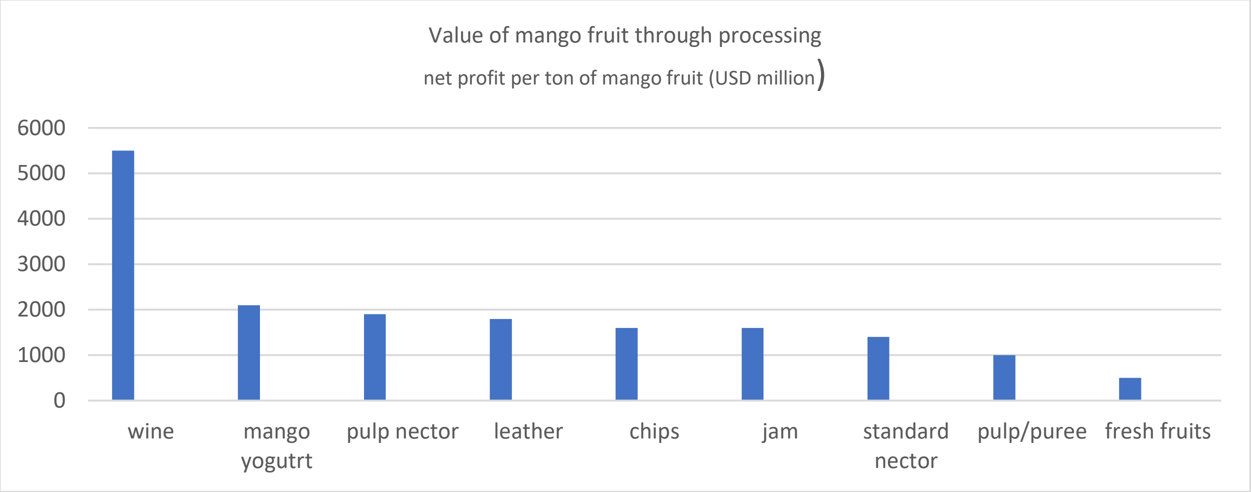

Figure 2. Net profits derived from processing one ton of mango (Source: FAO 2021 report)

3. Statistical Data of Mango Wine Production

France, Italy, and Australia have established themselves as leaders in the wine industry, thanks to their abundant grape production. India is ready to invest in its surplus mango production and transform it into value-added products. One option to maintain the flavor of mango fruit throughout the year is to create mango-based beverages, which will ultimately mitigate post-harvest losses during processing operations.

Figure 3. Representation of Indian wine export in 2002-2014 (Source: www.enterpreneurindia.co)

Despite the lack of statistical data on mango wine, this article aims to provide relevant information about mango wine production. According to available data, the Philippines is a major producer of mango-based alcoholic beverages such as mango wine, mango rum, and whisky. Mango wine is a popular home-brewed alcoholic beverage in the Philippines. However, the majority of beverages produced are for personal consumption. "Filipinos are manufacturing different types of wine and liquor that are set to take the global market," stated Ambassador Jose Maria Cariño, who heads the DFA's Cultural Diplomacy Unit. Developing nations such as India, Kenya, and Mexico are showing significant growth in fruit wine production. Mango wine is being developed by a group of mango growers in Andhra Pradesh. Five hundred farmers have registered and are collaborating to create value-added mango products. In addition, another 4,000 farmers are working to bring quality fruits, select, and process fruit concentrates and pulp for various mango delicacies.

4. Statistical Data of Mango Pulp

Mangoes are grown in India. In practically every region of the nation, there are numerous types to be found. Certain types of fresh mango fruit are used to make mango pulp. The completely developed mangoes are picked, swiftly transferred to the facility that processes the fruit, where they are examined and cleaned. Controlled ripening chambers are used to thoroughly ripen selected, high-quality fruits. Following thorough cleaning, the fruits are blanched, pulped, deseeded, centrifuged, homogenized, and concentrated as necessary. They are thermally processed and aseptically filled to maintain sterility. Mango pulp is a prominent export from India. During the years 2021–2022, the country exported 123,476.69 MT of mango pulp to the world for a total of Rs. 924.52 crores/124.11 USD Million. Half of the estimated 700,000 tonnes of mango pulp production worldwide come from India, which yearly produces 350,000 tonnes. India uses 150,000 tonnes of pulp domestically and exports 200,000 tonnes (APEDA). Major export destinations are Saudi Arabia, Yemen Republic, USA, Netherlands, UK, and Germany. Mango puree, also known as mango pulp, is a smooth and thick product that is processed to break up the fibrous, insoluble components of ripe mangoes. It retains all of the fruit juice as well as a significant amount of the naturally occurring fibrous material present in raw fruit. Mango puree is occasionally pasteurized to lengthen its shelf life.

DOI:https//doi.org/10.22452/mjs.vol44no1.11

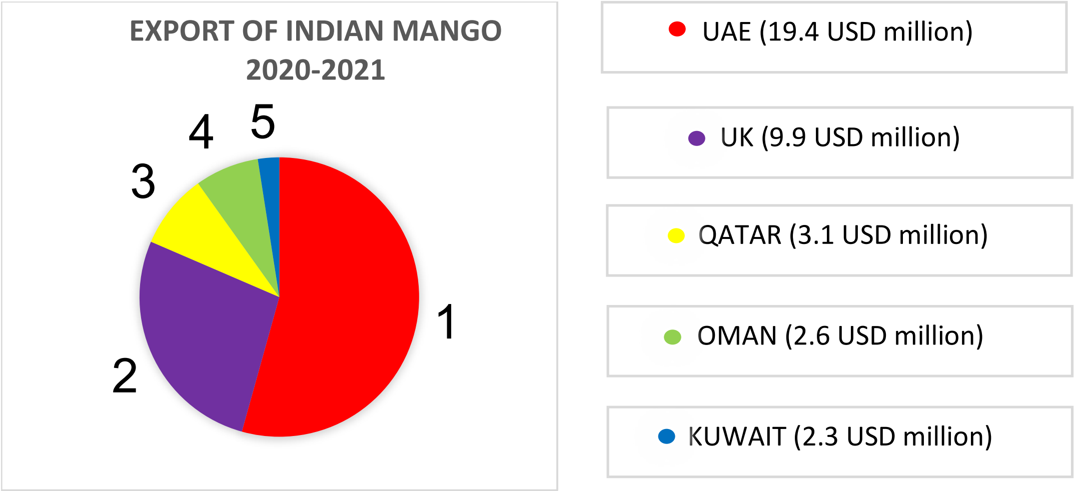

Figure 4. Export of Indian mangoes to different countries (Source. FAO report 2021)

The Middle East leads the market in both consumption and imports, with over 20% of all imports coming from the European Union. The fruit juice sector in Europe is the biggest consumer of mango puree, but it is also used in other industries, including ice cream and infant food. Mango pulp sales experienced exponential growth, and this trend is anticipated to continue. With a widely recognized variety of mangoes, mainly from India, being the leader among major mango farmers. Alphonso, Totapuri, and Kesar are employed in the pulp-making process. Mango pulp is a major food ingredient used in making mango-based beverages like mango juice and Mango wine.

5. Selection of Variety of Mango

Selection of mango variety depends on the percentage of mango juice yield and its quality, as well as its physicochemical characteristics. The availability of total soluble sugars (TSS) determines the amount of ethanol produced during fermentation. Furthermore, mangoes rich in glucose and fructose are readily available for yeast to convert into ethanol and carbon dioxide. Varieties like Alphanso, Banganpalli, and Totapuri are widely used in India for mango wine production, while Haden, Kent, Keitt, Ataulfo, and Tommy Atkins varieties are common choices in Mexico and Kenya. Previous studies have also utilized different types of South Indian mango varieties including Banganpalli, Alphonso, Raspuri, Totapuri, Banesha, Neelam, Mulgoa, Suvarnarekha, Rumani, and Jahangir (Reddy and Reddy, 2005). Among these, only a few varieties are suitable for winemaking. However, the present study aims to investigate the local mango varieties in Varanasi, Uttar Pradesh. Vikash Patel and Abhishek Dutt Tripathi (2020) screened five types of mango varieties, namely Banganpalli, Dashehari, Alphonso, Langra, and Totapuri. Among these, Banganpalli exhibited the highest mango juice yield, followed by Totapuri and Dashehari.

6. Selection of Yeast Strain

Sugar fermentation in wine is carried out by yeast cells in the inoculum. The primary factor separating wine from fruit juice is the function of yeast in the winemaking process. The potential alcohol content of the wine increases with the amount of sugars in the juice yield. Saccharomyces cerevisiae is the most prevalent yeast used in the production of wine. Different yeast strains were employed by various researchers. Each strain develops its distinct flavors during fermentation and has its own enzymatic patchwork. In this current study, Vikash Patel and Abhishek Dutt Tripathi (2020) used the freeze-dried Saccharomyces cerevisiae MTCC 178 strain collected from the Indian Institute of Microbial Technology, Chandigarh (India). The Department of Plant Pathology, Institute of Agricultural Sciences, Banaras Hindu University, Varanasi, provided another yeast isolate (ISY). These yeast strains were initially revived with peptone water and seeded onto PDA, which will be further used as inoculum preparation. Three Saccharomyces strains were employed by Reddy and Reddy in 2005. CFTRI 101 produced the most promising results during fermentation, followed by the other yeast strains isolated from palm wine and baker's yeast (Aman, 2022; Sing, 2021).

7. Fermentation

A complex substrate is turned into simple chemicals by the biological process of fermentation, which involves a variety of microorganisms including yeast, bacteria, and fungus (Ritika Joshi, Vinay Sharma, and Arindam Kuila*). Numerous investigations have revealed various fermentation methods utilized in the production of mango wine. The fermentation method differs in the use of various factors such as time, temperature, pH, and the type of yeast strain being implemented. However, Vikash Patel, Abhishek Dutt Tripathi (2020) used the batch fermentation technique carried out at 20°C for 15 days. Reddy and Reddy (2005) maintained the pH values at 3.5, 4, 5, and 6 and the temperatures at 20, 25, and 35°C for a period of 20 days.

8. Physicochemical Analysis of Mango Pulp

Physicochemical characteristics of mango juice include estimations of its total soluble solids, pH, and final titrable acidity. Through the use of a refractometer, brix readings were estimated. With the help of a pH meter and the DNS approach, the pH and reducing sugars were determined.

Physicochemical characteristics of mango juice include estimations of its total soluble solids, pH, and final titrable acidity. Through the use of a refractometer, brix readings were estimated. With the help of a pH meter and the DNS approach, the pH and reducing sugars were determined.

Table 1. Physiochemical properties of different mango varieties

Tests	Alphonso	Banganpalli	Alphonso	Banganpalli
TSS	18.60 ± 1.27	16.72 ± 1.28	16.0	20.5
Reducing Sugars	16.60 ± 0.80	2.1 ± 0.10	16.3	18.5
TA	0.44 ± 0.01	0.34 ± 0.06	0.350	0.326
PH	3.7 ± 0.80	4.2 ± 0.85	4.1	4.0

Source: (Vikash Patel & Abhishek Dutt Tripathi, 2020; Reddy & Reddy, 2005)

Volume of juice yield plays a crucial role in wine production, as it represents the ultimate amount of liquid obtained from fruits. Fruits with a high juice yield are preferred for wine making. According to estimates by Vikash Patel and Abhishek Dutt Tripathi (2020), Banganapalli and Totapuri varieties had the highest juice yield, with 16.72 and 13.26 TSS (Total Soluble Solids) respectively, whereas Alphanso and Langra had the lowest, with TSS of 18.60 and 15.57 respectively. Reddy and Reddy (2005) found that Banginapalli, with 20.5% TSS, was ideal for mango wine production. Li et al. (2012) conducted a study on three mango varieties (R2E2, Harum Manis) and concluded that Nam Doc Mai was the superior choice. These two studies showed slight variations in their findings.

9. Physicochemical Analysis of Mango Wine

According to research conducted by Vikash Patel and Abhishek Dutt Tripathi, the maximum ethanol concentration of the Banganapalli and Dashehari wines in the MTCC 178 (S2) yeast strain was 13% and 12% (v/v), respectively. The ethanol produced by the ISY (S1) sample also has close proximity with the ethanol produced by the MTCC 178 (S2) sample in Banganpalli and Dashehari varieties (13% and 11.5%). An earlier study by Reddy and Reddy (2005) revealed that using the CFTRI 101 yeast strain, the Banganapalli variety of mango produced 14.2% ethanol. The Langra (13.8) and Totapuri (11.8) varieties had high TSS, followed by Alphonso (11.0) with the S1 yeast strain. In both studies by Vikash Patel and Abhishek Dutt Tripathi (2020) and Reddy and Reddy (2005), the TA% value of the wine made from Alphonso was 0.600. The HPLC study of Dashehari and Langra wines also revealed the presence of gallic acid (3,4,5-trihydroxy-benzoic acid), a phytochemical with strong antioxidant qualities. The P-Hydroxybenzoic acid shows antioxidant, antibacterial, and antifungal properties (Vikash Patel, Abhishek Dutt Tripathi, 2020).

10. Factors Effecting Mango Wine Production

Alcoholic fermentation results from complex interactions involving the quantity of sugars present, yeast strain, and combinations of time and temperature. The ultimate quality of wine is significantly influenced by these factors. Numerous investigations have identified the elements that are evident during the fermentation process.

pH

The most significant controlling factor in the fermentation process is usually considered to be pH. Due to the activity of yeast during fermentation, the pH of wine is likely to increase. The ideal pH is proven to be crucial for the production of high-quality wines. So far, the Totapuri Variety Mango wine contains a high pH of 3.0, whereas the Langra variety of mango wine has a low pH of 4.0 (Vikash Patel and Abhishek Dutt Tripathi, 2020). Kumar et al. (2009) determined that a pH of 3.8 was suitable for mango wine fermentation.

Temperature

The fermentation process in winemaking largely depends on temperature. The ideal temperature for good quality wine is 68-86°F (20-30°C) (Reynolds et al., 2001). Wines that are fermented at low temperatures, such as 15°C, are lighter and more fragrant. When the proliferation of yeast cells doubles or declines, the temperature may rise or fall. Maintaining a constant temperature throughout the secondary fermentation is another efficient method for enhancing the quality of the final wine. Mango wine may be most effectively made around 25 °C.

Time

Since they have an effect on the end product's quality and content, fermentation time and temperature are essential (Mpho Maleke & Wesley Doorsamy, 2022). All varieties of Banganpalli, Totapuri, Langra, Mashehari, and Alphonso give better wine quality at a temperature of 25°C for 15 days (Vikash Patel and Abhishek Dutt Tripathi, 2020).

11. Medicinal Benefits of Mango Wine

Mangoes are claimed to be an excellent source of various vitamins, such as A, B, and C. Moreover, minerals like calcium, magnesium, iron, sodium, and phosphorous are found in mangoes along with vitamins. Additionally, malic, citric, and tartaric acids are present in small amounts in mangoes (Fizza Mubarik et al., 2020; Khongthaw et al., 2022; Dulta et al., 2021). Among multiple cultivars, the most common carotenoid is β-carotene, which is essential as a lipophilic radical scavenger. The total carotenoid content in mango wines ranges from 578-4330 g/100g, with Alphonso having the highest quantity at 4330 g/100g, followed by Sindhura at 4101 g/100g, Banginapalli at 2943 g/100g, Rumani at 2857 g/100g, and Totapuri at 690 g/100g (Reddy and Reddy, 2005). Ascorbic acid is another compound that increases during mango wine fermentation, effectively scavenging reactive oxygen and nitrogen species, including superoxide and hydroperoxyl radicals (Carol S. Johnston et al.,

DOI:https//doi.org/10.22452/mjs.vol44no1.11

2013). Reddy and Reddy's study on Alphonso mangoes revealed eleven distinct phenolic compounds. The Totapuri mango variety exhibited the highest content (1050 mg/l), followed by Alphonso, Banginapalli (725 mg/l), Sindhura (725 mg/l), and Sindhoora (490 mg/l), respectively. These polyphenols possess anti-inflammatory and antioxidant properties that could have advantageous preventive and/or therapeutic effects against obesity, cancer, neurological diseases, and cardiovascular ailments (Hannah Cory, Simone Passarelli, and Josiemer Mattei, 2018). In the research by Vikash Patel and Abhishek Dutt Tripathi, the Dashehari mango wine treated with S1 included gallic acid, a phytochemical with exceptional antioxidant properties that could serve as a potential functional food ingredient. The study also indicated that S1-treated Dashehari and Langra varieties of mango wine contained a significant amount of flavonoids and polyphenolic compounds.

12. Cost Economics

According to the study, 1305 ml of mango juice is required to make 1 L of wine. For 1L of wine, 2.25 kg of mangoes are required. The cost of raw materials is around Rs. 100, based on market prices. Therefore, the study provided evidence that 1L of mango wine will cost about Rs. 250. However, the Reddy and Reddy 2005 study showed a significant difference in the capital cost. There is only Rs. 100 cost for producing 1L of mango wine. The variation in the cost of 1L of mango wine in both studies is due to the cost of raw materials (mangoes) used and processing steps. The scale-up will, however, take the actual cost of production into account.

13. Other Fermented Products from Mango

Mango Feron

Mango Feron is the process of making ethanol from mango leaves. The students from Jiwaji University made an attempt to make wine from mango leaves and named it Mango Feron. The study reports that mango feron is rich in antibacterial properties and has shown significant results in the treatment of diabetes. The base wine contains approximately 8–12% ethanol.

Mango Vermouth

Mango vermouth is an aromatic fortified wine created from mango juice. Vermouth is described as a fortified wine with spices, aromatic compounds, and added flavors. Vermouth is another term for an aperitif.

Cashew Apple Wine

It is also one of the emerging alcoholic beverages in the brewery industry. It is usually made from the leftover part of the cashew fruit or false fruit. It is an effective method to utilize the waste generated from the cashew manufacturing industry.

14. Conclusion

One of the tropical fruits that are most widely grown worldwide is the mango. It is abundant in sugars and other crucial nutrients needed by humans. One of the beverage markets that is expanding the quickest globally is the fruit wine sector. By creating alternative fruit-based products like fruit wine, jams, and jellies as well as incorporating them into other foods, developed countries are able to utilize their excess fruit production. However, because of a lack of technology resources, developing countries fail to make the most of their fruit supply, resulting in a 5–10% fruit loss rate. This study focused on using the mango fruit to produce wine (*Mangifera indica*). This article provides a quick overview of the ethanol production process using local mango varieties such as Alphonso, Totapuri, Langra, and Dashehari. Mango wine consumption has many health advantages in contrast to its low alcohol content. The goal of this research is to promote fruit wine’s potential health benefits while also accelerating the market for the beverage.

15. References

Ahmad, A., Kaleem, M., Ahmed, Z., & Shafiq, H. (2015). Therapeutic potential of flavonoids and their mechanism of action against microbial and viral infections—A review. Food Research International, 77, 221-235.

Ajila, C. M., Naidu, K. A., Bhat, S. G., & Rao, U. P. (2007). Bioactive compounds and antioxidant potential of mango peel extract. Food chemistry, 105(3), 982-988.

Aman, J., Shahi, N. C., Lohani, U. C., Balodhi, D., Singh, R., Kumar, N., ... & Kumar, A. P. (2022). Process Optimization for Development of Guar Gum-Based Biodegradable Hydrogel Film Using Response Surface Methodology. Bioinorganic Chemistry and Applications, 2022.

Arribas MV, Polo MC. Wine making biochemistry and Microbiology: Current knowledge and future trends. Crit Rev Food Sci Nutr 2005;45:265-86.

C.SEKHAR, M. SELVARAJAN, A. POUNRAJ, and M. PRAHADEESWARAN, PRODUCTION AND EXPORT OF MANGO IN INDIA – A PARADIGM TO THE DEVELOPING NATIONS, January 2013, ISSN (CD-ROM): 2328-3688

da Silva, G. A., Augusto, F., & Poppi, R. J. (2008). Exploratory analysis of the volatile profile of beers by HS–SPME–GC. Food Chemistry, 111(4), 1057-1063.

Deshmukh, A. W., & Deshmukh, S. A. (2021). Herbal wine production from fruits and vegetable wastes and peels. International Journal of Engineering Applied Sciences and Technology, 5(9), 2455-2143.

Dias, D. R., Schwan, R. F., Freire, E. S., & Serôdio, R. D. S. (2007). Elaboration of a fruit wine from cocoa (Theobroma cacao L.) pulp. International journal of food science & technology, 42(3), 319-329.

Dulta, K., Koşarsoy Ağçeli, G., Chauhan, P., Jasrotia, R., & Chauhan, P. K. (2021). Ecofriendly synthesis of zinc oxide nanoparticles by

DOI:https//doi.org/10.22452/mjs.vol44no1.11

Carica papaya leaf extract and their applications. Journal of Cluster Science, 1-15.

Dulta, K., Thakur, K., Virk, A. K., Thakur, A., Chauhan, P., Kumar, V., & Chauhan, P. K. (2021). Comparison of different solvents for Antioxidant and Antibiogram Pattern of Bergenia ciliata rhizome Extract from Shimla district of Himachal Pradesh. Jordan Journal of Biological Sciences, 14(1).

Fehér J and Lugasi A, Antioxidant Characteristics of newly developed vermouthWine, Orv Hetil, 2005, 145, 2623-2627.

Fiscal, R. R., & Chavez, A. C. C. Wine Potential of Different Philippine Fruits..

Herrero M, Garcia LA and Diaz M 2003. The effect of SO2 on

Isitua CC, Ibeh IN. Novel method of wine production from Banana (Musa acuminata) and pineapple (Ananas cosmosus) Waste. Afr J Biotechnol 2015;9:7521-4.

Jordão, A. M., Vilela, A., & Cosme, F. (2015). From sugar of grape to alcohol of wine: Sensorial impact of alcohol in wine. Beverages, 1(4), 292-310..

Joshi VK and Parmar M. 2004. Present status, scope and future Strategies of fruit wines production in India. Indian Food Indus 24: 48-52.

Joshi VK and Parmar M. 2004. Present status, scope and future Strategies of fruit wines production in India. Indian Food Indus 24: 48-52.

Joshi VK, Attri BL, Panesar PS, Abrol GS, Sharma S, Thakur AD, Selli S. Specific features of table wine production technology, https://doi.org/10.1016/B978-0-12-800850-8.00007-7.

Joshi, V. K., & Parmar, M. (2004). Present status, scope and future strategies of fruit wines production in India. Indian food industry, 23(4), 48-52.

Khongthaw, B., Chauhan, P. K., Dulta, K., Kumar, V., & Ighalo, J. O. (2022). A comparison of conventional and novel phytonutrient extraction techniques from various sources and their potential applications. Journal of Food Measurement and Characterization, 1-26..

Khongthaw, B., Dulta, K., Chauhan, P. K., Kumar, V., & Ighalo, J. O. (2022). Lycopene: a therapeutic strategy against coronavirus disease 19 (COVID-19). Inflammopharmacology, 1-22.

Kumar KK, Swain MR, Panda SH, Sahoo UC, Ray RC. Fermentation of litchi (Litchi chinensis Sonn.) fruits into wine. Food 2008;2:43-7.

L.V. Trong, N.N. Khanh, L.T. Huyen and L.T. Lam, Changes in physiological and biochemical parameters during Growth and development of mango (Mangifera indica L.) fruit in Vietnam, 22(2): 137-142, 2020, DOI: 10.37855/jah.2020.v22i02.25

Li X, Bin Yu, Curran P and Liu SQ. 2012 Impact of two Williopsis yeast strains on the volatile composition of mango wine. Int J Food Sci Technol. 47: 808-815.

Li, X., Yu, B., Curran, P., & Liu, S. Q. (2011). Chemical and volatile composition of mango wines fermented with different Saccharomyces cerevisiae yeast strains. South African Journal of Enology and Viticulture, 32(1), 117-128.

Lu, Y., Chan, L. J., Li, X., & Liu, S. Q. (2018). Effects of sugar concentration on mango wine composition fermented by Saccharomyces cerevisiae MERIT. ferm. International Journal of Food Science & Technology, 53(1), 199-208.

Maleke M, Doorsamy W, Abrahams AM, Adefisoye MA, Masenya K, Adebo OA. Influence of Fermentation Conditions (Temperature and Time) on the Physicochemical Properties and Bacteria Microbiota of Amasi. Fermentation. 2022; 8(2):57. https://doi.org/10.3390/fermentation8020057.

Minh, N. P., Thao, D. T., Mai, P. X., Oanh, T. T. K., & Thai, H. Q. (2019). Different factors affecting the Mango (Mangifera Indica) Wine Fermentation. Journal of Pharmaceutical Sciences and Research, 11(3), 966-970.

Mohanty, S., Ray, P., Swain, M. R., & Ray, R. C. (2006). Fermentation of cashew (Anacardium occidentale L.)“apple” into wine. Journal of Food Processing and Preservation, 30(3), 314-322.

Moreno-Arribas, M. V., & Polo, M. C. (2005). Winemaking biochemistry and microbiology: current knowledge and future trends. Critical reviews in food science and nutrition, 45(4), 265-286.

Mubarik, F., Noreen, S., Farooq, F., Siddiqa, A., & Khan, M. (2020). Abasyn Journal of Life Sciences Open Access., DOI: 10.34091/AJLS.3.2.8.

Mukund, B.S. Reddy, S.B. Goudappa and Hiremath, G.M. 2019. Varietal Comparison of Mango Production and its Efficiency in Karnataka. Int.J.Curr.Microbiol.App.Sci. 8(11): 663-673. doi: https://doi.org/10.20546/ijcmas.2019.811.080

Owino, W. O., & Ambuko, J. L. (2021). Mango fruit processing: Options for small-scale processors in developing countries. Agriculture, 11(11), 1105.

Parmjit S Panesar, Narender Kumar, Satwinder S Marwaha And Vinod K Joshi, Vermouth Production Technology –An overview, Vol. 8(4), 2009, pp.334-344

Pino JA, Queris O. 2010. Analysis of volatile compounds Of mango wine. Food Chem (DOI: 10.1016/j.Foodchem.2010.09.056).

Pino JA, Queris O. 2010. Analysis of volatile compounds Of mango wine. Food Chem (DOI: 10.1016/j.Foodchem.2010.09.056).

Reddy LVA and Reddy OVS. 2007. Production of ethanol From mango (Mangifera india) juice fermentation. Res J Microbiol. 21: 441-445.

Reddy LVA and Reddy OVS. 2011. Effect of Fermentation Conditions on Yeast growth and Volatile composition of Wine produced from Mango (Mangifera indica L.) fruit Juice. Food Bioproduc Process. 89: 487-491.

Reddy LVA, Sudheer Kumar Y and Reddy OVS. 2009. Evaluation of volatile flavour compounds from wine Produced from mango fruits (Mangifera indica L.) by Gas chromatography and mass spectrometry (GC-MS). Ind J Microbiol 50: 183-191.

Reddy, L. V. A., Reddy, Y. S., & Reddy, O. V. S. (2010). Evaluation of volatile flavour compounds from wine produced from mangofruits (Mangifera indica L.) by gas chromatography and mass spectrometry (GC-MS). Indian J. Microbiol, 50(2), 183-191.

Sing, R. (2021). Sensory and nutritional qualities of multi-grain cookies supplemented with different level of rice bran. Food and Agriculture Spectrum Journal, 2(01), 5-7.

Sudheer Kumar, Y., Prakasam, R. S., & Reddy, O. V. S. (2009). Optimisation of fermentation conditions for mango (Mangifera indica L.) wine production by employing response surface methodology. International Journal of Food Science & Technology, 44(11), 2320-2327.

Sudheer Kumar, Y., Varakumar, S., & Reddy, O. V. S. (2012). Evaluation of antioxidant and sensory properties of mango (Mangifera indicaL.) wine. CyTA-Journal of Food, 10, 12-20.

The production of ethanol, acetaldehyde, organic acids And flavour volatiles during industrial cider fermentation. J Agric Food Chem 52: 3455-3459.

Varakumar S, Kumar YS and Reddy OVS. 2011. Carotenoid Composition of mango (Mangifera indica L.) wine and Its antioxidant activity. J Food Biochem. 35: 1538-1547

Williams D, Mishra S. The Indian Wine Market. USDA Foreign Agricultural Service, GAIN Report Number IN 1134, Global Agricultural Information Network; 2011.

Zhang, C., Yi, H., Gao, X., Bai, T., Ni, Z., Chen, Y., ... & Xie, D. (2022). Effect of Different Altitudes on Morpho-Physiological Attributes Associated with Mango Quality. Diversity, 14(10), 876.

MALAYSIAN JOURNAL OF SCIENCE
MJS
ISSN 1394-3065

Regular Issue

Malaysian Journal of Science 44 (1): 101-120 (March 2025)
https://mjs.um.edu.my

A Review on Modern Lunar Crescent Visibility Criterion

Muhamad Syazwan Faiz[1a], Mohd Saiful Anwar Mohd Nawawi[2b]*, Mohd Hafiz Mohd Saadon[3b] and Nazhatulshima Ahmad[4c]

Abstract: The modern lunar crescent visibility criterion is a criterion produced in the 20th century, which began with Fotheringham's criterion in 1910 and continued until the present date. A limited number of research studies have been conducted on the modern lunar crescent visibility criterion, with a majority of the studies placing focus on the design and social aspects of it. Therefore, this article aims to provide a review on the modern lunar crescent visibility criterion, which covers the scientific outlook of a lunar crescent visibility criterion: data locality, prediction strength and weaknesses, and its long-term legacy in visibility. The said review is conducted using systematic literature analysis, and specific inclusion and exclusion criteria, performed based on 27 works on the lunar crescent visibility criterion that pass the selection criteria. The review suggests that a new outlook on modern lunar crescent visibility criterion study can be obtained, by conducting an assessment of collected database of lunar crescent sightings, and by providing a comparative analysis tool for modern lunar crescent visibility criterion.

***Keywords:** : Review, lunar crescent, visibility, criterion.*

1. Introduction

The criterion used to predict the visibility of a lunar crescent during an observation is called the lunar crescent visibility criterion. Researchers have developed a lunar crescent visibility criterion based on records of lunar crescent sighting and their subjective definition of lunar crescent visibility, which can be telescopic definition, naked eye definition, or above the horizon definition. A telescopic definition of lunar crescent visibility criterion is based on visible lunar crescent sighting using a telescope, while the naked eye definition means that the criterion is based on naked eye visibility of lunar crescent, while an above-the-horizon definition is a lunar crescent visibility criterion that developed based on the position of a lunar crescent above the horizon, regardless of its visibility (Faid et al., 2022).

Schaefer highlighted that lunar crescent visibility is as one of the most non-trivial research projects in the field of astronomy. This is because lunar crescent visibility is directly involved in the calendrical making of the Muslim and Hebrew calendars. Muslims require visibility of the lunar crescent to determine dates of religious importance, such as the start of the fasting month of Ramadhan, the celebration of Eid Fitri, and the period of the Muslim pilgrimage. These events require a significant amount of raw material, human resources, traffic administration, and travel planning, involving millions of dollars in transfer every year. Karaites and Samaritans, being groups of Hebrew community found in Israel, use lunar crescent sighting to determine their lunisolar calendar: The Karaites need to observe the lunar crescent to determine their Rosh Chodesh holiday, while the Samaritans have developed a computation algorithm based on data of lunar crescent observation in order to determine their calendar (Faid, Nawawi, et al., 2024; Hoffman, 2003). This demonstrates the importance of research on lunar crescent visibility criterion in the present.

Authors information:
[a]Department of Islamic Studies, Centre for General Studies and Co-Curricular, Universiti Tun Hussein Onn Malaysia, 86400 Parit Raja, Johor, MALAYSIA. E-mail: mdsyazwan@uthm.edu.my[1],
[b]Academy of Islamic Studies, University of Malaya, 50603 Kuala Lumpur Malaysia. E-mail: saifulanwar@um.edu.my[2], mhms@um.edu.my[3]
[c]Department of Physics, Faculty of Science, 50603 Kuala Lumpur Malaysia. E-mail: n_ahmad@um.edu.my[4]
*Corresponding Author: saifulanwar@um.edu.my

Modern Lunar Crescent Visibility Criterion

Lunar crescent visibility was extensively studied during the medieval era since it was vital for purposes of calendrical making by the Islamic empire during that time (Mustapha et al., 2024). However, in keeping with the decline of science during the medieval times, the keenness to study the visibility of the lunar crescent diminished after the 16th century (King, 1991). Since then, the new Hijri month has been determined either with a lunar crescent sighting or a simple 29th-30th alternate rule. Research for lunar crescent visibility did not spark much interest among researchers until at least the 20th century (Ilyas, 1994). In 1910, Fotheringham sparked much interest in lunar crescent visibility research, followed by Maunder in 1911 and Danjon in 1936 (Danjon, 1936; Fotheringham, 1910; Maunder, 1911; Muhamad Syazwan Faid, Mohd Nawawi, and Mohd Saadon 2024). The interest then spread among the Muslim community, sparked by conflicting lunar crescent visibility reports and the determination of different dates for the new Hijri month (Moosa, 1998). This led to the first Muslim lunar crescent visibility criterion since the era of the Middle Ages, which is the Istanbul Declaration in 1976 (Mufid and Djamaluddin, 2023), followed by the Ilyas

Received: May 28, 2023
Accepted: December 7, 2023
Published: March 31, 2025

DOI:https//doi.org/10.22452/mjs.vol44no1.12

series of lunar crescent visibility criteria, the MABIMS lunar crescent visibility criterion in 1991, and later the Fatoohi lunar crescent visibility criterion in 1998 (Fatoohi, 1998; M. Ilyas, 1984; Mohd Nawawi et al., 2015).

The modern lunar crescent visibility criteria demonstrate frequent use of altitude, azimuth, and elongation parameters, and also the introduction of width and contrast threshold to further increase the accuracy of lunar crescent visibility prediction. Modern lunar crescent visibility criteria are more composite in parameters, and its designs are constructed through a larger compilation of lunar crescent visibility reports, in contrast to the lunar crescent visibility criteria in the Middle Ages (Faid, Mohd Nawawi, Abdul Wahab, et al., 2023). Since the rekindled interest in the lunar crescent visibility criterion by Fotheringham in 1910, which we marked as a starting point for the period of modern lunar crescent visibility criterion, at least 21 lunar crescent visibility criteria have beens produced, and various social aspects of lunar crescent visibility have been explored (M.S. Faid, Mohd Nawawi, and Mohd Saadon, 2023). Among the vast available literature on the lunar crescent visibility criterion, there have been a few attempts by Ilyas, Schaefer, and Fatoohi to provide a review on lunar crescent visibility. Ilyas (1994) was among the first to review the lunar crescent visibility criteria, including the Babylonian, Hindu, and Medieval lunar crescent visibility criteria. Ilyas's review, however, was biased towards his own lunar crescent visibility parameter. The Danjon limit, for example, was interpreted based on his finding of a 10.5 degree parameter. Ilyas also did not provide any solid counterargument for contradiction as highlighted by other researchers during his time. Zainal (2001) later summarised the review by Ilyas, largely only replicating Ilyas's argument without providing any additional thought on the study of lunar crescent visibility criteria.

Schaefer (1996) published another review on lunar crescent visibility criteria, supplementing each of his arguments with 294 lunar crescent observation records, providing a solid finding for each criterion's parameter. However, he took the same path as Ilyas, although with less severity, interpreting the lunar crescent visibility criterion reviewed under the glass of his own criterion. It was also found that Schaefer had miscalculated some of his findings (Loewinger, 1995), was inconsistent in deciding his constant coefficient (Fatoohi, 1998), and was unclear on the definition of the term lunar brightness (Sultan, 2007). Fatoohi (1998) produced a comprehensive review of lunar crescent visibility criteria, using more than 500records of lunar crescent observation. Fatoohi's review covers Ancient lunar crescent visibility criteria to Yallop's (1998) composite criteria. However, it was limited to records of lunar crescent observation that predate1998 and the criteria produced before the publication of his thesis. Fatoohi's review was dated almost 30 years ago, and in the last 10 years, there has been no review of the modern lunar crescent visibility criterion conducted by any researcher. The limited presence of review literature on modern lunar crescent visibility criterion signifies the research gap on this matter. Therefore, this research attempts to provide a review of the modern lunar crescent visibility criterion to provide a refreshed view on the subject.

2. Methodology

To achieve the aims of our study, a review was undertaken using the PRISMA review method (Rethlefsen et al., 2021). The selection criteria for including papers are as set out in Figure 2. Selected papers were retrieved from the Google Scholar, Scopus, Mendeley, and Web of Science databases on 30 April 2023 using the search terms lunar crescent visibility criterion, new moon visibility criterion, Imkanur Rukyah criterion, and hilal visibility criterion (n = 43). Duplicate records were removed, and the study was limited to journal papers to retain robust peer-reviewed references. Then, the lunar crescent visibility criterion that was published before 1910, which is the timeframe of the modern lunar crescent visibility criterion, was excluded. Any literature published later than 1910 but contained study of criterion that predates 1910 was also excluded. The same exclusion applies for literature that is not peer-reviewed, and published in non-indexed journals. Finally, literature that discusses the social aspects of lunar crescent visibility criterion, and does not provide its lunar crescent visibility criterion was excluded as well. A total of 27 articles on the lunar crescent visibility criterion passed the exclusion criteria. The selection criteria are set out in Figure 1. Meanwhile, Table 1 portrays literature that passes the inclusion and exclusion criteria.

Literature search and selection is the first exercise conducted in this research. The literature search was conducted using Google Scholar, Scopus, Mendeley, and Web of Science databases. The search keywords are: lunar crescent visibility criterion, new moon visibility criterion, *Imkanur Rukyah,* and hilal visibility criterion. A total of 43 articles were covered using the aforementioned search and selection criteria. Then, the lunar crescent visibility criterion published before the timeframe of the modern lunar crescent visibility criterion (which is 1910) was excluded. Literature published later than 1910, but contain study of criterion that predate 1910, were also excluded. Literature that is not peer-reviewed, and published in non-indexed journals, were excluded. Finally, literature that discusses the social aspects of lunar crescent visibility criterion, and does not provide its lunar crescent visibility criterion, is excluded. A total of 27 articles on the lunar crescent visibility criterion passed the exclusion criteria. Table 1 portrays the literature that passed the inclusion and exclusion criteria.

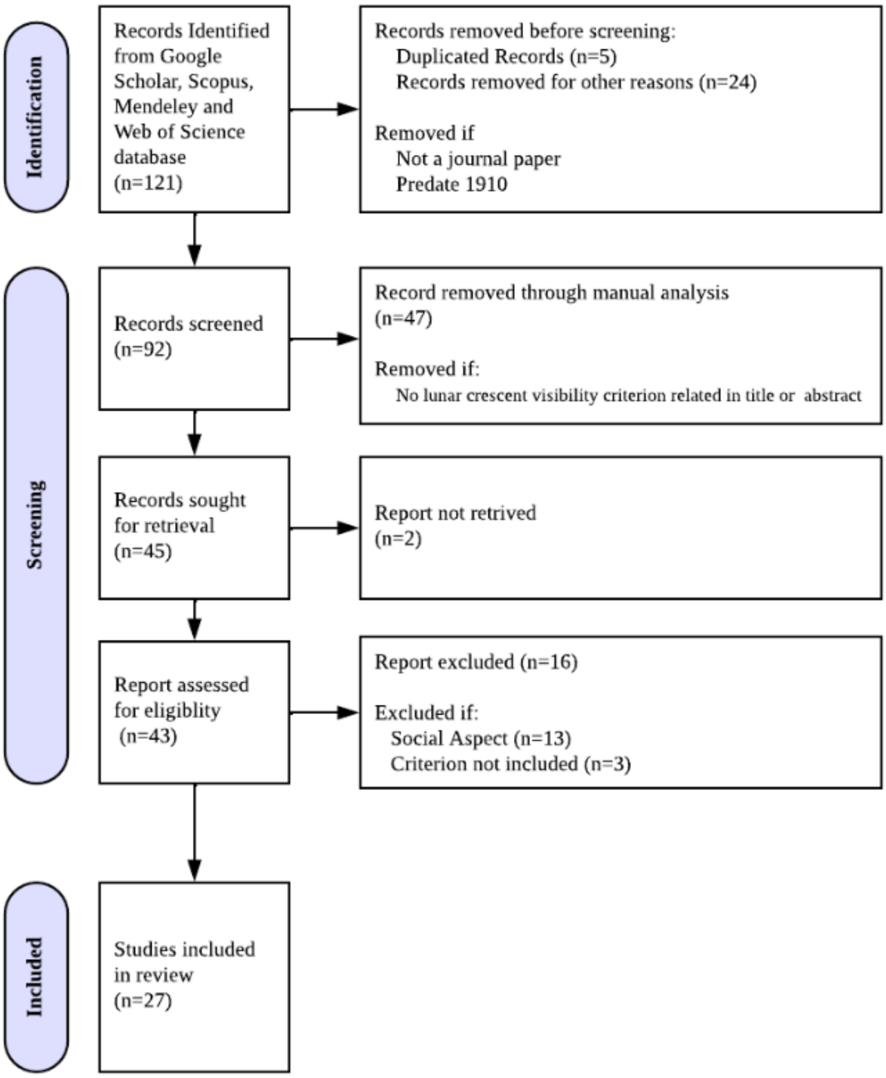

Figure 1. Selection Criteria for the literature review using the PRISMA review process.

Table 1. Lunar Crescent Criterion from Selected Publications

No	Parameter	Source	Year	Lunar Crescent Criteria Expression
1	Altitude & Azimuth	Fotheringham	1911	$ARCV \geq 12.0 - 0.008\Delta AZ$
2		Maunder	1912	$ARCV \geq 11 - 0.005\lvert\Delta AZ\rvert - 0.01\Delta AZ^2$
3		Ilyas	1984	$Arcv = -0.0027356815\, DAZ + -0.0136648716\, DAZ^2 + 0.0002119205\, DAZ^3 + 10.2832719598$
4		Fatoohi	1998	$ArcV_{Upper\ Limit} = 10.7638 + 0.0356\, \Delta Az - 0.0164\Delta Az^2 + 0.0004\Delta Az^3$ $ArcV_{Lower\ Limit} = 9.2714 - 0.0644\, \Delta Az - 0.0058\Delta Az^2 + 0.0002\Delta Az^3$
5		Krauss	2012	$Arcv^{Athenian} = 0.0291254840\, DAZ + -0.0098347831\, DAZ^2 + 0.0000475196\, DAZ^3 + 10.5981838905$
6		MABIMS 1995	1995	$ARCL \geq 3° \& ARCV \geq 2°$
7		Istanbul	2016	$ARCL \geq 8° \& ARCV \geq 5°$
8		MABIMS 2021	2021	$ARCL \geq 6.4° \& ARCV \geq 3°$
9	Elongation	Danjon	1936	$ARCL \geq 7°$

10		Ilyas	1983	$ARCL \geq 10.5°$
11		McNally	1984	$ARCL \geq 5°$
12		Schaefer	1991	$ARCL \geq 7.5°$
13		Fatoohi	1998	$ARCL \geq 7.5°\ for\ optical\ aided$ $ARCL \geq 9.1°\ for\ naked\ eye$
14		Odeh	2004	$ARCL \geq 6.4°\ for\ optical\ aided$ $ARCL \geq 7.7°\ for\ naked\ eye$
15		Sultan	2007	$ARCL \geq 5°$
16		Hasanzadeh	2012	$ARCL \geq 5°$
17	Singular Elongation Variable	Danjon	1936	$ARCL \geq 7°$
18		Ilyas	1985	$ARCL > 10.5$
19		McNally	1985	$ARCL > 5.0$
20	Arc of Vision & Lunar Width	Bruin	1977	$ArcV = 11.5621745317 - 7.944238328\, w' + 3.2608487770\, w'^2 - 0.4559413249\, w'^3$
21		Ilyas	1985	
22		Yallop	1998	$q = (ARCV - 11.8371 + 6.3226W' - 0.7319W'^2 + 0.1018W'^3)/10$
23		Odeh	2004	$V = ARCV - (-0.1018W^3 + 0.7319W^2 - 6.3226W + 7.1651)$
24		Qureshi	2012	$S = (ARCV - 0.351964\, W^3 + 2.222075\, W^2 - 5.422643\, W + 10.43418)$
25		Alrefay	2018	$ARCV_{Naked\ Eye} > 9.34 - 4.51w + 3.3W^2 - 1.01W^3$ $ARCV_{Optical\ Aided} > 7.83 - 4.35w + 3.22W^2 - 1.02W^3$
26	Lag Time & Elongation	Caldwell	2010	$lag\ (') > -0.9709\ arcl + 44.65\ for\ naked\ eye\ sighting$ $lag\ (') > -1.9230\ arcl + 43.13\ for\ optical\ aided$
27	Gautschy	Lagtime & Arc of Vision	2014	$Latime = 0.3342328913\, \Delta AZ + -0.0715608980\, \Delta AZ^2 + 0.0009924422 * \Delta AZ^3 + 33.8890455442$

The purpose of this review paper is to gather fragmented knowledge and place them into a single documentto provide a detailed perspective on the current state of lunar crescent visibility research. It should be noted that there are other reviews available that have a more focused method of conducting lunar crescent sighting criterion study, such as a comprehensive assessment of the lunar crescent visibility criterion (Fatoohi, 1998). Some articles consider a particular analysis viewpoint, such as lunar cycle analysis (Rahimi and Zainal, 2019; Rodzali and Man, 2021), while others focus on a specific parameter, such as the histogram bias analysis (Doggett et al., 1994), or provide only literature review without technical analysis, such as Zainal (2001). This review identifies the background and theory used to develop a lunar crescent visibility criterion by each researcher and examines the locality of the data used for the criterion developed. Each developed lunar crescent visibility criterion is portrayed in a table to enable its reconstruction using the regression technique. Each lunar crescent visibility criterion's strengths, weaknesses, and long-term impact of visibility research are highlighted to provide a neutral outlook of it. This review is critical and timely as studies on the lunar crescent visibility criterion are growing rapidly in number (Utama et al., 2023; Zulkeflee et al., 2022). The information given will aid those who are interested in the topic to gain an understanding of key methods and their applications. This review aims to highlight the solutions used in the past and identify ways in which they can be used and improved in the future.

3. Review of Modern Lunar Crescent Visibility Criterion

Studies on the visibility of lunar crescent diminished after the 16th century, in parallel with the fall of Islamic Science during the Middle Ages (King, 1993). Since then, the new Hijri month is determined either by way of lunar crescent sighting or by using the simple 29th-30th alternate rule. Research on the lunar crescent visibility limit did not garner much interest until the 20th century (M. Ilyas, 1997a). In 1910, Fotheringham sparked the interest in lunar crescent visibility limit research, followed by Maunder in 1911 and Danjon in 1936. Interest in the topic then rekindled among the Muslim community, following conflicting lunar crescent visibility reports and different dates applied for new Hijri months (Mohammad Ilyas, 1984). This led to the first Muslim lunar crescent visibility criterion since the era of the Middle Ages, Istanbul Declaration in 1976 (Rodzali & Man, 2021), followed by the Ilyas series of lunar crescent visibility criterion, the MABIMS lunar crescent visibility criterion in 1991, and the Fatoohi lunar crescent visibility criterion in 1998. The modern lunar crescent visibility criterion demonstrates frequent use of altitude, azimuth, and elongation parameter. Modern lunar crescent visibility criterion also saw the introduction of width and contrast threshold to further increase the accuracy of lunar crescent visibility prediction. Modern lunar crescent visibility criteria are more composite in parameter and their design constructed through larger compilation of lunar crescent visibility reports, in contrast to lunar crescent visibility criterion during the Middle Ages.

Fotheringham's Lunar Crescent Visibility Criterion

John Knight Fotheringham was born in 1874 in Britain. An expert in historical astronomy, he was also influential in establishing the chronology of the Babylon empire In 1910, Fotheringham published a study on the lunar crescent visibility criterion, incidentally sparking interest on the matter which has been stagnant for at least two centuries. While works of lunar crescent visibility has been published since 1868 by Johann Schmidt, a majority of the studies discuss the report of lunar crescent visibility and lunar crescent visibility criterion of the past, whereas Fotheringham was the first to introduce his own lunar crescent visibility criterion.

Fotheringham incorporated altitude and azimuth in his lunar crescent visibility criterion (Fotheringham, 1910). His curve can roughly be represented in the expression of,

$$Arcv = -0.1758223322\,\Delta AZ + 0.0225942071\,\Delta AZ^2 + -0.0009955850\,\Delta AZ^3 + 12.0825223783$$

3.1

Source: Researcher Data

His curve is calculated at sunset. Fotheringham does not state where he gathered ideas to construct the lunar crescent visibility curve using altitude and azimuth parameter, although Ilyas claimed that it was inspired by the Battani lunar crescent visibility curve (Ilyas, 1987). Fotheringham formulated his lunar crescent visibility curve from 55 positive data and 21 negative data of lunar crescent observation. His data is compiled from the collection of Mommsen and Julius Schmidt lunar crescent visibility data (Mommsen, 1883; Schmidt, 1868). He added that his lunar crescent visibility curve is applicable at any given location, with slight adjustments according to atmospheric extinction. The Fotheringham table of lunar crescent visibility curve is portrayed in Table 3.1 below.

Table 3.2. Fotheringham Table of Lunar Crescent Visibility Curve

Difference in Azimuth (˚)	Arc of Vision
0	12
5	11.9
10	11.4
15	11.0
20	10.0
23	7.7

Source : Fotheringham (1910)

The Fotheringham lunar crescent visibility criterion suggests that the lunar crescent will be visible at a lower altitude if separated by a considerable number of azimuths. Deducing from his visibility curve expression, at 38 degrees of azimuth, lunar crescent is visible at 0 degree of altitude. In real observation, it is not feasible for lunar crescent to be visible at 0 degree of altitude due to the effect of concentrated air mass and high level atmospheric extinction (Schaefer, 1986).

Maunder criticized the Fatoohi visibility curve, stating that his design is primarily based on positive lunar crescent visibility records and ignored a majority of negative sightings. Maunder adds that if a lunar crescent is reported visible at a given parameter at a certain location, it does not guarantee that the same lunar crescent parameter would bevisible at other times and other locations. This is because cloud and atmospheric conditions could hamper the visibility of a lunar crescent. Fotheringham's lack of attention to negative lunar crescent observation has caused its visibility curve to be located at a higher visibility threshold, consequently causing the inability to accurately predict several negative lunar crescent visibility reports (Fatoohi tand Stephenson, F. Richard; Dargazelli, 1999).

Fotheringham data compilation was carried out based on two sources, Mommsen, and Schmidt, both located in Athens. This made his visibility only viable for Athens, and susceptible to error at other latitudes. His data of altitude and azimuth were calculated without consideration of parallax and refraction, making his data subject to error up to 1 degree in real observation. Fatoohi, when examining Fotheringham's lunar crescent visibility criterion, discovered that Maunder's claim on the flaws of Fotheringham's lunar crescent visibility criterion was true. Fotheringham's high visibility curve ignored most of the negative lunar crescent sightings. In addition, Fotheringham's claim that his criterion is adaptable at any given latitude is erroneous as it was discovered that his criterion has been highly erroneous in predicting lunar crescent visibility at other latitudes (Fatoohi & Stephenson, F. Richard; Dargazelli, 1999).

DOI:https//doi.org/10.22452/mjs.vol44no1.12

Despite its shortcomings, the Fatoohi lunar crescent visibility criterion has sparked positive competition among astronomers in designing lunar crescent visibility criterion. His altitude and azimuth parameter led to the design of Maunder lunar crescent visibility criterion, and inspired research on other topocentric parameter of lunar crescent visibility such as elongation and width, His framework of altitude-azimuth parameter is still being used today by Muslim countries (such as the regional body MABIMS) to determine their new Hijri month (Fatoohi, 1998).

Maunder's Lunar Crescent Visibility Criterion

Edward Walter Maunder was a British resident, born in 1851. He was an influential astronomer in solar observation, famously associated with the term *Maunder Minimum* to describe the period of prolonged solar minimum from 1645 to 1715 (Eddy, 1976). In 1911, Maunder published a lunar crescent visibility criterion in his article "On the Smallest Visible Phase of the Moon". His article is a form of refinement of Fotheringham's works, which he heavily criticised as being too pessimistic in predicting lunar crescent visibility.

Similarly with Fotheringham, Maunder incorporates altitude and azimuth for his lunar crescent visibility criterion. His lunar crescent visibility criterion is demonstrated with a table and can be expressed in the form of a formula, as follows:

$$ArcV = 11 - 0.05\ \Delta AZ - 0.01\ \Delta AZ^2$$

3.1

Source : Researcher Data

The Maunder criterion is calculated at sunset, and the Maunder table of lunar crescent visibility curve is demonstrated in Table 3.2 below.

Table 3.3. The Maunder Table of lunar crescent visibility criterion

Different in Azimuth (°)	Arc of Vision (°)
0	11.0
5	10.5
10	9.5
15	8.0
20	6.0

Source : Maunder (1911)

Maunder applied the same altitude-azimuth framework as Fotheringham for his lunar crescent visibility criterion, the only difference being that the Maunder visibility curve is lower than the Fotheringham visibility curve. This is due to the consideration of negative observation in Maunder visibility curve (Krauss, 2012). The Maunder lunar crescent visibility criterion uses the same data as Fotheringham with an additional 11 data from various latitudes, amassing 87 data from lunar crescent visibility records, with 66 positive observations and 21 negative observations. In terms of location, the Maunder lunar crescent visibility data is clustered around Athens. Maunder insisted that his visibility curve is more reliable since it has considered both negative and positive observations. As the Maunder lunar crescent visibility curve uses the same framework with Fotheringham, his criterion would suggest that a lunar crescent is visible at 0 degree arc of vision and 30 degrees of difference in azimuth, which would be impossible due to atmospheric extinction and air mass. Alternatively, the Maunder visibility curve suggests that the lunar crescent is visible at 11.0 degrees arc of vision, whilst its azimuthal difference is 0 degree. This is not necessarily the case, as Fatoohi recorded a visible lunar crescent at as low as 6.2 degrees and 0.5 azimuthal difference (Fatoohi et al., 1998).

Maunder's correction of the Fotheringham visibility curve, although commendable, is still under the framework of altitude-azimuth visibility curve. Despite Maunder's attempt to accurately draw the line between positive and negative lunar crescent, his altitude-azimuth criterion has produced the sames issue as that which arose for the Fotheringham criterion. A high visibility curve would favour prediction for negative data but it would be unable to predict positive data, while attempts to lower the visibility curve will favour prediction for positive data but reduce the successful rate of negative data prediction. It is also noted that the framework of altitude-azimuth lunar crescent visibility criterion is dependent on latitude.

Fatoohi, in his assessment of Maunder's visibility curve accuracy, found that it has a contradiction rate of 17.8 percent in predicting positive observation, while 15.5 percent of the negative lunar crescent observation data was found to fall above Maunder's visibility curve. Thus, Maunder visibility curve can be said to be far superior to other visibility curves that adopt the altitude-azimuth framework, such as Neugebauer and Schoch. However, due to its adoption of the altitude-azimuth framework itself, its capability to predict lunar crescent visibility is not satisfactory (Neugebauer, 1929). Maunder's lunar crescent visibility criterion, despite its flaws, demonstrated how lunar crescent visibility is designed. Maunder showed that rather than favouring positive observation in the construction of lunar crescent visibility criterion, the consideration of negative observation greatly increases the accuracy of any criterion.

Danjon's Lunar Crescent Visibility Criterion

André-Louis Danjon was born in Caen, France in 1890. He was a notable French astronomer, famously credited for introducing a qualitative scale for measuring appearance and luminosity of the lunar crescent, known as the Danjon scale. In 1936, through a collection of 75 measurements and estimation of lunar crescent lengths, Danjon published a work entitled "Le Croissant Lunaire", or "The Lunar Crescent". In his work, Danjon explained the relationship between angle of separation from sun and moon or elongation against the length of a lunar crescent. Danjon stated that the length of lunar crescent increases from 0 degree to 180 degrees in proportion with elongation from 7 degrees to 180 degrees. He deduced that the lunar crescent is invisible for elongations below 7 degrees due to being shadowed of the lunar mountain. Danjon's compilation of 75 measurements of lunar he crescent length showed elongation ranging from 8 degrees to 90 degrees. This indicates that the value of 7 degrees is not the result of direct measurement of lunar crescent, instead it is a product of extrapolation from his graph. In fact, the lowest crescent length was recorded at 6.2 degrees with 8 degrees of elongation. This means that the result obtained of 7 degrees is an interpretation by Danjon and subject to other interpretations by other researchers (Danjon, 1936).

The limit of 7-degree elongation for crescent length, or currently known as the Danjon limit, has been highly contested by researchers. McNally argued that the average lunar radius has a variation of 0.6%, which is too small to cast a shadow that overcast lunar crescent length (McNally, 1983). He then explained that the deficiency of lunar crescent length is due to atmospheric seeing on the cusp of the lunar crescent. Atmospheric seeing cause the cusp brightness of the lunar crescent to be reduced, hence impact the shortening of the visible cusps of lunar crescent. Schaefer (1991) on the other hands, provided a different explanation of the shortening of the lunar crescentClick or tap here to enter text.. He agreed with McNally that it is not plausible to attribute lunar crescent shortening to the shadow of lunar mountain, as it requires a height of 12 km of lunar mountain shadow to overcast the lunar crescent. The highest mountain on the moon is Mons Huygens that has 5.5 km in elevation (Spain, 2009). However, Schaefer disagrees with McNally on the causative effect of atmospheric seeing on the length of lunar crescent. Schaefer supplemented his disagreement by stating that his Moonwatch project indicates that both telescopic and visual observations report the same length of lunar crescent. By McNally modelling, telescopic and visual observers should have different impact of atmospheric seeing, thus contributing to different lengths of lunar crescents (L. Doggett et al., 1994; Ilyas, 1983b). Schaefer conceded that McNally modelling is not applicable in explaining the length of lunar crescent. Schaefer suggested that the reason of the shortening length of lunar crescent at lower elongation is due to the sharp reduction of integrated brightness towards the cusps. The reduction in brightness decreases the detectable contrast, thus contributing to the shortening of lunar crescent. Schaefer then cemented his theory that a 7.5 degree of elongation would be a plausible elongation limit for detectable lunar crescent, or Danjon limit.

Agreeing with Schaefer, Ilyas (1983b) conceded that the shortening is due to the brightness deficiency at the cusps, making it undetectable in human eye Click or tap here to enter text.. However, Ilyas provided a different model to explain his theory, where he eliminated the 8-degree elongation data in Danjon measurement, and then provide a new extrapolation curve that has the lowest limit of 10.5 degree in elongation. He also supported his argument for 10.5 degrees in elongation by deriving the value of elongation from the lowest limit of width. He argued that the lowest limit of detectable width w= 0.25’ would attribute to elongation of 10.5 degrees using the formulation $W = dsin^2(\frac{L}{2})$.

Sultan (2007) attempted to provide a different explanation for the shortening of lunar crescent lengthClick or tap here to enter text.. He argued that lunar crescent visibility is dependent on the surface brightness per area of the lunar crescent, instead of total integrated brightness. This means that the absence of lunar crescent data for elongation below 7.5 degrees is due to the surface brightness of the lunar crescent at the cusps having a low contrast to be visible with the naked eye. However, optical aided observation is a different case. Sultan argued that optical aided observation would be able to break the 7-degree Danjon limit as optical aided observation can increase the size of the lunar disk while maintaining its surface brightness. Sultan then proved theoretically that optical aided observation at 200 magnifications is able to observe a lunar crescent at 5-degree elongation.

Hasanzadeh (2012) conducted a multi-test to examine the Danjon limit of lunar crescent visibility. Amir conducted experiments which involved extrapolation of elongation against the length of lunar crescent, with additional parameter of atmospheric seeing, lunar mountain shadowing and libration. Amir also experimented with Sultan’s method of determining Danjon limit, by observing the lunar crescent at 120 magnifications. Interestingly, all the experiments conducted by Hasanzadeh resulted in the limiteds elongation of 5 degrees for lunar crescent visibility.

Despite the differences in explaining the reasons for lunar crescent length shortening, Danjon, McNally, Schaefer, Ilyas, Sultan and Hasanzadeh have all contributed to understanding the limits of lunar crescent visibility. Danjon and Schaefer were correct to predict the visibility limit at 7 – 7.5 degree elongation, as it is proven that the naked eye is capable of detecting lunar crescent at 7.7 degree of elongation. The argument contended by McNally, Sultan, and Amir, that lunar crescent is possible to be sighted at elongation below 7 degrees, is warranted, with the 6.0 degree and 3.5 degree of elongation being applicable for optical aided and CCD observation. The claim for 10.5 degree elongation for naked eye limit by Ilyas is somewhat justified with a majority of the lunar crescent visibility falling under the range of 9.0 to 10.5 degree of elongation.

Bruin’s Lunar Crescent Visibility Criterion

Frans Bruin was born in 1922, in Hague, Netherlands. He was a professor of physics in American University of Beirut and director of Universität Bern Astronomical Institute observatory. He was one of the famous historians of astronomy and had the opportunity of working together with the likes of Otto Neugebauer and Edward Kennedy (King, 2002). In 1977, Bruin constructed a lunar crescent visibility criterion that pioneers in inclusion of astrophysical aspects of lunar crescent visibility. Bruin incorporates the parameter of lunar width, altitude, and azimuth in his criterion, which was expressed in the various values of width ranging from 0.5’,0.7’,1’, 2’ and 3’, with attribution of solar depression and arc of vision on its axis. The Bruin visibility curve s as portrayed in Table 3.3 below (Bruin, 1977).

Table 3.4. Bruin Tables of Value for Lunar Crescent Limiting Visibility

Lunar Width (‘)	Arc of Vision (°)
0.5	8.45
0.7	7.23
1	6.55
2	5.05
3	4.77

Source : Bruin (1977)

The application of Bruin lunar crescent visibility criterion is complicated. First, the width of the observed lunar crescent needs to be calculated. Taking for example a lunar crescent width of 2’, during lunar crescent observation, at 5.5 degrees of lunar altitude, the lunar crescent is visible at solar depression of 4.0 degrees until 0.8 degrees, meaning that it has a 12.8-minute window of opportunity. Bruin’s lunar crescent visibility criterion is not only able to predict the visibility of the lunar crescent, at the same time it is also able to estimate the time windows for successful observation. The Bruin lunar crescent visibility criterion is expressed in Equation 3.3.

$$ArcV = -0.1324039674w + 0.0009057913w^2 + -0.0000021108\,w^3 + 11.5621745317 \quad 3.2$$

Source : Researcher’s Data

In designing his criterion, Bruin has made the following assumption. First, he assumed that the sky brightness is uniform regardless of altitude and azimuth, with only solar depression as a single brightness variable (Koomen et al., 1952). Second, Bruin assumed that the brightness of the lunar crescent is uniform across its surface, with only the lunar crescent altitude acting as a presenter for atmospheric extinction. Third, Bruin assumed that the minimum contrast required for lunar crescent visibility is associated with lunar surface area. For this assumption, Bruin adopted the works of Siedentopf circular disk visibility threshold and converted it into lunar width (Bemporad, 1904). Bruin used the assumption in his design for lunar crescent visibility criterion, instead of using actual observation of lunar crescent. Bruin stated that his criterion has been experimented on for 10 years, and his assumptions are correct without requiring further refinement.

All three of Bruin’s assumptions were in fact incorrect. First, the assumption that sky brightness is uniform with only solar depression acting as a single brightness variable is entirely wrong. The model developed by Kastner demonstrated that the brightness of sky during twilight is dependent on solar depression, altitude, and azimuth of the observed object (Kastner, 1976). The Kastner modelling warrants a high accuracy and is still relevant for current application (Faid et al., 2016, 2018).

Second, the assumption that the brightness of the lunar crescent is singularly dependent on lunar crescent altitude is not entirely correct. Although lunar crescent altitude can represent atmospheric extinction in the simplest form, the impact of atmospheric extinction to lunar brightness is more complex and require complex variables. Schaefer has laid out the computations required to measure the impact of atmospheric extinction on lunar brightness, encompassing air mass, temperature, season, atmospheric layer, humidity, altitude, latitude, and wavelength. Thus, to simply express the impact of atmospheric extinction on lunar brightness in the form of lunar crescent altitude is an oversimplification. Third, Bruin adopted Siedentopf circular disk visibility threshold in his criterion by assuming its applicability for lunar crescent visibility threshold. Circular disk visibility and lunar crescent visibility threshold are heterogenous. This is because the surface area and the shape of lunar crescent are entirely different from that of circular disk. Blackwell's model of crescent visibility threshold in 1946 is more suitable for Bruin lunar crescent visibility criterion instead of Siedentopf’s works (Blackwell, 1946).

Fatoohi, in assessing the reliability of Bruin’s lunar crescent visibility criterion, discovered that Bruin has underestimated the capability of the human eye to detect the limiting width of lunar crescent (Fatoohi, 1998). There are 77 reports of lunar sightings with lunar crescent width of less than 0.5’ observed by the naked eye, with the thinnest width to be at 0.17’. This is way below the visibility limit of the Bruin lunar crescent width of 0.5’. Fatoohi further added that Bruin that miss predict 27.7% of the positive observation, 9.6% of negative observation. The Bruin lunar crescent visibility criterion, despite the incorrect assumption of lunar crescent visibility and its underestimation of the human eye detection capability, was a pioneer in designing an astrophysical lunar crescent visibility criterion. It created a pathway for Schaefer, Sultan, and Faid to create their own astrophysical lunar crescent visibility criterion (Bradley Schaefer, 1996a; Sultan, 2007b; Muhamad Syazwan Faid, Nawawi et al., 2023).

Ilyas’s Lunar Crescent Visibility Criterion

Ilyas was born in Meerut, India, in 1950. He is one of the Muslim pioneers in the research of lunar crescent visibility. Between 1983 and 1994, he published at least 10 articles on lunar crescent visibility and Islamic calendar. Ilyas played a pivotal role in bringing Muslim astronomers into research of lunar crescent visibility and Islamic Calendar, where during his time, a majority of these endeavours were carried out by Islamic Scholars without prior scientific or astronomical knowledge. His work on lunar crescent visibility and Islamic Calendar sparked the interest of other Muslim astronomers to study and examine the reliability of lunar crescent visibility criterion (Mohammad Ilyas, 1986).

Ilyas has produced various lunar crescent visibility criteria, moon age-latitude lunar crescent visibility criterion, lag time-latitude lunar crescent visibility criterion, lunar crescent altitude and sun-moon azimuth, revision of Danjon limit, revision of Bruin lunar width, arc of light and arc of vision. His primary lunar crescent visibility criterion is altitude-azimuth criterion as portrayed in Table 3.4 and Equation 3.5.

DOI:https//doi.org/10.22452/mjs.vol44no1.12

Table 3.5. Ilyas' Lunar Crescent Table Data

Azimuth Difference (˚)	Arc of Vision (˚)
0	10.3
5	9.9
10	9.15
15	7.9
20	6.4
23	5.6

Source: Ilyas (1994)

$$Arcv = -0.0027356815\,DAZ + -0.0136648716\,DAZ^2 + 0.0002119205\,DAZ^3 + 10.2832719598 \quad 3.3$$

Source: Researcher's Data

Ilyas suggested that the limiting elongation for lunar crescent visibility is 10.5 degrees, which is 3.5 degrees more than Danjon limit, while the limiting altitude for lunar crescent visibility is 10 degrees. Ilyas derived the lunar crescent altitude values from Maunder lunar crescent visibility criterion where Maunder's limiting threshold of lunar crescent altitude at 0 degree of azimuth is 11.0 degrees (Maunder, 1911). The 10.5 elongation limit is derived from reextrapolation of Danjon graph and a reinterpretation of Bruin limit of lunar width. Ilyas discovered that if the Bruin lunar width limit is lowered to 0.25, it would correspond to the geocentric elongation of 10.5 degrees. Ilyas claimed that the drawing of his lunar crescent visibility graph is a combination of Bruin's and Maunder's lunar crescent visibility criterion. Ilyas further cemented that his criterion is agreeable at any given latitude and contains a small value of uncertainty.

Fatoohi (1998) argued that Ilyas has suffered a fundamental flaw in his design of lunar crescent visibility criterion. Maunder's and Bruin's lunar crescent visibility criterion are not related to one another. Maunder derived his lunar crescent visibility criterion from 91 data of lunar crescent visibility, while Bruin designed his lunar crescent visibility criterion using theoretical value of sky brightness, lunar crescent illumination, and contrast threshold. Ilyas also did not make any attempt to demonstrate how the combination of two independent lunar crescent visibility criteria works. In addition, it is stipulated by Fatoohi that the Maunder lunar crescent visibility criterion does not work at all latitudes, whilst the Bruin lunar crescent visibility criterion has an extensive range of uncertainty. In addition, McPartlan commented that the Ilyas elongation limit to underestimation of human eye should be lowered by 0.5 degrees to account for the number of positive lunar crescent observations that fall under Ilyas' invisibility line (McPartlan, 1996).

Fatoohi discovered that the Ilyas altitude-elongation criterion has 29.8 percent contradiction rate in predicting invisibility, and 7.8 percent contradiction rate in predicting visibility. The Ilyas altitude-azimuth lunar crescent visibility criterion was unable to predict 28.6 percent of negative sighting, and 11.3 percent of positive sighting. His limiting value of elongation is also not dependable as the lunar crescent was found to be detectable at 7.7 degrees in elongation. Despite the flaws in his design of lunar crescent visibility criterion, Ilyas has shown there to be various possible presentations in designing lunar crescent visibility criterion. Ilyas was also perhaps the most influential astronomer in lunar crescent visibility research among Muslims.

Schaefer's Lunar Crescent Visibility Criterion

Bradley Schaefer was a Professor Emeritus in Louisiana State University. He was awarded with Nobel prize and Gruber prize for his team's discovery of Dark Energy. In 1983, Schaefer embarked on a journey of lunar crescent visibility research. In his publication on lunar crescent visibility entitled, "Algorithm of Lunar Crescent Visibility", he criticized the current lunar crescent visibility criteria to be limited to geometrical measurement, whereas visibility is a problem that involves atmospheric and human eye sensitivity (Schaefer, 1987). He proposed that the lunar crescent visibility criteria should be designed with consideration of physical, meteorological and physiological equation, the same framework that Bruin has designed for his lunar crescent visibility criterion. To achieve his goal of comprehensive lunar crescent visibility criterion, Bradley Schaefer launched the Moonwatch project, an open project for lunar crescent observation. Through the project, Schaefer was able to gather data of lunar crescent visibility through instrumentation, physiological and atmospheric perspective (L. Doggett et al., 1994; L. E. Doggett et al., 1988; L. Doggett & Schaefer, 1989). He also conducted a study on lunar brightness (Krisciunas & Schaefer, 1991; Schaefer, 1990), twilight sky brightness (Schaefer, 1987), atmospheric extinction (Schaefer, 1986), telescopic limiting magnitude (Schaefer, 1990), lunar physical observation (Schaefer, 1991), and visibility threshold (Schaefer, 1998) to further refine his algorithm. Schaefer tested his algorithm on sunspot visibility (Schaefer, 1991) and validated the date of Jesus crucifixion (Schaefer, 1990). In 1993, Schaefer produced his computation formula for his algorithm (Schaefer, 1993), and in 2000, 12 years later, he updated the final version of his algorithm computation formula (Schaefer, 2000).

Numerous researchers have tried to emulate Schaefer's lunar crescent visibility algorithm. Fatoohi (1998) commented that Schaefer never actually published the full version of his formulation, despite comparatively assessing his algorithm against other lunar crescent visibility criteria. Ilyas (1994, 8) highlighted that Schaefer's lunar crescent visibility algorithm was not published to the public during his time. He also added that Schaefer algorithm are too complicated and not practical for long-term prediction, particularly in application of Islamic calendar determination. Yallop (1998), in agreement with Fatoohi and Ilyas, also noted that it was difficult to replicate Schaefer's calculated algorithm as the information in regards to the algorithm is conflicting between his papers. It is not until recently that a Muslim astronomer, Faid, Nawawi et al. (2023) was able to emulate Schaefer's lunar crescent visibility algorithm. Faid et al., commented that most of the Schaefer visibility algorithms are available in his publication "New Method for Archeoastronomy", while pieces of formula are scattered in other Schaefer publications. Twilight sky brightness formulation can be collected from the "Heliacal Sky Rise" paper (Schaefer, 1987,11), the model of lunar crescent brightness can be collected from “Model of Moon Brightness” paper, telescopic visibility threshold can be collected from “Telescopic Limiting Magnitude” paper (Schaefer, 1990) and atmospheric extinction can be collected from “Atmospheric Extinction effect on stellar Alignment” paper. Faid also highlighted that Schaefer did not provide unit for most of his contrast formulations, making it even more difficult and requiring trial and error (Faid et al., 2024).

Due to its difficulty and unavailability, the reliability results of Schaefer’s lunar crescent visibility algorithm is not yet evaluated by any researcher. In partial assessment of Schaefer’s algorithm, Loewinger discovered that Schaefer miscalculated the lag time value of his data (Loewinger, 1995). Sultan also found that Schaefer has a confusing definition of lunar brightness, frequently interchanging the definition of integrated brightness and surface brightness (Sultan, 2004,11). Schaefer’s algorithm, despite its flaws, indicate that the approach to convert the computation of lunar crescent visibility into a full theoretical formulation is entirely plausible.

Yallop’s Lunar Crescent Visibility Criterion

In 1988, Bernard Yallop published a lunar crescent visibility criterion that can be categorized into ranges of visibility. Yallop formulated his lunar crescent visibility criterion by adapting arc of vision and sun-moon azimuth into q-value expression, where w is the topocentric lunar width. His arc of vision and sun-moon azimuth was not calculated at sunset, as done by his predecessor. According to him, this is because lunar crescent is not sighted during sunset, instead it is visible after the contrast between sky and lunar brightness can adequately be seen by observer, which would be during the minutes after sunset. The value is calculated during this best time, which Yallop expressed in Equation (3);

$$Best\ Time = Time\ of\ sunset + \frac{4}{9} lagtime \qquad (4)$$

Yallop categorized the values of q into ranges of lunar crescent visibility, which are: Easily Visible, Visible Under Perfect Condition, May Need Optical Aid to Find Crescent, Will Need Optical Aid to Find Crescent, Not Visible with a Telescope, and Not Visible. The categorization is as set out in Table 6.

Table 6. Yallop Lunar Crescent Visibility Criterion

Criterion	Range	Remarks
(A)	$q > 0.216$	Easily visible, ARCL> 12 °
(B)	$0.216 \geq q > -0.014$	Visible under perfect conditions
(C)	$-0.014 \geq q > -0.160$	May need optical aid to find crescent
(D)	$-0.160 \geq q > -0.232$	Will need optical aid to find crescent
(E)	$-0.232 \geq q > -0.293$	Not visible with a telescope, ARCL < 8.5°
(F)	$-0.293 \geq q$	Not visible, below Danjon limit, ARCL<. 8°

Yallop based his *q*-formulation from Indian lunar crescent visibility criterion, and Neugebauer lunar crescent visibility criterion (Fatoohi, 1998, 124; Neugebauer, 1929, 111). Yallop’s categorization of visibility ranges was based on 295 records of lunar crescent observation compiled by Schaefer and Doggett. Fatoohi commented that Yallop’s categorization, particularly the E & F categories, were not needed as both can be counted as invisible sighting. Fatoohi added that the Neugebauer and Bruin lunar crescent visibility criterion was not dependable enough to function as a basis for Yallop lunar crescent visibility criterion. Fatoohi also argued that Yallop’s categorization was not balanced as he found that from 295 data of lunar crescent sighting, 166 fall under category A, while only 68,26,14,4 and 17 fall under categories B, C, D, E and F, respectively. These disparities indicate that more data is needed for each category to validate the ranges of visibility (Fatoohi, 1998). In examining Yallop’s criterion, Fatoohi found that there was a high number of errors, except for category A. Fatoohi opined that Yallop’s criterion was highly unreliable as it was unable to accurately predict the lunar crescent visibility.

Fatoohi also criticised Yallop’s lunar crescent visibility criterion for its adoption of inconsistent visibility ranges, and weak mathematical foundation. Despite its weakness, Yallop is known for popularizing the concepts of visibility ranges and best times, which then influences researchers like Qureshi and Sultan to produce their definition of visibility ranges and best times, respectively (Qureshi, 2010; Sultan, 2006).

Fatoohi’s Lunar Crescent Visibility Criterion

Fatoohi’s PhD thesis was entitled “First visibility of the lunar crescent and other problems in historical astronomy”. In his thesis, Fatoohi (1998) suggested an altitude-azimuth lunar crescent visibility criterion as in Equation (9). The lunar crescent altitude located in between $ArcV_{Upper\ Limit}$ and $ArcV_{Lower\ Limit}$ is placed at a zone of uncertainty. Fatoohi’s lunar crescent visibility criterion graphs can be portrayed as in Figure 2 below.

Figure 1. Fatoohi's Lunar Crescent Visibility Criterion

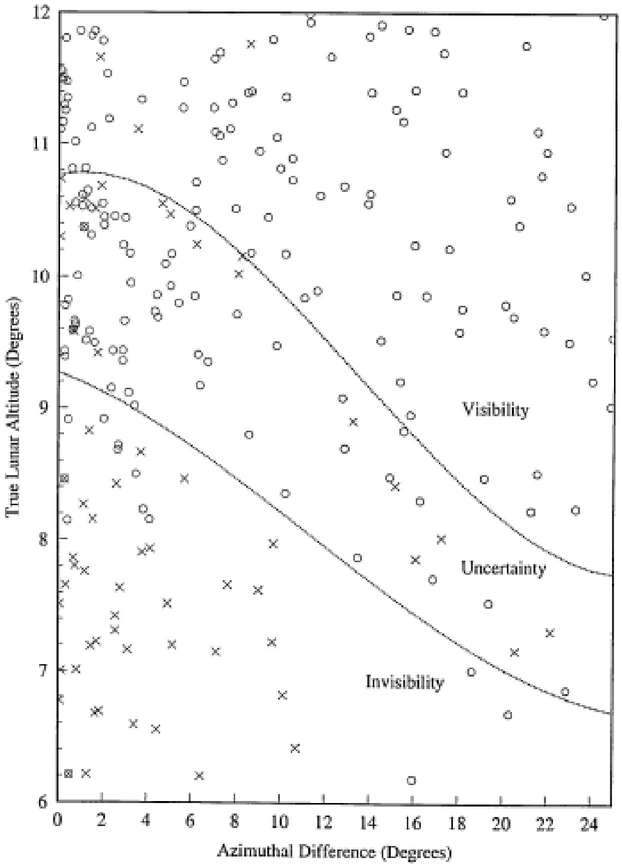

Source : Fatoohi, L, First visibility of the lunar crescent and other problems in historical astronomy, 1988, Durham University, 141

Fatoohi incorporated Ilyas' idea of zone of uncertainty into his design of lunar crescent visibility criterion. While Ilyas' idea of zone of uncertainty refers to the geographical latitude-longitude where the lunar crescent cannot be accurately predicted using his criterion in the International Lunar Date Line (Ilyas, 1997), Fatoohi incorporated the zone of uncertainty directly in his formulation of lunar crescent visibility criterion, where the visibility of the lunar crescent cannot be predicted accurately. Fatoohi noted that both the upper limit and lower limit of his criterion only has error of 5.9 percent in predicting negative lunar crescent sighting, and 3.6 percent in predicting positive lunar crescent sighting. However, in between both limits, the accuracy of lunar crescent prediction falls rapidly. In his test, Fatoohi found that the zone of uncertainty in his criterion can accommodate 27.4 percent of negative sighting error, and 16.4 percent of positive sighting error.

Fatoohi also noted that the implementation of his lunar crescent visibility criterion is more applicable for the determination of new Hijri month, where both the practice of astronomical calculation and lunar crescent sighting can be adopted. If the lunar crescent is located above the upper limit of the Fatoohi lunar crescent visibility criterion, then it can be confidently expected that lunar crescent will be sighted, and new Hijri month is commenced. If the lunar crescent is located below the lower limit of the Fatoohi lunar crescent visibility criterion, then it can be confidently expected that the lunar crescent will not be sighted, and the current Islamic month will continue until the 30th day. However, if the lunar crescent is located in between the upper limit and the lower limit, the lunar crescent needs to be sighted to confirm its visibility. Fatoohi noted that in his test on 300 months of Islamic Calendar in Mecca, Baghdad and Casablanca, there were around 7 percent of cases where the lunar crescent was located in the zone of uncertainty.

The idea of using lunar crescent sighting for zone of uncertaintyr looks practical on paper and relatable to the practice of the Prophet. However, in real cases, as discussed in the previous chapter, some countries have limitations in exercising lunar crescent sighting to determine the new Hijri month, making the idea of incorporating the zone of uncertainty on lunar crescent visibility criterion not feasible for real time application. The incorporation of zone of uncertainty also limits the usage of the lunar crescent visibility criterion for historic calendrical dating purposes, as lunar crescents located in the zone of uncertainty cannot be accurately calculated.

Odeh's Lunar Crescent Visibility Criterion

Mohamad Shaukat Odeh was born in Kuwait in 1979. He is a member of the Arab Union for Astronomy and Space Science. He is renowned for founding the global lunar crescent observation project, called the Islamic Crescent Observation Project, since 1998. The project has since then collected more than 2000 data of lunar crescent sighting worldwide. Odeh is also involved in the development of Accurate Time, an Islamic astronomy software that can function as a lunar crescent visibility calculator, Islamic calendar calculator, and prayer time calculator. He is one of the most influential lunar crescent sighting astronomers in our time.

Odeh published a lunar crescent visibility criterion in 2005. His lunar crescent visibility criterion is categorized into ranges of visibility, similar with Yallop's lunar crescent visibility criterion. Odeh's lunar crescent visibility criterion has 4 categories of visibility, with values to determine the ranges of visibility as set out in Table 7.

Table 7. Odeh's Lunar Crescent Visibility Criterion

Category	Remarks	Criteria
Zone A	Crescent visible by naked eye	$V \geq 5.65$
Zone B	Crescent visible by optical aid, and might be visible by naked eye	$2 \leq V < 5.65$
Zone C	Crescent visible by optical aid	$-0.96 \leq V < 2$
Zone D	Crescent is not visible by optical aid	$V < -0.96$

Odeh determine his V value using the same formula as Yallop used in determining his Q value. Odeh lowered his arc of vision threshold from 11.8371 degrees to 7.1651 degrees. Odeh lunar crescent visibility criterion is formulated through a compilation of

737 records of lunar crescent sighting. These include 294 records of lunar crescent sighting from Schaefer's list, 6 records from Jim Stamm, 42 records from South Africa Astronomical Observatory, 15 records from Mohsen Mirsaeed, 57 records from Alireza Mehrani and 323 records from ICOP. As Odeh follows Yallop's lunar crescent visibility criterion, it has the same weakness as the Yallop criterion. Although the Odeh visibility classification is more practical than Yallop's visibility classification, the number of lunar crescent sightings on each visibility group is not balanced with 46 lunar crescent sightings on Group D, 117 lunar crescent sightings on Group C, 255 lunar crescent sroup B, and 160 lunar crescent sightings on Group A. Furthermore, the ratio of positive to negative sightings on each group was found to be lopsided, with Group A having a majority of negative lunar crescent sighting, and group D having a majority of positive sighting. The contradiction rate analysis of Odeh's lunar crescent visibility criterion has not been examined by any scholar so far.

Qureshi's Lunar Crescent Visibility Criterion

Mohamad Shahid Qureshi is a Pakistan-born astronomer, mathematician, and astrophysicist. He is a former director and Professor at the Institute of Space and Planetary Astrophysics, Karachi Universiti, Pakistan. Shahid Qureshi's Doctoral thesis is entitled "Earliest Visibility of Lunar Crescent" making him an expert in designing lunar crescent visibility. Shahid Qureshi has published at least five papers concerning the visibility of lunar crescent in Pakistan.

Qureshi produced his own lunar crescent visibility criterion in 2010. Shahid Qureshi's criterion is in a similar framework with Yallop's and Odeh's criterion, which adapt ranges of lunar crescent visibility. Qureshi's ranges of visibility are categorized into Easily Visible, Visible Under Perfect Condition, May Require Optical Aid to Find Crescent, Require Optical Aid, and Not Visible with Optical Aid. His table for visibilities ranges is expressed ina Table 8.

Table 8. Qureshi Lunar Crescent Visibility Criterion

Visibility	Criteria
Easily Visible (EV)	s-value > 0.15
Visible under perfect conditions (VUPC)	0.05 < s-value < 0.15
May require optical aid to find crescent (MROA)	-0.06 < s-value < 0.05
Require optical aid (ROA)	-0.16 < s-value < -0.06
Not visible with optical aid (I)	s-value <-0.16

Qureshi's visibility ranges are based on s value. The s value takes the same arc of vision and width parameter used by Yallop and Odeh, however Qureshi changed the coefficient to fit with his data. Qureshi's data were calculated using a website which claimed to have adapted Schaefer's visibility logarithm. The website is, however, inaccessible to verify the computation. Qureshi highlighted that his s value is more accurate, as it considers the brightness of the sky, lunar crescent illumination and detectable contrast threshold. However he does not demonstrate howthe formulation of the S value is conducted. As Qureshi shares the same lunar crescent visibility criteria style as Yallop and Odeh, it does face the issue of unbalanced lunar crescent sighting data of each visibility group. The contradiction rate analysis of Qureshi lunar crescent visibility criterion has not been examined by any scholar so far.

Caldwell's Lunar Crescent Visibility Criterion

John Caldwell is an astronomer who graduated from California Institute of Technology in 1974. In 1979, he obtained his PhD from Princeton University. Previously he was a research fellow on the South African Astronomical Observatory, Cape Town, South Africa. In 2012, John Caldwell published a study on lunar crescent visibility criterion, on the Monthly Notes of the Astronomical Society of South Africa Journal. To date, John Caldwell's lunar crescent visibility criterion is the only published works from African countries on lunar crescent visibility criterion.

Caldwell incorporated moonset-sunset lag time and arc of light in his lunar crescent visibility criterion. Caldwell argued that lag time is a better parameter to determine lunar crescent visibility, as it is applicable at various degrees of latitude. This is because lag time is correlated to the separation angle between the sun and the moon, in contrast to altitude, where it is highly correlated to the local horizon. Lag time is also best paired with elongation as both do not have linear relationship to each other. Caldwell's lunar crescent visibility criterion is expressed in Table 9 below (Caldwell, 2011).

Table 9. Caldwell's Lunar Crescent Visibility Criterion

Criteria	Expression
A . Possible for Naked Eye Sighting	$lag\ (') > -0.9709\ arcl + 44.65$
B. Possible for Optical Aided Sighting	$-0.9709\ arcl + 44.65 > lag\ (') > -1.9230\ arcl + 43.13$
C. Not possible for sighting	$lag\ (') < -1.4150\ arcl + 36.76$

Caldwell's lunar crescent visibility criterion is based on 36 data of positive naked eye and 58 data of positive optical aided lunar crescent sightings from various latitude and longitude. As Caldwell's lunar crescent visibility criterion is based on a small dataset, this makes his criterion susceptible to error. In his graph, Caldwell included negative lunar crescent sighting. The details of negative lunar crescent sighting data are not included in this paper, making reassessment of his criterion to be limited. Lag time parameter was also heavily criticised by Ilyas (1994), and Fatoohi (1998) to be highly unreliable and dependent on latitude. The Caldwell criterion design also suffered from Yallop lunar crescent visibility design, due to unbalanced number of lunar crescent sighting reports on each visibility categorization. The Caldwell lunar crescent visibility criterion is, however, not yet assessed by any modern scholar of lunar crescent visibility criterion.

Lunar Crescent Visibility Criterion

In 2012, Rolf Krauss published a study on lunar crescent visibility using Babylon data of lunar crescent sighting. A 95-page article written by Krauss contains arguments about data validity, interpretation of modern lunar crescent visibility criterion based on Babylon data, effect of weather on lunar crescent visibility, and an azimuth-altitude lunar crescent visibility criterion.

Krauss included the seasonal factor into his criterion, citing the Schaefer visibility logarithm to support his inclusion. However, the inclusion has caused Krauss's criterion to have large deviation error, up to 1.8 degrees. For calendrical purposes, a large deviation error can lead to unreliable lunar crescent visibility criterion. The contradiction rate analysis of Krauss lunar crescent visibility criterion has not been examined by any scholar to date.

Table 3.10. Krauss' lunar crescent visibility criterion

	September to March Babylonian	March to September Babylonian	Atheni an
DAZ (°)	ArcV (°)		
0	10.1 ± 1.5	10.8 ± 1.4	10.6 ± 1.8
5	10.0	10.7	10.5
10	9.4	10.1	9.95
15	8.4	9.2	9.0
20	7.1	7.8	7.6
22	6.4	7.1	7.0

Source: Krauss (2012)

$$Arcv^{Sept-March} = 0.0246304381\,DAZ + -0.0100243996\,DAZ^2 + 0.0000590234\,DAZ^3 + 10.1050739464$$

$$Arcv^{March-Sept} = 0.0115318125\,DAZ + -0.0075992122\,DAZ^2 \pm 0.0000258220\,DAZ^3 + 10.8074774331$$

$$Arcv^{Athenian} = 0.0291254840\,DAZ + -0.0098347831\,DAZ^2 + 0.0000475196\,DAZ^3 + 10.5981838905$$

3.5

Source: Krauss (2012)

3.12 Gautschy's Lunar Crescent Visibility Criterion

Gautschy, in 2014, published his work on lunar crescent visibility criterion entitled "On the Babylonian sighting-criteria for the lunar crescent and its implications for Egyptian lunar data" (Gautschy, 2014). The article endeavours to produce a lunar crescent visibility criterion based on Babylon prediction and lunar crescent visibility records, and to utilise the produced criterion in establishing an absolute Egyptian chronology.

Gautschy used Yallop's lunar crescent visibility criterion to validate the Babylon records of lunar crescent sightings. Records that contradict Yallop lunar crescent visibility criterion were recalculated to ensure its accuracy. Inaccurate, or unclear records of lunar crescent sighting, were rejected. Gaustchy argued that Krauss' judgement to design a lunar crescent visibility criterion based on season was not justified, as it was proven that season does not affect visibility of lunar crescent. Gaustchy used parameter of lag time and difference in azimuth, as lag time is insensitive to difference calculation reference, either topocentric or geocentric. Gaustchy also evaluated her criterion using Odeh lunar crescent visibility criterion and found that the results she obtained followed Odeh's visibility prediction.

Gaustchy was able to provide a fresh outlook on lunar crescent visibility criterion based on Babylon's lunar crescent visibility records. While Kraus adopted modern altitude-azimuth lunar crescent visibility criterion, Gaustchy was adamant that lag time parameter, which is the parameter that has been adopted since the Babylonian age, was just as efficient as other topocentric parameters. While she admitted that lag time is dependent on latitude, it is applicable for her research purpose, which is to produce an absolute Egyptian chronology specific for latitudes in Egypt.

Table 3.11. Gaustchy's lunar crescent visibility criterion

DAZ (°)	0	2.5	5	7.5	10	15	20	25
Arc of Separation (°)	8.6	8.55	8.45	8.2	7.8	6.5	5.0	3.3
Lag time (')	34m	34m	34m	33m	31m	26m	20m	13m

Source: Gautschy (2014)

$$Latime = 0.3342328913\,\Delta AZ + -0.0715608980\,\Delta AZ^2 + 0.0009924422 * \Delta AZ^3 + 33.8890455442$$

3.6

Source: Gautschy (2014)

Alrefay's Lunar Crescent Visibility Criterion

Thamer Alrefay is an Assistant Professor from Space Research Institute, King Abdul Aziz City for Science and Technology, Riyadh, Saudi Arabia. He is a member of the Canadian Association for Physicists, and completed his PhD in University of New Brunswick, Canada in 2014 under the subject of space physics. Alrefay's interests are Space Physics, Fireball Observation, and Earth Bow Shock.

In 2018, Alrefay and his fellow researchers at King Abdul Aziz City for Science and Technology published their research on the earliest visibility of the lunar crescent. The research is conducted based on 545 observations of lunar crescent sighting in Saudi Arabia within a duration of 27 years. Alrefay et al. (2018) developed a lunar crescent visibility criterion using width and arc of vision parameter, in a similar fashion with Yallop, Qureshi and Odeh. The Alrefay lunar crescent visibility criterion is classified into two categories, which are naked eye and optical aided observation, as expressed in Equation 3.12 below.

$$ARCV_{Naked\ Eye} > 9.34 - 4.51w + 3.3W^2 - 1.01W^3$$
$$ARCV_{Optical\ Aided} > 7.83 - 4.35w + 3.22W^2 - 1.02W^3$$
3.7

Source : Alrefay (2018)

Alrefay argued that the Yallop lunar crescent visibility criterion, and the Odeh lunar crescent visibility criterion, are not consistent with other lunar crescent visibility data calculation reference. In addition, Yallop and Odeh both adopt a topocentric width parameter, without any argument as to why topocentric parameters would help in determining the limiting visibility of lunar crescents. Alrefay argued that his lunar crescent visibility criterion was based on geocentric lunar crescent parameters, and his criterion is consistent with other lunar crescent visibility data calculation reference. The Alrefay lunar crescent visibility criterion, however, was based on Saudi Arabia data and limited to 595 lunar crescent sightings, while the Odeh lunar crescent visibility criterion was based on 737 worldwide lunar crescent sightings. This makes Alrefay unreliable in determining the lunar crescent visibility outside Saudi Arabia. The contradiction rate analysis of Ahmad's lunar crescent visibility criterion has not been examined by any scholar so far.

Ahmad's Lunar Crescent Visibility Criterion

Nazhatulshima Ahmad is an astronomer from Malaysia, who is currently a Senior Lecturer in the Department of Physics, Universiti Malaya, Malaysia. She is highly experienced in the formulation of procedures to validate lunar crescent sightings and developing criterion of lunar crescent visibility in Malaysia. She is also experienced in research fields of spectroscopy of emission line stars; binary stars; asteroids; observation and imaging techniques in optical regions; spectroscopy, photometry, and astrometry. She is currently a member of the International Astronomical Union.

Ahmad published a lunar crescent visibility criterion in 2020. Ahmad et al. (2020,3) criterion is in similar framework with Yallop, Odeh, and Qureshi criteria, which by adapting ranges of lunar crescent visibility criterion. Ahmad applied a unique approach on parameter of lunar crescent, by using a circular regression model. Ahmad's lunar crescent ranges of visibility is categorized into three categories, which are visible to the unaided eye, may need optical aid, and not visible (Ahmad et al., 2022).

Table 12. Ahmad Elongation and Altitude Lunar Crescent Visibility Criterion

Category	EA-test value	N	Y	Total %	Interpretation
A	[0.0086, 00)	21	52	73 (29)	Visible to the unaided eye
B	[0.00516, 0.0086)	26	9	35 (14)	May need optical aid
C	(-00, 0.0052)	126	20	146 (57)	Not visible

Table 13. Ahmad Elongation and Arc of Vision Lunar Crescent Visibility Criterion

Category	EV-test value	N	Y	Total %	Interpretation
A	[0.0039, 00)	59	21	80 (31)	Visible to the unaided eye
B	[-0.0022, 0.0039)	24	16	40 (16)	May need optical aid
C	(-00,-0.0022)	90	44	135 (53)	Not visible

Ahmad's lunar crescent visibility criterion was expressed into two parameter pairings, namely elongation with altitude and elongation with arc of vision. Ahmad argued that the development of the criteria uses only linear statistical theory, while in fact most of the variables in crescent moon data are measured in degree/radians. However, Ahmad did not demonstrate his lunar crescent visibility criterion capability over linear lunar crescent visibility. In addition, Ahmad's lunar crescent visibility criterion was expressed in a form of complex mathematical expression, and not easily applied for Hijri calendrical purposes. Ahmad also did not provide any expression that can be used for lunar crescent visibility criterion analysis, as it is foundthat the expression provided in the research paper does not correlate to the results in Table 3.20 and Table 3.21. The contradiction rate analysis of Ahmad's lunar crescent visibility criterion has not been examined by any scholar so far.

Country Based Lunar Crescent Visibility Criterion

A country based lunar crescent visibility criterion is a criterion used for the purpose of a country's Hijri calendrical determination. A country-based lunar crescent visibility criterion is usually designed at a lower line of lunar crescent visibility, as it is to ensure that no lunar crescent is sighted below the criterion. In addition, a country-based lunar crescent visibility criterion is usually designed in a conditional style lunar crescent visibility criterion. This is in contrast to research-based lunar crescent visibility criterion such as Alrefay et al. and Gautschy, where they used expression style lunar crescent visibility criterion. It can be deduced that the conditional style lunar crescent visibility criterion is simpler for Hijri calendrical calculation, while equation style lunar crescent visibility criterion requires more computation power and advanced programming technique to calculate the Hijri calendar, particularly computations that involve long years of Hijri calendar.

Saudi's Lunar Crescent Visibility Criterion

Saudi Arabia houses the Muslim pilgrimage location, which are Mecca and Madinah. Muhamad was also born in Mecca, and Islamic expansion has Mecca and Madinah as its epicentre. This makes Saudi Arabia the most influential country among the Muslim community. Due to this, several countries follow closely Saudi Arabia's date of Hijri month. Dates of religion importance, such as the day of Arafah, and Eid Adha, impact Muslims worldwide as it relates to their religion practices. This makes a number of countries follow Saudi Arabia lunar crescent visibility criterion, such as Afghanistan, Albania, Algeria, Armenia, Austria, Azerbaijan, Bahrain, Belgium, Belgium, Bolivia, Bulgaria, Burkina Faso, Chechnya, Denmark, Finland, Georgia, Hungary, Iceland, Iraq (Sunnis), Italy, Japan, Kazakhstan, Kuwait, Kyrgyzstan, Lebanon, Mauritania, Palestine, Philippines, Qatar, Romania, Russia, Sudan, Sweden, Switzerland, Syria, Taiwan, Tajikistan, Tatarstan, Togo, Turkmenistan, U.A.E, and Uzbekistan.

As a large number of countries follow Saudi Arabia's lunar crescent visibility criterion, their early criterion is based on the Greenwich time zone. Saudi Arabia's old lunar crescent visibility criterion is simply conditioned as: new Hijri month begins when, after a moon conjunction, sunset occurs before moonset. The old criterion did not consider altitude, age and elongation (Mostafa, 2005). The old criterion was contested by Kordi (2003, 2), as it was not based on Saudi Arabian time zone, or any Saudi Arabian location reference point. In 2000, a new lunar crescent visibility criterion for Saudi Arabia is introduced. This is in conjunction with the new Umm al-Qurra calendar. The criterion condition is as follows:

a. The position of lunar crescent and sun is computed using the Holy Kaaba as reference for calculation.
b. If a lunar crescent is set before sunset during conjunction, an observation is conducted a day after.
c. If a lunar crescent is set after sunset, and its sighting is accepted in accordance with Islamic Jurisprudence of Saudi Arabia.

Mostafa (2005) stated that the new criterion is based on the capability of a lunar crescent sighting by an observer, rather than the capability of a lunar crescent sighting based on a criterion parameter. He added that this reduces errors in lunar crescent report from 14 percent for old criterion into 0 percent for the new criterion. However, as the new Saudi Arabia lunar crescent visibility criterion is solely based on moonset after sunset, there is still room for error in lunar crescent reporting. The world record for lag time is 30 minutes for naked eye, and 20 minutes for optical aid observations. Should a lunar crescent be observed below the world record limit, then the lunar crescent is highly contestable and should be rejected. However, based on Saudi Arabia's new lunar crescent visibility criterion, a lunar crescent sighting is accepted regardless of whether its lag time challenges the world record or not.

Turkey's Lunar Crescent Visibility Criterion

Although it does not have the same magnitude of influence as Saudi Arabia does over Muslim communities worldwide, Turkey has influence in the realm of lunar crescent visibility criterion. Turkey was the first to introduce a lunar crescent visibility criterion in 1978, earlier than Ilyas' series of lunar crescent visibility criteria (Mohd Nawawi et al., 2015). Turkey's1978 lunar crescent visibility criterion is the criterion that is believed to have inspired Malaysia's formation of lunar crescent visibility criterion in 1983. Turkey's 1978 lunar crescent visibility criterion is the result of an international conference in 1978. The conference was attended by representatives from 20 countries, including Malaysia and Indonesia. The purpose of the conference was to coordinate the determination of the new Hijri month among Muslim countries. Through the conference a number of resolutions were produced, among them is a resolution on the Turkey 1978 lunar crescent visibility criterion that had been mutually agreed upon by the representative. The criterion that has been agreed upon are as follows. The new Hijri month begins when a lunar crescent:

a. Has elongation parameter of more than 8 degrees; and
b. Has altitude of more than 5 degrees.

In 2016, Turkey proposed yet another lunar crescent visibility criterion. The proposal was through the Conference of Islamic Calendar in Istanbul, Turkey 2016M/1437H (Rodzali & Man, 2021). The conference representatives voted and resolved that;

a. The entire world is to be seen as one union where the new Hijri month begins on the same day throughout the world.
b. A new Hijri month begins when in any part of the earth, theSun-Moon elongation at sunset reaches more than 8 degrees or more, and the altitude of the lunar crescent is 5 degrees above the horizon.

This criterion, henceforth known as the Istanbul 2016 criterion, acts as a baseline for International Lunar Dateline. However, the Istanbul 2016 criterion seems to ignore a number of lunar crescent observation records. The world records for elongation are 7.7 degrees at naked eye, 6.0 degrees at optical aided, 6.8 degrees at telescopic observation, and 3.42 degrees at CCD imaging.(ICOP, 2022). The world records for altitude are 4.06 degrees at naked eye, 6.48 degrees at optical aided, 4.81 degrees at telescopic observation, and 4.62 degree at CCD imaging.

In 2017, Indonesia suggested another criterion known as Jakarta Recommendation 2017 (Sopwan & Al-Hamidy, 2020). The criterion acts as a supplement for the Istanbul 2016 criterion. The resolution on the criterion parameter was conducted through a discussion during a conference known as the "International Seminar on Astronomical Fiqh Opportunities and Challenges Implementation of the Single Hijri Calendar ", held in Jakarta on 29 to 30 November 2017. The conference was attended by participants from five countries, namely Indonesia, Jordan, Malaysia, Singapore, and Brunei Darussalam. This led to the formation of the Jakarta Recommendation 2017. The Jakarta Recommendation 2017 can be summarised as follows;

a. The Sun-Moon elongation at sunset reaches more than or equal to 6.4 degrees, and

b. Altitude of the lunar crescent during sunset is more or equal to 3 degrees above the horizon.

The Jakarta Recommendation 2017 is more suited for Hijri calendar determination, as it follows the International Crescent Observation Project world sighting records.

MABIMS's Lunar Crescent Visibility Criterion

Malaysia, Indonesia, Brunei and Singapore employed lunar crescent visibility criterion to determine their Hijri month (Azhari, 2021). These countries independently determined their own date of the first day of *Ramadan* and *Shawal,* at the same time they collaborate in formulating lunar crescent visibility criterion to determine the first date of the other Hijri months (Nawawi et al., 2015). In conjunction with the Association of Southeast Asian Nations (ASEAN), these four countries conjoined to form a governing body known as MABIMS (The Informal Meeting of Religious Ministries of Malaysia, Indonesia, Brunei and Singapore). The role of MABIMS is monitor the laws and principles on lunar crescent sighting and its visibility criterion to ensure that there is no disagreement among the members (Wahidi et al., 2019).

As an intercessor for these four countries, each of them is portrayed by their lunar calendar governing bodies: the Department of Islamic Development Malaysia (JAKIM) for Malaysia, the Ministry of Religious Affairs, Republic of Indonesia (KEMENAG RI) for Indonesia, the Islamic Religious Council of Singapore (MUIS) for Singapore and the Brunei Islamic Religious Council (MUIB) for Brunei. In summary, JAKIM, KEMENAG RI, MUIS, and MUIB are the governing authorities who are responsible for determining the dates of the Hijri calendar.

In 1995, Malaysia, Indonesia, Brunei and Singapore adopted the criterion for lunar crescent visibility known as as "*Imkan al-Rukyah*", which defines the beginning of the lunar months as "when the lunar crescent could be visible against clear skies" (Mamat, 2020). The concept of this criterion is the "possibility of visibility" which is based on the result of the visible crescent that has been sighted" - by using this lunar crescent visibility criterion (Azhari, 2012), the lunar crescent is expected to be seen when it fulfils one of the following conditions:

a. During sunset, the sun-moon elongation reaches more or equal to 3 degrees and the altitude of the lunar crescent reaches more or equal to 2 degrees above the horizon; or,

b. During the moonset, the moon age is more or equal to 8 hours.

The criterion suggests that if observation of a lunar crescent at a certain 29th Hijri day shows that it has altitude and elongation of more than 2 degrees and 3 degrees, respectively, then the next day is commenced as a new Hijri month. Based on the presence of the lunar crescent in Indonesia from the 1960s to the 1990s, the lunar crescent was reported to have appeared several times at an altitude of 2 degrees and elongation of 3 degrees. This criterion was then formulated based on the presence of the lunar crescent which was confirmed by KEMENAG RI at the time (JAKIM, 1991).

The lunar crescent altitude, elongation, and moon age parameter used in MABIMS lunar crescent visibility criterion were found be to conflicting with other research findings. Elongation criterion have been found by Schafer, Ilyas, Fatoohi and Odeh to be above 7 degrees for naked eye observation, and no lunar crescent was able to be sighted at an elongation of below 7 degrees, except for extreme optical aided observation. The same goes for the moon age and lunar crescent altitude, where the world records are 14 hours and 4 degrees for moon age and arc of vision respectively, a parameter that is significantly higher than MABIMS 1995 criterion. This indicates that the current lunar crescent visibility criterion adopted by MABIMS is outdated, without any current scientific evidence, and is not supported among lunar crescent visibility researchers.

In 2021, Malaysia, Indonesia, Brunei, and Singapore adopted a new criterion for lunar crescent visibility known as the Neo MABIMS Criteria. This criterion is the culmination of research and discussion among researchers, government officials, observatories, and universities in improving the previously flawed 1995 lunar crescent visibility criterion. The new criterion negates the use of moon age parameters, since it has been proven to be ineffective in finding lunar crescent visibility (N. Ahmad et al., 2020, 10; Alrefay et al., 2018,12; Anwar et al., 2016, 4; Ilyas, 1983, 1). The new criterion is formed considering the elongation parameter of Odeh lunar crescent visibility criterion (Odeh, 2004, 11), with additional MABIMS' own altitude parameter, originating from Jakarta Recommendation lunar crescent visibility criterion (Azhari, 2021, 11). The criterion is that the sun-moon elongation at sunset reaches more or equal to 6.4 degrees and altitude of the lunar crescent during sunset is more or equal to 3 degrees above the horizon.

4. Discussion and Conclusion

A review was conducted to demonstrate the scientific outlook of a lunar crescent visibility criterion: data locality, prediction of strengths and weaknesses, and its long-term legacy in visibility. The reviews demonstrate that each lunar crescent visibility criterion has its own strengths, limitations and application for calendrical determination and successful observation. From the reviews, there are a number of factors that cause the heterogeneity of a lunar crescent visibility criterion.

First, there is the differences of mathematical model. Caldwell used the lagtime parameter as the main variable in the criteria to show the existence of the influence of the geocentric model (Nawawi et al., 2012). Modern astronomers are more inclined towards mathematical models which are topocentric, that is by using the altitude, azimuth and elongation parameters change according to the position of the observer on the earth's surface. This parameter is used by the majority of experts who study the criteria such as Ilyas, McNally and Fotheringham. The differences

DOI:https//doi.org/10.22452/mjs.vol44no1.12

in terms of the mathematical model used will impact the criterion construction. This is because different mathematical models will be used for different parameters and subsequently provide heterogeneity in the criterion. This demonstrates the influence of mathematical models on the construction of criterion.

Next, there is the primary concept of the criterion designer. Each lunar crescent visibility criterion is built based on one primary concept that is produced by the researcher himself. This concept was derived based on the background of society and culture, which influences the researcher's thinking and motivation when producing the criteria. A key example of how a concept can influence a lunar crescent visibility criterion can be seen from Ilyas's lunar crescent visibility criterion. Ilyas is an atmosphere astronomer from Universiti Sains Malaysia. Most of the criteria produced by him are much significantly higher than other criteria of lunar crescent visibility. Researchers such as Fatoohi and Schaefer found that lunar crescent located above his criterion is easily detected by the naked eye. The construction of a high visibility criteria for the moon, which can usually be seen by the human eye, will facilitate the production of calendars for large lines of longitude. The construction of criteria for countries of great longitude is very difficult because the rate of lunar crescent visibility will decrease when going east. This demonstrates that it can influence the concept of the Universal Islamic Calendar to Ilyas lunar crescent visibility criterion.

Another factor for lunar crescent criterion dissimilarity is the preference on the type of visibility. There are times when the lunar crescent is easily spotted by the naked eye. There are also times when the lunar crescent is vaguely visible and can only be tracked by using a telescope. This results in major complications in the criteria construction because each researcher has different visibility preference in building visibility criteria. Some have built criteria based on the conditions that it is easily visible to the naked eye, and there are also those who construct criteria based on its telescopic visibility. Another example of how selection on the range of visibility can affect the results of the lunar crescent visibility criterion is exemplified by Fatoohi in 1998. This shows that the selection of the range of visibility of the moon, either easily seen with the naked eye, or can only be seen using a telescope affects how a crescent visibility criterion is constructed. An example is the difference in approach by Fotheringham and Maunder in the construction of their criteria. Lunar crescent visibility criterion expressed by Fotheringham is different from the criterion by Maunder, although both of them used almost the same data in their respective studies. This difference occurs because of the criterion built by Fotheringam based on naked eye visibility of the lunar crescent. When the parameter of the moon passes the conditions specified by Fotheringham, the crescent moon is definitely visible to the naked eye. Maunder, on the other hand, preferred critical limit of visibility between positive and negative naked eye sightings. Therefore, a lunar crescent located above Maunder limits is easily visible by telescope, but is not necessarily visible to the naked eye.

The final factor of criteria dissimilarity is the differences in data used for criterion construction. The lunar crescent visibility criterion is built based on empirical data collected by past researchers. There are researchers who have a large collection of lunar crescent sightings, and there are also researchers who build their criteria based on a limited collection of lunar crescent sightings. The amount of data on lunar crescent sightings and the distribuition of the data influences the graph and criterion of a lunar crescent sighting. An excellent example can be seen in the results of a study conducted by Yallop, Odeh, and Qureshi. The criteria built by Yallop, Odeh, and Qureshi used the same concept, which is the construction of criteria that take into account various ranges of visibility, including visibility with a telescope, visibility to the naked eye, and visibility with binoculars. Theyalso used the same model, which is the topocentric model, taking into account the width of the crescent moon as the main parameter. However, the Yallop, Odeh, and Qureshi criteria are different from each other. This is due to the differences of reference data on lunar crescent sightings between Yallop, Odeh and Qureshi. Yallop has 295 data, Odeh has 737 data, while Qureshi has 436 data. The differences in data reference and the distribution of the data makes the criteria produced by Yallop, Odeh and Qureshi differ from each other even though their criteria are constructed using the same mathematical concepts and models.

5. Acknowledgements

This research is supported by the University of Malaya Grant, under project number of UMG004L-2022 and RMF0068-2021.

6. References

Ahmad, N., Mohamad, N. I. N., Abdul Wahab, R., Mohd Nawawi, M. S. A., Zainuddin, M. Z., & Mohamed, I. (2022). Analysis Data of the 22 Years of Observations on the Young Crescent Moon at Telok Kemang Observatory in Relation to the Imkanur Rukyah Criteria 1995. *Sains Malaysiana*, *51*(10), 3415–3422. https://doi.org/10.17576/jsm-2022-5110-24

Ahmad, N., Nawawi, M. S. A. M., Zainuddin, M. Z., Nasir, Z. M., Yunus, R. M., & Mohamed, I. (2020). A New Crescent Moon Visibility Criteria using Circular Regression Model: A Case Study of Teluk Kemang , Malaysia. *Sains Malaysiana*, *49*(4), 859–870. https://doi.org/10.17576/jsm-2020-4904-15

Alrefay, T., Alsaab, S., Alshehri, F., Alghamdi, A., Hadadi, A., Alotaibi, M., Almutari, K., & Mubarki, Y. (2018). Analysis of Observations of Earliest visibility of the lunar crescent. *The Observatory*, *138*(1267).

Blackwell, H. R. (1946). Contrast thresholds of the human eye. *Journal of the Optical Society of America*, *36*(11), 624–643. https://doi.org/10.1364/JOSA.40.000825

Bruin, F. (1977). The first visibility of the lunar crescent. *Vistas in Astronomy*, *21*, 331–358. https://doi.org/10.1016/0083-6656(77)90021-6

Danjon, A.-L. (1936). Le croissant lunaire [The Lunar Crescent]. *L'Astronomie: Bulletin de La Société Astronomique de France*, 57–65.

Doggett, L., Schaefer, B., & Doggett, L. (1994). Lunar Crescent Visibility. *Icarus*, *107*(2), 388–403. https://doi.org/10.1006/icar.1994.1031

Faid, M. S. (2020). *Algoritma Penentu-sah Laporan Kenampakan Anak Bulan*. UiTM Shah Alam.

Faid, M. S., Mohd Nawawi, M. S. A., Abdul Wahab, R., & Ahamad, N. (2023). Hilalpy: Software to analyse lunar sighting criteria. *Software Impacts*, 100593. https://doi.org/10.1016/j.simpa.2023.100593

Faid, M. S., Mohd Nawawi, M. S. A., & Mohd Saadon, M. H. (2023). Analysis tool for lunar crescent visibility criterion based on integrated lunar crescent database. *Astronomy and Computing*, *45*, 100752. https://doi.org/10.1016/j.ascom.2023.100752

Faid, M. S., Mohd Nawawi, M. S. A., & Mohd Saadon, M. H. (2024). *Design, Development And Analysis Of Lunar Crescent Visibility Criterion With Python*. CRC PRESS.

Faid, M. S., Nawawi, M. S. A. M., Saadon, M. H. M., Ahmad, N., Ali, A., & Zin, M. (2022). Islamic Historical Review on Middle Age Lunar Crescent Visibility Criterion. *Journal of Al-Tamaddun*, *17*(1), 109–125.

Faid, M. S., Nawawi, M. S. A. M., Saadon, M. H. M., Nahwandi, M. S., Shariff, N. N. M., Hamidi, Z. S., Wahab, R. A., Norman, M. P., & Ahmad, N. (2023). Confirmation methodology for a lunar crescent sighting report. *New Astronomy*, *103*, 102063. https://doi.org/10.1016/j.newast.2023.102063

Faid, M. S., Nawawi, M. S. A. M., Saadon, M. H. M., Wahab, R. A., Ahmad, N., Nahwandi, M. S., Ahmed, I., & Mohamed, I. (2024). Assessment and review of modern lunar crescent visibility criterion. *Icarus*, *412*, 115970. https://doi.org/10.1016/j.icarus.2024.115970

Faid, M. S., Shariff, N. N. M., Hamidi, Z. S., Kadir, N., Ahmad, N., & Wahab, R. A. (2018). Semi empirical modelling of light polluted twilight sky brightness. *Jurnal Fizik Malaysia*, *39*(2), 30059–30067.

Faid, M. S., Shariff, N. N. M., Hamidi, Z. S., Sabri, S. N. U., Zainol, N. H., Husien, N. H., & Ali, M. O. (2016). Monitoring the Level of Light Pollution and Its Impact on Astronomical Bodies Naked-Eye Visibility Range in Selected Areas in Malaysia Using Sky Quality Meter. *Journal of Industrial Engineering and Management Science*, *2016*(1), 1–18. https://doi.org/10.13052/jiems2446-1822.2016.007

Faid, M. S., Shariff, N. N. M., Hamidi, Z. S., Wahab, R. A., Ahmad, N., Mohd Nawawi, M. S. A., & Nahwandi, M. S. (2024). Alteration of twilight sky brightness profile by light pollution. *Scientific Reports*, *14*(1). Scopus. https://doi.org/10.1038/s41598-024-76550-3

Fatoohi, L. (1998). *First visibility of the lunar crescent and other problems in historical astronomy*. Durham University.

Fotheringham, J. K. (1910). On The Smallest Visible Phase of the Moon. *Monthly Notices of the Royal Astronomical Society*, *70*, 527.

Gautschy, R. (2014). On the Babylonian sighting-criterion for the lunar crescent and its implications for Egyptian lunar data. *Journal for the History of Astronomy*, *45*(1), 79–90.

Hasanzadeh, A. (2012). Study of Danjon limit in moon crescent sighting. *Astrophysics and Space Science*, *339*(2), 211–221. https://doi.org/10.1007/s10509-012-1004-y

Hoffman, R. E. (2003). Observing the new Moon. *Monthly Notices of the Royal Astronomical Society*, *340*(3), 1039–1051. https://doi.org/10.1046/j.1365-8711.2003.06382.x

Ilyas, M. (1984a). *A Modern Guide To Astronomical Calculations Of Islamic Calendar, Times And Qibla*. Berita Publishing.

Ilyas, M. (1984b). Limb Shortening and the Limiting Elongation for the Lunar Crescent's Visiblity. *Quarterly Journal of Royal Astronomy Society*, *25*, 421–422.

Ilyas, M. (1986). A Shifting Date Line: An Interesting Feature of Solar Calendar. *Journal of Royal Astronomical Society of Canada*, *80*(3), 134–141.

Ilyas, M. (1994). Lunar Crescent Visibility Criterion and Islamic Calendar. *Quarterly Journal of Royal Astronomical Society*, *35*, 425–461.

Ilyas, M. (1997a). *Sistem kalendar islam dari perspektif astronomi [The Islamic calendar system from an astronomical perspective]*. Dewan Bahasa dan Pustaka.

Ilyas, M. (1997b). *Sistem kalendar islam dari perspektif astronomi [The Islamic calendar system from an astronomical perspective]*. Dewan Bahasa dan Pustaka.

King, D. A. (1991). Lunar Crescent Visibility Predictions in Medieval Islamic Ephemerides. In S.M. Seikaly, R. Baalbaki, & P. Dodd (Eds.), *Quest for Understanding: Arabic and Islamic Studies in Memory of Malcolm H. Kerr: Vol. IV*. American University of Beirut.

King, D. A. (1993). *Astronomy in the service of Islam*. Routledge.

Kordi, A. (2003). The Psychological Effect On Sighting of The New Moon. *Observatory*, 219–223.

Maunder, E. W. (1911). On the Smallest Visible Phase of the Moon. *The Journal of the British Astronomical Association*, *21*, 355–362.

McPartlan, M. A. (1996). Astronomical Calculation of New Crescent Visibility. *Quarterly Journal of Royal Astronomical Society*, 837–842.

Mohd Nawawi, M. S. A., Man, S., Zainuddin, M. Z., Abdul Wahab, R., & Ahmad Zaki, N. (2015). Sejarah Kriteria Kenampakan Anak Bulan di Malaysia. *Journal of Al-Tamaddun*, *10*(2), 61–75. https://doi.org/10.22452/JAT.vol10no2.5

Mostafa, Z. (2005). Lunar Calendars: The New Saudi Arabian Criterion. *The Observatory*, *125*, 25–30.

Mufid, A., & Djamaluddin, T. (2023). The implementation of new minister of religion of Brunei, Indonesia, Malaysia, and Singapore criteria towards the Hijri calendar unification. *HTS Teologiese Studies / Theological Studies*, *79*(1). https://doi.org/10.4102/hts.v79i1.8774

Mustapha, A. S., Zainol, N. Z. N., Mohammad, C. A., Khalim, M. A., Muhammed, N. K. W., & Faid, M. S. (2024). Al-Fatani's Perspectives on Islamic Family Law: Insights from Hidayah Al-Muta'allim Wa'Umdah Al-Muta'alim. *Journal of Islamic Thought and Civilization*, *14*(1), 247–265. https://doi.org/10.32350/jitc.141.15

Nawawi, M. S. A. M., Zainuddin, M. Z., Ahmad, N., Niri, M. A., Man, S., Wahab, R., Ismail, K., & Zaki, N. H. A. (2012). Application of scientific approach to determine lunar crescent's visibility. *Middle East Journal of Scientific Research*, *12*(1), 96–100. Scopus. https://doi.org/10.5829/idosi.mejsr.2012.12.1.1672

Neugebauer, P. V. (1929a). *Astronomische Chronologie*. Walter de Gruyter & Co.

Neugebauer, P. V. (1929b). *Astronomische Chronologie*. Walter de Gruyter & Co.

Qureshi, M. S. (2010). A New Criterion For Earliest Visibility of New Lunar Crescent. *Sindh University Research Journal (Sci. Ser.)*, *42*(1), 1–16.

Rahimi, A. A., & Zainal, B. (2019). Ketepatan Takwim Hijri Malaysia Berdasarkan Cerapan Fasa Bulan Purnama [The Accuracy Of Takwim Hijri Malaysian Based On Full Moon Phase Observations]. *AL-QIYAM International Social Science and Humanities Journal*, *2*(2), 12–23.

Rethlefsen, M. L., Kirtley, S., Waffenschmidt, S., Ayala, A. P., Moher, D., Page, M. J., Koffel, J. B., Blunt, H., Brigham, T., Chang, S., Clark, J., Conway, A., Couban, R., de Kock, S., Farrah, K., Fehrmann, P., Foster, M., Fowler, S. A., Glanville, J., … Young, S. (2021). PRISMA-S: an extension to the PRISMA Statement for Reporting Literature Searches in Systematic Reviews. *Systematic Reviews*, *10*(1). https://doi.org/10.1186/s13643-020-01542-z

Rodzali, M. Z., & Man, S. (2021). Relevansi Takwim Uhadi Dengan Syarat-Syarat Ditetapkan Kongres Istanbul 2016 Bagi Takwim Hijri Global. *Online Journal of Research in Islamic Studies*, *8*(1).

Schaefer, B. (1987a). An Algorithm for Predicting the Visibility of the Lunar Crescent. *Bulletin of the American Astronomical Society*, *19*, 1042.

Schaefer, B. (1987b). Heliacal Rise Phenomena. *Journal for the History of Astronomy, Archaeoastronomy Supplement*, *18*, 19.

Schaefer, B. (1990a). Lunar Visibility and the Crucifixion. *Quarterly Journal of Royal Astronomical Society*, *31*(53–67).

Schaefer, B. (1990b). Telescopic Limiting Magnitude. *Publications of the Astronomical Society of the Pacific*, *102*, 212–229.

Schaefer, B. (1991a). Length of Lunar Crescent. *Quarterly Journal of Royal Astronomical Society*, *32*, 265–277.

Schaefer, B. (1991b). Length of the Lunar Crescent. *Quarterly Journal of Royal Astronomical Society*, *29*, 511–523.

Schaefer, B. (1991c). Sunspot visibility. *Quarterly Journal of the Royal Astronomical Society*.

Schaefer, B. (1996a). Lunar Crescent Visibility. *Quarterly Journal of Royal Astronomical Society*, 759–768.

Schaefer, B. (1996b). Lunar Crescent Visibility. *Quarterly Journal of Royal Astronomical Society*, 759–768.

Schaefer, B. (2000). New Methods and Techniques for Historical Astronomy and Archaeoastronomy. *Archaeoastronomy*, 121.

Schoch, C. (1921). The Earliest Visible Phase of the Moon. *The Classical Quarterly*, *15*(194).

Sultan, A. H. (2003). Hijiri Calendar & Lunar Visibility: A Physical Approach. *3rd Islamic Astronomical Conference on Astronomical Applications in Islamic Sharia'*.

Sultan, A. H. (2004). New Explanation for Length Shortening of The New Crescent Moon. *Seminars of the United Nations Programme on Space Applications*, 83.

Sultan, A. H. (2006). "Best Time" For the First Visibility of the Lunar Crescent. *The Observatory*, 115–118.

Sultan, A. H. (2007a). First Visibility Of The Lunar Crescent: Beyond Danjon's Limit. *The Observatory*, *53–59*.

Sultan, A. H. (2007b). First Visibility Of The Lunar Crescent: Beyond Danjon's Limit. *The Observatory*, *127*(1), 53–59.

Utama, J. A., Zuhudi, A. R., Prasetyo, Y., Rachman, A., Sugeng Riadi, A. R., Nandi, & Riza, L. S. (2023). Young lunar crescent detection based on video data with computer vision techniques. *Astronomy and Computing*, 100731. https://doi.org/10.1016/j.ascom.2023.100731

Yallop, B. D. (1998a). A Method for Predicting the First Sighting of the Crescent Moon. In *Nautical Almanac Office*. Nautical Almanac Office.

Yallop, B. D. (1998b). A Note on the Prediction of the Dates of First Visibility of the New Crescent Moon. In *Astronomical Information Sheet*.

Zainal, B. (2001). *A Selective Literature Review of Young Moon Crescent Visibility Studies*. International Crescent Observation Project. http://www.icoproject.org/paper.html#english

Zulkeflee, A. N., Yussof, W. N. J. H. W., Umar, R., Ahmad, N., Mohamad, F. S., Man, M., & Awalludin, E. A. (2022). Detection of a new crescent moon using the Maximally Stable Extremal Regions (MSER) technique. *Astronomy and Computing*, *41*, 100651. https://doi.org/10.1016/j.ascom.2022.100651